Untersuchung zur semi-kontinuierlichen Separation von Wasserstoff-Isotopen für die Fusion

Investigation on the Semi-Continuous Separation of Hydrogen Isotopes for Fusion

Zur Erlangung des akademischen Grades eines

Doktors der Ingenieurwissenschaften (Dr.-Ing.)

von der KIT-Fakultät für Maschinenbau des

Karlsruher Instituts für Technologie (KIT)

genehmigte

Dissertation

von

Cyra Felicitas Georgina Neugebauer M.Sc.

aus Freiburg im Breisgau

Tag der mündlichen Prüfung: 04.11.2022

Referent:	Prof. Dr.-Ing. Robert Stieglitz
Korreferent:	apl. Prof. Dr.-Ing. Leo Bühler

Kurzfassung

Um die hohe Effizienz einer Fusionsreaktion zu gewährleisten, muss der Fusionsbrennstoff die beiden Wasserstoffisotope Deuterium (D_2) und Tritium (T_2) im nahezu äquimolaren Verhältnis aufweisen. Die Menge des dritten Isotops Protium (H_2) darf eine Obergrenze in der Größenordnung von 1 % nicht überschreiten. Deshalb erfordert ein Fusionsreaktor einen Brennstoffkreislauf, der das Fusionsabgas und das im Blanket erbrütete Tritium so aufbereitet, dass dieser Brennstoff jederzeit bereitgestellt wird. In dem Teil des Brennstoffkreislaufes „Protium Removal & Isotope Rebalancing“ wird Protium kontinuierlich abgetrennt und das Verhältnis von Deuterium und Tritium angepasst. Bisher wird eine Technologie eingesetzt, die eine lange Prozesszeit und damit ein hohes Tritiuminventar aufweist. Ziel dieser Arbeit ist es, eine alternative Technologie zu entwickeln und qualifizieren, mit der sich Fraktionen von Wasserstoffisotopen anreichern lassen.

Hierzu wird ein neuartiges diskontinuierliches Konzept zur Trennung der Isotope entwickelt, das zwei Trennungsprinzipien kombiniert: Gasdiffusion und Wasserstoff-Metall-Wechselwirkungen in einem zyklischen Prozess. Dieses als "Membrane Coupled - Temperature Swing Absorption" (MC-TSA) Prinzip erfüllt die Anforderungen des zukünftigen Fusionskraftwerks DEMO. Das neue zweistufige Verfahren aus MC und TSA beinhaltet:

Stufe 1: Membrane werden für Gastrennungsanwendungen eingesetzt, nicht jedoch zur Trennung verschiedener Wasserstoffisotope. Der positive Trenneffekt von Membranen wurde in die Prozessentwicklung einbezogen und in Experimenten nachgewiesen. Die Trennwirkung beruht auf der Diffusion der Isotope durch die Poren der Membran. Für den DEMO-Upscale kann eine Tritiumreduzierung um bis zu 38.5 % erreicht werden.

Stufe 2: Wasserstoff-Metall-Wechselwirkungen werden in erster Linie zur Wasserstoffspeicherung und nicht zur Abtrennung genutzt. Für meinen Zweck wurden die Eigenschaften von zwei verschiedenen Materialien analysiert, um den Isotopeneffekt nachzuweisen. Zusätzlich wurde ein Prüfstand entwickelt, um das Verhalten von Temperatur und Druck zu bestimmen. Pd und $TiCr_{1.5}$ erwiesen sich als geeignete Kandidaten. Palladium absorbiert das leichtere Isotop bevorzugt, während die Legierung aus Titan Chrom das schwere Isotop präferiert aufnimmt.

In einem nächsten Schritt wurde ein zweiter Hauptprüfstand entworfen und gebaut, um die beiden Trennstufen MC und TSA experimentell zu untersuchen. Die zwei zuvor untersuchten Materialien wurden in dieser Anlage in jeweils in eine Kolonne gefüllt. Durch Temperaturzyklen und Strömung zwischen den beiden Kolonnen erfolgt eine Auftrennung. An jedem Ende der Kolonne reichert sich, abhängig vom Material,

ein Isotop an. Die experimentelle Trennung der Wasserstoffisotope wurde erfolgreich demonstriert und die TSA-Stufe mit einem angepassten Simulationsmodell validiert. Für diese Stufe wurden insgesamt drei Parameterstudien durchgeführt. Der Parameter mit dem besten Ergebnis (Trennwirkung über die Zeit) wurde für die nächste Studie verwendet. In der ersten Studie wurden vier Temperaturen verglichen, wobei 288-383 K als das beste Ergebnis ermittelt wurde (Anreicherung von H_2 von 42,2 % auf 58,5 %, D_2 von 57,8 % auf 77 %). In der zweiten Parameterstudie sind drei verschiedene Prozessschritte durchgeführt worden (schnelle Ventileinstellungen, Zusatzbehälter, stationärer Zustand), wobei der Behälter die besten Anreicherungsergebnisse lieferte (H_2 von 42,2 % bis 66,54 %, D_2 von 57,8 % bis 78,54 %). In der letzten Studie wurden drei verschiedene Anzahlen von Zyklen miteinander verglichen (3, 5 und 10), wobei sich 3 Zyklen als die beste Einstellung herausstellten.

Ein Scale-up in Bezug auf DEMO auf der Grundlage der in den Versuchen ermittelten besten Parameter hat gezeigt, dass dieses zweistufige Prinzip die Anforderungen erfüllt. Die MC-Stufe ist wichtig, um das hohe Tritiuminventar zu reduzieren, und die TSA-Stufe ist für die Entfernung von Protium unerlässlich.

Abstract

To ensure the high efficiency of a fusion reaction, the fusion fuel must contain the two hydrogen isotopes deuterium (D_2) and tritium (T_2) in an approximately equimolar ratio. The amount of the third isotope protium (H_2) is not allowed to exceed an upper limit in the range of 1 %. Therefore, a fusion reactor requires a fuel cycle that processes the fusion exhaust gas and the tritium breeded in the blanket in a way that this fuel is provided at any time. In the "Protium Removal & Isotope Rebalancing" part of the fuel cycle, protium is continuously removed and the ratio of deuterium and tritium is rebalanced. So far, a technology is used that has a long process time and thus a high tritium inventory. The aim of this work is to develop and qualify an alternative technology to enrich fractions of hydrogen isotopes.

For this purpose, a novel discontinuous concept for the separation of the isotopes is developed, which combines two separation principles: Gas diffusion and hydrogen-metal interactions in a cyclic process. This principle, known as "Membrane Coupled - Temperature Swing Absorption" (MC-TSA), satisfies the requirements of the future fusion power plant DEMO. The new two-stage process consisting of MC and TSA includes:

Stage 1: Membranes are used for gas separation applications, but not for separating different hydrogen isotopes. The positive separation effect of membranes has been included in the process development and proven in experiments. The separation effect is based on the diffusion of the isotopes through the pores of the membrane. For the DEMO upscale, a tritium reduction of up to 38.5 % can be achieved.

Stage 2: Hydrogen-metal interactions are primarily used for hydrogen storage rather than separation. For my purpose, the properties of two different materials have been analysed to demonstrate the isotope effect. In addition, a test rig has been developed to determine the behaviour of temperature and pressure. Pd and $TiCr_{1.5}$ proved to be suitable candidates. Palladium absorbs the lighter isotope preferentially, while the alloy of titanium chromium absorbs the heavy isotope in a preferred way.

In a next step, a second main test rig was designed and built to experimentally investigate the two separation stages MC and TSA. The two materials previously investigated have each been placed in a column in this facility. Temperature cycling and flow between the two columns causes separation. At each end of the column, an isotope enriches, depending on the material. The experimental separation of the hydrogen isotopes has been successfully demonstrated and the TSA stage validated with an adapted simulation model. A total of three parameter studies have been carried out for this stage. The parameter with the best result (separation effect over time) has

been used for the next study. In the first study, four temperatures have been compared and 288-383 K has been identified as the best result (enrichment of H_2 from 42.2 % to 58.5 %, D_2 from 57.8 % to 77 %). In the second parameter study, three different process steps have been carried out (fast valve settings, additional tank, steady state), with the vessel giving the best enrichment results (H_2 from 42.2 % to 66.54 %, D_2 from 57.8 % to 78.54 %). In the final study, three different numbers of cycles have been compared (3, 5 and 10), with 3 cycles proving to be the best setting.

A scale-up in terms of DEMO based on the best parameters determined in the experiments has shown that this two-stage principle meets the requirements. The MC stage is important to reduce the high tritium inventory and the TSA stage is essential for protium removal.

Table of Contents

Latin symbols and constants

Symbol	Description	Unit
A_M	Surface of membrane	(m^2)
c	Concentration	(mol_Q/mol_{Me})
d	Molecule diameter	(m)
d_p	Pore diameter	(m)
D_p	Particle diameter	(m)
D	Diffusivity	(m^2/s)
F_G	Permeation gas flow in the membrane	(mol/s)
F_n	Flux between two nodes	(mol/s)
$\bar{G}_H$	Molar Gibbs free energy	(kJ/mol)
$\bar{H}_H$	Molar enthalpy	(kJ/mol)
I	Inventory	(mol)
k	Boltzmann constant	($m \cdot kg/s^2$)
Kn	Knudsen number	(/)
K_s	Sieverts constant	$Pa^{0.5}/((mol_Q/mol_{Me}))$
L_M	Length of membrane	(m)
L_n	Length per node	(m)
m	Mass	(kg)
M	Molar mass	(g/mol)
n_Q	Number of hydrogen atoms	(/)
n_s	Number of metal atoms	(/)
p	Pressure	(Pa)
$\bar{P}_G$	Permeance	($mol \cdot s/(m \cdot kg)$

R	Gas constant	(J/(mol·K)
S_H	Molar enthalpy	(J/(mol·K)
T	Temperature	(K)
X_P	Part from the outlet stream permeate	(/)
X_R	Part from the outlet stream retentate	(/)

Greek symbols and constants

Symbol	Description	Unit
α_{HD}	Separation factor for protium-deuterium	(/)
α_{HT}	Separation factor for protium-tritium	(/)
Δ	Difference	As indicated
ε	Porosity	(/)
λ	Mean free path	(m)
η	Dynamic viscosity	(Pa·s)
$\bar{\sigma}$	Standard deviation	(/)
$\hat{\mu}$	Arithmetic average	As indicated
τ	Tortuosity	(/)
ν_i	Degree of freedom	As indicated

Indices

Index	Description
abs	Absorption
cool	Cooling
D	Deuterium atom
D_2	Deuterium molecule
des	Desorption
gas	Gas phase
H	Protium atom

H_2	Protium molecule
heat	Heating
Q	Hydrogen atom (all three isotopes)
Q_2	Hydrogen molecule (all three isotopes)
solid	Solid phase
T	Tritium atom
T_2	Tritium molecule

Abbreviations

Abbreviation	Description
bcc	Body Centured Cubic structure
C1	Column 1
C2	Column 2
CD	Cryodistillation
DEMO	DEMOnstration power plant
DIRL	Direct Internal Recyling Loop
EPS	Exhaust Processing System
fcc	Face Centered Cubic structure
hcp	Hexagonal Closed Package
GAIA	Gas Analyser for Ionized Atoms (Name of Test facility)
GC	Gas Chromatography
GCE	Gas Centrifugation
GD	Gaseous Diffusion
HESTIA	Hydrogen Experiments for Separation with Temperature Initiated Absorption (Name of Test facility)
IIE	Inverse Isotope Effect
INTL	INer Tritium Loop
IR	Isotope Rebalancing
ISS	Isotope Separation System

ITER	International Thermonuclear Experimental Reactor (Latin: the way)
MAGIS	Magentically Activated and Guided Isotope Separation
MAIA	MAterial Investigations for Absorption (Name of Test facility)
MC-TSA	Membrane Coupled-Temperature Swing Absorption
Me	Metal
MFC	Mass Flow Controller
MS	Molecular Sieve
NIE	Normal Isotope Effect
O-site	Octahedral site
OUTL	Outer Tritium Loop
NBI	Neutral Beam Injection
PID	Piping and Instrumentation Diagram
PR	Protium Removal
PSA	Pressure Swing Adsorption
QMS	Quadrupole Mass Spemtrometer
QS	Quantum Sieving
SEM	Secondary Electron Multiplier
STP	Standard Temperature and Pressure
T-site	Tetrahedral site
TCAP	Thermal Cycling Absorption Process
TH	Thermal Diffusion
ZPE	Zero Point Energy

Danksagung

Vielen Dank an Herrn Prof. Robert Stieglitz für die offizielle Betreuung und Beratung während der Doktorarbeit. Danke auch an Herrn Prof. Leo Bühler für die Übernahme als Zweitprofessor.

Ein großer Dank geht an Herrn Dr. Christian Day für die fachliche Betreuung. Danke, dass Sie mir den nötigen Freiraum zur Selbstentfaltung gegeben haben, aber immer für mich da waren, wenn ich Sie gebraucht habe. Durch Ihre fachliche und strategische Expertise haben ich viel von Ihnen lernen können und ich hatte stets große Freude an meiner Arbeit.

Danke Volker Hauer für deine Hilfsbereitschaft, dein breites Wissen jederzeit und mit großem Engagement mit mir zu teilen. Meinen Mitdoktoranden Dr. Benedikt Peters, Yannick Kathage und Dr. Yannick Hörstensmeyer möchte ich für den fachlichen Austausch danken, sowie auch für die Zusammenarbeit und Unterstützung bei der Modellierung. Alex Vazquez-Cortes möchte ich für die Unterstützung, Freundschaft und auch Korrekturen meiner Arbeit danken – muchas gracias. Danke Katharina Battes für deine Hilfestellung und Geduld bei der Optimierung des Massenspektrometers, deine weibliche Unterstützung in der Gruppe und die Freundschaft, die sich in den letzten Jahren entwickelt hat. Danke Martin Jäger und Thomas Johann, dass ihr mir immer mit hoher fachlicher Kompetenz und Flexibilität geholfen habt, wenn ich mechanische Fragen hatte – und mit mir regelmäßig interessante Gespräche beim Kaffee trinken geführt habt.

Ein großer Dank geht an Stefan Hanke, der mich durch seine Betreuung während der Masterarbeit so gut in die Gruppe eingeführt hat, dass mir das „Ja“ Sagen zur Doktorarbeit leicht gefallen ist. Zudem bin ich froh, mit Stefan, Santiago und Matthieu so tolle Menschen kennengelernt zu haben, mit denen sowohl das Arbeitsklima als auch jegliche Freizeitaktivitäten viel Spaß gemacht haben – muchas gracias und merci beaucoup.

Jürgen Jung und Hartmut Stump möchte ich für die Unterstützung auf der elektrischen Seite danken. Der größte Dank geht an Peter Pfeil auf der elektrischen und Jürgen Weinhold auf der mechanischen Seite. Danke, dass ich mich bei allen Fragen an euch wenden konnte und ihr mit großem Engagement die Anlage aufgebaut habt. Ich habe sehr viel von eurer jahrzehntelangen Erfahrung gelernt. Ohne euch beide würde die Anlage nicht so stehen und funktionieren wie sie es tut.

Auch außerhalb der Gruppe habe ich viele tolle Menschen kennengelernt, mit denen sowohl der fächerübergreifende Austausch, Gespräche beim gemeinsamen auf die Arbeit und Nachhause radeln, als auch die gemeinschaftlichen Ausflüge, wie morgendliches Schwimmen und Abende sehr bereichernd waren. Danke dafür an Shahab, Kai, Wolfram, Melanie, Manu, Ingeborg, Tina und Fabian. Auch möchte ich meinen weiteren Freunden Tugce, Maria, Tanja, Annabel, Rima und Nadine, sowie meinen tollen Mitbewohnern Miri, Lea, Anne und Jona danken. Ihr ward eine große Entlastung und es war schön, immer einen vertrauensvollen Gesprächspartner zu Hause zu haben, sowie einfach Essen von euch nehmen zu können – ein herzlicher Dank von eurer Lieblings-Boomerin.

Muchas muchas gracias an Dr. Ester Diaz. Du warst mit die größte Unterstützung während meiner Doktoranden Zeit. Ich bin so dankbar, dich während meiner Zeit am ITEP kenngelernt zu haben und dich inzwischen als eine meiner engsten Freudinnen zählen zu dürfen. Die vielen fachlichen und zwischenmenschlichen Gespräche, unsere stundenlangen Sprachnachrichten, Mädelsabende, ... haben mir so gut getan. Danke Ester, dass du in mein Leben gekommen bist, auf die nächsten gemeinsamen Jahre. Auch meinen anderen Freunden, die immer für mich da waren, möchte ich an dieser Stelle danken. Vielen Dank an Laura, dass du meine Erstversion durchgelesen und korrigiert hast und ich mich mit dir immer über fachliche Themen austauschen kann. Auch möchte ich Christine und Anne danken. Ich bin sehr froh so lange Freundschaften zu haben. Ihr habt mir immer zugehört (auch wenn ich Dinge 100 Mal wiederhole) und habt mich aufgefangen, wenn ich mal das ein oder andere Tief hatte. Thanks to Vanessa, für die sprachliche und freundschaftliche Unterstützung. Ich bin so froh, euch alle in meinem Leben zu haben.

Am allermeisten möchte ich meiner Familie für die Unterstützung danken. Ohne euch wäre ich nicht da, wo ich jetzt bin. Danke an Susanne und Norbert, dass ihr für mich da seid. Und Norbert, vielen Dank für deine Fusionskenntnisse, deine mentale Unterstützung während der Doktorarbeit und beim Schreiben, denn du weißt wie sich das anfühlt. Vielen Dank an meine tolle Mama, dass du immer für mich da bist, mich stärkst, unterstützt und mir gut zuredest. Auch meinem Papa möchte ich für die lebenslange Unterstützung sowie den fachlichen Austausch während meiner gesamten Doktorarbeit und für die mehrfache Korrektur meiner Arbeit danken. Ich habe von dir, deinem Ingenieurwissen und strukturiertem Denken viel gelernt. Danke, dass ihr immer an mich geglaubt habt und wusstet, dass ich es hinbekomme. Und auch danke, dass ihr mich meinen eigenen Weg habt gehen lassen und dabei immer stärkend an meiner Seite ward. Das Ganze gilt auch für meine Schwester Maja. Du bist einer der Menschen die mich mit am Meisten kennt und die mir unendlich wichtig ist. Meine erste Anlage

(MAIA) ist dir gewidmet. Meine gesamte Arbeit möchte ich mein Großeltern widmen, die für mich ein ganz wichtiger Teil in meinem Leben waren. Leider haben sie meine Arbeit nicht mitbekommen, sie wären aber sicherlich sehr stolz auf mich.

Bei einer Doktorarbeit lernt man nicht nur viel fachliches Wissen, sondern man entwickelt sich auch persönlich unglaublich weiter. Ich bin sehr froh, dass ich diese Erfahrung, auch wenn sie mit einigen Hürden verbunden war, erleben durfte.

1 Introduction

In the following chapter, the fundamentals of nuclear fusion to motivate the topic of this thesis are presented. Subsequently, the objectives of this dissertation and finally its structure are described.

1.1 Nuclear Fusion as an Energy Source

The world is facing the challenge of an increasing need for energy supply and the necessity to significantly reduce the carbon footprint. The only way out of the climate crisis is the usage of carbon free energy sources, as renewable or nuclear energies. For the latter, two options arise - fission and fusion. In fission, energy is generated by splitting of heavy nuclei, while in fusion this is done by merging of light nuclei. In contrast to nuclear fission, nuclear fusion has not yet been commercially utilised to produce energy. In nature, this process arises in the sun, which mainly consists of the lightest hydrogen isotope protium (H) with 75 %. With the temperature of 15 million Kelvin in the sun's core, protium is present as plasma. Due to appropriate conditions, protium nuclei are able to overcome repulsive Coulomb forces during their impact. According to Lawson's criterion, the three parameters confiment time τ, plasma density n and plasma temperature T are required to continue the reaction [1]. Two different concepts exist:

i) Inertial Confinement Fusion (ICF): In this regime, extreme high density plasma combined with extreme short confinement time τ is used. Energy is often provided with laser light and the fuel is available in pellet form.

ii) Magnetic Confinement Fusion (MCF): Thinner reactor plasma together with a relative long confinement time scenario along magnetic field lines fulfils the Lawson Criterion at a given temperature. Researchers intend to reproduce this process on earth [1], and this is the basis for this thesis to focus on.

However, suitable conditions with protium on earth are much more difficult to achieve. In return, under achievable conditions, this leads to a low reaction rate. That is why it is important to use other reactants for the fusion reaction. Figure 1.1 gives an overview of the energy dependent cross section for different educts. The cross-section indicates the probability of the interaction between two particles. The reaction DT with the heavy hydrogen isotopes deuterium (D) and tritium (T), containing one and two neutrons in their nucleus, possesses by far the highest cross-section at the lowest energy. Although tritium is a radioactive gas with a half-life time of 12.32 years, only

this reaction is accessible without excessive temperatures. While deuterium is extracted from seawater, tritium is extremely rare in nature and must be breeded in the fusion power plant [1]. This happens in the so-called breeding blanket, which is a module surrounding the reactor. Tritium is produced relying on the neutron bombardment of lithium, which is present in the breeding blanket (using the neutrons from the plasma).

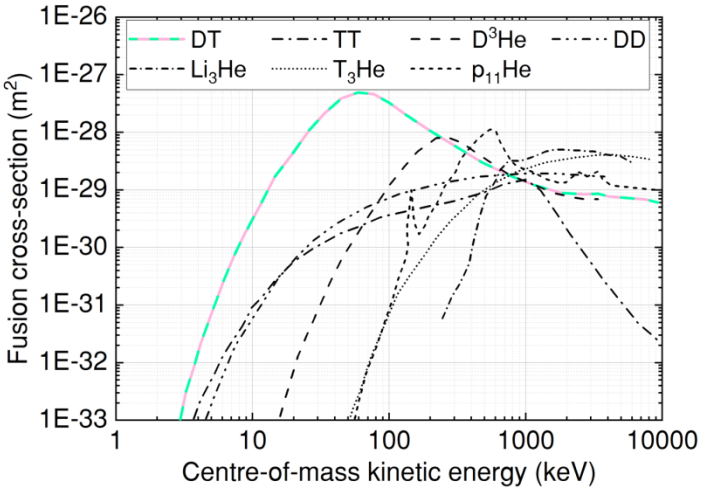

Figure 1.1: Cross-section of different possible fusion reactions as a function of kinetic energy of the system adapted from [1].

Selecting the DT fusion, the reaction of deuterium and tritium is the following:

$$\mathrm{D} + \mathrm{T} \rightarrow {}^{4}\mathrm{He} + \mathrm{n}. \tag{1.1}$$

The produced ^{4}He carries an energy of 3.5 MeV, which is used for plasma heating. The energy of the neutron (14.1 MeV) is transformed into heat when the walls of the reactor are hit. This heat is conventionally transformed into mechanical power by a steam turbine and finally converted into electricity [1; 2; 3].

1.2 EU-DEMO as a Nuclear Fusion Device

Several experimental fusion devices exist in the world. This thesis attends to the European DEMO (DEMOnstration power plant), a future fusion power plant, which aims to fill the gap from experimental devices to commercial operation, providing electricity into the grid. A power plant consists of several main parts (as the tokamak, in which the reaction occurs), with the fuel cycle being one essential element for it to succeed. As this thesis is related to one part of the fuel cycle, the focus lays only on the fuel cycle and is shown in Figure 1.2. Summarising this, the fuel is generated in the requested composition for the fusion and cleans up the exhaust gas that arise during the reaction. As the reactivity of a fusion reaction is limited, only a certain fraction of

DT fuses, so that most of the fuel exits the torus, together with impurities (as protium) and fusion products (as helium), and needs to be supplied to the torus again. It is important that the tritium inventory needs to be limited due to its shortage as well as radiation safety requirements. Based on this, it is necessary to reduce the cycle time, which has a direct influence on the total plant tritium inventory. Continuous process technologies are therefore preferable wherever possible. Due to the inventory, the fuel cycle is divided into three main parts, the Direct Internal Recycling Loop (DIRL), the INner Tritium Loop (INTL) and the OUter Tritium Loop (OUTL). 80 % of the hydrogen isotopes from the torus are passed directly through the DIRL into the torus, where primarily vacuum pumps are utilized. This reduces the cycling time and therefore also the tritium inventory in the other parts of the fuel cycle drastically. The remaining gas, which enters the inner and outer loop, consists of the three hydrogen isotopes, impurities and plasma enhancement gases (N_2, Ar, Xe), which are added for radiative cooling for plasma control. These two loops are mainly constituted of purification stages. The INTL preserves appropriate conditions for the fusion reaction, by keeping the isotopes in a required composition (in the Isotope Rebalancing and Protium Removal stage) and extracting plasma enhancement gases (in the Exhaust Processing stage). The final cleaning steps, such as further reduction of the tritium content from the gas mixture, are done in the OUTL.

This work deals with a technology that needs to be developed for the **Isotope Rebalancing (IR)** and **Protium Removal (PR)** subsystems, situated in the INTL (subsystem marked in blue).

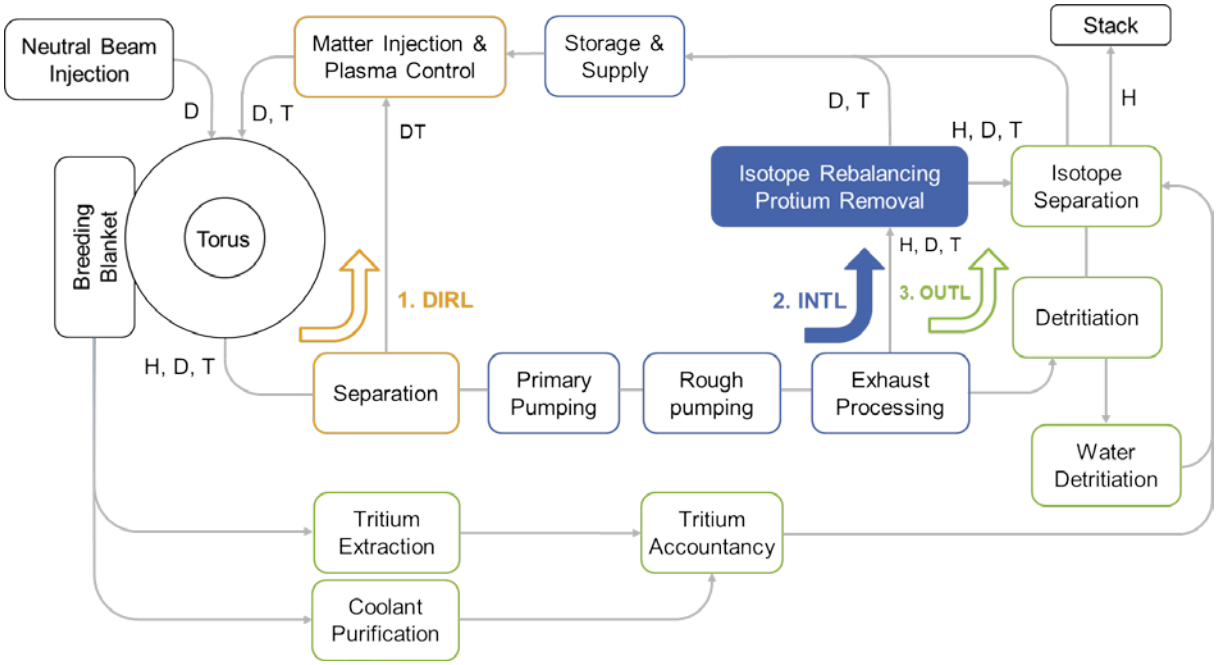

Figure 1.2: Overview of the fuel cycle of the EU-DEMO with the three cycles DIRL (orange), INTL (blue), OUTL (green), and its main subsystems adapted from [4]. The subsystem that is being discussed in this thesis is highlighted in blue.

The primary functions for IR and PR are:

i) To remove protium from the gas mixture:
ii) To balance deuterium and tritium to a certain required ratio.

For a stable reaction, it is important that both requirements are fulfilled.

i) Protium is not implemented for fusion, albeit it is inevitable as it enters the fuel cycle through outgassing from an exchange reaction of the plasma with the wall. In order to prevent a further increase of protium, which leads to an instability of the fusion reaction, a fraction of the protium gas therefore needs to be extracted in the Protium Removal System. The enriched protium stream from the INTL is purified in the OUTL via cryo-distillation (CD) and discharged to the atmosphere via the stack.
ii) The ratio of deuterium to tritium influences the fusion power, as seen in Figure 1.3. The aim is to operate at the maximum (composition 50:50 in the torus) to achieve the highest efficiency.

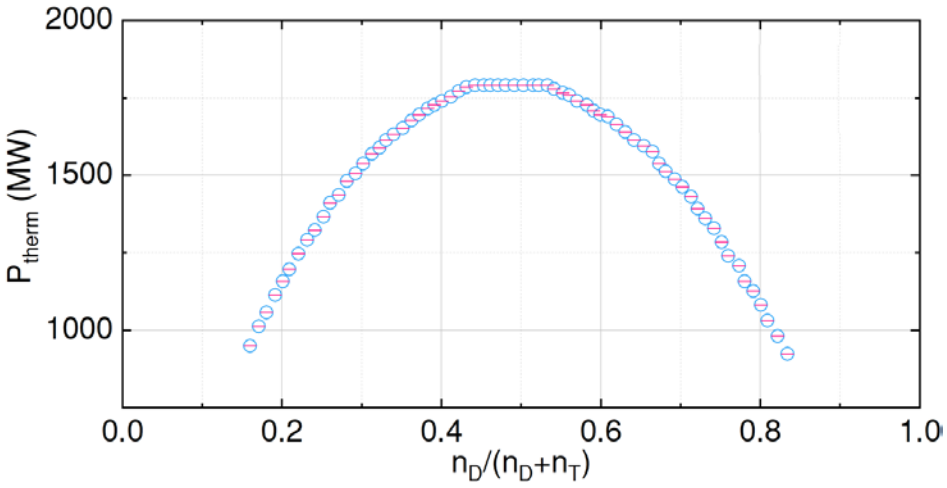

Figure 1.3: Thermal fusion power P_{therm} as a function of the D-T ratio adapted from [5].

Considering different parts of the fuel cycle, the D-T mixture becomes imbalanced. One major impact is coming from one of the heating systems for the plasma, especially the Neutral Beam Injection (NBI), as it is permanently flushed with pure deuterium and returns deuterium gas with trace tritium. Diffusion pumps downstream the torus have an isotope effect, which leads to an additional imbalance in the DIRL and the INTL. Another isotope effect arises also from tritium decay or selective hydrogen isotope permeation through the walls. The Isotope Rebalancing System needs to counteract this behaviour, otherwise the achievable fusion power declines, leading to a less stable operating mode.

1.3 Objective of Work

The main objective of this thesis is the **Demonstration of hydrogen isotope separation** (protium and deuterium) for the IRPR system. The logical chain to achieve this aim is shown in Figure 1.4, indicating that three other objectives have to be met first, all of which are related to each other.

At first, **1a) Concept development** of the IRPR has to be executed. The selection of an appropriate technology, its actual development and dimensioning is crucial.

Second, **1b) Material characterization** for isotope separation needs to be performed. Materials and their behaviour utilised for the separation process are one of the key elements. Verification and validation of identified materials require a test rig to be designed and assembled as well as to identify the impact of process parameters on efficiency.

Third, **1c) Model development** has to be implemented. To analyse the efficiency of the entire process chain of the IRPR, it is modelled by means of a system analysis tool, where ASPEN Custom modeller is used. In this model the material data measured are integrated. The results of this model are used to directly compare and validate the experimental results.

For the main objective **2) Demonstration of hydrogen isotope separation** on a laboratory scale associated with adequate measurement techniques, the separation feasibility and technology suitability for fusion is ascertained with a self-designed test rig.

Finally, the obtained results are used for a **3) Scale up for DEMO** fusion reactor to identify feasibility on technology gaps to be mastered in the future.

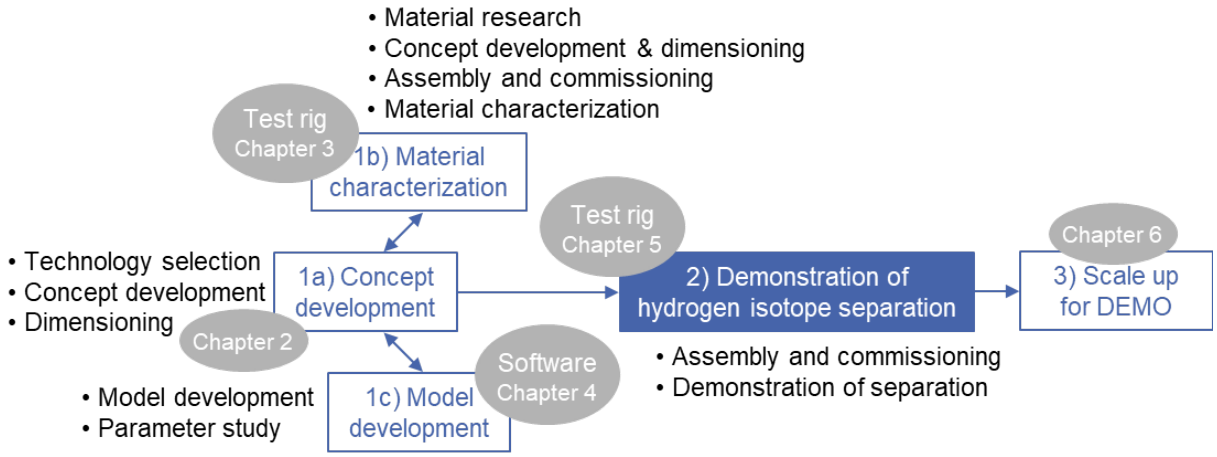

Figure 1.4: Logical chain of the main components to conceptualise, design and demonstrate hydrogen isotope separation.

1.4 Structure of Work

The structure of the work follows the workflow shown above.

Chapter 2 assesses various technologies for hydrogen isotope separation, including the one that has been selected and further developed. The fundamental principles of separation are explained more in detail.

In **Chapter 3**, the materials being used for separation of hydrogen isotopes are discussed further. At the beginning, different materials are compared with respect to identified requirements and the advantages and disadvantages are considered. The design including the measurement principle of the MAIA test rig is then presented. Next, the experimental procedure is discussed and the results of two selected materials with protium and deuterium are analysed.

Chapter 4 shows the modelling of the process in Aspen. First, basic structure and the most important formulas are explained and all assumptions made are listed. In the second part, parameters which are important for the configuration of DEMO are considered. Also, the results of the parameter study, which are subsequently also partly applied in the experimental separation, are explained.

In **Chapter 5**, parameters (temperature, process steps, amount of cycles) based on parameter study, including modelling results, are selected for experiments. The design of the test rig for hydrogen isotope separation is examined in further detail. The analysis device, which is necessary to quantify the process, is described. Finally, the procedure of the experiments, a parameter overview and commissioning is given.

In **Chapter 6**, all separation results are shown and compared to the modelling results.

In **Chapter 7**, extrapolation to tritium and hydrogen isotopologues is explained. An upscale is carried out and a statement is made regarding the feasibility for EU-DEMO with the modelling and experimental results. Next steps and considerations which need to be improved in the future are included.

Finally, **Chapter 8** gives a conclusion.

For abbreviations and symbols, the following terminology can be explained: The term hydrogen refers to all isotopes. This is abbreviated as Q_2 (as a molecule) or Q (as an atom). When it comes to specific isotopes, they are referred to as protium (H_2 or H), deuterium (D_2 or D) or tritium (T_2 or T). The consistent colouring and symbolism runs through the work: The curves of protium are filled symbols from the orange colour palette. Deuterium has non-filled symbols from the blue colour palette. For tritium, non-filled crossed out symbols from pink colour palette are used. Furthermore, to provide a clear overview, important points or decisions are marked in bold.

Since the technology under investigation is the first to be evaluated for separation of hydrogen isotopes, all experiments will be carried out with protium and deuterium only, and without the radioactive tritium. This is perfectly adequate to demonstrate the separation as such. Accordingly, visualisations and explanations are also given with H_2 and D_2 only, in order to maintain consistency for the experiments.

The term separation is often used in this work. However, in line with the intended application of the technology this is considered to be enrichment rather than a complete separation of the isotopes.

2 Development of a Hydrogen Isotope Separation Concept

This chapter is divided into two major sub-chapters. In the first part, the requirements for isotope separation, a description of different possible technologies and the selection process are discussed. In the second part, the new concept proposed in this thesis, as well as the basics of the separation principles are explained in detail.

2.1 Potential Technologies for Isotope Rebalancing and Protium Removal (IRPR) in a Fusion Reactor Fuel Cycle

In DT fusion devices prior to EU-DEMO, the hydrogen mixture has been completely separated into the individual isotopes with the cryo-distillation technology. This strategy is very inefficient, as the isotopes have to be intermixed afterwards to send them back to the torus. Instead, the approach pursued for the EU-DEMO is to only enrich the gas mixture and thus bring the isotopes into equilibrium. High purity is therefore neither necessary nor desirable for the "Isotope Rebalancing" system. However, for the "Protium Removal" system, a certain amount of separation is required.

2.1.1 Requirements for the IRPR Technology

It is important to distinguish between three classes of requirements, which are all interrelated:

i) Plant level requirements: They are necessary on the reactor level. A main criterion is the **minimization of the total tritium inventory**, which is directly related to the reduction of the residence time of tritium in each subsystem of the fuel cycle. For the "Isotope Rebalancing" subsystem, the molar ratio of deuterium to tritium is envisaged as 50:50. For the "Protium Removal" system, the maximum permitted amount of H_2 has been set to 1 % [6].

ii) Fuel cycle level requirements: The "Protium Removal" system requires providing a high purity of the deuterium-tritium gas mixture, which can be achieved by a technology with a **high separation factor**. A **continuous process** facilitates the reduction of the residence time. This is mainly important for the "Isotope Rebalancing" subsystem, as a high throughput is needed here. **Cryogenic temperature** has to be

avoided whenever feasible, as this translates into significantly increased infrastructure, and also puts considerable demands on the safety system due to gas vaporization. **Safety and environment** is one of the most important aspects for a safe operation. A sufficiently high **technical readiness level** is important for the selection of the process technology. Another aspect that is only secondary to the decision, but should not be disregarded, is the **operational cost**.
iii) Operational requirements: Aside from the separation factor, also the **temperature and pressure** need to be feasible. A temperature, as mentioned above cryogenic and below high-temperature application (preferably smaller than 473 K) is reasonable. For the pressure, lower values are preferred, especially below atmospheric pressure, due to tritium confinement safety aspects as well as reduction of the tritium inventory. Material **capacity** matters, as this has a direct impact on the performance. Another factor is the acceptable **disproportion** behaviour, which is essential for the durability of the material.

The requirements have been weighted with the pairwise comparison method and are shown in the Appendix A1 in Table A.1. Safety and environment, low tritium-inventory and high separation factor have been identified as the most important requirements. This is followed by technical readiness level and continuous process.

2.1.2 Potential Separation Techniques & Selection Process for IRPR

A number of possibilities exist for the separation of isotopes. In the following section an overview of technologies is given. Some of them have already been successfully tested with hydrogen, others have only been tested for the separation of other isotopes. The selection of the most suitable technology has been identified with the pairwise comparison method including the weighted requirements. This selection is shown in Appendix A1 with the results listed in Table A.2 to Table A.12. The final result is shown Table A.13:

Cryo-distillation (CD): This technology has proven to be a successful technology for separating the isotopes. The principle of separation is based on the different vapour pressures of the individual isotopes. At cryogenic temperatures, the isotopes, with H_2 being the most volatile, are liquefied successively between 20 and 30 K and can thus be separated from each other [7].

Magnetically Activated and Guided Isotope Separation (MAGIS): This technology involves polarising isotopes by using optical pumping. In this process, light reacts on an atom to change its magnetic state. The isotopes intended to separate are

pumped to a 'low-field-seeking state', while the remaining isotopes are pumped to a 'high-field-seeking state'. This is all done under vacuum to ensure that there are no collisions between the molecules, which can otherwise distract them. In summary, this method consists of three steps: (i) The source, by which the motion of the atoms is generated; (ii) The preparation, which brings the movement of the atoms into selected states, allowing magnetic separation; (iii) The steering, which splits the previously prepared atoms into trajectories. Separation of the ^{6}Li and ^{7}Li isotopes has been demonstrated [8; 9], but not for any other chemical species.

Gaseous Diffusion (GD): With this technology, diffusion occurs through a porous membrane due to a pressure difference. The pore diameter is chosen to be that small that there are no interactions between the molecules, but only interactions with the membrane wall. The difference in diffusion between the individual isotopes depends only on the molar mass, which means that the light hydrogen diffuses more quickly, resulting in a separation. The separation factor is also only dependent on the molar mass, with 1.41 for protium-deuterium as an ideal case [10; 11]. This technology has been used so far, for example, in the purification of uranium isotopes and the separation of hydrogen with other gases.

Gas Centrifugation (GCE): Centripetal forces are exploited to enable separation. Thereby the heavy isotope is enriched at the periphery of the device. The lighter isotopes are located in the centre of the device. The separation factor depends on the absolute mass difference instead of the ratio of molecular masses. Factors of 1.01 have been observed [12]. It has been invented as an alternative to GD for the separation of uranium isotopes. For hydrogen isotopes it has not yet been used.

Quantum Sieving (QS): Diffusion through a porous membrane without molecule-molecule interaction occurs here as well. In contrast to gaseous diffusion, however, there are two significant differences. The pore diameter is significantly smaller and is comparable to the de Broglie wavelength. Furthermore, diffusion takes place at cryogenic temperatures. Due to a quantum effect, the lighter isotope has a stronger barrier to overcome diffusion. This results in the heavy isotope having increased mobility through the porous membrane [13; 14].

Thermal Diffusion (TD): In this technology the different diffusion rates of the individual isotopes are utilised. A temperature gradient is applied in a column. This results into a shift of the isotopes, which is dependent on the molar masses as well as the forces between them. The heavy isotope is located in the warm region, whereas the light isotope is located in the cold region. The working principle of separation has been proven to work for uranium isotopes [15; 16].

Gas chromatography (GC): This technology is operating in a batch modus and already successful applied for separation of hydrogen isotopes. The used temperature reaches from cryogenic range up to more than 1000 K and is dependent on the applied material. This material is filled in a column and possesses different affinities for the individual isotopes. The isotope with the highest attraction is, according to the temperature, adsorbed or absorbed by the material. The other, isotope is consequently located in the gas phase. The addition of a carrier gas makes the gas in the column to move, resulting in a purified gas stream (mostly of the heavy isotopes) at the end of the column. Experiments have demonstrated that a high separation is possible [17; 18].

Thermal Cycling Absorption Process (TCAP): This technology is an upgrade of the GC. Also here the affinities of isotopes regarding certain materials are utilised. Instead of only one column, two columns are in operation, in which the isotopes flow fore- and backwards. This flow is generated due to temperature cycles in the columns. The applied temperature is related to the materials and can go from cryogenic to high temperatures. The main improvement is up to a semi-continuous flow, as no carrier gas is needed. At the end of one column, the purified light isotope, and at the end of the other column, the purified heavy isotope can be extracted. Research has shown that an enrichment at both ends of the columns of 98 % is possible [19].

Pressure Swing Adsorption (PSA): This technology is similar to TCAP, except that instead temperature is cycled, the temperature remains constant and the pressure is cycled. This process utilises the adsorption ability of the different gases. An increase in pressure leads to a physisorption of gases on the material's surface and inside its pores. Each gas has a different affinity for the material in use. This makes it possible to separate gases. Some separations have been performed with only one column, others use two columns. Based on experiments with protium and deuterium, as well as protium and tritium, it has been shown that separation with this technology is possible for hydrogen isotopes [20; 21].

The last two technologies have similar properties. Materials can be used in the cryogenic range as well as at higher temperatures. However, from a safety point of view, TCAP has a clear advantage as in the event of an accident, the gas remains stored in the material due to chemisorption, whereas with PSA the gas is only adsorbed to the material due to pressure. In addition, the pressure for PSA is significantly higher than for TCAP, which can result in a higher tritium inventory [19; 22]. In practical terms, the largest challenge comes from the necessity to involve a tritium-compatible compressor (I speak about some 10^7 Pa), which is not available. With regard to the separation efficiency, it is difficult to give a statement, as this depends strongly on the materials used.

The pairwise comparison leads to the conclusion that TCAP is the most suitable candidate for the "Isotope Rebalancing" and "Protium Removal" subsystems. This TCAP separation process was first developed in 1981 and has been enhanced over the decades [23]. The TCAP is based on hydrogen-metal interactions. A column is filled with a bulk material that has affinity for the lighter isotope, such as Pd. A second unfilled column is connected to the first one, whereby gas can flow. A development led to a second column filled with bulk material, functioning at cryogenic temperature, which has an affinity for the heavier isotope (e.g. molecular sieve (MS)). When inserting a gas mixture, the two columns are anticyclically heated and cooled, which leads to desorption and absorption effects and, thus, to a change in pressure inside the column. This causes a pressure difference between the two columns, leading to a flow between the two columns. This temperature and flow cycling leads ultimately to a separation of the hydrogen isotopes. The design of the facility is in such a way, that only one operation is possible, reducing the flexibility and process conditions.

2.2 Development of a Membrane Coupled-Temperature Swing Absorption Technology (MC-TSA)

TCAP has been selected as the best starting point for the most suitable DEMO technology. However, there are still some disadvantages:

i) It requires cryogenic temperature, as molecular sieve (MS) is used,
ii) Is provides only limited process conditions,
iii) It cannot run in continuous operation.

This process needs to be optimised in order to match DEMO requirements.

i) Cryogenic temperature has to be avoided whenever possible. Therefore, molecular sieve is replaced with a different material, operating at higher temperature.
ii) The limited process has to evolve into a more flexible setup and improvement of isotope order in the column for the developed test rig.
iv) An important goal for DEMO is the tritium inventory reduction in the fuel cycle. For that, the residence time must be minimized and the tritium content of the individual fuel cycle elements must be reduced. Besides the columns, an addition of a membrane can alleviate this restriction due to a partially continuous operation. This pre-separation reduces throughput and separation effort, directly leading to a decrease of tritium inventory. Additionally, material and energy costs can be reduced. However, as a membrane has limited separation efficiency, a second technology is required.

This technology improvement leads to a combination of **two separation principles**: Isotope-dependent gaseous diffusion and hydrogen-metal interactions, named the **Membrane Coupled-Temperature Swing Absorption (MC-TSA)**.

Figure 2.1 shows a simplification of these two separation principles. For the membrane, given in a), a mixture of hydrogen isotopes (Q_2), depicted in a solid blue line is continuously separated into two outlet streams (dashed, blue lines): one in which the lighter isotope H_2 and a second in which the heavier isotopes D_2 in the gas mixture are enriched. One of the enriched output streams from the membrane constitutes the input to the second separation principle, the TSA; while the other bypasses the second step. Depending on the input and required output composition, it is flexible which output stream is sent to TSA and which is sent around. In the depiction, the enriched protium output is forwarded as an input to TSA. It also works the other way with enriched deuterium send to TSA. These three outputs (one from MC and two from TSA) are then either fed back to the torus or to further purification steps in the OUTL.

For the Temperature Swing Absorption Process (Figure 2.1 b) two parts must be distinguished: The closed cycle (including steps 2-5) and the open cycle (including steps 1, 6 and 7). The closeod cycle (with repeated cycles) is performed until a satisfying enrichment is attained. In the open cycle, the enriched isotopes are extracted, deuterium in step 6 (following step 2) and protium in step 7 (following step 4). The amounts, which have been extracted from both ends, must be refilled (step 1).

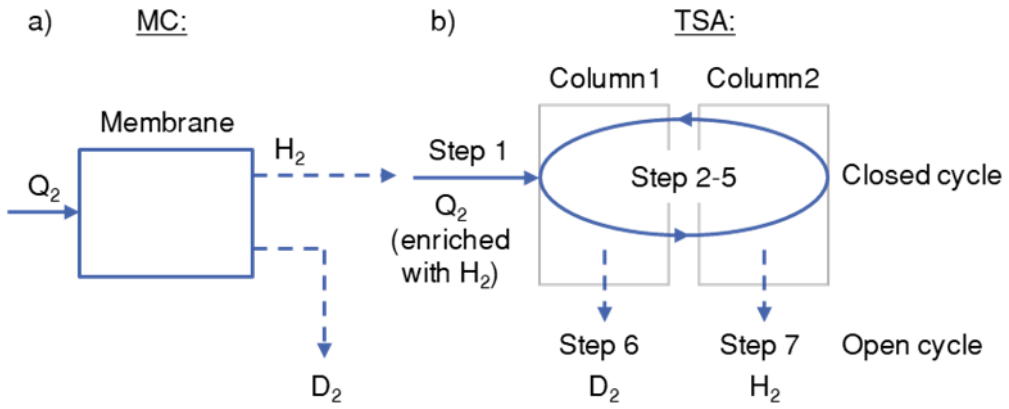

Figure 2.1: Simplification of the two separation principles a) Membrane Coupled (MC) and b) Temperature Swing Absorption (TSA) with the input streams shown in solid blue lines and the output streams in dashed blue lines.

The process needs two columns, connected by a valve. They are filled with bulk materials, each with an affinity for one of the two isotopes (see Figure 2.2). This affinity is expressed with the separation factor α_{HD} [24]:

$$\alpha_{HD} = \frac{I_{gas,H2} \cdot I_{solid,D}}{I_{gas,D2} \cdot I_{solid,H}}, \tag{2.1}$$

with $I_{gas,H2}$ and $I_{gas,D2}$ as the inventory of molecules in the gas phase and $I_{solid,H}$ and $I_{solid,D}$ inventory of atoms in the solid phase. Materials exhibit different, temperature dependent, separation factors. If α_{HD} <1, then the lighter isotope (H_2) is predominantly absorbed, for α_{HD} > 1, the heavier isotope (D_2) is prevailing absorbed. In column 1 (C1), a material with a separation factor smaller than 1 is applied. Thus, the light isotope remains in the solid phase, whereas the heavy one stays in the gas phase, producing a gas mixture enriched with D_2. For column 2 (C2), the material features the opposite affinity; the heavy isotope is preferentially absorbed.

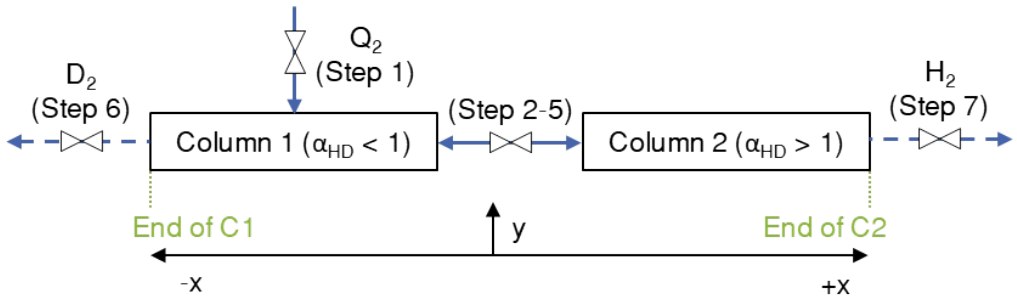

Figure 2.2: Depiction of the process configuration of column 1 and column 2.

Temperatures in both columns are anticyclical, one is cooled while the other is heated and vice versa. In principle, gas is absorbed by a material at low temperatures and released again at high temperatures. Applying different temperatures therefore leads to different pressures in both columns. By opening the valve which connects the two columns, a flow is generated through the pressure gradient.

The combination of material properties and temperature in the individual steps is essential to generate the separation effect. Figure 2.3 a) illustrates the temperature profile in relation to the steps for one closed cycle. The resulting pressures are shown in Figure 2.3 b). This is a qualitative analysis; quantification is provided in the results section. Detailed theoretical background of this sorption effect is explained subchapter 2.3.2. Initially, a mixture of isotopes (H_2+D_2) is added to column 1 at low temperature in step 1, whereby a major proportion is absorbed into the material, albeit more protium. Observing the pressure, a small increase is identified, with the partial pressure of deuterium being greater with respect to protium. This can be observed continuously in column 1, which is related to the above-mentioned effect that the material absorbs

the light hydrogen preferentially. Step 2 constitutes the beginning of the closed cycle. Column 1 is heated with a linear heat rate, causing the gas to be desorbed again. More gas is desorbed at the beginning and it flattens out as the temperature increase reaches a predetermined value asymptotically. Meanwhile, column 2 is cooled. In step 3, the valve between the two columns is opened. Due to a higher pressure in column 1 relative to column 2, gas flows into column 2 until the pressure is equalised, while hydrogen is absorbed into the material in column 2. At this point, it can be observed that the partial pressure of column 2 for deuterium is now lower compared to protium. This is due to the fact that this material has the reverse effect to column 1, the heavier isotope is absorbed in preference. In Step 4, column 1 is being cooled while column 2 is being heated. This operation correlates to step 2, but in reverse heating/cooling. Thus the pressure in column 1 decreases and pressure in column 2 increases. In Step 5, the two columns are connected again, the gas from column 2 flows back into column 1 at this point. When the pressure is equalised in step5, one closed cycle is completed and a new closed cycle with step 2 begins. The resulting sorption pressures in the two columns are not the same as different materials are used, which behave differently with regard to pressure at equal temperatures. With each cycle a higher enrichment is achieved. The closed cycles are repeated until the separation requirements are achieved.

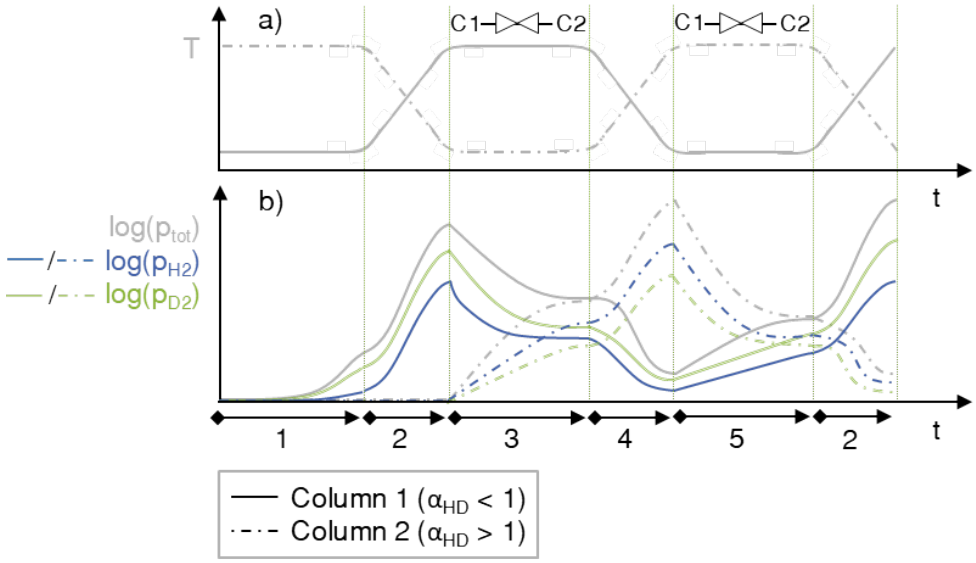

Figure 2.3: Temporal process flow of the TSA process with qualitative representation in a) of the temperature curve and in b) the pressure in at the individual process steps, with the isotopes H_2 (blue line) and D_2 (double green line).

An illustration of the shift of the isotope concentration along the columns, correlating to the temperature-pressure behaviour, is shown in Figure 2.4 a). As the length is much bigger than the diameter of the columns, the concept of a plug flow reactor is assumed.

There, axial diffusion (x-axis) is dominant, and no gradient of hydrogen isotope concentration occurs in the radial direction (y-axis).

In step 1, the gas to be separated is fed exclusively into the middle of column 1. As the material has preference for protium, it is absorbed directly at the inlet, while deuterium has to diffuse further along the axial direction. As temperature is increased, gas gets desorbed (step 2). Up to this point, no significant pressure gradient occurs, which results in neglible gas flow within column 1. In step 3, gas from column 1 flows into the pre cooled column 2 and thus gets absorbed there. Deuterium is preferentially absorbed, while protium moves further (along the +x-axis). Next, gas gets desorbed again (step 4) and gets absorbed by material in column 1 (step 5). After step 5 and the second step 2, already a small separation along the length is noticeable. Repeating this, more gas enriched with a specific isotope is located at the ends of the columns. In the open cycle, extraction of the enriched isotopes is obtained by heating to desorb the gas species in the desired column. For column 1, after step 2, enriched deuterium is extracted in step 6. This is followed by step 3 and 4, where column 2 is heated and enriched protium can be extracted in step 7. Step 5 is conducted, followed by step 1 for the open cycle, as the extracted amount of hydrogen needs to be refilled. A visualization of the influence of repeating cycles is given in Figure 2.4 b).

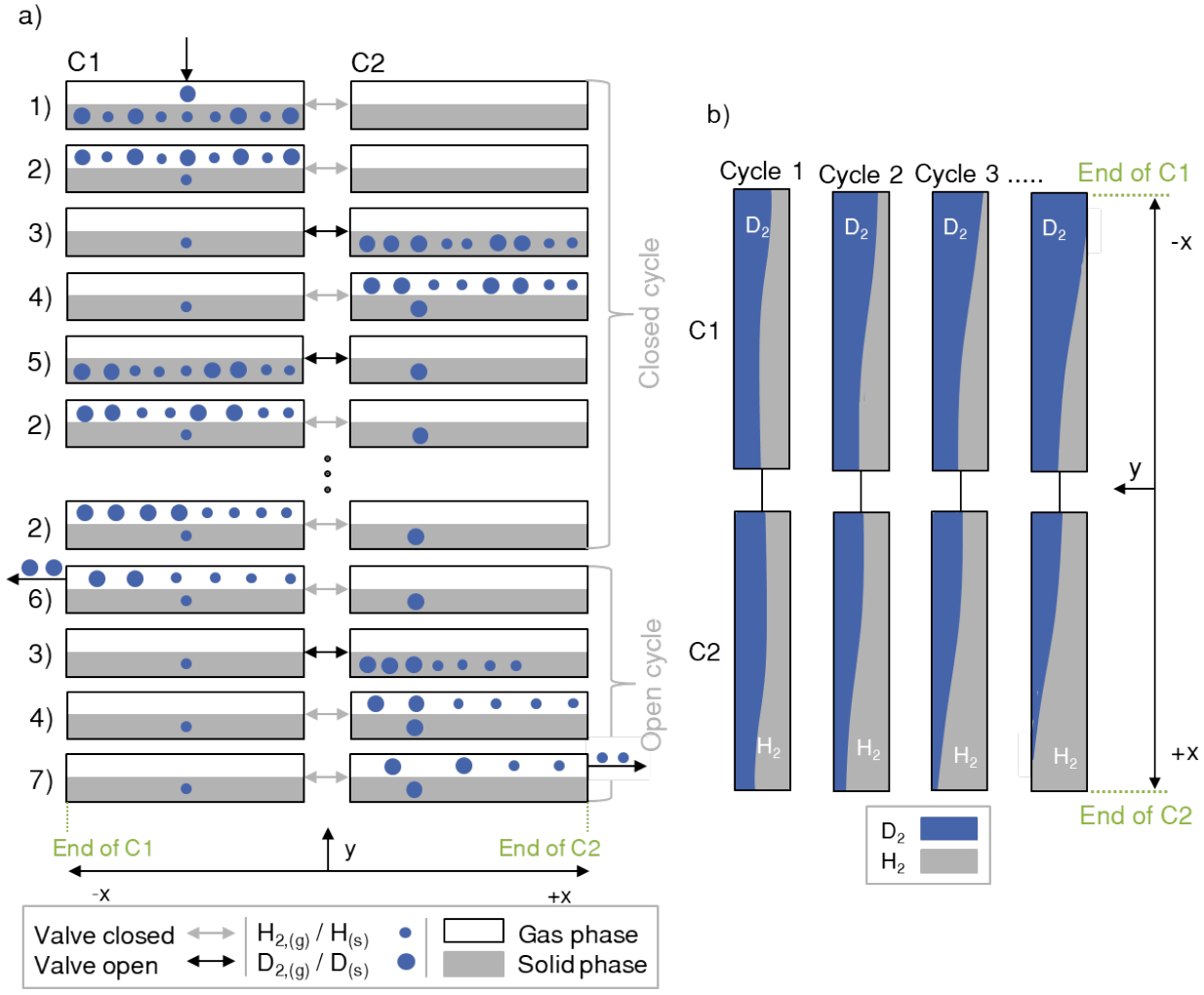

Figure 2.4: In a) The flow of the isotopes H_2 and D_2 along the two columns within the steps of one cycle are shown and in b) the shift of H_2 and D_2 over four closed cycles.

2.3 Physics of Isotope Separation

In this section the theoretical background of the two separation principles Membrane Coupled (first part) – Temperature Swing Absorption (second part) is given.

2.3.1 Separation through Gaseous Diffusion

The first of the two separation principles is gaseous diffusion with a porous membrane. In general, membranes can be classified in dependence of their nature, separation regime and geometry (see Figure 2.5). The nature and geometry can further be divided. The separation regime can be classified into dense, porous and ion exchange membranes, while here only porous membranes are considered.

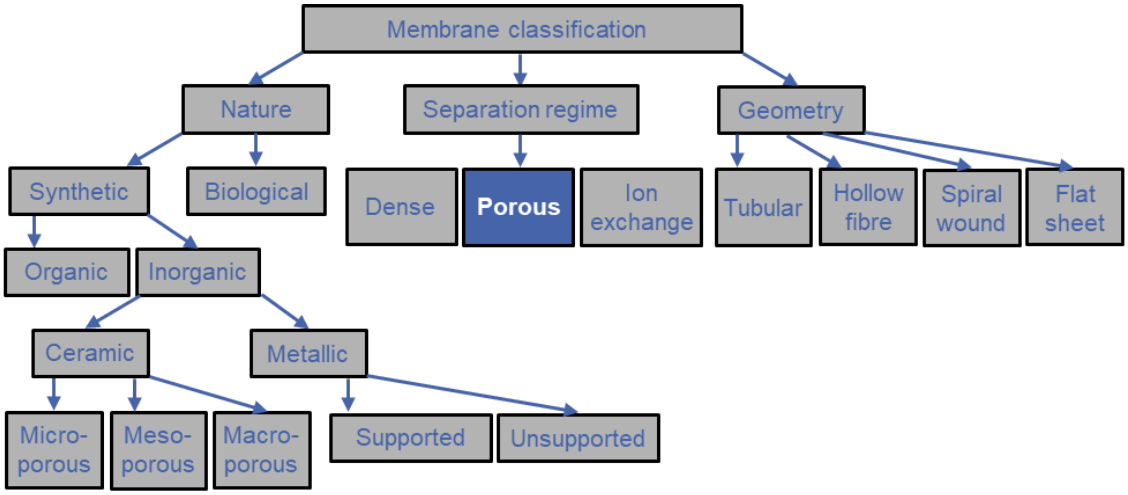

Figure 2.5: Overview of membrane classification adapted from [25].

In porous membranes, three different transport mechanisms occur depending on the Knudsen number. The Knudsen number is defined as follows [26]:

$$\mathrm{Kn} = \frac{\lambda}{d_p}, \tag{2.2}$$

with d_p as the pore diameter and λ as the mean free path of the gas molecules:

$$\lambda = \frac{k \cdot T}{\sqrt{2} \cdot \pi \cdot d^2 \cdot p}, \tag{2.3}$$

where k is the Boltzmann constant, T is the temperature, d is the diameter of the molecule and p is the pressure. For 298.15 K and 10^5 Pa the mean free path for hydrogen is $1.09 \cdot 10^{-8}$ m. The different transport mechanisms divide into three flow regimes [26]:

i) Kn > 0.5: Free molecular flow,
ii) 0.01 < Kn < 0.5: Transition regime,
iii) Kn < 0.01: Viscous flow.

In Figure 2.6 a) a principle setup of a porous membrane is shown. Gas enters at one side of the membrane. Through a pressure difference between the inlet and the outlet sides of the membrane, some gases diffuse through the pores of the membrane to form the permeate stream, the remaining forms into the retentate stream. With gaseous diffusion, a separation can be achieved. This occurs predominantly at free molecular flow conditions. To ensure this, the pore diameter has to be smaller than $200 \cdot 10^{-9}$ m for the above given conditions. If this is the case, then the collisions between molecules and the wall dominate, as opposed to the collisions between molecules. Separation of gas mixtures is then attained due to gas-specific kinetic velocities [27]. There are also other mechanisms besides gaseous diffusion (i), such as surface diffusion or molecular sieving,

shown in Figure 2.6 b) for one pore, respectively. For surface diffusion (ii) a gas is preferentially adsorbed at the membrane surface. For molecular sieve (iii) pores are of similar size than the gas, resulting into a cut-off for bigger molecules and an easy transition and thus an enhanced penetration probability for smaller molecules [28; 29]. Since the other mechanisms take place at low temperatures and smaller pore diameters, gaseous diffusion can be considered as main mechanism at elevated temperatures. Low pressures (increasing the mean free path) and membranes with a pore size of approximately $2{\cdot}10^{-9}$ m or slightly higher (even if gas diffusion theoretically occurs with a significantly larger pore diameter) result in higher Kn numbers and hence help to strengthen this mechanism even further, whereby gaseous diffusion can be seen as the only occurring mechanism [30; 31].

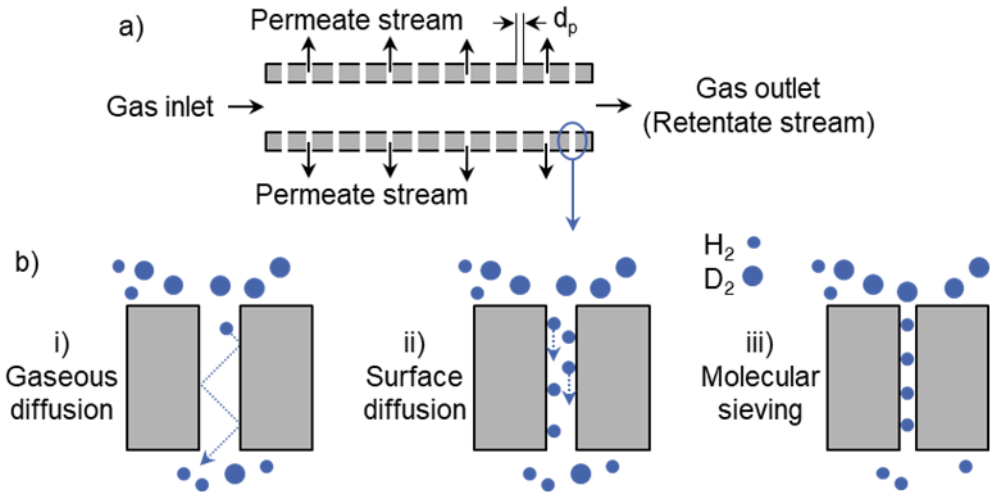

Figure 2.6: a) Principle flows of a porous membrane and b) three different mechanisms adapted from [28; 32].

The permeation gas flow rate through the membrane is defined as:

$$F_G = P_G \cdot A_M \cdot \Delta p, \tag{2.4}$$

Where P_G is the permeance, A is the surface of the membrane in, Δp the pressure difference between the inlet and outlet stream in. The parameters of the membrane are included in the permeance, with its equation:

$$\bar{P}_G = \frac{\varepsilon \cdot d_p}{\tau \cdot L_M} \cdot \left(\frac{8}{9 \cdot \pi \cdot M \cdot R \cdot T}\right)^{0.5}, \tag{2.5}$$

with ε as the porosity, τ as the tortuosity and L as the length of the membrane in (m). The tortuosity can be determined with several methods, for example by calculations with a model or x-ray miscroscopy [33], which is often stated by the manufacturer. M is the molar mass of the isotope and R the universal gas constant. A material without absorption effects, as γ-Al_2O_3 is often applied. The diffusivity D_G for free molecular

transport is a function of the membrane-parameters in the first part and the gas kinetic velocity in the second part of the equation:

$$D_G = \frac{\varepsilon \cdot d_p}{\tau} \cdot \left(\frac{8 \cdot R \cdot T}{9 \cdot \pi \cdot M}\right)^{0.5}. \tag{2.6}$$

In this equation it is apparent that the diffusion of different gases only depends on their specific molar masses. The difference in molar masses is therefore the only influence on the separation. It can also be expressed by the ratio of the permeance and retentate streams, resulting from the partial pressure of the flow:

$$\alpha_{HD} = \sqrt{\frac{M_D}{M_H}} = \frac{X_P \cdot (1 - X_R)}{X_R \cdot (1 - X_P)}, \tag{2.7}$$

with X_P and X_R as the respective parts from the outlet streams retentate and permeate. As the differences in molar masses are the biggest for hydrogen isotopes compared to all other isotopes, the separation is the most effective one. This results into a theoretical separation factor of 1.41 for protium-deuterium. The composition of permeate and retentate stream can be determined from a McCabe Thiele diagram, which is visualized in Figure 2.7. The selectivity curve is specific to the gas mixture and is related to the separation factor. Starting from the initial conditions X_S, a line can be drawn from the operating line to the selectivity curve. Literature states that the slope of this line (1 → 2) is associated to the permeation. A correlation persists between the flow and the concentration, which is related to the steepness of the curve. The steeper the curve is, the lower is the permeation flow with a maximum increase of the permeation concentration [34]. This is shown graphically with two different steepness of the curves. Also two starting points have been graphically represented, once for an equimolar composition (X_S=0.5), the other for a gas mixture, where the quantity of one isotope is much smaller compared to the other. For the balanced mixture, compared to the latter scenario, there is a large relative enrichment for a step. This shows that a membrane is suitable for rebalancing the isotopes, rather than for the removal of protium. For this reason, a second separation technology (TSA) is required.

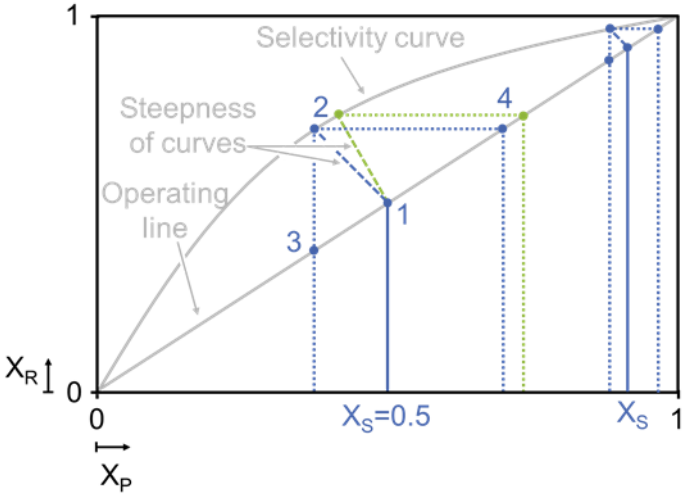

Figure 2.7: Illustration of McCabe Thiele diagram with the composition of permeate stream on the x-axis and retentate stream adapted from [34].

2.3.2 Separation through Metal Hydrogen Interactions

The second separation process TSA involves hydrogen-metal interactions: Hydrogen is absorbed or desorbed by a metal under certain conditions. Typically today, these kinds of materials are often applied for solid hydrogen storage. As the sorption behaviour is different for the individual isotopes, separation can be enabled. Thereby, certain materials react with hydrogen and thus form a hydride, corresponding to the **reaction**:

$$Me + x/2 \cdot Q_2 \leftrightarrow Me \cdot Q_x. \tag{2.8}$$

Elemental hydrides can be divided into three different classes, depending on their **bonding type**. In the case of i) Ionic or saline hydrides, all alkali metals and alkaline earth metals react with hydrogen. Hydrogen is present as a negatively charged ion (H^-). This type of bond is usually very stable, some examples are CaH_2 or $LiAlH_4$. (ii) Covalent hydrides are all non-metals (SiH_4, $(BH_4)_3$ ...). These hydrides are usually not directly formed by adding hydrogen, they have to be specially prepared. Therefore, these compounds are not of our interest. The focus here is on iii) **Metallic hydrides**. Here, a metallic bond is formed between transition metals (TiH_2, ThH_2...) and the gas by direct addition of hydrogen. In reality, the different types of bond cannot be clearly separated. Most hydrides have a mixture of different bond types [35, 36].

During this hydride formation, for most materials (as Pd, V, Ti) heat is released, as it is an exothermic process. The reverse process step, desorption, is endothermic. To remove hydrogen from the material, the material must be heated accordingly. However,

some materials (as Cu, Ni) possess the opposite behaviour [37]. Absorption includes in general of several sub-steps, shown in Figure 2.8. First, hydrogen from the gas phase (i) reaches the surface of the material, and is first physisorbed (ii) at the surface. In the next step (iii) the molecule is chemisorbed and dissociated to atoms at the material surface. As a last step the atoms diffuse into the material (iv). These steps belong to the indirect dissociation. It occurs when the kinetic energy of the molecules is not high enough to overcome activation barriers. A direct dissociation happens, when the kinetic energy is high enough, whereby a molecule is directly split into atoms [38; 39].

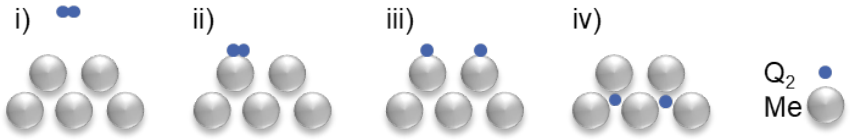

Figure 2.8: Principle depiction of the process steps for a metal-hydrogen interaction with i) Diffusion of hydrogen in the gas phase to the material surface, ii) Physisorption of hydrogen, iii) Dissociation into hydrogen atoms and iv) Diffusion into the bulk. Adapted from [38].

An **energy diagram** in Figure 2.9 explains these steps in detail. In the gas phase and at a distance from the material surface, the energy of a hydrogen molecule is considered zero. Atomic hydrogen has a positive potential energy at this stage, which corresponds to the dissociation energy. Far enough from the surface, no forces influence the gas. At some point closer to the material surface, attractive forces appear. Near the surface, repulsive forces are prevailing. Due to strong covalent bond of the hydrogen molecules, first only weak van der Waals interactions appear (E_p). At the crossing point of both curves, hydrogen is chemisorbed and split in atoms (E_c). The reason for this is that the orbital of the molecule attains the Fermi level of the material surface. Electrons from the material occupy antibonding orbitals, leading to the weakening of the hydrogen bonds. Afterwards the molecular orbitals are shifted below to the Fermi level of the metal, which leads to chemisorption. In this state, the electron of each atom is available to form chemical bonds with the material surface. Several factors, as defects, impurities, surface hydrogen coverage, or the applied materials, especially if it is activated or non-activated, have an influence. For materials with a non-activated behaviour, additional energy is required to be able to dissociate a molecule. Naturally, the density of d-electron states at the Fermi edge is large for transition metals. This passes to molecular orbits, causing spontaneous dissociation. The atoms diffuse into the bulk by jumping between interstitial sites [39]. In Figure 2.9, the energy level in the metal is shown for both, materials with an exothermic as well as endothermic behaviour.

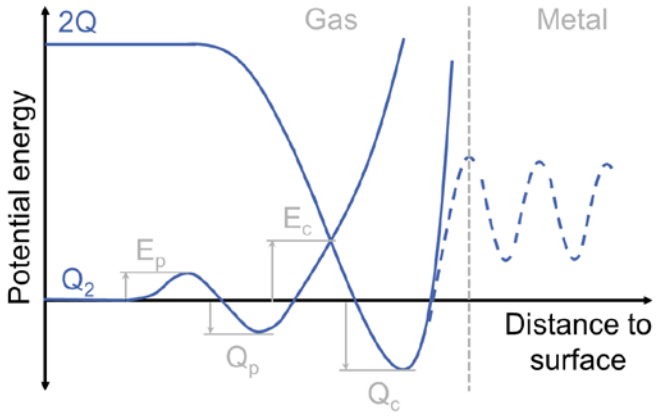

Figure 2.9: Simplified potential energy diagram for atomic and molecular hydrogen with the activation energies E_p and E_c as well as the heat of sorption Q_p and Q_c adapted from [39].

There are now two possibilities for the hydrogen to move in the material lattice: i) it can dissolve as an interstitial between the lattice atoms or ii) it can displace a host metal [40]. The interstitial movement is much more likely. The three major **crystal structures** with their interstitial sites are shown in Figure 2.10 with the octahedral (O-site) and tetrahedral (T-site) sites. In the body-centred cubic (bcc) structure, one metal atom has three O-sites and six T-sites on hand. Typical materials are vanadium or niobium. In the face-centred cubic structure (fcc), for each metal atom one O-site and two T-sites exist. Therefore, for small to medium concentration of hydrogen, O-sites are preferred. Palladium is a typical example of an fcc structure. In a hexagonal close packed (hcp) structure, for small hydrogen concentration tetrahedral sites are preferred. Also here, one O-site and two T-sites are obtainable. Titanium (below 1155 K) consists of this structure [41].

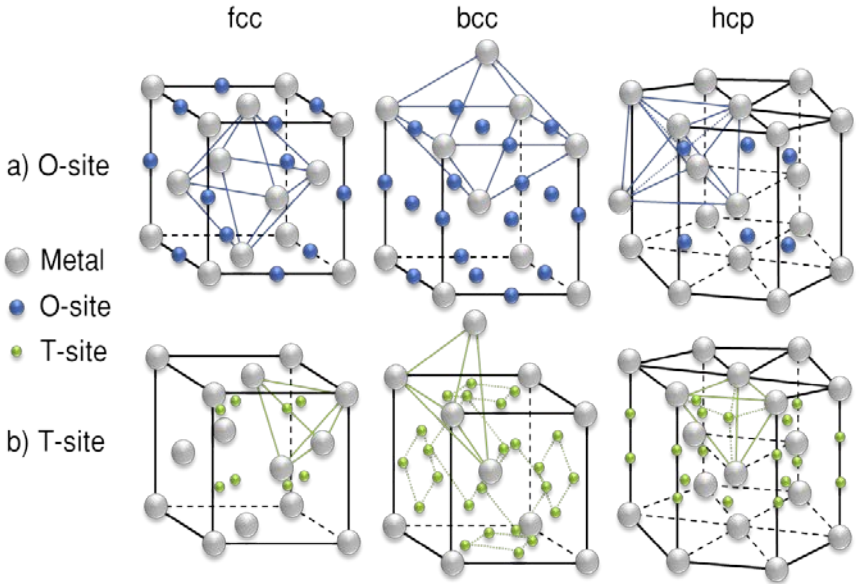

Figure 2.10: Schematic depiction of the interstitial sites in the body-centered cubic (bcc), face-centered cubic (fcc) and hexagonal closed package (hcp) crystal structures for a) octahedral sites (O-sites) and b) tetrahedral sites (T-sites) adapted from [35; 41; 42].

There exists a rigorous **thermodynamic framework** to describe interaction between hydrogen gas and solid metals. Thermodynamic equilibrium between the molecular hydrogen in the gas phase and the atomic hydrogen in the solid phase is established within a certain period of time. It can be described with the following equation:

$$Q_{2,(g)} \leftrightarrow 2Q_{(s)}. \tag{2.9}$$

The enthalpy H determines the tendency to hydride formation. Materials with a positive enthalpy of solution (endothermic) in relation to Q_2 (e.g. Fe, Mo, W) do not react with hydrogen under standard conditions. Materials with a negative enthalpy of solution (exothermic), on the other hand, have a strong tendency to form hydrides. The enthalpy thus gives a reference unit for the bond strength [43]. For low hydrogen concentrations, the enthalpy of solution ΔH^0 and entropy of solution ΔS^0 can be used. Table 2.1 shows literature values at 300 K, for materials with both a positive and a negative enthalpy. The larger the value in negative enthalpy, the stronger is the bond.

Table 2.1: Enthalpy and entropy of solution for a number of metal-hydrogen systems 300 K [43].

M-H System	ΔH^0 (kJ/mol)	ΔS^0 (J/(mol·K))
Y-H	-79	-48
Gd-H	(-62...-76)	
Nb-H	-40	-65
V-H	-32	-61
Pd-H	-10	-51
Fe-H	+24	-54
Mo-H	+52	-45
W-H	+100	-39

Using enthalpy and entropy, a mathematical correlation can be given to describe hydrogen behaviour in a metal, which can be expressed in **phases**. For low concentration, the following equation is applied, which corresponds to the Sieverts' law:

$$\sqrt{\frac{p_{Q_2}}{p_0}} = \frac{n_Q}{n_s} \cdot exp\left(\frac{\Delta H^0}{RT} - \frac{\Delta S^0}{R}\right) = K_s \cdot n_Q, \tag{2.10}$$

with n_Q as the number of hydrogen atoms and n_s the number of metal atoms. As electronic and elastic contributions do not matter for low concentrations, this Sieverts' law can be applied in the so called **α-phase**. In this solid-solution, Q atoms do not occupy rigid interstitial sites, they are movable. Thereby the lattice of the material expands with a function of the concentration by around $2 - 3$ Å^3. For a further increase of the hydrogen content, the Sieverts' law is not practicable to be applied, as the hydrogen interactions are a cause of the expansion matter. For this purpose the van't Hoff law is adjusted. With regard to the dissociation into atoms and the assumption that the entropy change of the different phases is negligible, the equation is [43; 44; 45]:

$$\ln\sqrt{\frac{p_{Q_2}}{p_0}} = \frac{\Delta H_{\alpha-\beta}}{RT} - \frac{\Delta S_{\alpha-\beta}}{R}, \tag{2.11}$$

with $\Delta H_{\alpha-\beta}$ as the enthalpy and $\Delta S_{\alpha-\beta}$ as the entropy of transition for the formation of hydride for one atom of hydrogen. Thereby a hydride (called the **β-phase**) is formed, with the atoms being in ordered positions. The region between these two phases exhibits a miscibility gap, known as the **α-β-phase**. In this region a structural change from solid solution to a hydride phase is developed. In a schematic **pressure-concentration diagram with isotherms (PCT)**, shown in Figure 2.11 a), the coherences are illustrated. Literature values in a PCT diagram always consider

thermodynamic equilibrium, wherefore the equilibrium pressure is given on the y-axis. Kinetic effects are not derivable from this. On the y-axis of the diagram, equilibrium pressure of hydrogen molecules in the gas phase is plotted. The x-axis denotes the concentration of hydrogen atoms in the material. Different units are employed in literature (e.g. wt.-%). In this thesis I use the atomic ratio (mol_H/mol_{Me}) for all concentration values. Basically, for exothermic systems, the pressure rises with increasing temperature in all phases. In the α-phase, the pressure also increases with rising hydrogen content. When the α-phase is saturated, the two phase region α-β is formed. The phase boundary is depicted as a dotted, blue line. In this miscibility gap, a plateau is formed, leading to a constant pressure for increasing concentration. The α-portion gradually diminishes and the β-portion becomes more predominant. At a certain point, 100 % β-phase is reached, causing the pressure to increase fast with growing concentration. The concentration keeps increasing until a maximum value, dependent of the material, is reached. Above the critical temperature (T_c), no plateau area exists, an undefined structure is present [46]. From the plateau, points of the individual isotherms can be extracted and plotted over the reciprocal temperature (Figure 2.11 b)), which corresponds to the van't Hoff law. The enthalpy represents the slope of the obtained straight line, the entropy the intercept. This display is particularly suitable for a direct comparison of the performance of different materials in terms of hydrogen.

The plateau is significantly important in systems of interest for this work. Some materials even possess several plateaus, they therefore have at least two types of interstitial sites. The width of the plateau is a measure of the reversible capacity, whereas the plateau pressure is expressive for the stability of a hydride. For increasing temperature, the width of the plateau decreases. The process steps physisorption, chemisorption and diffusion are all fully reversible. This reversible capacity can be limited to significantly less than the maximum concentration value and differs for each system. This reversible phenomenon makes hydrogen-metal interaction a favourable candidate for separation purposes [38; 45; 47; 48; 49].

In reality, some systems deviate from the ideal behaviour in the plateau region and exhibit a certain slope in the two-phase region. This is primarily related to localized defects, surface inhomogeneities or cycle instabilities. As a slope may pose limits on the hydriding of the material, it is advisable to reduce it, e.g. via proper heat treatment (for arc-melted alloys). A second non-ideal effect is the hysteresis, shown in Figure 2.11 c). Thereby the pressure of the absorption is always higher than for desorption. For increasing temperature this effect gets reduced. It is seen as a loss of energy during the sorption cycles and has different causes. This effect has to be, similar

than for the plateau, kept as small as possible [45; 50]. PCT diagrams are mainly characterized for pure isotopes. Only limited information is given on diagrams for gas mixtures. Nevertheless some research has been performed for a hydrogen-Palladium system with four different compositions of protium and deuterium at 323 K. Two conclusions can be drawn from this: i) the slope of the plateau increases for an isotope mixture and ii) the resulting desorption pressure of the mixtures are located between the values of the single isotopes [51].

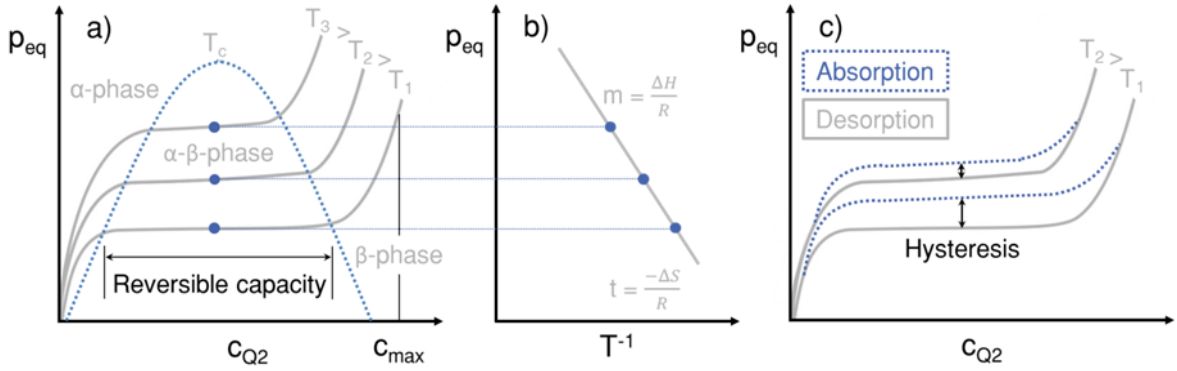

Figure 2.11: Principle depiction of a pressure-concentration diagram in equilibrium in a), the van't Hoff plot in b) and the hysteresis effect in c) adapted from [45].

So far, the fundamental behaviour of material-hydrogen-interaction has been described. For the separation of isotopes, the difference of the individual isotopes is of key importance and will therefore be explained hereafter.

The basis of the **isotope effect** is discussed using Figure 2.12. As the molar mass of deuterium is twice as big as for protium, the relation of the zero point energies (ZPE) is $\sqrt{2}$, with 269 meV for H_2 and 191 meV for D_2 (shown in ii). In principle, it can be said that the isotope at which a smaller change in ZPE occurs (in the hydride phase compared to the gas phase) preferentially remains in the gas phase. A reason for this is that with a lower ZPE, higher activation energy has to be provided for the bond to be cracked. During absorption, the atoms are filled either predominantly in octahedral (O-site) or tetrahedral (T-site) interstices. The quantum harmonic oscillator approximation, in which these vibrational energies are described, depends, also, on the force constant. Since this constant is smaller for O-sites than for T-sites, the potential wells are flatter. This can be seen in Figure 2.12, with a description of a T-site in i) and O-site in iii). Considering first the energies from the tetrahedral interstices, the following can be observed: The energy change from H_2 to H is smaller compared to D_2 to D, resulting into a preference of the heavy isotope in the solid state. For octahedral sites, the opposite is observed. Here the change in energy is smaller for deuterium, whereby the lighter isotope is preferentially in the solid state [44; 52; 53]. In literature

different nomenclature is used for this tendency, amongst others: positive isotope effect (D_2 in preference) and negative isotope effect (H_2 in preference). In this thesis I use a different nomenclature: **Normal Isotope Effect (NIE)** for materials which absorb the lighter isotope preferentially and **Inverse Isotope Effect (IIE)** for materials which absorb the heavier isotope preferentially. The justification is that more materials prefer to absorb protium, which legitimises the word "normal".

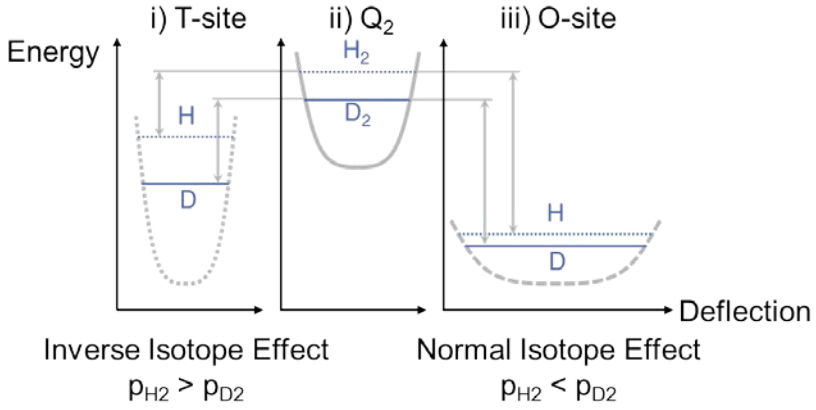

Figure 2.12: Schematic display of potential wells and zero point energies for protium and deuterium in the gas phase (ii) as well as in the solid phase for an inverse isotope effect (i) and a normal isotope effect (iii) adapted from [52].

This isotope effect is defined by the **separation factor** α_{HD} and is specifically characterized for each material. For a separation factor of 1, the material has no isotope effect at all. The further α_{HD} deviates from 1 ($\alpha_{HD}<<1$ and $\alpha_{HD}>>1$), the greater this effect is, see equation (2.1). For materials with a normal isotope effect α_{HD} is smaller 1, for those with an inverse isotope effect it is larger than 1. To obtain a first estimation of the isotope effect, the equilibrium pressure from a PCT diagram in the plateau region, for both isotopes at the same concentration, can be taken and compared. In equation (2.1), the portions in the solid phase are thus shortened, resulting in the pressure ratio for both isotopes. For an accurate determination of the isotope effect, however, an integration of the pressure over a certain concentration range is necessary from c_1 to c_2 [54; 55; 56]:

$$ln\alpha_{HD} = \frac{1}{2 \cdot c} \cdot \int_{c_1}^{c_2} \ln\left(\frac{p_{H_2}}{p_{D_2}}\right) dc. \tag{2.12}$$

The correlations for the pressure can be determined from experimental values. The separation factor depends on a number of parameters. The strongest influence is the temperature. The lower the temperature, the more distinctive the isotope effect, and thus it deviates more significantly from 1. Other influences are the composition of the isotopes or the absorbed amount [54; 57].

Since the isotope effect is described with vibration energies, tritium values can also be extrapolated that way. The relation of the vibrational energies is known as: $\hbar\omega_D = \hbar\omega_H/\sqrt{2}$ and $\hbar\omega_T = \hbar\omega_H/\sqrt{3}$ [58]. If the separation factor α_{HD} is known, e.g. by carrying out experiments, the ratios of the energies can be used to assess the separation factor α_{HT} for protium-tritium, based on quantum mechanics arguments. With regard to the sorption pressure for tritium, the simplification from equation (2.1) has been used for both materials; accordingly the pressure of protium has been divided by the calculated separation factor α_{HT} to obtain the sorption pressure for T_2.

Other factors of the material, such as particle diameter or impurities, can have an influence on the formation of hydrides. Additionally, kinetic effects can be responsible for deviations from thermodynamic equilibrium predictions. Investigation of kinetics is an active field of research but it has been observed that experiments are difficult to realise, especially with regard to their accuracy [49]. Impurities can also have an impact on the performance. Thereby both, impurities from the gas and the metal can be crucial. Pure metals exhibit catalytic properties due to electrons in d-orbital, which can be reduced through adsorption of other substances, leading to an increase of an energy barrier [59]. Impurities in the gas phase have the ability to occupy parts of the metal surface and therefore to reduce the amount of space for dissociation of hydrogen molecules. This inhibits chemisorption and thus diffusion in the metal. It has been shown that even smallest amounts can have an influence. This can, besides reducing hydrogen absorption, also lead to embrittlement [39]. Regarding pore diameter and shape, contrary statements have been made in literature. The Kozeny-Carman equation describes the pressure drop through a packed bed, with the porosity as an influence [60]. Particle diameter has a squared influence on permeability, showing that increased particle diameters result in a better performance [60]. On the other hand it has been shown that separation decreases for an increase of flow, which automatically occurs when the porosity increases [61]. Experimental studies on palladium for different sizes (in nm range) have shown that with decreasing diameter, an increase of the solubility in the α-phase and concurrently a decrease in the sorption capacity in the β-phase occur [35]. Due to different statements and individual behaviour of metals, not a clear statement can be given. For the purpose of the process feasibility demonstration being delivered by this thesis, porosity and pore diameter is not varied, so its influences are taken as given.

As **alloys** have a higher level of complexity, it is interesting to mention some rules on the formation of the intermetallic compounds. They are composed of an element "A" which is forming a high temperature stable hydride and an element "B" forming a non-hydride. The most common combinations are AB_5, AB_2, A_2B and AB.

Similar as for metallic hydrides, hydrogen dissociates into atoms and diffuses into the interstitial sites [62]. According to Dornheim [38], the “A” elements are generally located on the left hand side of the periodic system of elements (usually rare earth or alkaline earth metal, e.g. Mg, Ti, V, Zr) whereas the “B” elements are usually located on the right hand side (often a transition metal, e.g. Cr, Fe, Co, Mo).

The four main alloys are AB_5, A_2B, AB and AB_2. AB_5 has for the "A" element a tendency to lanthanides (at. No. 57-71), or elements such as Ca, Y, Zr and the "B" element is mostly based on Ni with substitutional elements as Co, Al, Mn, Fe, Cu, Sn, Si, Ti. In A_2B, "A" is typically of the group IVA elements Ti, Zr or Hf and "B" is a transition metal, typically Ni. In AB_2, "A" is often of the IVA group (Ti, Zr, Hf) and/or rare earth metals with atomic number 57-71 or Th. "B" has a large variety of transition and non-transition metals with preference for atomic numbers of 23-26 (V, Cr, Mn, Fe).

This thesis concentrates on an alloy of type AB_2. AB_2 type is sensitive to impurities in hydrogen, and passivation has been observed. Around 500 different compounds are reported for this type. They show good kinetics and its pyrophoric behaviour is high, especially when Zr and Mn are involved. Cr and Ti seem to be less pyrophoric. At AB_2, alloys tend to disproportionate when lanthanides are used for the "A" element. Ti or Zr based alloys are more stable in this respect [63; 64; 65].

3 Material Selection & Characterization of Absorption Based Separation

This chapter is divided into five main sections. First, the material requirements are listed and several materials with normal isotope effect (NIE) and inverse isotope effect (IIE) are compared with each other in order to choose the most suitable. Following this, the structure of the test rig is explained in more detail. Then the procedure of the experiments is explained, followed by the experimental results of the material characterisation of the two chosen materials. In the end the suitability of the materials is given.

The behaviour of materials for metal hydrogen interactions is the key aspect for the intended process development. Literature research has shown that information is limited, mainly given for protium in thermodynamic equilibrium. For alloys, there is little information about the influences of different compositions. Anyhow, for the application of hydrogen isotope separation it is essential to know the behaviour for all isotopologues and how the isotopic effect depends on the chosen material. These reasons led to a development of the test rig MAIA (MAterial Investigations for Absorption) for material characterization in order to characterize the suitability of candidates for hydrogen isotope separation.

3.1 Material Selection for Metal Hydrogen Interactions

For hydrogen isotope separation, two different materials with specific requirements have to be combined. The chief requirement is the separation factor, which is strongly linked to the temperature- and pressure ranges. Two different materials are needed: Material 1 must feature a normal isotope effect (separation factor $\alpha_{HD} < 1$), whereby the lighter hydrogen isotope gets absorbed preferentially. For material 2, the inverse isotope effect (separation factor $\alpha > 1$) needs to be fulfilled. If this behaviour for both materials is not accomplished, the material is disqualified. Merely by the use of these interactions the mixture of isotopes can be purified and extracted from the end of the columns.

The temperature range is the condition for the process to have both high separation and fast process conditions. The lower the temperature, the more distinctive the isotope effect is. However, due to DEMO requirements, absorption shall not require cryogenic temperatures. In order to make the conception of the test rig easy to implement, I set

the maximum temperature to 473 K. This fact concluded in a range from ambient temperature up to 473 K with several intermediate steps for material characterization. For this range, a high separation potential is covered, including technical feasibility for the conception of a test rig.

The desorption pressure needs to be higher than 10^5 Pa to generate a pressure-driven flow in the process. Correspondingly, the absorption pressure has to be in rough vacuum. The resulting absorption and desorption pressures of the two columns must be of the same order of magnitude, otherwise the separation efficiency is not guaranteed due to low overall flow between the columns.

Figure 3.1 gives an overview of different materials over the reciprocal temperature ($1000 \cdot T^{-1}$) on the x-axis and the logarithmic pressure on the y-axis. The data have been collected from several authors and brought together to have different materials in one graph for a better overview. The required temperature and pressure range is highlighted as blue rectangle. For that reason, the material selection is focussed on this area. Materials with a normal isotope effect are in solid orange lines, materials with an inverse isotope effect in dashed red lines. The individual materials are elaborated in more detail in the next chapters 3.1.1 and 3.1.2.

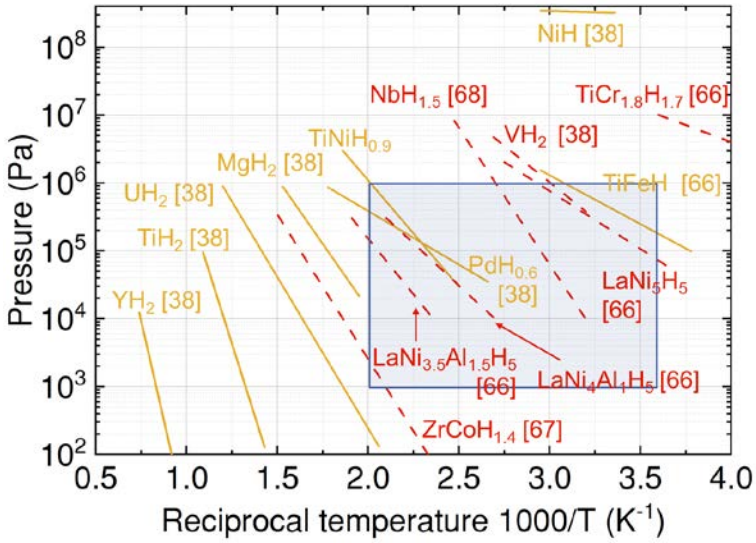

Figure 3.1: Literature values of van't Hoff diagram for different materials with a normal isotope effect (solid yellow lines) and inverse isotope effect (dashed red lines) adapted from [38; 66; 67; 68].

In addition to the essential criteria, other aspects have to be considered in order to optimise the process with respect to the hydrogen isotope separation. The further the separation factor deviates from 1, the more appropriate this material is. Consequently, if two materials exist with similar properties, such as suitable temperature and pressure ranges, the material with a higher separation factor is selected. More properties, as the total amount of hydrogen, which can be absorbed by the material, the time until

thermodynamically equilibrium is reached, or the particle size and porosity, also need to be considered, as they can influence the separation.

3.1.1 Materials with a Normal Isotope Effect

In this chapter, materials with a normal isotope effect ($\alpha < 1$) are presented. Seven different types are discussed and compared against each other, mainly based on the separation factor and the temperature-pressure range. Additional information, which is essential for the decision, as pyrophoric behaviour, is given for the specific materials. Here, also information with tritium is stated. As the separation factor is given for the individual materials at different temperatures and concentrations, a direct comparison of the materials is not practicable. Therefore, this analysis is more qualitative.

Depleted Uranium is a candidate with a normal isotope effect and is widely used in hydrogen isotope storage. The separation factor at 600 K for a protium-deuterium system is α_{HD}=0.75 [54]. The separation factor deviates further from 1 with an increase in temperature. For the temperature range used, it can be expected that the separation factor is correspondingly lower (in other words, better, as α<1), which is an advantage of uranium. Some authors, however, state a separation from 0.72-0.91 [57]. In addition to this concern, a number of disadvantages arise that does not make it a suitable candidate. A disadvantage is that uranium exhibits pyrophoric behaviour already at room temperature if it is in fine forms, an aspect which must be paid attention to in the safety-relevant design [69]. The main issue however is the sorption range. Literature states a pressure of around $4{\cdot}10^3$ Pa at 573 K [57]. For ambient temperature the pressure is in high vacuum. These conditions do not fall into our desired operational window, hence this material has not been selected. Furthermore, even depleted uranium falls under IAEA regulations as nuclear material, which is disadvantageous.

Titanium has similar properties to uranium, the separation factor is α_{HT}=0.67 at 623 K [54]. Also for this material, pyrophoricity is an issue. Titanium, however is not as sensitive as uranium, the ignition temperature for dust clouds is between 605 and 861 K [70]. The resulting pressure is, similar to uranium, too low for our conditions. To reach 10^5 Pa, the temperature needs to be higher than 873 K [71], which is why also titanium is excluded.

An **alloy with titanium** is one option to raise the sorption pressure of titanium. Some have a normal isotope effect, such as α_{HT}=0.74 (for TiNi at 313 K), α_{HT}=0.85 (for TiCo at 313 K) or α_{HT}=0.92 (for TiFe at 273 K) [54]. As all possess a relatively weak separation factor close to unity, these alloys are eliminated. Moreover, the resulting sorption pressure of TiFe is too high ($5{\cdot}10^5$ Pa at 303 K) [72]. Literature shows that by

substituting a certain amount of titanium with another, such as zirconium, the pressure can be reduced. At the same time, though, the amount of hydrogen that can be absorbed by the material is decreased [72]. For TiNi, different pressures are stated, some with the absence of a plateau. Therefore the pressure is strongly dependent on the concentration. At 473 K and for a concentration of 0.45 mol_H/mol_{TiNi} the pressure varies from around $5 \cdot 10^5$ Pa [73] to around $20 \cdot 10^5$ Pa [74].

For **nickel**, the separation factor at 298 K is weak, with $\alpha_{HD}=0.92$ [54]. For this reason alone, the material has to be cut out. Additionally, the equilibrium pressure at ambient temperature exceeds $3 \cdot 10^8$ Pa [75]. To meet the pressures required for the process, significantly lower temperatures have to be necessary. As a result, this material is not a suitable candidate.

Magnesium is characterised by a very high hydrogen capacity of 7.7-wt % [65]. Literature states only a higher capacity for the alloy LiB. The magnesium hydride undergoes several structure changes (more than only two phases) [76]. The pressure in the α-phase is low and begins at 623 K at 10^5 Pa [77]. For the β-phase a pressure of 10^5 Pa exists at ambient temperature [78]. The γ-form is a metastable form in high pressure [77]. Magnesium has a slow kinetic and a high thermodynamic stability [79]. The fact that magnesium hydride is so stable makes it not suitable for separation. It is possible to add other metals to compensate for these effects. However, the performance in terms of isotope effect and pressure is modified. Additionally, only limited information is given on the separation. A strong separation factor is stated with $\alpha_{HD}=0.53$, although it has to be minded, that this factor concerns, unlike the standard factor, absorption kinetics, whereas no isotope effect has been identified for desorption [80]. Based on the mentioned disadvantages, magnesium is not further considered.

For interactions with **yttrium**, the resulting separation factor is weak, with $\alpha_{HD}=0.7$ at 273 K [81]. Also, the resulting equilibrium pressures are much too low for the applied temperature range. At 1273 K the pressure is already in a rough vacuum (around $2 \cdot 10^3$ Pa), thus at 473 K and below the pressure is be in a high vacuum [82]. This material is therefore not suitable for isotope separation.

Palladium offers a number of advantages. The most important aspect, a strong separation factor, of $\alpha_{HD}=0.46$ and $\alpha_{HT}=0.34$ at 273 K, exists [54]. Furthermore, it is very well investigated, the thermodynamic characteristics are well understood, and the pressure is in the appropriate range. Desorption pressure in the plateau phase for protium is approx. $4 \cdot 10^3$ Pa and increases at 463 K to just under $2 \cdot 10^5$ Pa [83]. Additionally, it has a catalytically very active surface [69] and it stays ductile even under a high hydrogen concentration [37]. **Palladium** is a material that has potential and is therefore **selected and characterized**.

The **Pd-H system**, first reported by T. Graham in 1866, has a face-centered cubic (fcc) structure. In the α- and β-phase the hydrogen atom is located at the centre of the O-site. Some reports also show that deuterium atoms can reserve T-sites in the β phase for increases pressure and temperature. A reason is the thermal activation and the lower zero-point vibrational energy compared to hydrogen [35; 84].

For standard temperature and pressure (STP) palladium has a lattice constant of 3.889 Å. In the α-phase for small hydrogen concentration, the lattice parameter is 3.895 Å and in the β-phase it grows to 4.025 Å. Both values are dependent on the concentration and temperature and may vary within the range 84]. Hydrogen and palladium form a binary intermetallic hydride. In contrast to many other metal hydrides, only a slight macroscopic deformation of the palladium lattice occurs. Nevertheless, microscopic lattice defects occur due to repetitions of sorption. This is related to irregular growth of α and β-phases. However, these defects are usually reversible and can be remedied by an annealing process. To counteract this effect, silver can be added to palladium [84]. Though, with addition of silver, sorption pressure decreases and the plateau is steeper. In a composition with 40 % silver, no plateau is visible any longer. In addition, the amount of hydrogen that can be absorbed by the material decreases. With a 40 % silver content, only about 25 % can be absorbed compared to pure palladium [37]. For these reasons, it has been decided not to use an alloy.

In Figure 3.2 a), literature data of a PCT diagram for protium in palladium for four different temperatures are shown. The three phases α, α-β and β are clearly visible. The boundaries of the phases shift with temperature, but are approximately at a concentration from 0.05 to 0.6 mol_Q/mol_{Pd}. For the phase boundaries, an isotope effect exists. The two-phase region is widest for protium and then narrows for deuterium and tritium. From the α to the α-β phase, the tritium boundary is shifted to the right by around 0.008 mol_Q/mol_{Pd} compared to protium. From the α-β to the β phase the shift is around 0.04 mol_Q/mol_{Pd} to the left [85]. For the critical point an isotope dependency also exists, for protium it is highest at about 570 K. Above this temperature, there is only the α- or β-phase [69; 84].

Figure 3.2 b) shows a PCT diagram of the three different isotopes in palladium at 343 K. The isotope effect is clearly visible here. For protium, the pressure in the plateau region is at around $8 \cdot 10^3$ Pa, for deuterium it is higher at around $3 \cdot 10^4$ Pa, and the highest pressure is at $5 \cdot 10^4$ Pa for tritium. The ratio of the pressures of H_2 to D_2 is bigger than for D_2 to T_2. This is consistent with the theory of zero-point energy which is based on the molar masses of the isotopes.

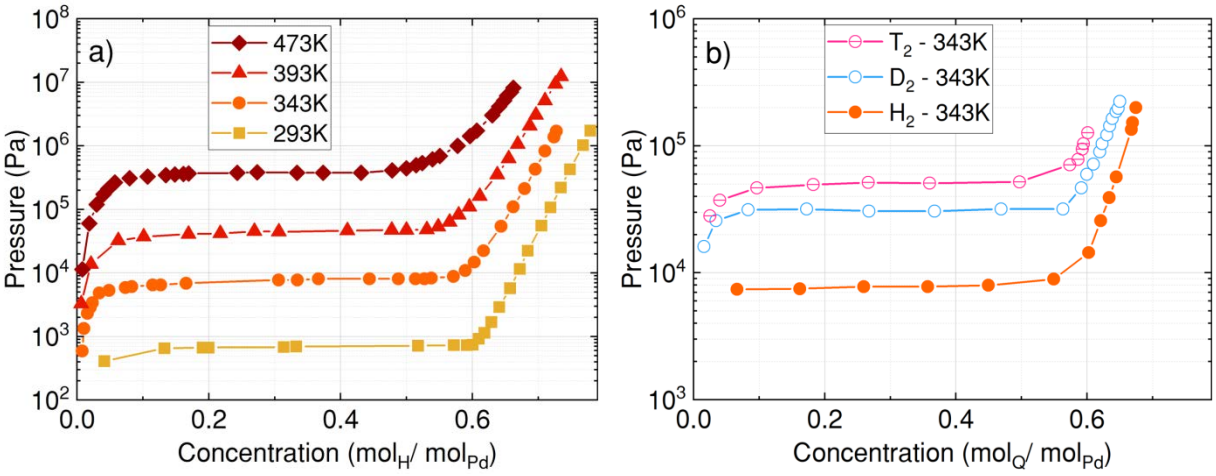

Figure 3.2: Literature values of PCT diagrams with the concentration in the x-axis and the pressure in the y-axis of a) protium-palladium system at 293 K (rectangle yellow), 343 K (circle orange), 393 K (triangle red) and 473 K (rhombus brown) adapted from [86] and b) protium (circle orange filled), deuterium (circle blue non-filled) and tritium (circle pink non-filled and crossed) in palladium at 343 K adapted from [87].

3.1.2 Materials with an Inverse Isotope Effect

In this chapter, materials with an inverse isotope effect ($\alpha>1$) are explained. As more materials hold a normal isotope effect, fewer materials are described below compared to the chapter with a normal isotope effect [43].

Vanadium and **Niobium** are materials with similar properties. Both have high separation factors, with α_{HD}=1.73 at 313 K and α_{HT}=1.91 at 273 K for Vanadium [54] and α_{HD}=1.73 at 333.6 K for Niobium [54]. However, both materials have an increased dead inventory, which is caused by the fact that several plateaus exist. The first plateau starts in the vacuum range and is therefore unusable for this application [83]. For vanadium, the protium pressure of the second plateau is about $5{\cdot}10^5$ Pa (for 313 K). At this temperature, the deuterium pressure is lower than $2{\cdot}10^5$ Pa. This plateau starts at about 1mol$_Q$/mol$_V$ [88]. The situation is similar for niobium. The pressure for protium at 333.6 K is about $4{\cdot}10^5$ Pa, for deuterium about $3{\cdot}10^5$ Pa. Here, this plateau also starts at about 1mol$_Q$/mol$_V$ [88]. In order to be compatible to palladium, lower temperatures have to be used than those for Pd. Both materials have good potential for isotope separation. However, the conditions to remove the oxide layer for sorption complicates the application, as high temperatures are required: 900 K for vanadium [89] and 1073 K for niobium [90]. This means an extensive change and effort in the design and configuration of the components, so vanadium and niobium are not pursued further.

As pure metals do not satisfy the requirements, I focus on alloys from now on, as the necessary pressure range can be adjusted modifying the alloy composition. Rather, the separation factor and other properties, such as disproportionation or pyrophoric behaviour, are more important here, since the temperature- and pressure range can possibly be adapted with the composition.

An **alloy of zirconium and nickel** has the benefit of a high storage capacity [67]. However, the separation factor is very low with α_{HT}=1.05 at 300.6 K [54]. In addition, the alloy has two plateaus. The resulting pressure for ambient temperature of the first plateau is in high vacuum, the second at a pressure of approx. 30 Pa [67]. Since only the second pressure range is considerable for this purpose, this material has a dead zone in which gas is stored, but which is not available for the separation. The required pressure range is so much higher than the pressure of the first plateau, that the possibility to change the composition in order to adjust the ranges cannot be used. This alloy is therefore not suitable for this particular application.

An AB_5 group **alloy of lanthanum nickel and aluminium** has several advantages. It is significantly less pyrophoric compared to uranium, for example [69]. For ambient temperatures the pressure of $LaNi_5$ is a bit smaller than $2{\cdot}10^5$ Pa [49], still too high for our application. As previously shown in the van't Hoff diagram, the change in alloy composition (adding Al) has a strong influence on the resulting pressure. It has a lower disproportionation behaviour compared to other alloys, which is due to the stability of the lanthanide-hydrogen [69]. However, a decomposition of the alloy therefore leads to hydrogen being irreversibly bound in the material. The separation factor of this alloy is small, with α_{HD}=1.62 at 195 K for $LaNi_5$ [54]. Replacing some amount of nickel with aluminium leads to separation factors of α_{HD}=1.2 at 333 K for $LaNi_{4.5}Al_{0.5}$ and of α_{HD}=1.3 at 333 K for $LaNi_4Al$ [54]. Another disadvantage is the change from inverse to normal isotope of the $LaNi_5$ system for an atomic fraction of the heavy isotope at around 0.6 [54]. This material is, though it possesses some interesting properties, due to the above mentioned properties not considered further.

Zirconium cobalt has been widely studied for hydrogen storage. A disadvantage of this alloy is the disproportionation behaviour, which increases with increasing temperature and hydrogen pressure [67]. Since the maximum hydrogen storage of this material is at a molar ratio of 1:1, and thus the disproportionation can be reduced, this composition has often been studied in the literature. However, the pressure for this purpose is too low, at only 2 Pa for 423 K [91]. Similar to LaNi, also for this material the isotope effect changes depending on temperature, composition and concentration from inverse to normal [91]. For these reasons, this alloy is not used.

Alloys of titanium and chromium have some advantages. The pyrophoric behaviour is low, although it is an AB_2 type [63]. In addition, disproportionation does not occur [63]. The separation factor is high, with α_{HT}=1.54 at 313 K for an equimolar ratio of Ti to Cr, and α_{HT}=2.03 at 273 K for $TiCr_2$ [54]. This shows that the composition influences the separation factor. The ratio of titanium to chromium also has a strong influence on the resulting pressure. Pure titanium has already been shown for the normal isotope effect, with a pressure of 10^5 Pa at 873 K [71]. When chromium is added, the pressure increases and the lattice constant decreases [92]. This behaviour can be observed in Figure 3.1, shown with a composition of $TiCr_{1.8}$. The influence of chromium to titanium shows that the selection of the composition is essential in order to select the most suitable pressure range. Literature states a change of the plateau pressure from $2{\cdot}10^4$ Pa to $2{\cdot}10^5$ Pa for an atomic ratio of chromium from 57.5 % to 62.6 % [92]. An alloy of titanium chromium has many advantages, leading me to select this material. Since the pressure range of 57.5 % to 62.6 % can be used for the application, the composition is chosen depending on the separation factor. For alloys of titanium, research has shown that the optimum of the separation factor is 5.2 valent electrons per metal atom, which results into a composition of 40 mol-% Ti (from now on referred as $TiCr_{1.5}$) [54; 92]. For this reason, the alloy **$TiCr_{1.5}$** is **selected for the material characterisation** and potentially the isotope separation.

Titanium and its alloys can be present in different crystal structures, which depend on factors as the alloy composition, temperature or manufacturing process. For pure titanium, an allotropic transformation takes place at 1155 K. Below this temperature, the hexagonal closed package (hcp)-structure (α-Ti) exists. Above, it will transform into a body cubic centered (bcc)-structure (β-Ti) [93]. By adding other materials, the structure is modified so that a classification is made between α- β and neutral stabilisers. With α-stabilisers, the α-phase is stabilised. These are metals such as Al, Ga, C, N or O. The β -phase is stabilised with metals such as V, Nb or Cr. The neutral stabilisers, such as Zr, Sn or Hf, have no influence on the α-β phase transformation [94]. An alloy of Ti and Cr belongs to the group of AB_2 types. With this stoichiometry, Laves phases are formed. These phases occur when the atomic size ratio is between 1.05 and 1.67 [95]. Three types of Laves phases exist: cubic $MgCu_2$ (C15), hexagonal $MgZn_2$ (C14) and hexagonal $MgNi_2$ (C36) [95; 96]. In these phases, atom A has an ordered structure, while atom B is arranged in tetrahedral positions around the A atom. The formation of these Laves phases depends on various factors, including the temperature and the composition of the alloy. The Mendeleev number has been developed to indicate the characteristic phase for different alloy compositions [95]. For titanium as atom A and chromium as atom B, the structure C15 is the most stable. This is found over a wide temperature range. For high temperatures, C14 is the most

stable and for temperatures in between, C36 is the most predominant [95]. However, some authors have also found C14 in the according region [92].

Figure 3.3 shows the PCT diagram for different compositions of the TiCr alloy. The composition $TiCr_{1,5}$ selected for further material characterisation (Ti(X)Cr(100-x) with x=40) has been highlighted – filled, yellow rectangles for the absorption pressure and filled, orange circles for the desorption pressure. The resulting averaged absorption pressure in the plateau is approx. $2{\cdot}10^5$ Pa, the desorption pressure $5{\cdot}10^4$ Pa.

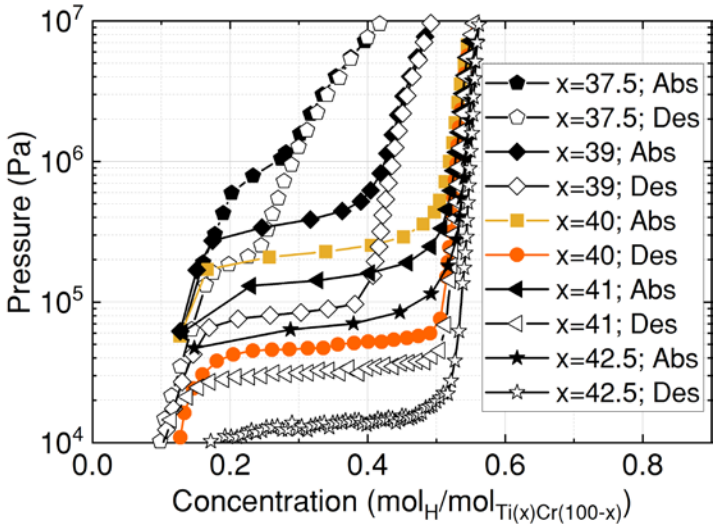

Figure 3.3: Literature values of PCT diagram with the concentration in the x-axis and pressure in the y-axis for protium in different composition of TiCr. $TiCr_{1.5}$ (x=40) is highlighted in rectangles, yellow for the absorption pressure and circles, orange for the desorption pressure adapted from [92].

3.2 Design and Setup of Test Rig MAIA

The main goal of this test rig is to obtain pressure-concentration diagrams for several isotherms (PCT) for protium and deuterium. These PCT diagrams can be determined from the measured pressure and temperature as well as the calculated concentration. Two main methods are used, the gravimetric method and the volumetric or manometry method [97]. For the first method, the amount of hydrogen absorbed is measured by the change of weight of the material [98]. I focus the design of the test rig on the volumetric method, also called the "Sieverts' Method" [84]. The principle of this method (shown in Figure 3.4) is the usage of two vessels. In the pre-vessel a defined amount of hydrogen is added. In the vessel, the bulk material is filled in. By opening the valve between both vessels, gas flows due to a pressure difference and gets absorbed by the material.

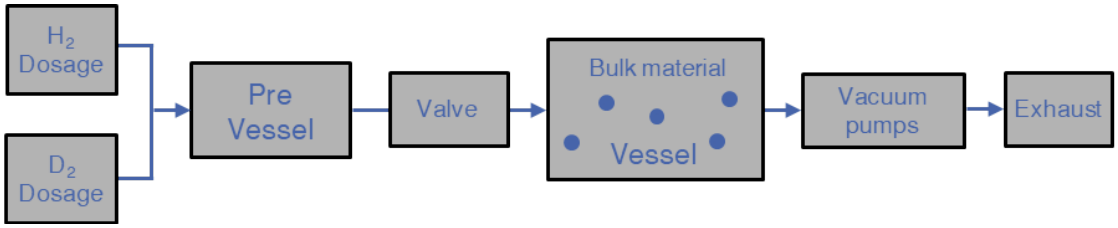

Figure 3.4: Principle of experimental setup.

Literature reports a list of issues concerning the accuracy. Knowing and considering this is necessary to obtain reliable results [97]. This mainly is derived from commercially available Sieverts apparatuses. I tried to address and overcome these by our in-house set-up. The ten factors are divided into three sections:

i) Whole setup: Hereby all points are listed, which are relevant for the complete setup and must be considered for the inlet and both vessels:

- Calibration: A distinction is made between the accuracy of the sensors and the precision of the volumes. The uncertainties of the sensors directly influence the derived number of concentration and need to be carefully selected. To measure the pressure, capacitance manometers have been selected, as they offer, besides high accuracy, an additional advantage of a gas type independent measurement. This is especially important for gas mixtures, as the exact composition is not always known. They are also zeroed regularly to counteract a drift. A sheath resistance thermometer has been chosen for the temperature measurement. As the sensor projects into the vessel, this Pt100 measuring principle can be used to measure the correct temperature.

  The volumes of both vessels, including all pipes and valves, have been calibrated with a high accuracy by usage of the Boyle-Mariotte law using argon as gas [99]. A calibrated volume (with the distilled water method) filled with argon has been attached to the MAIA vessels and separated with a valve. By applying the law, the volume of the vessels can be determined by pressure differences before and after opening the valve.
- Temperature control: Temperature gradients may arise in the facility, especially for higher temperatures. To ensure that this is not the case with our system, I ensured that the glass wool insulation is uniform along the entire length of the vessel. Another aspect is the homogeneity of the temperature over the entire vessel. I took utmost care that the heating cord is evenly distributed over the entire vessel. In addition, the sheath resistance thermometer does not measure temperature at a particular point, but averaged over a length of at least 50 mm. This ensures that the regulation of the heating is smoothened.

- Leaks: Especially through valves leaks have a falsifying effect as the remaining gas in the different vessels is not reliable. Only components with claimed leak rates smaller than 10^{-9} mbar·l·s^{-1} have been selected. Before experiments, a helium leak test has been performed. To prevent the bulk material from damaging moving parts (especially valve seats) and to ensure that it stays in the right position, filters are used.

ii) Inlet: The condition for the gas to enter (H_2 or D_2 dosage) are considered here:

- Purity of gases: A standard for the BET-analysis for gas adsorption, which is used for the determination of surface size, quotes a required purity of greater than 99.99 %. This application does not deal with the BET method, anyhow I take this value as benchmark. Protium used is of purity 99.999 % (5.0) [100]. Deuterium has 99.8 % purity, the remaining 0.2 % consists mainly of HD [101]. Both gases are therefore pure enough for the application.

iii) Vessel: The most parts are related to the vessel filled with bulk material, as the PCT diagrams are measured in it.

- Sample temperature measurement and thermal effects: These are both effects which are more sensible for the gravimetric method, as sensors can be located better and heating from exothermic reaction fade away easier due to interactions with the wall.
- Equilibrium: The definition of the pressure and concentration equilibrium needs to be selected thoughtful. I defined the steady state in such a way that the deviation of 60 sequential values, with a time interval of each 1 s, have to be less than the accuracy of the pressure sensors. Since it is not possible to measure pressure more accurately, this is a justifiable assumption.
- Amount of materials: According to literature, too small amounts can reach the lower detection limit. In my case, I made sure, that all sensors are adapted to the required range, whereby this issue is not seen here. For porous materials, it is stated that masses should be higher than 50 mg. For hydrides an advice of masses from 0.1 to 100 g has been given. As I use masses of several grams, this issue is not concerning.
- Volume of vessels as a ratio to the amount of material: This is mainly important for kinetic experiments and therefore less relevant for the MAIA design. This topic has only been examined little in the past, however a few basic statements can be made. No ratio is stated, but it is important that the volume is neither too big not too small. The volume compared to the amount of material cannot be too small, hence the expansion of material, leading to a decrease of the volume, has an influence. On the other hand, the volume has to be small enough so that the resulting pressures at the beginning and end are

sufficiently different compared to the uncertainty of the pressure sensors. If, on some point, kinetic effects want to be investigated with MAIA, the setup can be adapted anytime.

- Degassing of material: Before the actual experiments, the material needs to be properly activated. For the materials in MAIA, this has been performed accordingly to the manufacturer's specification (see subchapter 3.3). Also, the pathway of a material may have an influence. For my purposes I ascertained to receive materials which have been manufactured for this application and which have been under an inert storage until the filling into MAIA. Additionally the vessel has been baked out at 473 K under high vacuum for several hours. Degassing has therefore no influence.
- Thermal transpiration effect: This effect can occur and has a big influence up to 100 %, if the diameter of the vessel is similar or smaller than the mean free path (see equation. Thereby a temperature gradient along the length of a vessel can arise, leading to a pressure gradient. As the lowest pressure in MAIA is in rough vacuum, the mean free path is always smaller than the diameter. This influence is therefore not relevant.

The Piping and Instrumentation Diagram (P&ID) of MAIA is shown in Figure 3.5, with the parts shown in Figure 3.4 highlighted in blue.

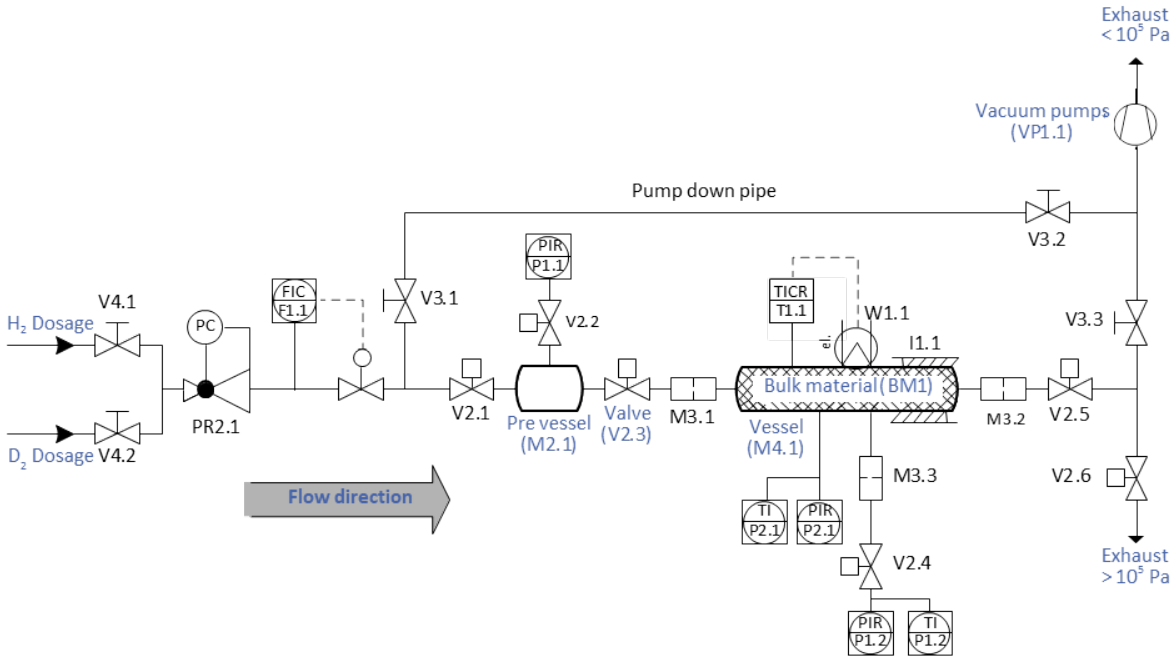

Figure 3.5: PID of the test rig MAIA.

The properties of components which are required for the determination of the PCT diagrams are listed in Table 3.1, including the size and accuracy of both volumes,

without material filled in, as well as the range of measurements and accuracy for the temperature and pressure sensors. A component list for all parts of the test rig, in which the abbreviation is described in more detail, is given in A3 in the Appendix.

Table 3.1: Components important for material characterization and their properties.

Abbr.	Component	Properties
M2.1	Pre vessel	32.00 ± 0.44 ml
M4.1	Vessel	73.07 ± 0.92 ml
T1.1	Sheath resistance thermometer	293 K ± 0.12 K – 473 K ± 0.3 K
P1.1 P1.2	Capacitance Manometer	1 mbar ± 0.1 mbar – 10000 mbar ± 12 mbar

A picture of the MAIA test rig, including its main components, is shown in Figure 3.6.

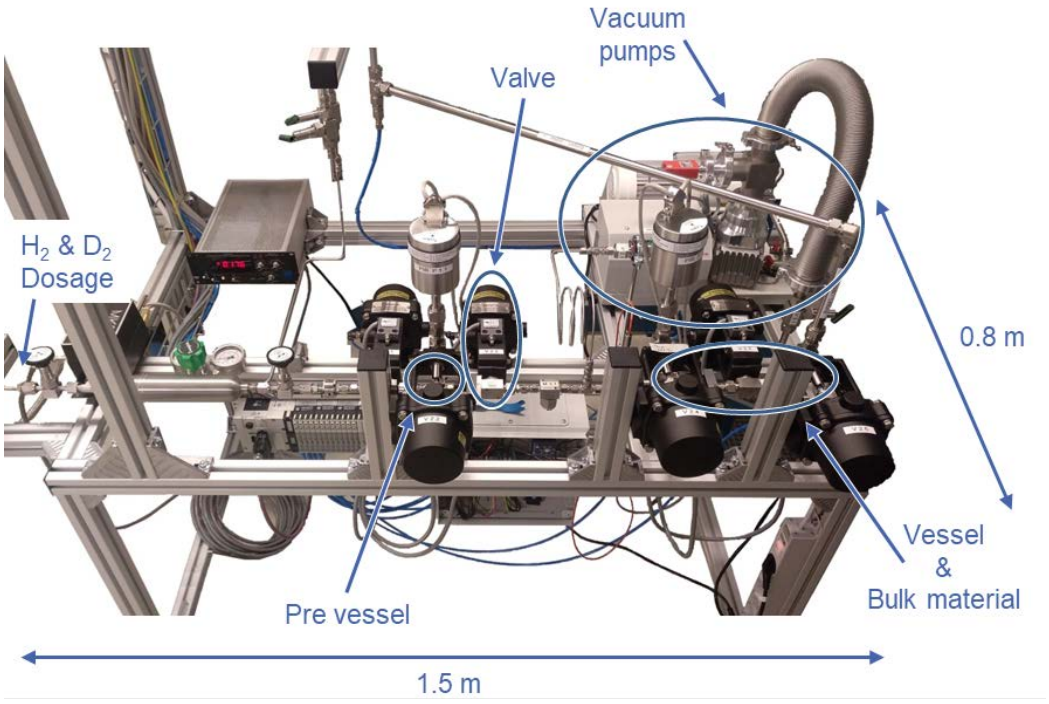

Figure 3.6: Component arrangement and dimensions of the test rig MAIA.

3.3 Procedure of Experiments

The isotherms in the pressure concentration diagrams along the complete concentration range have not been measured directly but generated pointwise by measurements at the same amount, but varying temperatures. For this, I consider three different procedures (shown in Figure 3.7). The left diagram shows the "a) piecewise dosage". In this process a certain amount of gas (step 1a) is added to the vessel, it is then heated up in a number of temperature-stages (step 2a and 3a) and cooled down again (step 4a). Another amount is added to the vessel (step 5a) and the process is repeated until the complete concentration range is covered (step 9a). For diagram "b) overall dosage", a certain amount (step 1b) is also added here and heated up (step 2b and 3b). In contrast to diagram a), however, no additional hydrogen is added. Instead, the desorbed hydrogen is pumped out (step 4b) and in the next step (step 5b) a higher amount of hydrogen is added. Diagram "c) overall dosage backwards", the amount of hydrogen for the maximum concentration is added (step 1c). Like the other procedures, the temperatures steps are carried out (step 2c, 3c and 4c). A certain amount of hydrogen is removed such that the concentration is running backwards. The absorption of hydrogen at ambient temperature results in an absorption pressure. As the temperature increases, all subsequent resulting values are desorption pressures. Therefore, due to hysteresis effect, differences can occur in the individual results. All data from PCT diagrams are values in steady state. Therefore, the state has been maintained at isothermal conditions until this steady state has been reached. Only after this the temperature for the next point has been increased. Steady state is defined for the experiments in such a way that the deviation of the values within one minute (equals to 60 values) is less than the accuracy of the pressure sensors.

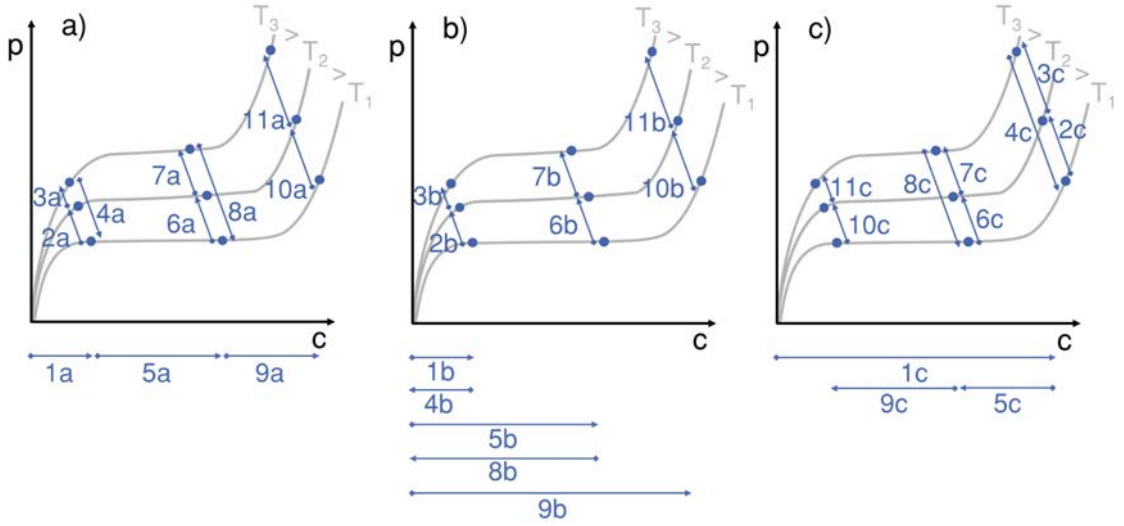

Figure 3.7: Overview of different procedures for material characterization with a) piecewise dosage; b) overall dosage; c) overall dosage backwards, illustrated in a pressure-concentration diagram.

All these procedures exhibit advantages and weaknesses with regard to the evaluation of the results, as shown in Table 3.2. Compared to procedures a) and c), the duration of an experiment takes longer for procedure b), as hydrogen has to be held longer at elevated temperature to pump out the gas (steps 4b and 8b). The accuracy of the information on concentration for procedure a) is slightly lower than for the other two procedures, as the errors accumulate due to piecewise dosage. However, the piecewise dosing has the major advantage that the relative position of the x-axis is provided by the addition of the individual hydrogen amounts (property 3). For procedure b) this is not given, as the pumping out of hydrogen does not ensure everything has been desorbed completely. Consequently, there may still be hydrogen in the material, which is not considered in this approach. One further aspect is the determination of the distances between the individual test points (property 4). This is important, because in the α- and β-phase, the individual points must be measured at smaller intervals, as in these zones a strong shift of the sorption pressure occurs with the addition of hydrogen. For procedures a) and b), the distances can be adjusted freely, as this only depends on the amount of hydrogen in the pre-vessel, which can be set by the mass flow controller (MFC). For procedure c), however, the stages are not adjustable, as the gas amount removed from the vessel is not controlled by an MFC, but is determined by pressure balancing during valve opening. Considering these aspects, **procedure a)** has been chosen as the process for the experiments, because it has the most advantages. Besides the scientific properties, an engineer property also needs to be considered, which also leads to procedure a) as best approach. Some materials hold a high hydrogen capacity. To reach the maximum concentration in case for b) and c), either the pressure in the

pre-vessel has to be high or the volume of this pre-vessel has to be increased. Both lead to a more complex design of the test rig. Characterisation of the two isotopes has been performed one after the other with the piecewise dosage (a)). Between the two experiments, the system has been heated up and pumped down for several hours in order to minimise gas residues in the material.

Table 3.2: Comparison of operational properties for the procedures a) piecewise dosage, b) overall dosage and c) overall dosage backwards with their suitability for interpretation and evaluation of the measured the data, ranked from ++: very good to --: very bad.

Operational properties	a) Piecewise dosage	b) Overall dosage	c) Overall dosage backwards
1. Duration of experiments	++	+	++
2. Accuracy of concentration	+	++	+
3. Relative position to c-axis	++	0	++
4. Determination of the steps	++	++	--

For the piecewise dosage, the calculation of concentration consists of different terms. The basic formula is the ideal gas law, and it is employed to calculate the amount of hydrogen for the used amount of the material to be analysed. Before gas is injected, both vessels are pumped down to vacuum. Then, gas is injected into the pre vessel (V_{PV}), which depicts the first term of equation (3.1). With opening the valve ($p_{V2.3,open}$), gas is distributed (the pressure is measured) and absorbed in the bulk material in the vessel ($V_{V\text{-}BM}$). With the subtraction of the second term the actual amount of absorbed hydrogen can be calculated. For piecewise dosage, gas from the previous dosage has to be subtracted (term 3). The resulting concentration for elevated temperature is given by the last term. Schematic depictions for each term are given in A4 in the Appendix.

$$\frac{c_{H/BM}}{mol_H/mol_{BM}} = \sum_{i=1}^{N}\left(\frac{p_{V2.3,closed,i+1}\cdot V_{PV}}{R\cdot T_{amb}} - \frac{[p_{V2.3,open,i+1}\cdot(V_{PV}+V_{V-BM})]}{R\cdot T_{amb}} - \frac{[p_{V2.3,open,i}\cdot V_{V-BM}]}{R\cdot T_{amb}} - \frac{(p_{V2.3,closed,i+1,T}-p_{V2.3,open,i+1})\cdot V_{V-BM}}{R\cdot T_{elev}}\right)\cdot 2\frac{M_{Pd}}{m_{Pd}}. \quad (3.1)$$

In order for the materials to develop their complete absorption capacity, activation needs to be conducted prior to the characterization to remove other substances on the surface. The procedure of activation is different for each material and is usually specified by the manufacturer. According to the information, both materials must be activated with protium.

Palladium has been flushed with protium at 473 K [1]. For validation, the absorption capacity has been tested and compared with pressure concentration diagrams for the palladium-hydrogen system from literature. The activation has been carried out, until the maximum concentration has been reached. For palladium, literature values show the transition from the α-β to the β-phase at about 0.6 mol_H/mol_{Pd}. The activation reduced PdO to Pd. This reduction has been confirmed in an X-ray analysis performed, shown in Figure 3.8. 2·theta refers to the incoming and reflecting beam, whereby a shift of the non-activated palladium powder (PdO) from 42° to 40° for the activated powder (Pd) is visible. The reduction of the powder is visible here [102].

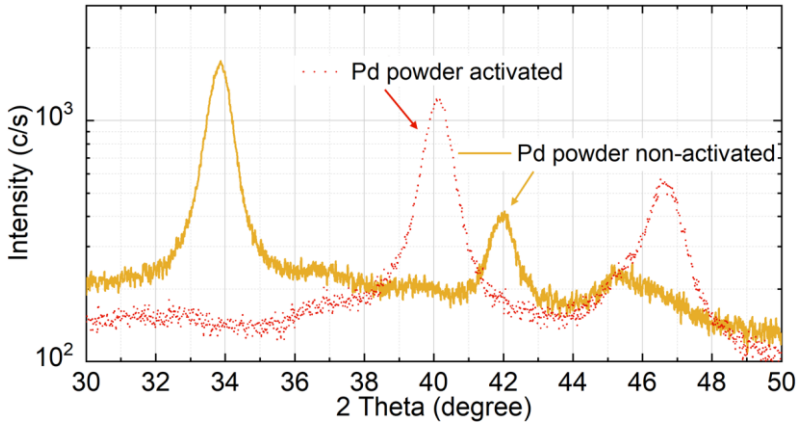

Figure 3.8: X-ray of a non-activated (solid yellow line) and activated (dotted orange line) palladium powder.

For $TiCr_{1.5}$, two-stage activation is necessary. In the first step, the material is gradually heated to 573 – 673 K and held there for a few hours while evacuating the vessel. In the second step, protium is added in a batch process and held for a short time and then the gas is pumped out. The temperature is stepwise increased from 473 to 573 K. This ensures stabilisation of the material[2].

3.4 Experimental Characterization of Absorption Materials

In the first subchapter, the experimental results of protium and deuterium with Pd are presented. In the next subchapter, the results with $TiCr_{1.5}$ are given. For both materials, firstly their respective properties and ensuing their PCT diagrams are given.

[1] Declaration by the manufacturer Research Centre Jülich GmbH

[2] Declaration by the manufacturer SAES Getters

The separation factors for both materials and their specific characteristics, including kinetic effects, are provided.

3.4.1 Characterization of normal isotope effect materials (H_2-Pd and D_2-Pd)

Palladium coated on a porous surface with 30 wt.-% is used. This has two advantages. A porous surface enables more palladium to be available for the reaction. Also, cost can be reduced by this. All pellets are of same size, with 0.8 mm diameter. In Table 3.3 an overview of its properties is given as well as a picture of the material in Figure 3.9.

Table 3.3: Overview of the properties for palladium[3].

Properties	Pd
Composition	30-wt% Pd on γ-Al_2O_3
Particle size	0.8 mm pellets
Amount characterized	7.74 ± 0.00077g
Porosity	0.86
Density	8314 ± 10007.2 $\frac{kg}{m^3}$
Bulk density	1200 ± 29.96 $\frac{kg}{m^3}$

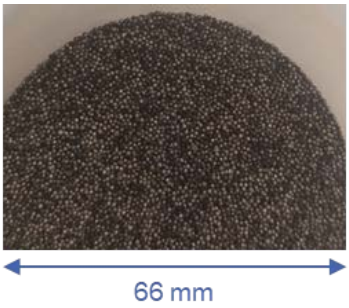

Figure 3.9: Picture of palladium.

For palladium, isotherms in 5 K steps from ambient temperature to 473 K have been constructed from the measurement data. Holding each temperature for 30 minutes ensures that steady state is reached. In principle, for this material, the absorption of protium is faster compared to deuterium. The PCT diagrams for both isotopes are shown in Figure 3.10, with protium in a) and deuterium in b). The values for the uncertainties are shown in the appendix A5 in Table A.18 to Table A.20 for protium and Table A.21 to Table A.23 for deuterium (a visual summary is shown in Figure A.1 and Figure A.2). The deviation of the temperature from the set point and the uncertainty of the sensor are even lower than per mille range and are therefore negligible. For Pd-H_2, the uncertainties of the concentration are from 0.15 % to 0.71 %. For the pressure, the worst uncertainty is 21.4 %. As, however, this value is at the beginning of the α-phase, it is out of interest, as this range is not going to be used for isotope separation. The interesting concentration range starts from c≈0.4 mol_H/mol_{Pd},

[3] Declaration by the manufacturer Research centre Jülich GmbH

with an uncertainty of the pressure from 0.31 % to 2 %. For Pd-D_2, the uncertainties for the concentration range from 0.17 % to 1.02 %. For the relevant concentration range, the uncertainties for the pressure are from 0.22 % to 1.19 %.

Comparing the pressures of both isotopes at a given concentration, the pressure for protium is lower than for deuterium. This proves conclusively that palladium has the required normal isotope effect. Looking at the curves for both isotopes, two aspects become apparent. First, the amount desorbed increases towards the β-phase. At the boundary from α to α-β-phase, the concentration decreases from 0.1 at room temperature to 0.088 mol_H/mol_{Pd} at 473 K. This means that about 14 % of the gas is desorbed. In the middle of the concentration range, at c=0.31 mol_H/mol_{Pd}, approximately 16 % is desorbed at 473 K. In the β-phase, at a concentration of 0.64 mol_H/mol_{Pd}, almost double, about 28 % is desorbed at 473 K. Since it is important to use the maximum amount of gas possible, later in the isotope separation, it is desirable to work in the end α-β towards the β-phase. This is the case for protium as well as for deuterium.

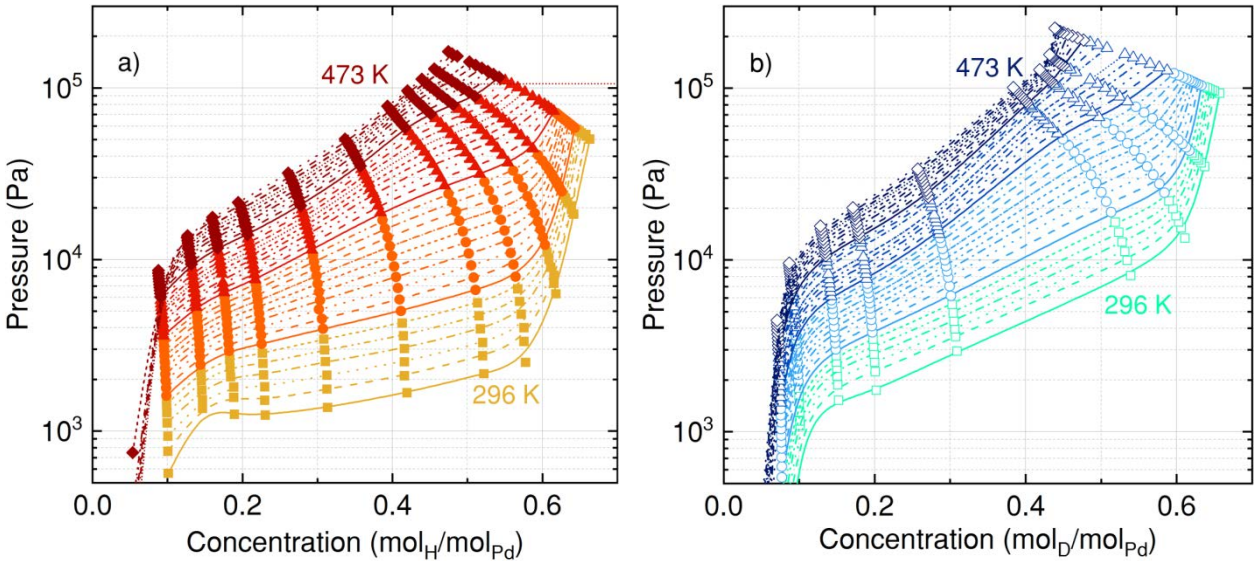

Figure 3.10: Experimental pressure as function of concentration for a) protium in Pd measured in 5 K steps from 296 – 473 K: 296 – 323 K (yellow rectangles), 328 – 373 K (orange circles), 378 – 423 K (red triangles), 428 – 473 K (brown rhombus) and for b) deuterium in Pd measured in 5 K steps from 296 – 473 K: 296 – 323 K (cyan rectangles), 328 – 373 K (light blue circles), 378 – 423 K (blue triangles), 428 – 473 K (royal blue).

Second, it can be seen that there is no clear plateau for both isotopes. According to literature [103; 104], this is mostly related with an enthalpy effect at high amounts of hydrogen sorbed and inefficient removal of heat due to absorption can occur. Reflecting the differences in reaction enthalpy, this effect is expected to be more pronounced for deuterium than for protium.

To ascertain whether the excess in heat is relevant, further tests have been performed. In contrast to the PCT-experiments before, the experimental amount of gas has not been added all in one go, but instead, a flow rate of 2 sccm has been set with a mass flow controller (MFC) and thus gas has been added with a lower flow rate to the palladium. The results are shown in Figure 3.11. For protium, filled, yellow rectangles represent the results from PCT diagram at ambient temperature. The filled, orange symbols depict the new results with the MFC addition. For protium, a slight improvement can be seen if the gas is added using an MFC. For deuterium, this effect is even more apparent (open, blue circle symbols for MFC, rectangles for values from PCT diagram). The pressure of the ideal case "MFC" is higher, and at the border to the β-phase the values correlate with the values from the PCT diagram. The experiments with the MFC have only been intended to investigate this phenomenon, which endorses the above mentioned theory, that heat influences the result. A slight slope is still visible, which can arise from localised deformations or non-homogeneous surfaces [47]. For the modelling, the values of the piecewise dosage have been taken, since in the future separation experiments not a slow flow (as in the MFC experiment) is set, but the gas is added in a single stage. The PCT diagrams from Figure 3.10 are therefore closer to reality.

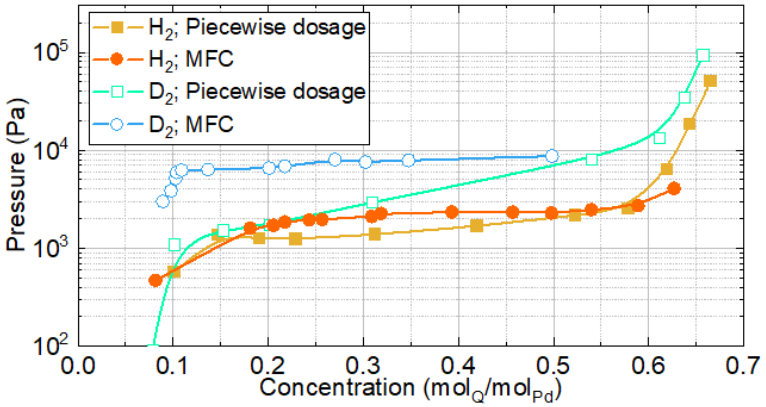

Figure 3.11: Comparison of experimental pressure as function of concentration from piecewise dosage (rectangle symbols) and MFC-dosage (circle symbols) for protium (filled symbols orange colour palette) and deuterium (open symbols blue colour palette) for ambient temperature.

The experimental data show deviations compared to the literature, illustrated in Figure 3.2. The literature plateau for protium is about $7 \cdot 10^2$ Pa at 293 K [86]. The data from MAIA are in the range of 10^3 - $2 \cdot 10^3$ Pa in the low temperature range. Two reasons arise, one of them is the minor deviation of the slightly different temperature. In the MAIA experiments it is approximately 296 K, which results in a higher desorption pressure. For 473 K, the values from the literature are around $3 \cdot 10^5$ Pa in the plateau region. Values from MAIA lie between 10^4 and 10^5 Pa. The primary cause

of the difference, however, is not the temperature, but most probably the hysteresis effect. In the case of the experiments in MAIA, the data at ambient temperature represents absorption values. However, most of literature indicates desorption values, resulting in a lower sorption pressure. At lower temperatures, this phenomenon is prominent and decreases with increasing temperature. This can also explain that at room temperature the MAIA values are larger than the literature values and at 473 K it is reversed. Since, as shown in the MFC experiments, the ideal pressure is higher, the values can be compared with those from the literature.

The experimental data points from material characterization are implemented in correlations. On the basis of different laws a fit and interpolation are used. The α-β-phase follows the van't Hoff law, with a plateau in this region which results into a linear behaviour for ln(p) vs. T. In an ideal case, the pressure in the plateau does not depend on the concentration. However, for experiments at MAIA with the above discussed enthalpy effect the plateau possesses a slight slope for both isotopes. Therefore, the concentration has to be implemented in the pressure equation. In order to realize this equation for each measured temperature equations have been set up in the first place. With help from this, pressure for constant concentrations over the α-β-phase (c=0.3; 0.4; 0.5) have been calculated. All this results into an equation for protium:

$$\frac{p_{H2}}{Pa} = \exp\left(5.73945 + 19.7921 \cdot \frac{c}{\frac{mol_H}{mol_{Pd}}} - \left(0.95105 + 5.60855 \cdot \frac{c}{\frac{mol_H}{mol_{Pd}}}\right) \cdot \frac{1000 \cdot K}{T}\right) \cdot 10^2, \quad (3.2)$$

with c as the concentration of hydrogen in the material in (mol_Q/mol_{Me}). For deuterium in palladium, the same procedure has been used, resulting in:

$$\frac{p_{D2}}{Pa} = \exp\left(6.44996 + 16.1909 \cdot \frac{c}{\frac{mol_D}{mol_{Pd}}} - \left(1.22701 + 3.66465 \cdot \frac{c}{\frac{mol_D}{mol_{Pd}}}\right) \cdot \frac{1000 \cdot K}{T}\right) \cdot 10^2. \quad (3.3)$$

In order to compare the MAIA results with literature, a concentration of c=0.55 mol_Q/mol_{Pd} has been set, as the range from c=0.45-0.65 mol_Q/mol_{Pd} is relevant for the separation tests. The resulting pressure is shown in Figure 3.12 in direct comparison to literature values.

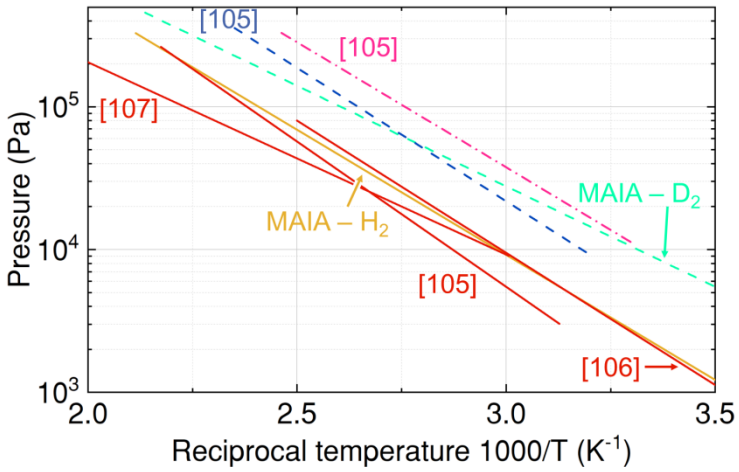

Figure 3.12: van't Hoff diagram – Comparison of protium values from experimental pressure as a function of concentration at c=0.55 mol_H/mol_{Pd} (solid yellow line) and literature data (solid orange lines), deuterium values from experimental data (dashed green line) and literature data (dashed blue line) and literature data of tritium (dashed-dotted pink line) adapted from [105; 106; 107].

Slight deviations with the literature values shown still exist. The plateau pressure of the experiments lie, however, in the distribution of the literature values.

The separation factor has been integrated from experimental values, applying equation (2.12), with c_1=0.45 and c_2=0.65. This range has been selected, as it is foreseen for separation. The resulting equation for the separation factor is the following:

$$\alpha_{HD,Pd} = -0.33339 + 3.5527 \cdot 10^{-3} \cdot \frac{T}{K} - 2.36443 \cdot 10^{-6} \cdot \left(\frac{T}{K}\right)^2. \quad (3.4)$$

For 273 K it results into a value of 0.46. This corresponds to the integral separation factor over a concentration range. For a less precise approximation of the separation factor, the pressures of protium and deuterium can be compared for a specific concentration. Looking at these at c=0.2 mol_Q/mol_{Pd}, the separation factor is 0.67, whereas at c=0.5 mol_Q/mol_{Pd} it is 0.23. This shows that it is important for the separation to work in the back region of the α-β-phase. An overview of the experimental result compared to literature values is shown in Figure 3.13. This diagram shows that the separation factor varies and depends on several conditions.

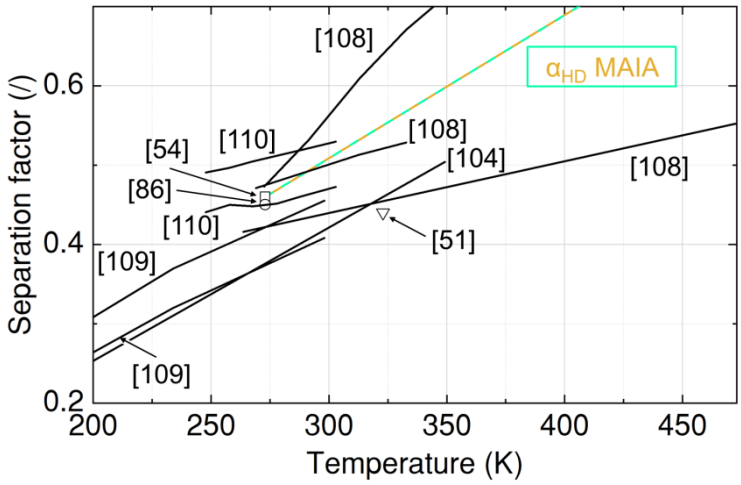

Figure 3.13: Comparison of separation factor α_{HD} as function of temperature from experimental data (dashed yellow green line) and literature data (solid black lines and solid points) adapted from [51; 54; 86; 105; 108; 109; 110].

At 298 K the separation factor changes from 0.4 to 0.46 for a protium ratio of protium of 0.2 to 0.8 [109]. Also the storage has an influence. For 10 % deuterium the separation factor decreases from 0.45 to 0.511 for 278 K after 3.5 years of storage [1110]. For low concentration range using a 1 mm Pd wire, the factor for 273 K gives a value of α_{HD}=0.45 [86]. For a molar ratio of 40 % for protium ($PdH_{0.4}$), at 273 K the separation factor is α_{HD}=0.46 [54]. For the higher concentration range up to 323 K and 10^5 Pa, as well as D/H=1/1, measurements on a Pd black sample with small specific surface area, a value of α_{HD}=0.39 is obtained [86].

Also for the separation factor, the experimental result lies in the distribution of the literature values. As both, plateau pressure and separation factor, provide plausible results, **I have been able to verify the MAIA results and the feasibility of the experimental procedures in the test rig** for a normal isotope effect for H and D in Pd. For this reason, I consider it also applicable for the characterization of material data for other materials.

3.4.2 Characterization of inverse isotope effect materials (H_2-TiCr and D_2-TiCr)

In order to compare the behaviour of $TiCr_{1.5}$ with Pd, the same amount of bulk material has been used. However, the material has not been coated onto a porous surface, leading to a reduction in porosity. The particle size has a distribution between 0.1 and 1 mm. The material properties, including uncertainties, are given in Table 3.4 and a picture of the material is shown in Figure 3.14.

Table 3.4: Overview of the properties for the titanium chromium alloy [4].

Properties	$TiCr_{1.5}$
Composition	40-at% Ti, 60-at% Cr
Particle size	0.1-1 mm pellets
Amount characterized	7.75 ± 0.00077g
Porosity	0.67
Density	$6830 \pm 6749.8 \frac{kg}{m^3}$
Bulk density	$2243 \frac{kg}{m^3}$

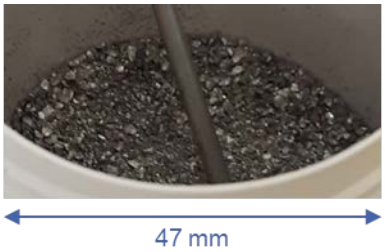

Figure 3.14: Picture of the titanium chromium alloy.

For $TiCr_{1.5}$, isotherms have been constructed via measurements from ambient temperature to 473 K in 10 K steps. Each temperature has been kept for 45 minutes to ensure that steady state is reached. The PCT diagrams for protium and deuterium are shown in Figure 3.15.

The values for the uncertainties are shown in the appendix A5 in Table A.24 to Table A.26 for protium and Table A.27 to Table A.29 for deuterium (a visual summary is shown in Figure A.3 and Figure A.4). Also for titanium chromium, the deviation of the temperature from the set point and the uncertainty of the sensor are even lower than per mille range and can be neglected here as well. In the relevant concentration range, which starts at $c \approx 0.15\ mol_H/mol_{TiCr1.5}$, the uncertainty of the concentration for protium lies between 0.43 % and 0.6 %. For the pressure, the uncertainty at low pressures is at 8.58 %, but drastically reduces down to 0.12 %. For $TiCr_{1.5}$-D_2, the uncertainties for the concentration lie between 0.41 % and 0.52 %. For the relevant concentration range, the uncertainties for the pressure go down to 0.22 %.

By comparing the pressures of both isotopes at a certain concentration, it becomes clear that this material features the inverse isotope effect, as the pressure is higher for protium than for deuterium.

Similar to palladium, the amount desorbed depends strongly on the concentration. At low concentrations, little gas is released at 473 K, whereas towards the end up to about 30 % is desorbed.

[4] Declaration by the manufacturer SAES Getters

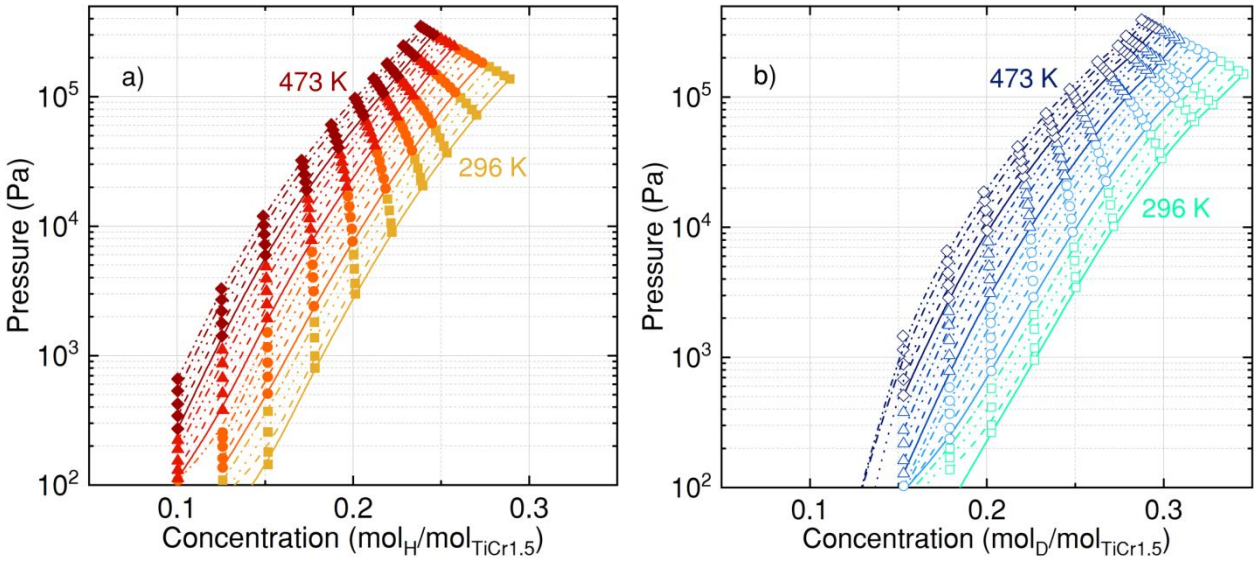

Figure 3.15: Experimental pressure as a function of concentration for a) protium in $TiCr_{1.5}$ measured in 5 K steps from 296 – 473 K: 296 – 323 K (yellow rectangles), 328 – 373 K (orange circles), 378 – 423 K (red triangles), 428 – 473 K (brown rhombus) and for b) deuterium in $TiCr_{1.5}$ measured in 5 K steps from 296 – 473 K: 296 – 323 K (cyan rectangles), 328 – 373 K (light blue circles), 378 – 423 K (blue triangles), 428 – 473 K (royal blue).

Palladium shows a plateau both in the literature and, within the uncertainties discussed above, also in the experiments. Titanium-chromium draws a plateau in the literature. However, the $TiCr_{1.5}$ used in our experiments does not exhibit a plateau.

The main reason why this material does not exhibit a plateau comes from the manufacturing process, which has been different than usual for the purpose of having quickly a first candidate material to study. A titanium-chromium alloy is usually produced by arc melting under a high-purity argon atmosphere. Subsequently, it is heat treated in vacuum under argon atmosphere and then cooled in ice water. The duration of the heat treatment and the temperature used have a strong influence on plateau formation [111]. This means that alloys with a certain composition do not always behave identically, but that additional influences, such as the manufacturing process, has to be considered.

The non-existence of the plateau leads to limited reversibility. Between the characterisation of deuterium and protium, a bake-out at 673 K for several hours has been carried out. An increase to 673 K instead of the standard 473 K ensures that more than double the amount of gas is desorbed. This reduces the shifting effect, as less gas stays in the material. But even at 673 K a shift still occurs. In order for the isotope effect, and thus also the separation factor, to be determined correctly, I methodologically corrected this effect with a correction factor. To calculate the separation factor, an integration of the pressure over a certain concentration range has

been conducted (see equation (2.12)). Integration has been performed in the range from c_1=0.15 to c_2=0.32 for several temperatures and a formula for the separation factor has been extrapolated:

$$\alpha_{HD,TiCr_{1.5}} = 3.09792 - 4.37086 \cdot 10^{-3} \cdot \frac{T}{K} + 1.508 \cdot 10^{-6} \cdot (\frac{T}{K})^2. \quad (3.5)$$

This results into a separation factor of 2.02 for 273 K. Comparing this value with data from the literature, which is approximately 2, this result is in good alignment [54].

3.5 Applicability of Materials

The experimental investigation of the two materials Pd and $TiCr_{1.5}$ has demonstrated that they fulfil the requirements of isotope separation and can be utilised for further separation tests. Some aspects, however, have to be taken into account. For a good interaction of the two materials, combination of the two materials have to be suitable in terms of separation factor, pressure range and absorption capacity. At low temperatures, the separation factor for Pd is only slightly different (8 % better at 273 K) in comparison with $TiCr_{1.5}$: with $\alpha_{HD,Pd}$= 0.46 and $\alpha_{HD,TiCr1.5}$= 2.02. For a concentration of 0.1 mol_Q/mol_{Me}, $TiCr_{1.5}$ can absorb 7 times more hydrogen than Pd. For Pd, higher concentrations of the α-β-phase and the beginning of the β-phase have to be used due to a higher separation factor and larger amount of desorbed gas. This must be borne in mind when filling the columns with material. Also the pressure range of the two materials align well. The pressure is around 10^3 Pa (for 293 K) for Pd and TiCr1.5, depending on the concentration range, and increases to around 10^5 Pa for 473 K. For palladium, the pressure of deuterium is higher than that of protium, for the titanium-chromium alloy it is the opposite.

With regard to the tritium inventory, the consideration of the residual inventory in both materials after desorption is worthwhile looking at. Complete desorption is not possible for the temperature range used; residues always remain in the material. This can be accepted as long as this background inventory achieves a steady-state value which is of acceptable order. It is not possible to give a quantitative statement on how much residual gas is left in the material. Looking at the PCT diagrams of the two materials, a maximum of the amount indicated at 473 K remains (for Pd in the β-phase, for example, still a concentration of 0.46). However, since the steady-state changes during pumping down, more gas will be desorbed in the end.

4 Model Description of the TSA Process

This chapter is divided into two main sections. In the first part, the structure of the model is explained. The model with the mathematics behind already exists and has been taken from a previous work [6]; this will be explained first. For the purpose of this work, mainly material-specific data as well as design-specific data has been implemented in the existing work. All assumptions that have been applied for this are also discussed qualitatively in the first part of this chapter. The second part presents the results. First, the selection of the parameters is explained and then the results of the parameter study are listed and discussed with regard to the further experiments of isotope separation.

The main objective of the conceptual design and performance of the experiments is to answer the question of whether the MC-TSA technology proves to be a suitable technology for isotope separation. The correlation between the separation efficiency and the associated effort (higher number of cycles, longer separation times or more separation columns), and indirectly the tritium inventory, plays a significant role. I illustrated this relationship in Figure 4.1. The enrichment is initially efficient but is associated with strongly increasing effort, the higher the intended enrichment shall become. As the gas mixture becomes purer, it becomes more difficult to extract an even cleaner isotope. The separation follows an asymptotic behaviour until complete purification is achieved. The longer this process lasts, the larger the tritium inventory becomes. However, the aim is to achieve a high purification with a low tritium inventory. Since these two effects are contradictory, an optimum is to be identified. The position of this optimum is to be established with the modelling and the resulting experimental schedule. Various parameter studies are carried out in the process. The criterion for the best result is the one that shows good enrichment with the shortest duration in comparison. Since the enrichment is stronger with a low number of cycles, the aim is to work in the lower cycle range.

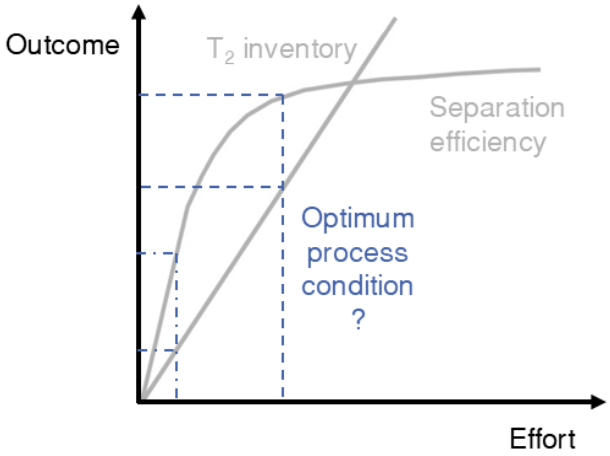

Figure 4.1: Theoretical behaviour of the separation process: Enrichment accompanied as a function of effort (e.g. number of cycles or temperature range) and the increase of the tritium inventory.

4.1 Model Development

In this chapter, first an overview of the mathematical equations used are given, then material properties are adapted and in the end the assumptions including an explanation is given.

4.1.1 Mathematical Background & Implementation of all Process Conditions

For the development of the model the simulation program ASPEN® Custom Modeler is used and the process is treated as a transient 1D-system. This linear equation system is calculated by the implicit Euler algorithm, which is a numerical method for the solution of ordinary differential equations. Figure 4.2 a) shows the flowchart of the separation process with two columns ("C1" filled with Pd and "C2" filled with $TiCr_{1.5}$) and different gas flows. The "hydrogen input" is the stream which is added in C1. Two outlet streams "protium_free" (in which the heavy isotopes are extracted from C1) and "protium_rich" (in which the light isotopes are extracted from C2). Additionally, the columns are connected with two connecting tubes.

In Figure 4.2 b) the principle is shown. Both columns have been split into a defined number of nodes n, which represent the theoretical stages. The decision on the number of nodes is a balance between a high resolution (large number) and a fast realisation of the modelling (small number). Examination has shown that 100 nodes is a good solution between fast simulation and accurate results, and it has therefore been chosen for both columns. The two columns are connected with connecting tubes, at n=100 at

column 1 and n=1 at column 2. The enriched isotopes are extracted at the end of the respective columns, i.e. at n=1 for column 1 and n=100 for column 2.

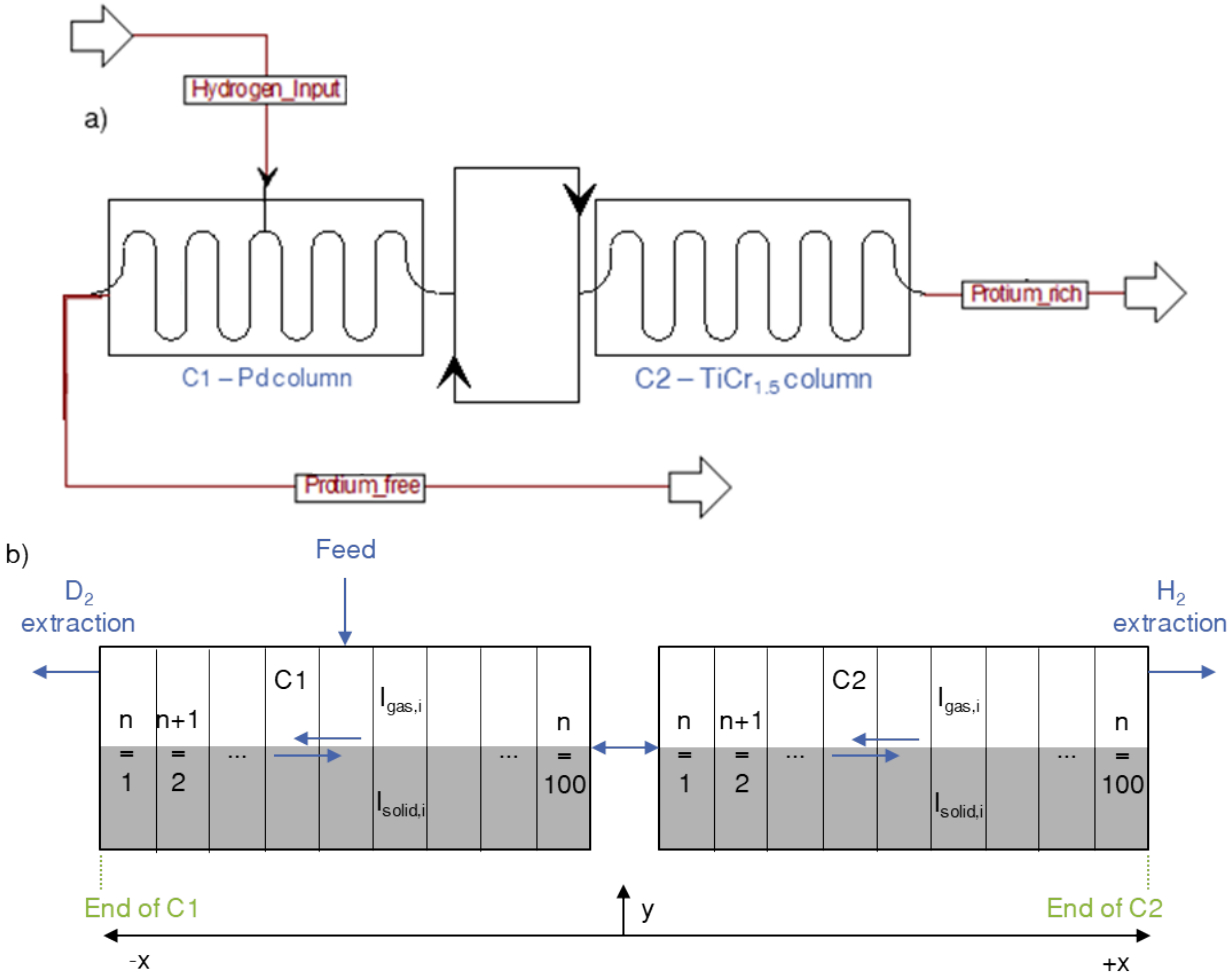

Figure 4.2: Flow chart of the separation process including the two columns and streams in a) and discretized as a 1-dimensional principle setup in b).

Parameters (as the inventories) are calculated for each node, resulting in gradients over the length of the column. The distribution of the isotopes in the gas and solid phases depends on the respective material and the temperature used. This results in four inventories inside each column: $I_{solid,H}$, $I_{solid,D}$, $I_{gas,H2}$ and $I_{gas,D2}$. This correlation can be described by the equation (4.1) and can be used for both isotopes for each node:

$$I_{ges,n,Q} = I_{gas,n,Q2} + I_{solid,n,Q}. \tag{4.1}$$

Since the columns are split into a defined number of nodes, the model is solved by the finite volume method. The 'finite volume' refers to the total inventory of the isotopes. Every node is connected by a flow and therefore calculated by the conservation of mass law:

$$\frac{dI_{\mathrm{ges,n}}}{dt} = F_{\mathrm{n-1}} - F_{\mathrm{n}}, \tag{4.2}$$

with the flow F in (mol/s). Depending on the pressure difference within the volumes, the flow direction can change. This is calculated by the Hagen-Poiseuille law, which is applicable for Newtonian fluids in a laminar flow through a long cylindrical pipe of constant cross section and combined with the ideal gas law:

$$F_n = \frac{p_n \cdot \pi \cdot r^4}{8 \cdot \mu \cdot R \cdot T} \cdot \frac{\Delta p_n}{L_n} \cdot \frac{I_{gas,i}}{I_{gas}}, \tag{4.3}$$

with L_n as the length per node, r as the column radius, Δp_n as the pressure difference between two nodes and μ as the dynamic viscosity, which depends on temperature, gas pressure and hydrogen isotopes.

The extraction of the isotopes at one end of each column is described with a defined percentage of the basic total inventory per component and the connecting flows of column 1 and 2 are calculated by the Hagen-Poiseuille law, with the difference of the gas pressures in the columns. The same amount which has been extracted from both columns must be fed in the system again (feed stream), in order there to remain a constant total inventory in the columns.

4.1.2 Alignment of Material and Model Properties for Isotope Separation Experiments

For the model to provide usable results, it is important to adjust the boundary conditions and to implement facility-specific data. The following points need to be considered:

i) Dimensions of columns: For both columns, a diameter of $6 \cdot 10^{-3}$ m is used. Column 1 is 3 m and column 2 is 6 m long, corresponding to the dimensions of the test rig.
ii) Composition of gas mixture: The ratio of the initial composition of protium to deuterium is 42.2 % to 57.8 %which is used for the experiments.
iii) Time for heating and cooling: In the model a linear heat rate has been applied. However, the heating and cooling rate at the test rig is not linear, since the temperature is maintained with a preheated and precooled oil reservoir. This difference in behaviour is illustrated in Figure 4.3.

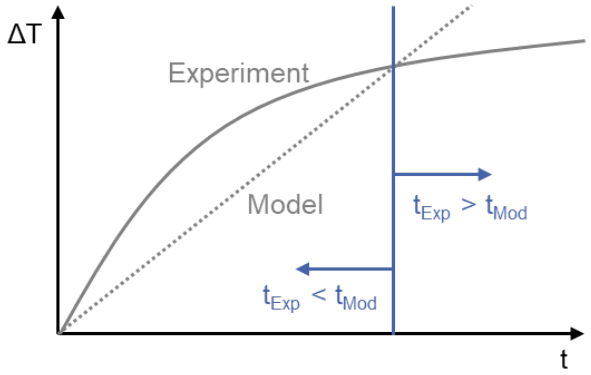

Figure 4.3: Theoretical behaviour of heating and cooling times for the model and the experiment.

For experiments small temperature in- or decreases are reached within a very short time. For larger temperature differences, the change behaves asymptotically, as the temperature approximates the temperature from the oil reservoir. Dependent on the temperature difference, either the value in the experiment or the model is reached faster. This behaviour must be reflected and the modelling results modified accordingly, as it is decisive for the decision of the best temperatures. For this reason, preliminary tests on the heating rates and cooling power have been determined at the test rig. Fits of the temperature development are shown in equations (4.4) and (4.5) for the column1 (filled with palladium) and equations (4.6) and (4.7) for column 2 (filled with titanium chromium). The heating ($t_{C1,heat}$ and $t_{C2,heat}$) and cooling ($t_{C1,cool}$ and $t_{C2,cool}$) times, all in (s), have consequently been aligned. The major reason that the heating and cooling time for column 2 is higher is due to the fact that the column is longer.

$$\frac{t_{C1,heat}}{s} = \exp\left(\frac{\frac{\Delta T_{C1}}{K}+0.81}{25.4}\right). \tag{4.4}$$

$$\frac{t_{C1,cool}}{s} = \exp\left(5.27 - 0.037 \cdot \frac{\Delta T_{C1}}{K} + 3.088 \cdot 10^{-4} \cdot \frac{{\Delta T_{C1}}^2}{K^2}\right). \tag{4.5}$$

$$\frac{t_{C2,heat}}{s} = -58.3 \cdot \left(1 - \exp\left(0.02 - \frac{\Delta T_{C2}}{K}\right)\right). \tag{4.6}$$

$$\frac{t_{C2,cool}}{s} = \exp\left(5.26 + 9.17 \cdot 10^{-5} \cdot \frac{\Delta T_{C2}}{K} + 6.2 \cdot 10^{-5} \cdot \frac{{\Delta T_{C2}}^2}{K^2}\right), \tag{4.7}$$

whereby ΔT_{C1} is the temperature increase or decrease for column 1 in (K), ΔT_{C2} for column 2 in (K).

iv) Time for sorption: In the model, the sorption time has been set individually for each temperature until pressure balancing has been occurred. This setting is necessary for the modelling, otherwise the model can break down. In the experiments, though, it is not maintained until total pressure equilibrium has been reached. Thus, as with the heating rate, preliminary tests have been carried out and also here an equation has

been set, which is based on the pre-tests and model results (see equation (4.8)). Not the temperature difference, but the desorption temperature is needed here, as the resulting desorption pressure has a major impact on the sorption time t_{sorption}. As the two columns interact with each other, only one equation is applied. This time has also subsequently been adjusted in order to be able to compare the results.

$$\frac{t_{\mathrm{sorption}}}{s} = 3344.778 - 13.66836 \cdot \frac{T_{des}}{K} + 1.4814 \cdot 10^{-2} \cdot \left(\frac{T_{des}}{K}\right)^2, \tag{4.8}$$

With T_{des} as the desorption temperature and $t_{sorption}$ as the time needed for sorption between the two columns. The preliminary tests on sorption time only reflect the average time. Each experiment behaves slightly differently in terms of time, even under the same conditions. For this reason, slight deviations exist between the times of the tests and those of the modelling.

v) Material properties: Several characteristics from MAIA are applied here. The equations (3.4) and (3.5) are used for the separation factor. Other material properties, as the density of the bulk material, are taken from Table 3.3 and Table 3.4.

Regarding pressure-concentration behaviour, equations have been elaborated. The pressure for palladium in the plateau regime has been shown in equations (3.2) and (3.3)) in subchapter 3.4.1. However, since the formula in the phase transitions are not continuous, they cannot be used in the modelling. Therefore, a polynomial formula for the pressure, depending on temperature and concentration, has been generated for both isotopes and both materials equation (4.9) presents the general form usable for both materials. The related parameters for protium and deuterium are listed in Table 4.1.

$$\frac{p_{Mat,QH2}}{Pa} = \sum_{n=0}^{4} \frac{A_n}{\left(\frac{mol_Q}{mol_M}\right)^n} \cdot c^n + \sum_{n=1}^{4} B_n \cdot \left(\frac{T}{K}\right)^n + \sum_{n=1}^{3} \frac{C_n}{\frac{mol_Q}{mol_M} \cdot K^n} \cdot c \cdot T^n + \sum_{n=1}^{2} \frac{D_n}{\left(\frac{mol_Q}{mol_M}\right)^2} \cdot c^2 \cdot \left(\frac{T}{K}\right)^n + \frac{E}{\left(\frac{mol_Q}{mol_M}\right)^3 \cdot K} \cdot c^3 \cdot T. \tag{4.9}$$

Table 4.1: Parameters for the pressure equation for protium and deuterium for both materials.

Parameter	Pd-H_2	Pd-D_2	$TiCr_{1.5}$-H_2	$TiCr_{1.5}$-D_2
A_0 (/)	$-2.415 \cdot 10^4$	$-8.079 \cdot 10^4$	$6.749 \cdot 10^4$	$7.522 \cdot 10^4$
A_1 (/)	$-9.379 \cdot 10^3$	$-3.818 \cdot 10^4$	$-1.333 \cdot 10^6$	$-7.511 \cdot 10^5$
A_2 (/)	$1.566 \cdot 10^5$	$2.838 \cdot 10^5$	$8.052 \cdot 10^6$	$4.657 \cdot 10^6$
A_3 (/)	$-1.135 \cdot 10^5$	$-1.822 \cdot 10^5$	$-1.753 \cdot 10^7$	$-1.019 \cdot 10^7$
A_4 (/)	$6.548 \cdot 10^4$	$7.145 \cdot 10^4$	$1.153 \cdot 10^7$	$6.739 \cdot 10^6$
B_1 (/)	$3.085 \cdot 10^2$	$8.843 \cdot 10^2$	$-1.165 \cdot 10^2$	$-4.695 \cdot 10^2$
B_2 (/)	-1.384	-3.533	-0.238	1.489
B_3 (/)	$2.642 \cdot 10^{-3}$	$6.121 \cdot 10^{-3}$	$3.326 \cdot 10^{-4}$	$-2.628 \cdot 10^{-3}$
B_4 (/)	$-3.881 \cdot 10^{-6}$	$-3.881 \cdot 10^{-6}$	0	$1.806 \cdot 10^{-6}$
C_1 (/)	$5.762 \cdot 10^2$	0	$3.257 \cdot 10^3$	$1.769 \cdot 10^3$
C_2 (/)	-1.174	-0.708	0	0
C_3 (/)	$7.276 \cdot 10^{-4}$	$1.19 \cdot 10^{-3}$	$-1.623 \cdot 10^{-3}$	$-8.979 \cdot 10^{-4}$
D_1 (/)	$-6.419 \cdot 10^2$	$-1.275 \cdot 10^3$	$-1.888 \cdot 10^4$	$-1.061 \cdot 10^4$
D_2 (/)	0.823	1.524	6.121	3.637
E (/)	$9.416 \cdot 10^1$	$3.111 \cdot 10^2$	$2.67 \cdot 10^4$	$1.482 \cdot 10^4$

4.1.3 Process-related Assumptions & their Qualitative Impact

Most assumptions have been taken from the previous work [6]. The assumptions I have made are stated at the respective statements. All are listed below and divided into certain categories. A quantified uncertainty analysis is not possible for such assumptions. Instead, justifications for the choice and qualitative errors are given for each of the following assumptions:

Fluid mechanics:

- A laminar, steady flow is assumed which justifies the Hagen-Poiseuille equation to be applied. For lower pressures, a laminar flow, with a Reynolds number of 1000 can

be guaranteed. For high pressures the Reynolds number rise up to 66000, leading to a turbulent flow and therefore to an underestimation of the mass flow.

- Pressure losses inside the pipelines due to their lengths and valves are not considered. This is a physical simplification that results in an overestimation of the flow characteristic.
- Counter current flow is neglected during the sorption phase. This can cause an increase in the separation, as it is assumed that the gas has completely flown into the other column for separation.
- In the modelling, both columns are connected with two connecting tubes, whereas in reality only one pipe connects the columns. This is done to simplify the simulation.
- An equally, time dependent temperature distribution along the column is assumed. So it is assumed that the isotopes are ab- and desorbed simultaneously along the length of the column. In reality, that is not the case, which can lead to a back-mixing of the isotopes.
- The columns are considered 1-dimensional. Gradients in radial direction are thus neglected. Since the length of the column is orders of magnitude bigger than its diameter, this simplification is possible without any impact.

Thermodynamics:

- All resulting data are in steady state. Kinetic effects are neglected. As all our data from the PCT diagram originate from measurements in MAIA, kinetic effects are not considered. If there are any, they result in smaller sorption pressures for heating and larger ones for cooling.
- The columns are isotherm and the hydrogen isotopes do not permeate through the walls. With this assumption, boundary conditions are simplified.

Time effects:

Pre-tests with the separation test rig have been performed in order to understand its behaviour regarding heating, cooling and sorption. Accordingly, all times have been adapted based on these pre-tests. Therefore the assumptions regarding time effects are created for this thesis.

- In the model linear heat and cooling rates have been fixed. Linear heating rates simplify the mathematics of the model. In reality, the heating rate is not linear, in fact the temperature change first rises exponentially and declines asymptotically in the end. Since this is one of the most important criteria for the separation, because it is directly related to the tritium inventory, the time has been adjusted subsequently on the basis of preliminary tests (see equations (4.4) to (4.7)).

- The sorption times have been set in a way that pressure equalisation between the two columns occurs. This is necessary as the model breaks down otherwise. Since the sorption times are crucial (similar to the calculation of the times for the temperature changes) the results have been adjusted afterwards, also using preliminary tests (see equation (4.8)).

Material performance:

- Long-time material degradation due to cycling repetitions is neglected. This simplification can be made for Pd, as this material is not sensible to disproportionation. For $TiCr_{1.5}$ there is little information. However, literature indicates that AB_2 type alloys with Ti are stable. This assumption can therefore also be made here.
- Both materials are activated and no impurities are de- or absorbed. This ensures that the entire surface is available for the reaction with hydrogen. This assumption can be made with no effect, as complete activation with both materials is possible (I have shown this in the characterisation at MAIA). Furthermore, by correctly preparing a facility, impurities can be excluded. And finally, the application in the fuel cycle of a power plant at the location of the TSA process does also involve only pure hydrogenic gases.
- For the different phases α, α-β and β only one equation for the temperature- and concentration dependent pressure has been applied in order to receive a continuous equation throughout the phase change (see equation (4.9)). This is necessary since the implicit Euler cannot be calculated otherwise. In reality, each phase has its own formula (Sieverts´ law in the α-phase, van't Hoff law in the α-β-phase). This assumption changed compared to the previous model, as there data from literature are used, which have been continuous equations.
- Hysteresis phenomena observed for the ab- and desorption of hydrogen in the materials are neglected. This simplifies calculation and avoids singularities during the change from ab- to desorption.
- One separation factor for each material has been applied, independent from the concentration. This is a simplification, since I have shown in MAIA that the separation factor also depends on the concentration range. For example, if the concentration range of Pd is shifted in the direction of α phase by $0.05\,mol_Q/mol_{Pd}$, the integral separation factor is reduced by nearly 10 %. However, since I have deliberately adjusted the integration of the separation factor to the range where separation experiments are to be run, this does not have a big influence.

Hydrogen isotope behaviour:

- The only existing gases in the columns are protium and deuterium and they behave as an ideal gas. Since isotopes are available in a high purity, this assumption can be made. At the operational pressure range up to maximum 10^6 Pa, hydrogen does still behave as ideal gas, as the compressibility factor of hydrogen at $1.1 \cdot 10^6$ Pa and 298 K is only 1.0066 and can therefore be neglected [112].
- No formation of the isotopologue occurs during the cycles in the column. This is a very strong simplification. In order to be able to make a concrete statement about isotopologue formation, some further material characterisations are required. The resulting sorption pressure must then be determined as a function of not only concentration and temperature, but also of isotopic composition and then implemented in the model.

4.2 Modelling Results of the H/D Separation

The study with the selected parameters has been carried out in preparation for the subsequent separation tests shown in chapter 6.

4.2.1 Parameter Selection in regard to EU-DEMO

Table 4.2 gives an overview of parameters, which are investigated in this chapter. Since the temperature has a substantial influence on the separation effect and time, a parameter study has been carried out with in total 14 different temperature ranges (in studies S1 – S4). The four temperatures giving the best results are afterwards compared with experimental data (see subchapter 6.1). On the basis of these temperatures, further studies have been undertaken. The enrichment in the closed cycle in both columns has been analysed over the length of the column to determine the separation efficiency and also the amount to be removed (study S5). Since the composition at the entrance of IR-PR can change for DEMO, the influence of different H_2 to D_2 ratios has been analysed (study S6). In the end, the influence of different amounts of extracted gas between the closed and open cycles has been investigated (study S7).

Table 4.2: Overview of possible influences considered for the following parameter study.

Study	Influences regarding separation	Goal for observation
S1	Influence for same ΔT for C1 and C2 at different temperature range (TR1 vs. TR2)	Best temperature applied for separation
S2	Influence of varying ΔT, same for C1 and C2 (TR3 – TR6)	Best temperature applied for separation
S3	Influence of varying temperature difference, same for C1 and C2 (TR7 – TR10)	Best temperature applied for separation
S4	Influence of different temperatures in C1 and C2 (TR11 – TR14)	Best temperature applied for separation
S5	Composition distribution of H_2 and D_2 along the length of columns	Maximum amount, which can be extracted
S6	Influence on different initial composition on gas mixture	Changes in separation
S7	Influence on the amount extracted	Maximum amount, which can be extracted

4.2.2 Parameter Study of Factors influencing Isotope Separation

For the temperature study, in total fourteen different temperatures have been investigated and the best four are applied in the test rig afterwards for validation. All results are thereby compared at three cycles. In the first comparison, influence for same temperature difference (**study S1**) two temperatures with the same ΔT but different ranges are analysed. TR1 runs from 288-383 K, while TR2 is used between 363 and 458 K. These temperatures are applied for both columns. Same ΔT have been selected in order to directly determine the behaviour of the isotopes regarding temperature. Figure 4.4 shows the enrichment of protium and deuterium over the cycles. The diagram demonstrates that the enrichment of both isotopes is considerably better for 288-383 K (TR1) compared to 363 and 458 K (TR2). It can be seen that after e.g. three cycles, deuterium is enriched to 75 % and protium to 67 %. Based on the initial composition, this corresponds to an enrichment by 30 % for D_2 and 58 % for H_2. TR2, on the other hand, only achieves an enrichment by 15 % for D_2 and 43 % for H_2. This

behaviour is due to the fact that the isotope effect becomes stronger as the temperature decreases. When selecting the temperature, this has to be taken into account accordingly. **288-383 K (TR1)** is one of the four temperatures that will be investigated in more detail.

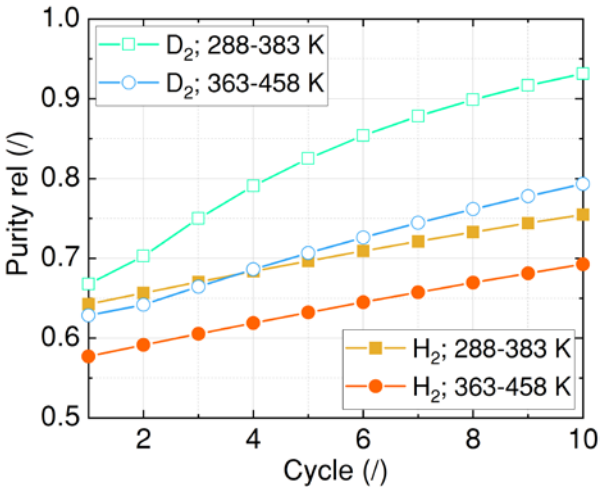

Figure 4.4: Modelled isotopic purity in the end stage for two different temperature ranges: 288-383 K (TR1) and 363-458 K (TR2) for protium enrichment at n=100 in C2 (filled symbols, orange colour palette) and deuterium enrichment at n=1 in C1 (open symbols, blue colour palette).

Since a low absorption temperature improves the separation process, it is kept low for all further comparisons and the desorption temperature is increased incrementally. In Figure 4.5 (a) the results are shown over the number of cycles. It can be seen that the separation increases with increasing temperature difference. This results into the lowest separation in the range of 283-403 K (TR3), where deuterium can be purified to 78.1 % and protium to 66.9 %. When the desorption temperature is increased to 458 K (TR6), the deuterium purity increases to 81.8 %, while protium increases to 67.5 %, which gives the highest separation. As the temperature difference for the second study S2 is greater than for the previous study S1, the enrichment results yield better separation values. However, not only the number of cycles but also the time is relevant, as larger ΔT implicate larger cycle times (see Figure 4.5 (b)). Thereby it can be seen that the order is reversed. TR6, which previously delivered the best result, is now by far the worst. This is due to the fact that the heating rate is asymptotic with higher temperature. For TR3 (283-403 K), one cycle lasts 1245 s, whereas for T6 it is nearly the double, with 2406 s. TR3 (283-403 K) and TR4 (283-418 K) show similarly good results, however **TR3 (283-403 K)** is slightly better, especially in the first cycles, which is more important for this purpose. Therefore, this temperature is chosen as the second one for a more detailed analysis.

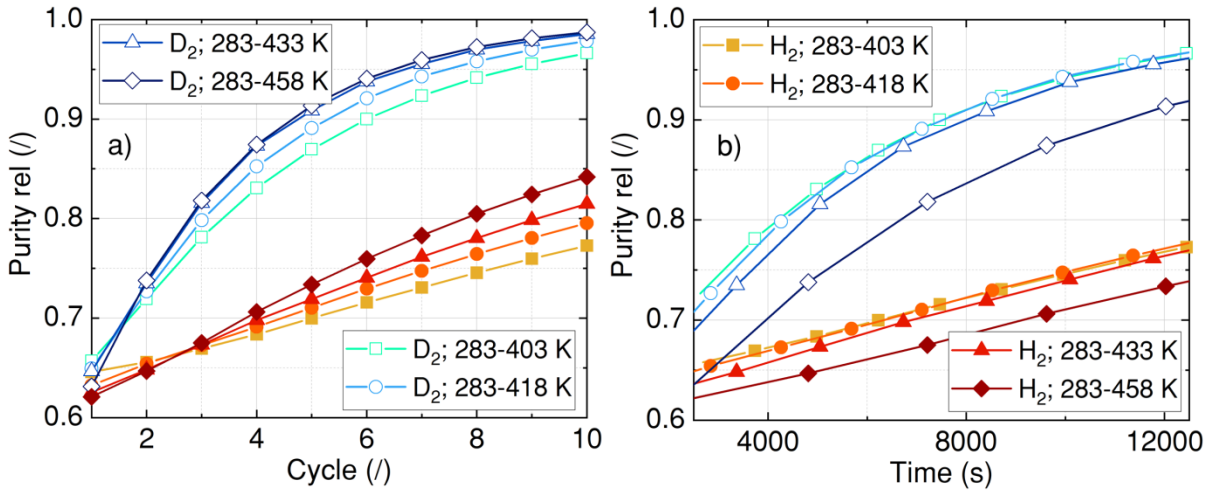

Figure 4.5: Modelled isotopic purity in the end stage for four different temperature ranges: 283-403 K (TR3), 283-418 K (TR4), 283-433 K (TR5) and 283-488 K (TR6) plotted against the amount of cycles in (a) and the time in (b) – for deuterium enrichment in the palladium column1 (open symbols, blue lines; legend shown in (a)) and protium enrichment in the titanium-chromium column2 (filled symbols, orange lines; legend shown in (b)).

As demonstrated in the two previous comparisons, a low temperature is crucial as well as a certain difference. For this reason, **in study S3** the absorption temperature is reduced even further from 283 to 278 K, with desorption temperatures kept constant. The trend for the number of cycles (Figure 4.6 a)) is like the comparison before - TR7 (278-403 K) with the smallest ΔT shows the poorest result, while TR10 (278-458 K) shows the best result. Looking at the enrichment over time (Figure 4.6 b)), the effect is reversed here as well. TR7 (278-403 K) and TR8 (278-418 K) are similarly good, with a slight tendency towards TR8. In order to be able to compare larger differences in temperature later in the experiments, **TR8 (278-418 K)** is selected. TR8 shows an enrichment of 79.7 % for deuterium and 67.4 % for protium in 3 cycles, which is slightly higher than for TR3 (283-403 K).

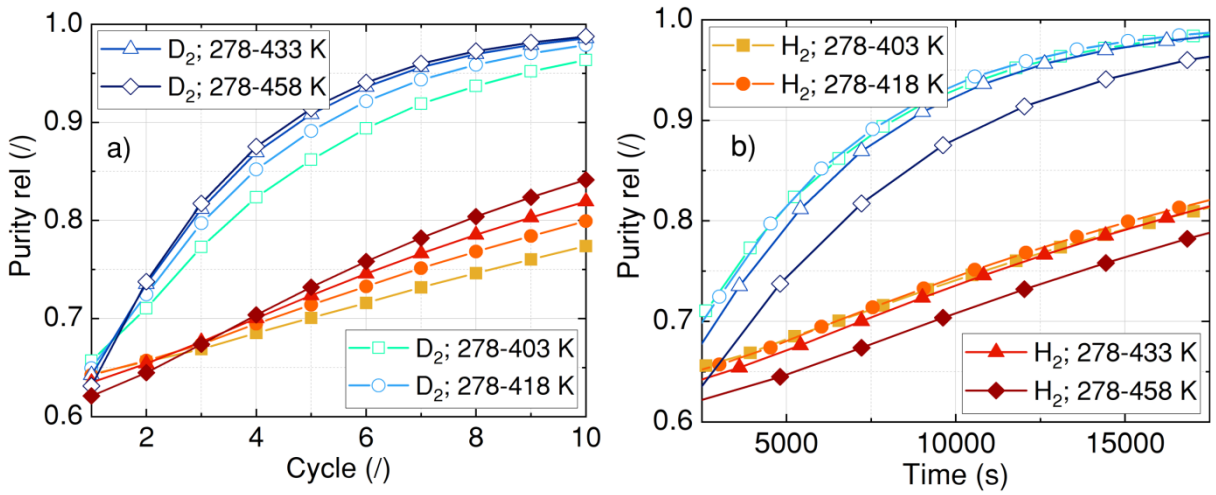

Figure 4.6: Modelled isotopic purity in the end stage for four different temperature ranges: 278-403 K (TR7), 278-418 K (TR8), 278-433 K (TR9) and 278-458 K (TR10) plotted against the amount of cycles in (a) and the time in (b) – for deuterium enrichment in the palladium column1 (open symbols, blue lines; legend shown in (a)) and protium enrichment in the titanium-chromium column2 (filled symbols, orange lines; legend shown in (b)).

In the last temperature comparison **study S4**, different temperatures have been applied to the two columns (see Figure 4.7 a) for the amount of cycles and Figure 4.7 b) for the time). TR11 and TR12 show alternately 278 and 283 K for absorption and 433 K for desorption. For TR13 and TR14, 283 K is set for absorption, desorption is then distinguished between 403 and 433 K. For deuterium, considering time, TR11 (283-433 K) is best, with TR13 (283-403 K) following. For protium, TR11 and TR12 show equally good results. Therefore, **TR11 (278(C1), 283(C2)-433 K)** has been chosen as the last of the four selected temperature ranges. In cycle 3, deuterium with 81.5 % and protium with 67.2 % purification are in the range of the other values.

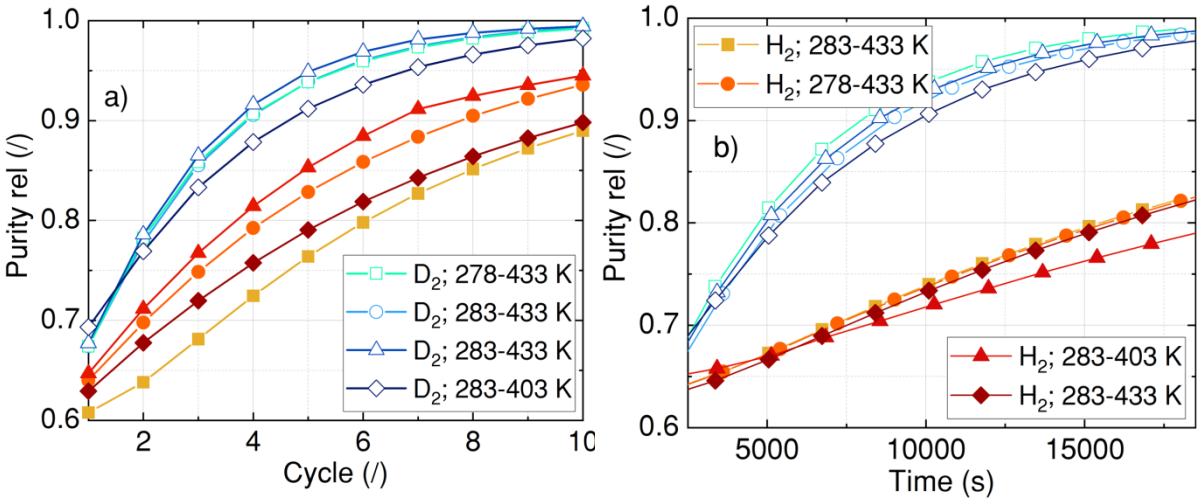

Figure 4.7: Modelled isotopic purity in the end stage for four different temperature ranges: 278(C1), 283(C2)-433 K (TR11), 283(C1), 278(C2)-433 K (TR12), 283-433(C1), 403 K(C2) (TR13) and 283-403(C1), 433 K(C2) (TR14) plotted against the amount of cycles in (a) and the time in (b) – for deuterium enrichment in the palladium column1 (open symbols, blue lines; legend shown in (a)) and protium enrichment in the titanium-chromium column2 (filled symbols, orange lines; legend shown in (b)).

Study S5 is important, as later on, more than just 1 % of the gas quantity is being extracted (see Figure 4.8). Therefore, the distribution of composition for the four selected temperatures has been analysed over the length of the column. With this information, the percentage which is appropriate to extract can be determined. For all temperatures, it is perceived that the gradients in concentration are smaller in than in C2. Here, the enrichment decreases faster over the length. All temperatures perform in a similar way; therefore TR1 is used as an indicator. The composition of the isotopes after 3 cycles along the column is observed. The results are compared with the composition at the respective end of the column (n=1 for C1; n=100 for C2). Looking at the composition after 3 cycles, in C1 it is the same for n=50 (extraction ≙ 50 %) as for n=1. For n=60, however, it drops sharply to 88.4 % of the value for n=1. In C2, the purity of protium is constant up to n=70 (extraction ≙ 30 %). For n=40 it drops to 94.9 % from the initial value at n=100 and for n=50 even to 79.2%. As the separation factor of Pd is better relative to $TiCr_{1.5}$, a higher and also longer purity over the column length is thus achieved. To ensure a high, stable enrichment for both columns, **40 % extraction** at both columns from the gas inventory during the isotope separation experiments is going to be applied.

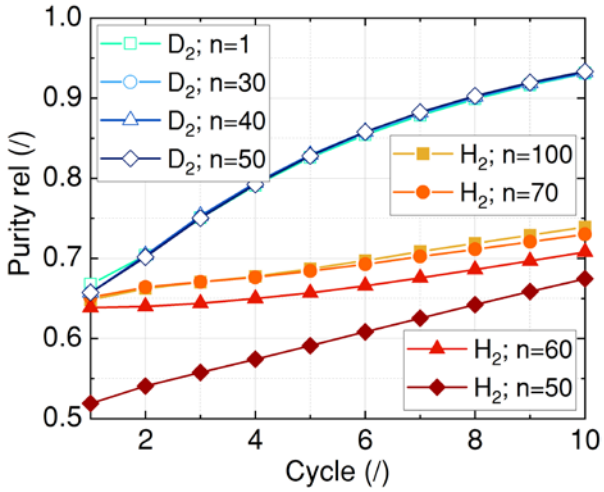

Figure 4.8: Modelled different isotopic composition at four different positions along the column length n=1, n=30, n=40 and n=50 for column 1, n=100, n=70, n=60 and n=50 for column 2 at temperature TR1 (288 K – 383 K); plotted against the amount of cycles– for deuterium enrichment in the palladium column1 (open symbols, blue lines; legend shown in (a)) and protium enrichment in the titanium-chromium column2 (filled symbols, orange lines; legend shown in (b)).

Another parameter **study S6**, which is not studied experimentally afterwards, is the influence of different compositions. In Figure 4.9, this is displayed exemplarily on the basis of TR1 and 3 cycles. The following compositions have been examined: 42.2-57.8 % for H_2-D_2 (rectangular symbols), as this represents the composition for the experiments. Furthermore, 50-50 % for H_2-D_2 (round symbols) and 57.8-42.2 % for H_2-D_2 (triangular symbols) are included. What is clearly noticeable is the behaviour for both isotopes. The curves run in parallel, the composition has no influence on the result.

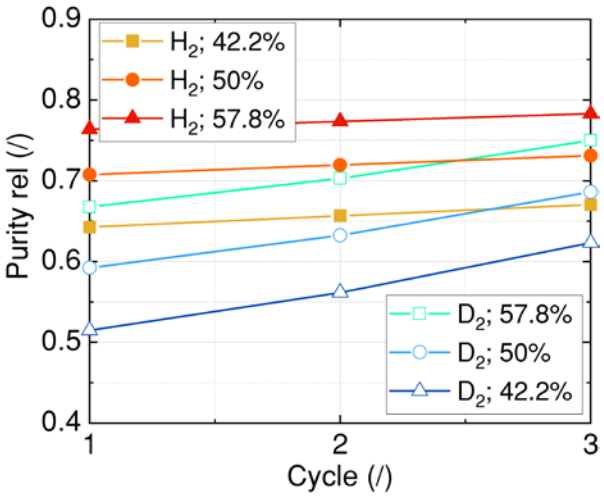

Figure 4.9: Modelled different initial conditions for protium (filled symbols, orange colour palette) and deuterium (open symbols, blue colour palette).

In the last **study S7**, the influence of enrichment has been investigated with gas extraction from the columns, shown in Figure 4.10, protium in a) and deuterium in b). The rectangular symbols (H_2/D_2; 0 %) represent the previously shown results at the respective end of each column in which no gas has been removed. For the data with the round symbols, 1 % of the total inventory for both columns (instead the gas inventory of 40 % for one column) has been subtracted from the total amount, for both the gas and solid phase. The triangular symbols show the extraction of 2.5 % of the total amount. For both 1 % and 2.5 %, 3 closed cycles have been run first, followed by one open cycle and one closed cycle alternately. The points of the open cycles are displayed bigger for a better overview. For deuterium, the amount of extraction has no influence; all three curves have the same course. For protium, 1 % of the extraction amount has no influence. For 2.5 %, however, a slight degradation can be seen at the points of extraction. However, this has no influence on the overall result. As soon as a closed cycle is performed, the system stabilises again. The reason for the deterioration with protium in contrast to deuterium is that the separation factor of $TiCr_{1.5}$ is worse than that of Pd, which causes the system to be less stable.

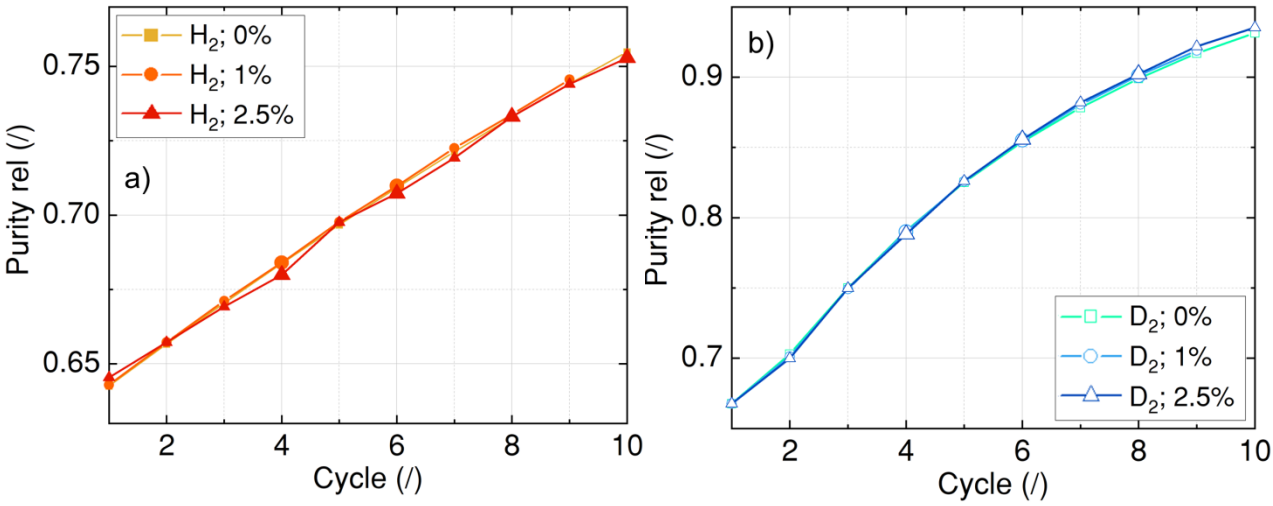

Figure 4.10: Modelled different amount of extraction for protium in (a); filled symbols, orange colour palette) and deuterium in (b); open symbols, blue colour palette).

The parameter study demonstrated various influences on the enrichment of the isotopes. Since temperature is one of the most significant influences, the experimental runs focus on the four temperatures that have shown the best values in terms of enrichment and duration in the parameter study. An overview of these is listed in Table 4.3.

Table 4.3: Overview of the enrichment values of the four best temperature regarding enrichment and duration for three cycles from the initial H_2:D_2 composition of 42.2:57.8.

Temperature range	D_2 enrichment (%)	H_2 enrichment (%)	Time (s)
TR1 (288 - 383 K)	75	67	3144
TR3 (283 - 403 K)	78.1	66.9	3402
TR8 (278 - 418 K)	79.7	67.4	4785
TR11 (278(C1),283(C2) - 433 K)	81.5	67.2	6618

Within this chapter, the **fundamental prerequisite of the TSA experiments has been established**. Needed parameters (e.g. temperature) have been identified and determined suitable for the experiments. **The TSA process can be validated** by comparison of the input variables and its results obtained from this previously verified model.

5 Complete Hydrogen Isotope Separation process demonstration

The goal is the demonstration of hydrogen isotope separation. Firstly, the setup of the test facility is outlined and design criteria are explained. Then the device used for analysis, necessary for the quantification of the results, is described. The procedure of the experiments follows, as well as the parameter selection for testing.

5.1 Design Justification & Setup Description of Demonstration Facility HESTIA

The goal of the test rig is to separate the hydrogen isotopes protium and deuterium and to verify the feasibility regarding application at DEMO. Figure 5.1 shows the basic structure of the HESTIA (Hydrogen Experiments for Separation with Temperature Initiated Absorption) test rig. In order to be able to study both components individually, the membrane and columns are connected in parallel. In order to allow the compatibility of both stages to also be tested, the design has been conducted in such a way that a serial connection can easily be added.

A pressure difference between the retentate and permeate side is required at the membrane to enable separation. Therefore additional vacuum pumps have been installed at the outlet of the permeate side. For the columns, the driving pressure difference is established by the sorption effects themselves. The columns are heated and cooled anticyclically, that is, one column has low pressure due to absorption effects while the other has a high pressure due to desorption effects. The bulk materials are filled in the columns and remain inside during the separation tests. A valve separates the two columns and it is opened so that the flows equalize the pressures. After the separation proceeded in the two stages (MC and TSA), the extracted gas is analysed in a QMS (Quadrupole Mass Spectrometer).

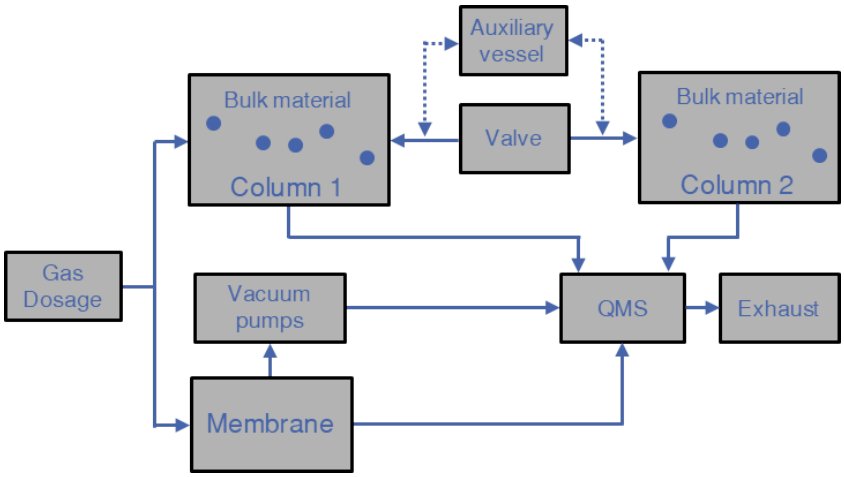

Figure 5.1: Schematic arrangement of components and indication of flow paths in the HESTIA facility.

In order to achieve an optimum design of the test rig, the process requirements and constructive aspects have to be reflected. A list of the most important components are provided in Table 5.1. In the following, the individual requirements are discussed and the corresponding design is explained.

Table 5.1: Components important for hydrogen isotope separation and their properties: for column1 (C1), column2 (C2) and membrane (M).

Component	Properties	Quantity
Volume Column 1	271.2 ± 3.01 ml	1x
Volume Column 2	390.32 ± 3.39 ml	1x
Volume (membrane)	116.85 ± 3.48 ml	1x
Sheath resistance thermometer	263.15 K ± 0.09 K – 473 K ± 0.3 K	2x (C1), 2x (C2), 2x (M)
Capacitance Manometer	100 Pa ± 10 Pa – 10^6 Pa ± $1.2{\cdot}10^2$ Pa	1x (C1), 1x(C2)
Capacitance Manometer	0.1 Pa ± 0.01 Pa – 10^3 Pa ± 0.12· Pa	1x (C1), 1x(C2)
Capacitance Manometer	10 Pa ± 1 Pa – 10^5 Pa ± 12· Pa	2x (M)
Pressure transducer	0 - $4{\cdot}10^6$ Pa	2x (C1), 2x C2)
Bellow valves	$3.4{\cdot}10^6$ Pa (for 477.15 K)	21x (C1, C2, M)
Mass flow controller	2 ± 0.1 – 100 ± 1.05 sccm 20 ± 1.02 – 1000 ± 10.49 sccm	1x (C1, C2, M) 1x (C1, C2, M)

Figure 5.2 shows a highly simplified process flow diagram. The complete PID including the list of components' characteristics can be found in the appendix in chapter A7. The main parts are, besides the two columns and the membrane, the heating system (HS) for the membrane and the heating and cooling system (HS&CS) for the columns. The gas inlet is controlled by a mass flow controller (MFC), and the measurement is performed with several temperature and pressure sensors. At the permeate side of the membrane, in order to generate a pressure difference, and at the rest of the facility in order to remove gas, vacuum pumps are installed.

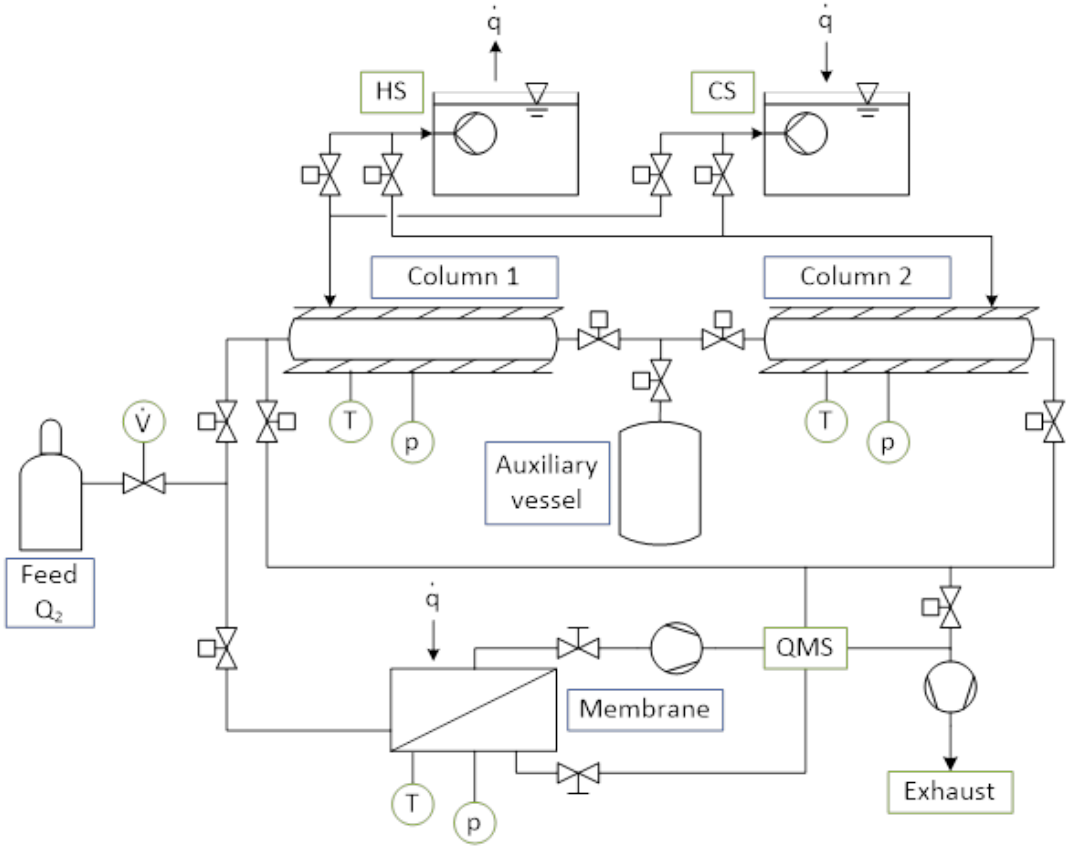

Figure 5.2: Schematic flow diagram and temperature-pressure profiles of the test rig HESTIA.

Temperature range is a process condition that has to be satisfied in the design of the test rig. It is important to keep the operation in mind and at the same time to select the temperature range in a way that suitable materials can be tested. Considering the material research, it is important that cryogenic temperatures are avoided and that the temperature does not become too high, so that permeation through the wall (which later becomes relevant for the tritium application) remains negligibly small. This results into a temperature window between 263 K and 473 K has been identified after material reasearch. It is crucial to provide both fast heating and cooling rates, to meet the requirements of fast processing at the later application in DEMO. Because of the advantage of using one medium for heating and cooling, thermal oil has been chosen due to its quick response. This also has the operational advantage that no separate systems are needed, unlike for example with electric heating and water cooling. To

expedite this process even further, the oil is pre-heated or cooled in baths before it enters the columns. The oil flows around the columns in a milled plate, serving as a double-walled tube heat exchanger. In addition, the plate is used for partial insulation, as it is made of a composite material made of resin-bonded glass fabric with a low thermal conductivity. Regarding the membrane, a temperature range from ambient temperature to 473 K is sufficient, as this parameter does not have an impact on the separation itself, only on the throughput. Heating is conducted with a heating cord around the membrane housing. All heated parts in the test rig are insulated with glass fibre yarn and mineral rock wool.

Sheath resistance thermometers as sensors have been installed inside each column in order to quantify the temperature distribution along the length of the column. For the membrane a sensor at the inlet and another at the permeate stream, with contact to the membrane, are installed. All sensors are inserted in the heating or cooling medium to such an extent that a reliable measurement can be guaranteed.

As a first design reference, the maximum operating **pressures** in MAIA are $2{\cdot}10^5$ Pa for deuterium in Pd and $4{\cdot}10^5$ Pa for protium in $TiCr_{1.5}$. However, since the system is not only to be designed for these two materials, a higher pressure range from 0.1 to 10^6 Pa has been chosen as design pressure range of the facility. In addition, another aspect that must be taken into account is the resulting pressure in case of a potential oxy-hydrogen explosion. In a safety analysis, this pressure has been estimated to be below $2.1{\cdot}10^6$ Pa. As measure of explosion safety, all components are able to sustain this pressure over the entire temperature range. The need to achieve the minimum pressure affects the design, since the absorption occurs in vacuum and no air ingress is allowed in the presence of hydrogen and the materials. The test rig must be pumped down before each experiment, by means of vacuum pumps. The membrane stage also operates under vacuum conditions, since the permeate stream needs to be pumped out continuously.

Since the hydrogen composition in the gas phase cannot be exactly known in the experiments, the pressure sensors must be gas type independent. Hence capacitance manometers are used. Each column has two sensors with a range from 10^2 Pa to 10^6 Pa and down to a fine vacuum from 10^{-1} Pa to 10^3 Pa. Complementary, redundant piezo sensors are provided with an relative range from 0 to $4{\cdot}10^6$ Pa. The sensors are used to measure the pressure, when the range from the capacitance manometer is exceeded (10^6 Pa). As the capacitance manometers only withstand a pressure slightly higher than its operation range, valves are connected and their setting is controlled by the piezo sensors. For the membrane, the inlet and retentate stream is each measured with a capacitance manometer (range from 10 Pa to 10^5 Pa), the permeate is measured with a thermal conduction vacuum gauge (range from $1.3{\cdot}10^{-2}$ Pa to $1.3{\cdot}10^2$ Pa).

System safety is a significant factor in the design. Primary, secondary and tertiary explosion safety measures are considered. i) Limitation of the gas supply of a maximum

of one gas tank with mutually interlocked valves, ii) Use of explosion-proof components in the gas storage facility, iii) Shutdown of the gas supply in the event of a failure via redundant valves in the gas storage facility, iv) Lack of ignition sources (mass spectrometer behind orifice), v) Guarantee of technical tightness of the system (e.g. by leak tests as well as regular checking of the tightness), vi) Monitoring in the room through the use of hydrogen sensors, vii) Checking the operating status of the system by means of redundant temperature and pressure sensors, viii) Overpressure limitation via bursting discs (supported by PLC monitored functionality), ix) Use of a pressure-resistant design of the system components.

Accuracy interrelates directly with measurement technology. This is directly related to the uncertainty calculation of the components, with all calculations and relations listed in the appendix (chapter A2). Identifying the points that require high accuracy due to their high impact on the overall uncertainty, and those that do not is important. For example, for the measurement of temperature in the columns, the accuracy is much more essential than for the membrane. This is due to the fact that the temperature has a much more direct influence on the separation result in comparison to the membrane. In addition, the diffusion through the membrane scales less than linearly with the temperature (square root dependence). Consequently, the same type of sensor has been chosen for both separation stages, but they have only been calibrated for the columns to increase their accuracy. Heated capacitance manometers have been chosen for their high accuracy. The particular importance of the temperature in the columns comes from the fact that its value has a direct influence on the determination of the amount of gas absorbed. Also the evaluation of the accuracy is important. In addition, the inaccuracy of pressure sensors depends not only on the pressure range applied but also on the temperature. Hence, a thermocouple has been installed on each pressure sensor, in order to determine the exact temperature. The volumes and the gas inlet are also important for the definition of the amount of gas. A large cylinder has been calibrated beforehand for this purpose and was connected to the test rig, where each volume has been determined by applying the Boyle-Mariotte law. The amount of gas entering the system is determined by a mass flow controller (MFC, with two ranges, one up to 100 sccm, and the other up to 1000 sccm). This has been calibrated beforehand and MFCs are only used in the upper 80 % range, being more accurate there.

Data acquisition of the test rig HESTIA is carried out with a combination of a Siemens® PLC system and a ProfiMessage® system by Delphin®. With the Delphin system it is possible to gather and control data at the same time as well as perform process control tasks. The coupling to a PLC-control for data exchange is possible as well as a connection to a computer with a network interface [113; 114]. On the computer, the programs Siemens WinCC® and ProfiSignal® (by Delphin Technology®) are installed. With these programs, the components are controlled.

A Gas analyser assesses the hydrogen isotope enrichment. The choice of the device, its configuration and the adjustment with regard to hydrogen is explained in detail in the following subchapter 5.2.

Leak tightness is a further requirement of the system. Since the system operates in overpressure and underpressure, only a high level of leak tightness can guarantee that hydrogen neither escapes into the hall nor does air enter the test rig. In addition, it is obviously essential that the hydrogen resides at wherever point is needed. In all areas of the test rig containing hydrogen, exclusively bellows valves have been installed, as they come with a very low leak rate of less than 10^{-9} mbar·l/s. Only the heating and cooling circuits have been equipped with simple ball valves. The system has partly been welded, but mostly connected with Swagelok compression fittings. VCR instead of Swagelok fittings have only been used in some parts for disassembly purposes (e.g. when replacing materials). Before the first experiments have been performed, a leak test has been executed, resulting in integrated leak rate of $2 \cdot 10^{-9}$ mbar·l/s.

Cleanliness is important, as impurities can have an impact on the result. The pipes of the columns have been cleaned so that they are free of oil and open pipes as well as connections have always been covered during transport and assembly to exclude dirt contamination of the test rig. All gases used have a high purity: Argon, protium and nitrogen with a cleanliness of 6.0 (≙ 99.9999 %), and deuterium with 2.8 (≙ 99.8 %), with protium being the largest part of the impurities. Other contamination, mainly water, has been removed by baking out at 473 K and pumping down the test rig for hours. Through these procedures, surface effects do not have a big influence in the operational range.

Dimensioning is important, as column inner diameter and the ratio of length to diameter affect the separation efficiency. The literature shows a minimum ratio of 500:1. Multiple columns have been manufactured for future investigations at HESTIA to explore this effect. For the first experimental campaign, a column with a length of 3 m and a diameter of 8x1 mm (≙ 6 mm of inner diameter) has been selected for column 1 (filled with Pd). Column 2 also has a diameter of 6 mm, but a length of 6 m. The selection of small diameters ensures that radial diffusion is avoided. As a general rule, it is deemed that the higher the ratio of these two parameters, the better the separation. Since the separation factor of $TiCr_{1.5}$ is lower compared to Pd, a longer column is chosen to compensate this effect. As the columns are several metres long, it is advisable to bend them to save space. They have been formed in such a way that the overall width is compressed to 1 m. The exact shape of the coiling can be seen in the appendix in A8 and in Figure 5.3. Besides the space factor, this type of bend has two other advantages. Firstly, connecting pieces have been welded onto each top bend (9 in total), allowing the material to be filled in. Secondly, the gas inlet, sensors, valves or bursting discs are connected to these pieces for the experiments. For instance, the gas inlet in column 1 is placed in the middle to start with, and the position can be changed.

Isotope sequence is the final design aspect. The aim is to inverse the sequence of the isotopes to improve the efficiency of the process. This idea has been implemented with the assembly of auxiliary vessels. A detailed explanation of its function is given directly to the results explanation in subchapter 6.2. This auxiliary vessel is not part of the standard procedure of experiments.

Permeation is important for the analysis, as it is decisive to know how much hydrogen permeates through the columns and if this influences the results. This requires determining the amount of permeation and the difference between protium and deuterium. Permeation depends on several factors, especially on the material and the temperature involved. For estimation, worst case assumptions have been taken. The lower the temperature, the lower is the permeation; however, the difference between the isotopes increases. Since the test rig is designed to operate at a maximum temperature of 473 K, permeability values for stainless steel 316L have been taken from the literature at that temperature. For a worst case assumption, the duration of the longest experiment (12978 s; see experiment "steady state" from subchapter 6.2) and the largest pressure difference across all experiments ($2.86 \cdot 10^{5}$ Pa; see experiment "TR1" from subchapter 6.3) have been considered. The amount of gas permeating through the wall is maximum $2.3 \cdot 10^{-10}$ mol, with a permeation rate of $3.3 \cdot 10^{-11}$ mol·m^{-1}·s^{-1}·MPa$^{-0.5}$ at 473 K [115]. This corresponds to $2.3 \cdot 10^{-7}$ % of the inventory and can therefore be neglected. The difference in permeation of protium to deuterium is a factor of 2.06 for 473.15 K and increasing to 3.29 for 263.15 K [116]. This difference is large, but as the overall permeation is extremely small, the isotope effect of wall permeation can be neglected and does not need to be taken into account for the analysis.

A picture of the test rig HESTIA is shown in Figure 5.3, with its main components highlighted.

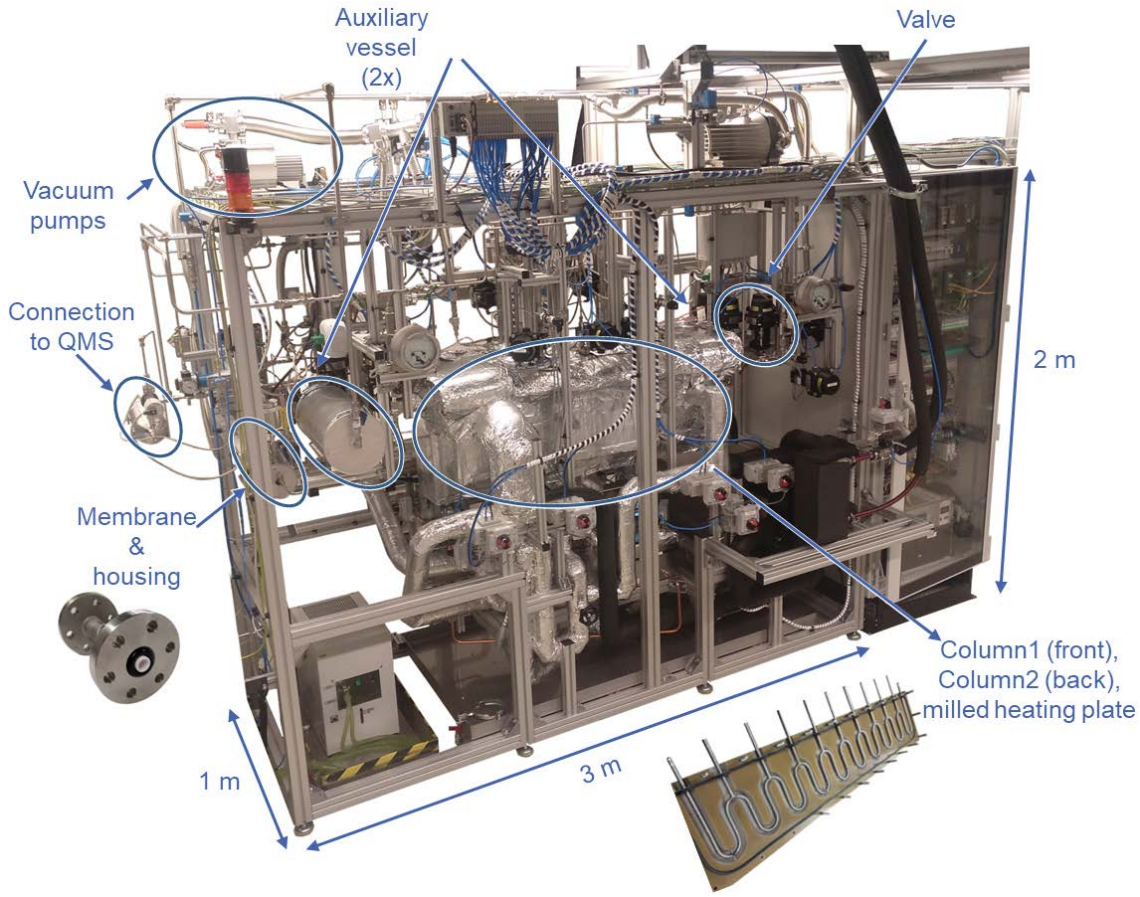

Figure 5.3: Picture of the test rig HESTIA, including pictures of the two stages membrane & housing and column & milled plate.

5.2 Features of the analysis Device for the Qualification of the MC-TSA process

In order to verify the quantity of the isotope separation, a mass spectrometer is needed. For this purpose, an already existing analysis device Gas Analyser for Ionized Atoms (GAIA) has been modified. The scheme of this device is given in Figure 5.4.

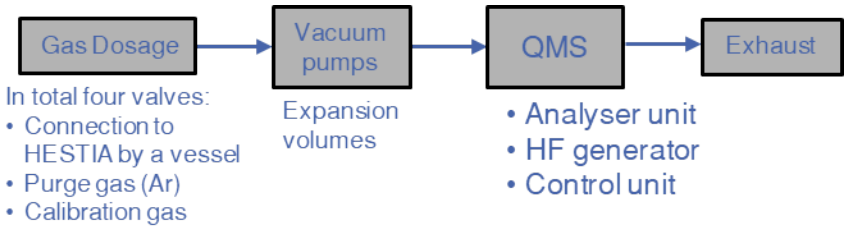

Figure 5.4: Schematic depiction of the connection of the individual parts of the mass spectrometer.

Four valves are installed at the gas inlet for the following purposes. HESTIA is connected to one of the valves by a vessel. Argon is also permanently installed at another valve. An inert gas is important to purge the analyser between every experiment. Since helium has a similar mass to deuterium, argon has been chosen

deliberately. Other gases, such as a calibration gas, can be connected to the other two valves at any time. Self-written scripts are used for the control of the respective valves for the necessary purpose.

Vacuum pumps are installed in the system. Low pressure is required as the working pressure of the mass spectrometer is maximum $6 \cdot 10^{-4}$ Pa. Dilution of the inflowing gas is achieved with expansion volumes (100 mm^3 and 1 dl vessels). This allows the pressure to be reduced to the necessary range. The mass spectrometer itself is continuously pumped down with a high vacuum pump.

The measuring principle of mass spectrometers (RGA) consists of neutral particles being ionised by electrons emitted through a filament. These ions are separated from each other in a rod system based on their mass/charge ratio. For this analysis device, a Secondary Electron Multiplier (SEM) is used for ion detection. The ion source, the rod system and the detector are all built into the analyser unit. The generator supplies the system with a constant source of energy. This is all connected to the quadrupole controller. The control of this device and evaluation are done with the software QuadStar^{TM}. Table 5.2 gives an overview of the main components and their properties.

Table 5.2: Components important of the analysis device and their properties.

Functional component	Type	Properties
Analyser unit	QMA 410	Rod diameter = 16 mm rod length = 300 mm mass number range: 1-128
HF generator	QMH 400-1	Frequency = 2.05 MHz Power = 7 kVA
Quadrupole controller	QMS 421	

In order for a mass spectrometer to detect the correct gases, it must first be calibrated. The cracking pattern of protium is at mass numbers 1 and 2, deuterium at mass numbers 2 and 4. As the fraction of D at mass 2 is not constant over varying compositions, calibration is performed at mass 1 for H_2 and 4 for D_2. The gas used for calibration had a composition ratio of 42.2% to 57.8% (H_2 to D_2). Before each measurement, a calibration has been performed and the calibration factor determined subsequently has been used for the respective experiment.

A mass spectrometer can contain several sources of uncertainties. To minimise errors, I set up the analyser in a way to neglect a large proportion of these uncertainties. The pressure in the analyser is up to 10^{-4} Pa and the ion current after SEM is up to 10^{-6} A. This is high and therefore orders of magnitudes away from the detection limit. So the uncertainty due to the minimum detectable pressure and

concentration can be neglected. Outgassing can also be neglected, as the background peaks of water are three orders of magnitude lower than the peaks from the hydrogen isotopes in the experiments. For quantitative interpretation of the RGA measurements, the dependence of the measured signal on the total pressure has to be considered. However, since the vessel which connects GAIA and HESTIA is always filled with the same pressure from the HESTIA system and the inlet sequence into the analyser is controlled over time, it can be ensured that there are no changes in pressure in the analysis chamber. The temperature of the gas can be neglected as the analysis is performed in the Knudsen regime. The temperature fluctuations of the electronics do not play a role, as the sensitive components are heated. After each measurement, the vessel towards HESTIA is pumped down to high vacuum and a background measurement is started before a new measurement. This way, remains from the previous measurement can be subtracted. The inaccuracy of the mass resolution depends on the step settings. Since this analyser takes 64 values per atomic mass unit, the resulting uncertainty of the **resolution is 100/64 %**. For the **sensitivity, the average calibration factor** over all measurements has been taken and the deviation to it is determined. In the end, a factor, based on (equation A5) from the appendix, is applied. Assuming that the measurement outcome is 50% reliable, this additional value is 2.

A picture of the analysis device, including the main components highlighted, is shown in Figure 5.5.

This analysis device is in use for several years and its **results have been verified** [117].

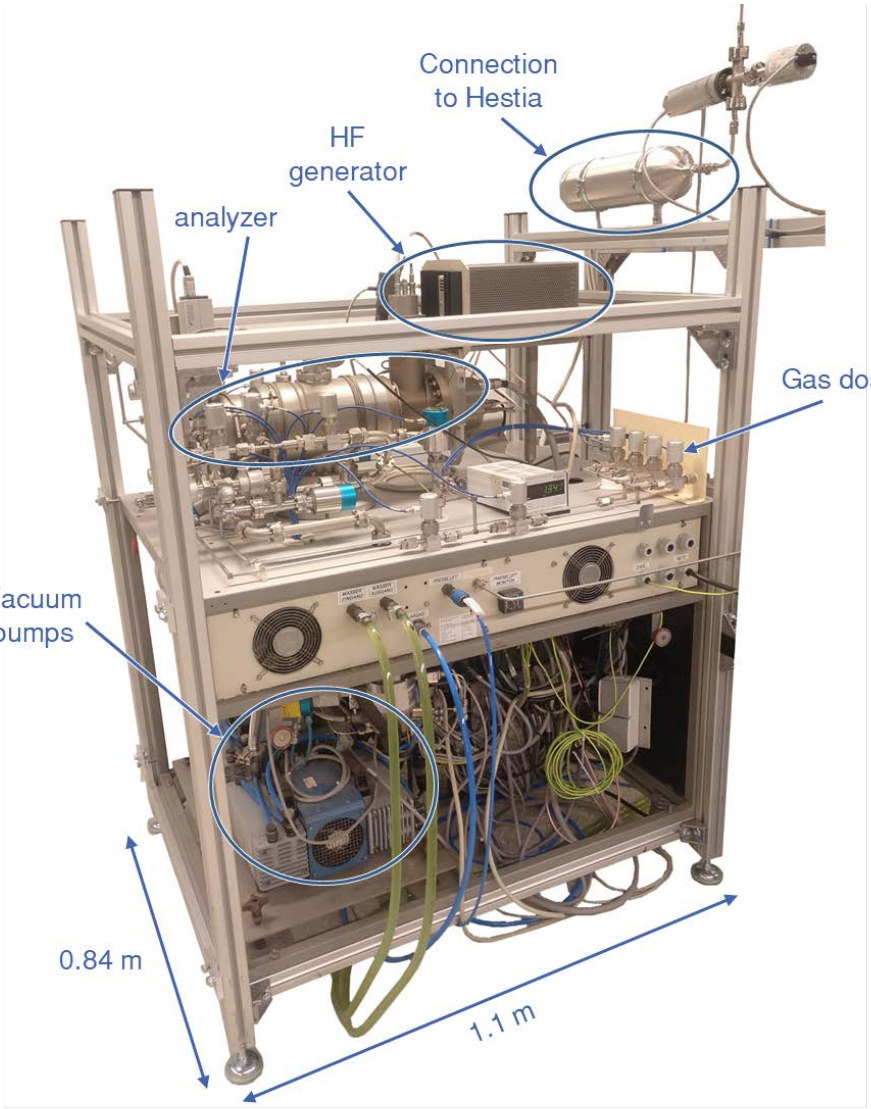

Figure 5.5: Picture of the analysis device.

5.3 Experimental procedure of MC and TSA experiments

In DEMO, both MC and TSA separation stages are connected in series. To examine the functionality, however the test procedure of the two stages is conducted independently from each other. The uncertainty calculation is the same for both stages. In addition to the characteristics of the analyser, resolution (100/64) and sensibility (mean value of calibration factor), the uncertainty of the temperature sensors is also taken into account.

TSA experiments: Since the gas flows back and forth between the two columns, and therefore both materials interact with each other, their amount has been adjusted to match each other's performance (as storage capacity and p-T behaviour). $TiCr_{1.5}$ can absorb about 7 times more hydrogen per mol_Q/mol_{Me} than Pd. This stems the installation of a larger amount of Pd compared to $TiCr_{1.5}$. On the other hand, the

complete concentration range can be utilised for Pd unlike for $TiCr_{1.5}$, as the sorption is reversible. Here only a small range ($0.1\,mol_Q/mol_{Me}$) is applied as a worst case assumption. Consequently, the amount for Pd is still a bit larger, with 101.69 ± 0.0102 g, and 74.51 ± 0.00756 g for $TiCr_{1.5}$.

The bulk material has been activated following the same principle as for the material characterisation in MAIA. Pd has been filled in HESTIA and activated inside the column, as 473 K is sufficient temperature. Finally, the gas has been pumped out at 473 K to have the material pure for the tests.

As the activation of $TiCr_{1.5}$ requires up to 673 K, and the maximum temperature in HESTIA is limited to 473 K, this material has been independently activated in MAIA. Before filling, the gas has been desorbed at 673 K and pumped out in MAIA to ensure that $TiCr_{1.5}$ has as little protium as possible in the material. As an activated material is not allowed to get in contact with air, argon in overpressure has been added to the material while still attached to MAIA. Argon remained in the vessel for the transport and refilling of the material into HESTIA.

For the experiments, a pre-defined inventory (around 0.1 mol) of the HD gas mixture is added to column 1 (H_2 : D_2 - 42.2 % : 57.8 %). This gas inventory is adjusted via the previously determined volume and the set flow on the MFC. As literature stated, that the flow can have an influence on the separation, a flow of 600 sccm has been used for all experiments [61], in order to compare the experiments directly with each other. Same flow rate for all tests provide same conditions to allow comparability. The objective is to add as much inventory as needed to perform absorption at the end of the α-β phase and the beginning of the β phase for palladium. These phases have the considerable advantage of a greater separation factor (α-β) and more gas being desorbed (β), meaning more gas passes back and forth between the two columns and is thus separated.

To ensure that a sufficient amount of gas is desorbed and that both columns are "clean" for the next test, HESTIA is baked out and pumped down to vacuum at 473 K for 12 hours between each run.

As it is important to reduce the cycle time, I shortened the process slightly before the required temperature is reached. Once a large part of the gas flows from one column to the other, the valves are closed again. This new process step is performed when the course of the pressure reaches an asymptotic progress. Similar counts for temperature, shortly before the required temperature is reached, the next step is undertaken. All experiments proceed in the same way unless indicated otherwise. The complete gas inventory is added in the middle of column 1, resulting in absorption due to the pre-cooled column. Column 1 is then heated to a certain temperature, while column 2 is cooled. Close before the temperature has been reached, the valves between the columns are opened and pressure is roughly equalised. Column 1 is then cooled again and column 2 is heated. These steps correspond to one cycle.

However, analyses take place at a higher temperature as the gas is released at those conditions and thus a larger amount of gas can be analysed. Therefore, the valves must be opened again so that the gas flows into column 1. This is then heated up again. The aim is to separate as much gas as possible from the column, while maintaining the purity. As the purity decreases over length, it is important to find an optimum between the amount of extraction and the remaining purity. The principle of the purity behaviour over the length of the column is shown in Figure 5.6 a), with the location of the extraction point relative to the column length in Figure 5.6 b). The modelling results from subchapter 4.2.2 have exhibited an extraction capability of 40 % of the gas inventory. Since this condition is a good compromise between the extraction of a certain amount of gas and the preservation of the purity, this amount has been used for all experiments. As the purity is the highest at the end of the column (L=0) and decreases with length, it has to be guaranteed that gas at 40 % (L=40) of the column length is analysed. One option is to extract the complete 40 % and send this gas mixture to the intermediate vessel and then to the analysis device. However, a purity gradient within this 40 % is existent, the purity at L=0 is higher than L=40. As a complete mixing cannot be guaranteed within the analysis device (and therefore it is not clear which composition is measured) this option goes along with a potentially high, not known, uncertainty. That's why another option is applied. A bit less gas (~38 %) is removed first (step 1). This quantity is determined by the pressure drop in the column. The gas enters the intermediate vessel between HESTIA and GAIA and is completely pumped out. Afterwards this intermediate vessel is filled up again to $3 \cdot 10^2$ Pa with gas from the column (equal to the rest 2 %, leading to 40 % of gas; step 2) and the gas is then analysed. With this approach it is ensured that the defined location which needs to be analysed can be guaranteed. Based on the pressure in the intermediate vessel, the previously calibrated volume and the applied temperature in the relevant column, the extracted inventory is calculated.

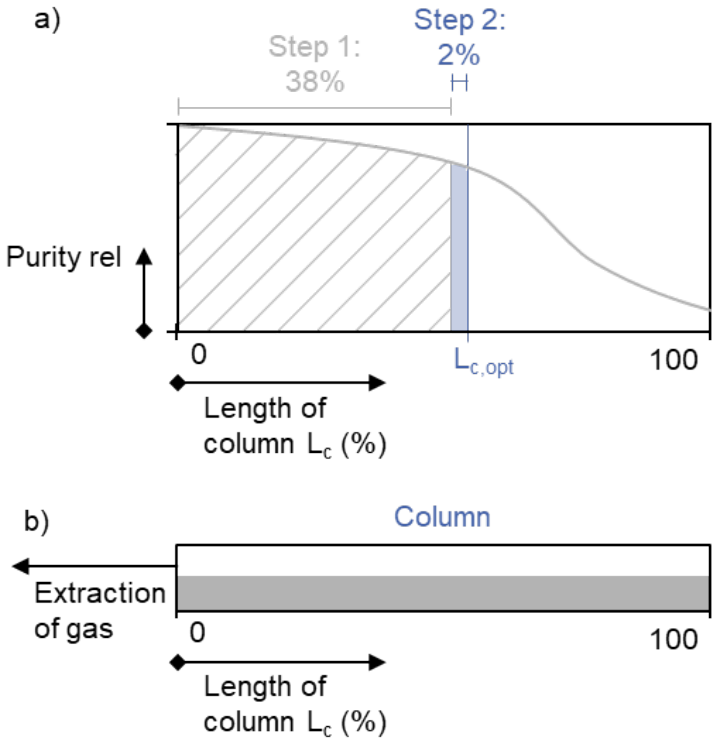

Figure 5.6: Principle of purity behaviour dependent on the length of the column with two steps, including the optimum length ($L_{c,opt}$) of the extraction amount.

Due to the behaviour of TiCr1.5 and the resulting decrease of the total inventory, an identical reproducibility of the tests is difficult to demonstrate. In addition, the experiments are very time-consuming, making multiple repetitions unfeasible. However, for one temperature (278-418 K; TR8), the experiment has been repeated, which shows that the results are not random. The reliability is high, with a deviation of only 1 %.

MC experiments: The same gas mixtures has been used for the membrane experiments: H_2 : D_2 - 42.2 % : 57.8 %. With this mixture, different temperatures and different flow rates have been applied. The mass flow controller has been zeroed before the experiments and a stable temperature has been established as well to ensure that temperature has no influence on the flow. Thereby, the influence on the separation as well as permeate and retentate streams, are analysed. For all experiments the previously mentioned parameters are set and the gas is pumped out from both streams – with a turbo molecular pump for the permeate side and scroll pump for the retentate side – in order to achieve a pressure difference. This is realised for a few minutes in order to achieve equilibrium in the resulting pressure, flow and concentration. When this has been reached (after five minutes), both streams are successively removed to the intermediate vessel and analysed.

5.4 Operational Parameters for the TSA stage

The aim of the experiments is to demonstrate the feasibility of the TSA process. This is assessed using three types of experiments, overviewed in Table 5.3 (<T<, <n_{cycle}<, <t<). Some parameters have an influence on the separation, a few of these have been selected for closer investigation. For TSA, temperature is important as it has a direct influence on the separation factor. The first parametric assessments are the "<T< temperature" experiments, and the focus is on the four temperature ranges that have shown the highest potential in the modelling (TR1 (288-383 K), TR3 (283-403 K), TR8 (278-418 K) and TR11 (278(C1), 283(C2)-433 K).

The temperature range that produces the best results in terms of time and separation effect is examined in more detail using the next experimental test ("<n_{cycle}< process steps"). In this case, three different operations are carried out on the system at the best temperature. One operation contains the fast control of the vales in order to reduce the cycle time. In the second, experiments in steady state are carried out. In the last operation, the sequence of the isotopes is changed with the addition of an auxiliary vessel in order to improve the process.

In the last operation "<t<-amount of cycles", the influence on the amount of cycles is examined with the best operation and temperature obtained from <T< and <n_{cycle}< experiments. Thereby the experiments at cycle number three, five and ten are compared with each other.

Table 5.3: Overview of experiments <T< to <t< for TSA with <T<.

Experiment	Influences regarding separation	Goal for observation
<T<	Parameter study “temperature”	Best temperature and comparison to modelling results
<n_{cycle}<	Parameter study “process steps”	Best operation of test rig – result vs. time
<t<	Parameter study “amount of cycles”	Best number of cycles – result vs. time

For the membrane, temperature and flow have an influence of the permeantion. Therefore, different values of these parameters have been set in order to check the behaviour.

5.5 Commissioning and Preliminary Tests

In commissioning, a difference is made between safety and process regulations. For facility safety, all aspects have been checked for their functionality before operation with hydrogen. This also applies to all process-relevant aspects (non-safety-related), such as the functionality of the valves and sensors.

The material still contains residues from the activation with protium. Before the actual tests, preliminary tests must be performed to ensure that the system is in equilibrium with respect to H_2 and D_2. In these tests the gas mixture is added to the columns is the same one used later for the experiments (H_2 : D_2 is 42.2 % : 57.8 %). The hydrogen composition at the ends of the columns (where the isotopes are enriched) as well as the total amount of hydrogen from the gas phase have been analysed for both columns after each preliminary test. In total, 12 times the same amount of this gas mixture has been added to the columns, each time undergoing three separation cycles, until equilibrium of H_2 and D_2 has been reached. After these preliminary tests, the actual separation tests have started.

Prior to presenting and discussing the results of the experiments, it is important to understand the effect of different concentration ranges. For the temperature range TR8 (278-418 K), two experiments have been realised, each at slightly different total gas inventory. This leads to a shift in sorption along the x-axis of a PCT diagram, yielding a different impact of the α-β and β-phases. At a lower total inventory, the D_2 enrichment is 79.8 % (extraction from column 1), while H_2 is 61.5 % (extraction from column 2). If the total gas inventory increases by about 3 %, the D_2 enrichment decreases to 77.4 %, while the H_2 enrichment increases to 65.6 %. Therefore, it is important to add the results for D_2 and H_2 up for the individual tests and compare the combined enrichment values. This yields a similar overall value (with 1 % deviation). This demonstrates the importance considering the results not only for each isotope separately, but rather as a wider picture, and only afterwards coming to conclusions about the separation efficiency. This opportunity that the enrichment of both isotopes can be influenced with the inventory, provides a higher flexibility later for DEMO applications.

Due to dissociation of the isotopes at the material surface, the isotopologue HD occurs. During the experiments, it has been shown that its formation, however, only takes up a small percentage. The formation of the isotopologues has no influence on the demonstration of separation as well as its operation. Thereafter, and above all to make the results more compatible with the modelling, HD formation is neglected in the comparisons in the results chapter 6. For the DEMO upscale, however, the results of HD are considered.

6 Experimental demonstration of H/D Separation using Membrane Coupled-Temperature Swing Absorption Process

This chapter first shows the TSA stage experiments with the three different parameter studies, and finally experiments with the membrane.

6.1 TSA – Impact of operational Temperature Range

Figure 6.1 shows the experimental results from the parameter study **<T< – "temperature"**, as well as the modelling data for a direct comparison. The relative purity after three cycles is compared with each other.

Experimental versus modelling data are displayed for protium enrichment in (a) and deuterium enrichment in (b). The corresponding modelling results are shown as curves with the purity at cycle three marked with a vertical line for a direct comparison to the experimental results. The data points embody the experimental values, including their uncertainties. The calculation of the uncertainties is shown in appendix A2. The reason why the uncertainties of the purity (in the y-axis) are not the same for the respective points is due to the calibration values. This depends on how close or how far a given value is from the averaged calibration value. Protium and deuterium behave in opposite ways. This can be observed especially for TR8 (278-418 K). While the uncertainty for protium is large towards the upper end and small towards the lower end, it is the exact opposite case for deuterium. The temperature in the legend is the average value for each test across the length of each column and for all the cycles, as directly measured in the experiment. In order to have less deviation in the comparisons, the modelling has been executed with these respective averaged, experimental temperatures. Also, the exact extracted amount of gas from experiments (values are specified in Table 6.1) has been taken into account to the model. The experimental results have been analysed after 3 cycles and around 40 % of extraction.

In view of the qualitative behaviour of the experimental values over all temperatures (from Figure 6.1), it becomes clear that the separation efficiency enhances with increasing temperature difference as well as lower absorption temperatures for both isotopes. This dependency has been correctly predicted by the modelling. In the following, a direct quantitative comparison of the purity with respect to the three cycles and time is given.

At TR1 (288-383 K) enrichment to 77 % can be accomplished for deuterium, with a deviation of 1 % to the model (enrichment of 75.3 %). For protium 58.8 % enrichment

has been achieved, while 59.9 % in the model (discrepancy of 1.9 %). Analysing both isotopes combined, the difference between the experiments and the modelling is merely 0.5 %. Also the duration (x-axis value of Figure 6.1) for 3 cycles is coincident, with merely 1.6 % deviation.

Considering the values of the individual isotopes for TR3 (283-403 K), the deviation from the model is stronger than for the previous temperature TR1 (288-383 K). Deuterium is enriched to 81.4 % at TR3, (283-403 K) yielding a 3.7 % deviation from the model (result 78.5 %). Protium is enriched to 58.3 %, while the model indicates 61.4 % (deviation of 5 %). The effect of the concentration range on the results becomes apparent here.

The result of protium for TR3 (283-403 K) should have been higher than for TR1 288-383 K), however, the value is a little lower. Deuterium, on the other hand, is higher than expected. In a total balance of both isotopes, the deviation is only 0.1 %, which further reinforces the theory of the dependency of the concentration range.

TR8 (278-418 K) features the opposite effect in enrichment to TR3 (283-403 K). The deuterium enrichment is thereby lower, being only 79.8 % but with a lower deviation of just 1 % to the model (80.7 %). Protium yields values of 61.5 % enrichment with a discrepancy of 3.7 % to the model (63.8 %). The overall difference is 2.3 %, higher compared to the two previous temperatures. A reason for this might be the notably and distinctive high uncertainty for this temperature, as its calibration factor deviated the most from the average value.

For TR11 (283-433 K), the deuterium enrichment of 80.6 % is lower than the modelling result (81.8 %, with a deviation of 1.5 %), while protium with a 68.5 % is above the model result of 64.7 % (deviation 5.9 %). Integrally, this measurement set has a deviation of 1.8 % compared to the modelling result. The divergence of the experimental time, as for the other temperatures, is larger. For the first two temperatures TR1 (288-383 K) and TR3 (283-403 K), the real time slightly shorter than that of the modelling, for TR8 (278-418 K) and TR11 (283-433 K) it is longer.

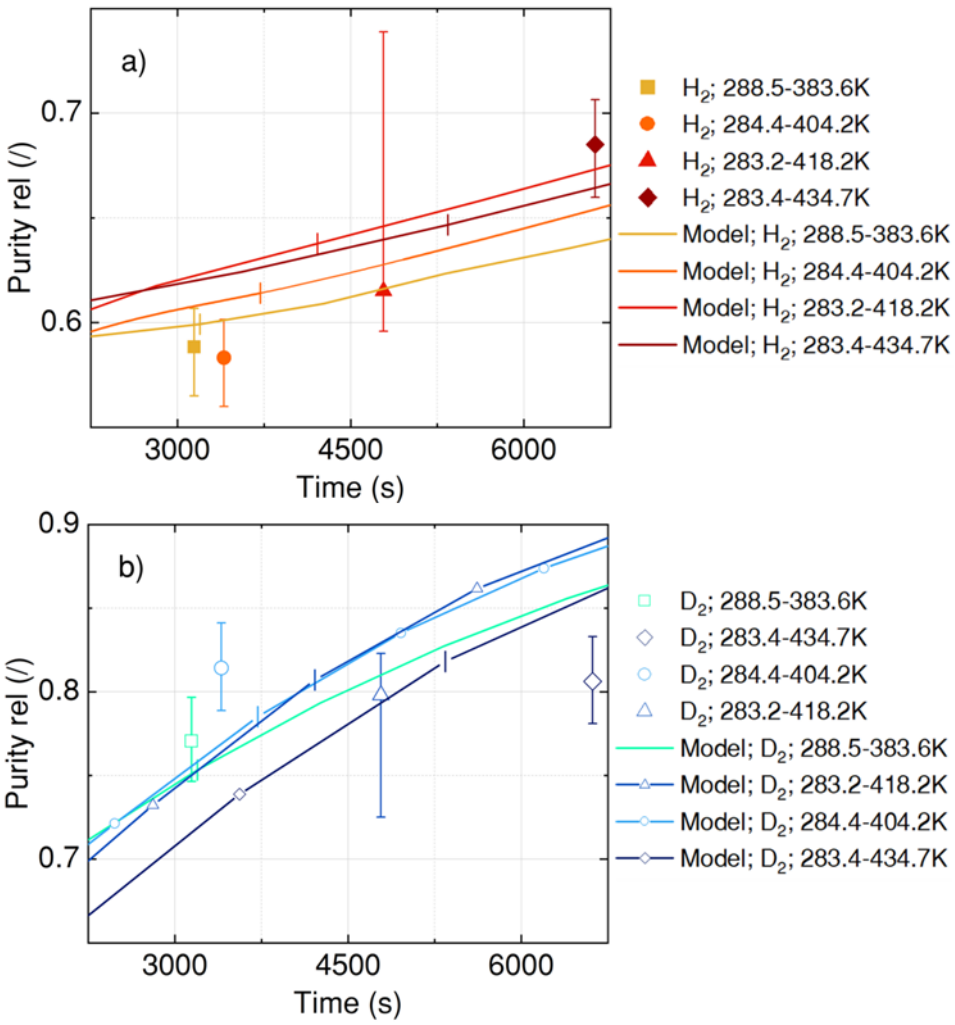

Figure 6.1: Experimental purity as a function of time (H_2 in (a) and D_2 in (b)) shown as single points including uncertainties for four different temperature ranges: TR1 (288-383 K); TR3 (283-403 K), TR8 (278-418 K) and TR11 (278(C1), 283(C2)-433 K) and comparison to modelling results shown as curve with point after three cycles marked in big.

In addition to the separation effect and the duration, the extracted amount of inventory is also important. An overview of gas inventories is given in Table 6.1. In the first row, the gas inventory applied in each individual test is listed. The second line gives the exact amounts that have been extracted from both columns, the third line shows the amount of gas inventory extracted, with 40 % as target. In the fourth line the ratio of extracted gas from both columns in relation to the gas inlet is specified.

Table 6.1: Amount of gas inventory supply for each experiment, extracted inventory for analysation, extracted gas inventory and ratio of extracted to inlet inventory for both columns.

Properties	TR1 (288-383 K)	TR3 (283-403 K)	TR8 (278-418 K)	TR11 (278(C1), 283(C2)-433 K)
Total gas inventory (mol)	0.108 ± 0.0014	0.108 ± 0.00139	0.105 ± 0.00132	0.108 ± 0.00134
Extracted inventory (mol)	0.0114 (C1) 0.00495 (C2)	0.0093 (C1) 0.00516 (C2)	0.00868 (C1) 0.00545 (C2)	0.00911 (C1) 0.00491 (C2)
Extracted gas inventory (%)	44.76 (C1) 45.03 (C2)	41.5 (C1) 42.58 (C2)	49.9 (C1) 34.49 (C2)	41.27 (C1) 41.06 (C2)
Total ratio extracted (%)	15.21	13.43	13.47	13.03

For all temperatures more gas is extracted from column 1 compared to column 2. This is due to the fact that, at equal temperature, the sorption pressure of Q_2 in Pd is higher than the one of $TiCr_{1.5}$. This is material given due to the fact that for $TiCr_{1.5}$ the concentration is at low values at the beginning of the experiments, resulting in a low pressure. This behaviour changes in further experiments. The extracted quantities are within a similar range for the four temperatures, except for TR1 (288-383 K), for which the total amount extracted is slightly higher. Overall, it is proven that the extracted amount has no big impact on the decision for a temperature. Table 6.2 summarizes the enrichment results and duration of the temperature study.

Table 6.2: Overview of the separation results and the corresponding duration for 3 cycles.

Properties	TR1 (288-383 K)	TR3 (283-403 K)	TR8 (278-418 K)	TR11 (278(C1), 283(C2)-433 K)
Duration for 3 cycles (s)	3144	3402	4785	6618
H_2 enrichment (%)	58.84	58.33	61.5	68.5
D_2 enrichment (%)	77.05	81.42	79.8	80.62

All results from the modelling are within the uncertainty range of the experiments, mostly also close to the experimental value. Protium extraction for TR11 (278(C1), 283(C2)-433 K) and for TR3 (283-403 K) are the only value, where the model result does not lay in the uncertainty range of the experiment.

Two major conclusions can hence be deduced from the analysis: i) **I have been able to validate the experiments** with the model, ii) TR1 (288-383 K) leads to the clearest and best result in terms of separation efficiency and duration. This is why the analysis of the different process steps in further experiments, are performed with **TR1 (288-383 K)**.

6.2 TSA – Extraction Efficiency as function of Process Steps

The best result from the temperature analysis from subchapter 6.1 is used here and named "previous" to directly compare it to the following experiments. In this second phase $<\mathbf{n_{cycle}}<$ – **"process steps"**, different conditions have been investigated with regard to the following aspects: i) Simultaneous operation, ii) Steady state and iii) Auxiliary vessel. It is noted that the experiments shown in this section do not reflect a systematic variation, but are nevertheless considered to reveal how the system performance depends on different parameter settings.

The enrichment results are shown in Figure 6.2, along with the "previous" results from the parameter study for a direct comparison and a clearer visualisation. During the first test "simultaneous operation", the two columns are heated/cooled and immediately afterwards the valves are operated, while for the "previous" experiment the valves have only been operated once the temperature has been reached. The aim is to understand if the direct start of sorption at the beginning of the heating/cooling phase has an impact on the separation result. In the protium comparison, a slight improvement of 1.9 % to an enrichment of 60 % is noticeable. Deuterium, in contrast, shows a significantly worse result of only 68.3 %. Overall, the result of "simultaneous operation" is almost 6 % worse compared to the "previous" test series. This means that operating the valves sooner has a negative influence on the separation. Nevertheless, it is also apparent that "simultaneous operation" functions almost twice as fast, making it preferable from an overall performance point of view. This result is explained by the fact that early start of the flow into the other column results in partial re-mixing. If the valves are left closed during heating, the gases are desorbed without any change in their position along the x-axis of the column.

To confirm this hypothesis, another test has been carried out in "steady state". This means waiting until the required temperature is reached and pressure is established in steady state. Valves are only operated after this. The conditions for steady state are described in the material characterisation part of chapter 3. This test has another great benefit, as this is the only way to depict the ideal case and give exact values for concentration ranges. Values of this experiment are listed in Table A.30 in the appendix A6.

As expected, the diagram shows that the outputs from “steady state'' exhibit the best separation effect. This correlates with the values shown previously. For protium, the enrichment has increased by 13.3 % compared to the "previous" test, while deuterium has improved by 5.6 %. Overall, the result has improved by 8.9 %, and even by 15.4 % with respect to the "simultaneous operation". However, as this test series’ operation procedure takes about six times as long as the "simultaneous operation", it is discarded for DEMO application despite the best results.

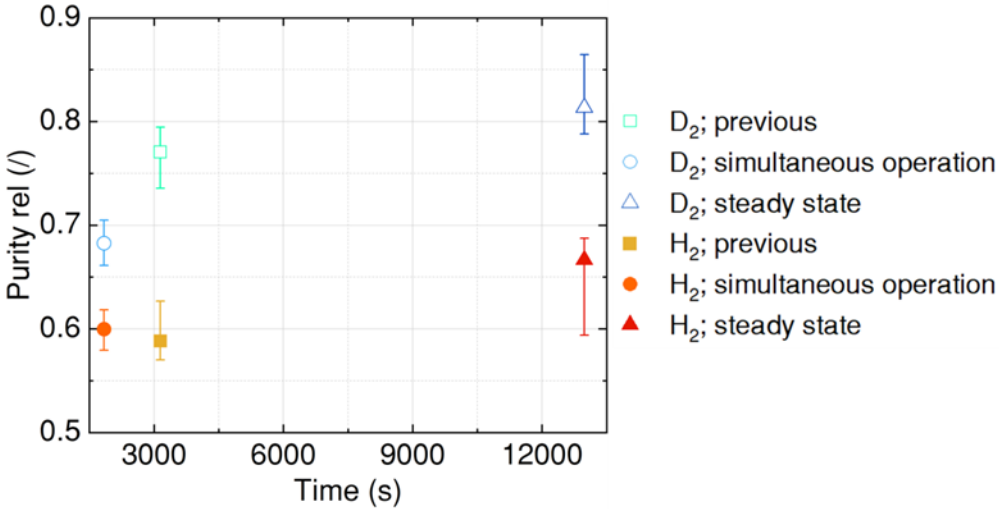

Figure 6.2: Experimental purity as function of time for two different process steps – simultaneous operation and steady state, all at temperature TR1 (288-383 K); in comparison to the previous experiment at TR1 for H_2 (filled, orange symbols) and D_2 (open, blue symbols).

The experiments above described have shown different results (one of short duration and one with high purity). It is now crucial to establish an experimental procedure with high purity and short duration. For this reason, the auxiliary vessel has been integrated as part of the HESTIA system. This vessel has not been used in any previous experiment. The difference in the process control is that before the gas flows from one column directly to the other, it first flows into the auxiliary vessel and in this way the isotope sequence can be reversed. A direct comparison of the new experiment “auxiliary vessel” is shown in Figure 6.3. For both, protium and deuterium, the separation improves versus the “previous” results. Deuterium enhances about 1.9 % to an enrichment of 78.54 %, whereas protium increases around 13.1 % to 66.54 %. The outcome results in an integral improvement of 6.8 % compared to the “previous” and even to 13.1 % compared to the “simultaneous operation” experiment. The values of this test are with 2 % slightly lower than for “steady state”. These results confirm the validity of the idea of the inversion of the isotope sequence. Concerning the time, the cycles are performed slower than for the “simultaneous operation”, as the filling of the additional vessel with gas takes time. Nevertheless, it is faster than for the standard procedure, as the sorption time can partially be reduced with the vessel.

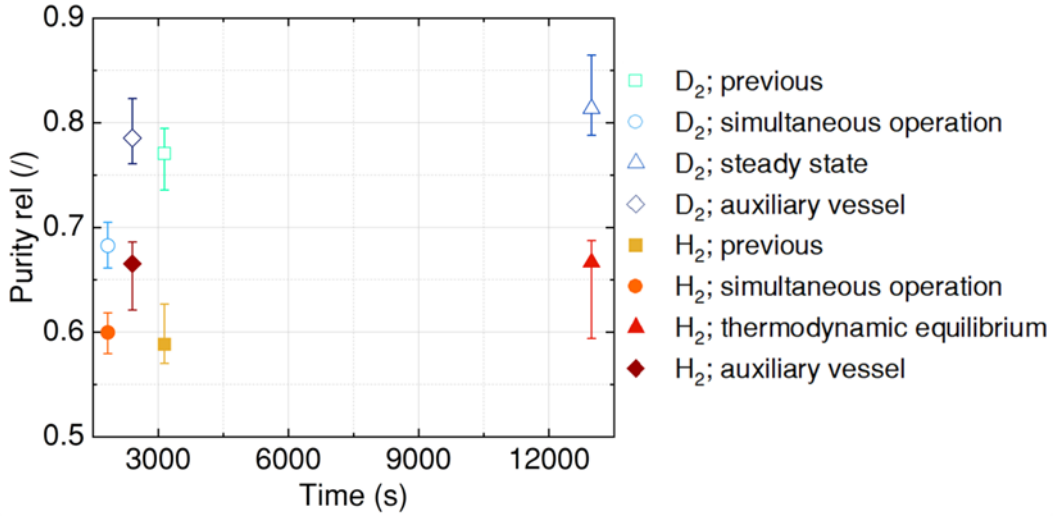

Figure 6.3: Experimental purity as a function of time for the process step auxiliary vessel (marked), in direct comparison to the previous experiment, simultaneous operation and steady state, all at temperature TR1 (288-383 K); for H_2 (filled, orange symbols) and D_2 (open, blue symbols).

The explanation of the improved separation is based on the contribution of the isotopes along the columns. It can be noticed that the H_2 pass the D_2 when flowing from one column to the other and vice versa. A representation of the hydrogen distribution, which leads to an overtake, is illustrated in Figure 6.4. In column 1, deuterium is enriched at the outer left end of the column, while protium is located at the right side (leading to the interface with column 2). As the aim is to extract protium in column 2 (outer left end of the column), it is practical to have deuterium on the right side of the column absorbed first by material. However, in this particular design, this is not the case. Protium is absorbed first, whereby deuterium is located further to the outer end of the column, reducing the separation effect.

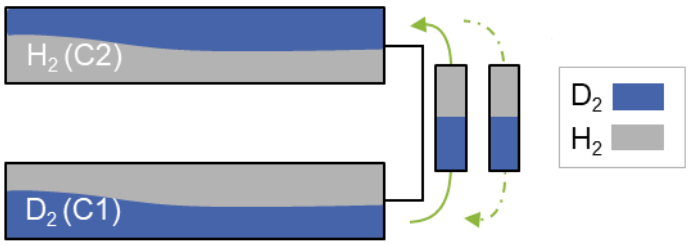

Figure 6.4: Hydrogen isotope distribution in the columns.

In order to counteract this effect, an auxiliary vessel, connected to both columns, has been installed (see Figure 6.5)). This vessel is filled with kieselguhr, a diatomaceous earth with a high porosity. Thus, it can be assumed that the speed of the gas is not the thermal velocity, but the diffusion velocity, as the vessel is completely filled with material (the hydrogen slows down). The second assumption is that the two isotopes have not yet equalised and thus have not mixed, as the next process step (open valve to the next column) has started before the pressure has balanced out.

The new and improved configuration carries out the process in the following manner. Coming from column 1, protium flows first into the vessel and diffuses to the back, whereas deuterium follows and ends up located at the beginning of the auxiliary vessel. In this state, deuterium flows first from the vessel into column 2 and get absorbed. The isotope sequence has been inversed. The same applies when the process is developed in the opposite direction (from column 2 to column 1). In this adjustment, deuterium flows first from column 2 in the auxiliary vessel, followed by protium. Thereby the sequence is reversed and protium can flow first into column 1 from the vessel. This inversion leads to an improved separation, which has been demonstrated with the experiment.

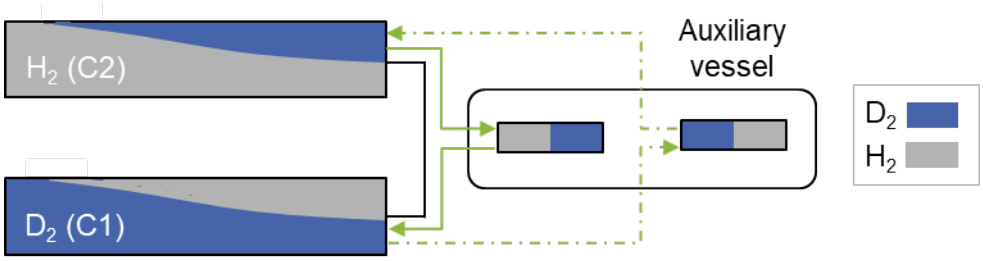

Figure 6.5: Inversion of isotope sequence by means of an auxiliary vessel.

The gas inventory and amount extracted for the three different process steps are listed in Table 6.3.

Table 6.3: Averaged temperature, amount of total gas inventory supply for each experiment, extracted inventory for analysation and ratio of gas inventory extracted as well as extracted to inlet inventory for both columns.

Properties	Simultaneous operation	Steady state	Auxiliary vessel
Temperature (K)	287.63-382.06 (C1) 290.95-383.24 (C2)	287.11-379.95 (C1) 288.75-388.14 (C2)	288.75-382.6 (C1) 289.8-384.05 (C2)
Total gas inventory (mol)	0.104 ± 0.001313	0.105 ± 0.00111	0.102 ± 0.00125
Extracted inventory (mol)	0.0119 (C1) 0.00339 (C2)	0.01 (C1) 0.00441 (C2)	0.00764 (C1) 0.0035 (C2)
Extracted gas inventory (%)	39.4 (C1) 41.7 (C2)	37.7 (C1) 39.2 (C2)	43.5 (C1) 41.7 (C2)
Total ratio extracted (%)	14.76	13.78	10.96

Also for this parameter study, more gas has been extracted from column 1, as the pressure of Pd is higher for the given temperature. For the "auxiliary vessel"

experiment, the total amount extracted is smaller compared to the other two experiments. Table 6.4 presents the enrichment results and duration for the process steps.

Table 6.4: Overview of the separation results and the corresponding duration for 3 cycles.

Properties	Simultaneous operation	Steady state	Auxiliary vessel
Duration for 3 cycles (s)	1839	12980	2406
H_2 enrichment (%)	60.0	66.65	66.54
D_2 enrichment (%)	68.26	81.34	78.54

Since the ratio of separation efficiency to operation time of the "auxiliary vessel" experiment is the best, the process step **TR1 – auxiliary vessel** has been decided on.

6.3 TSA – Process enhancement by Cycle Number Adaption

<t< – "amount of cycles": In view of the fact that all experiments up to now have been carried out with 3 cycles, it is worth observing the change in the performance with different number of cycles. The modelling has shown that the separation increases markedly at the beginning of the cycles and then flattens out asymptotically after a certain time. This effect is stronger for deuterium than for protium. Further experiments, shown in Figure 6.6, are compared with the previous experiment of TR1 - auxiliary vessel. The individual points including the uncertainties represent the experimental values. The modelling is shown as curve, with the purities as function of the number of cycles (three, five and ten) indicated by a line. The numbers of total cycles to be tested are 5 and 10. For deuterium, a 0.8 % improvement is seen in the enrichment from 3 to 5 cycles (78.5 % for 3 cycles and 79.2 % for 5 cycles). For protium, the result increases to 68.9 % enrichment for 5 cycles (by 3.6 %). Integrally, the enrichment for 5 cycles is 2.05 % better than for 3 cycles. The results after 10 cycles compared to 3 cycles show an improvement of deuterium by 2.4 % to 80.4 %, and an increase of protium by 1.8 % to 67.7 %. Integrally, the enrichment has increased by 2.1 % compared to the 3 cycles case and it is therefore only slightly better than for 5 cycles. Considering first only the qualitative trend of the curve, the enrichment increases initially stronger with a small number of cycles and the asymptotic flattening towards a larger number of cycles, is given. However, a large deviation from the modelling values can be observed. A possible cause is the non-reversible sorption behaviour of the titanium chromium alloy. The alloy absorbs more gas than it desorbs. Therefore, the total inventory in palladium decreases with the

amount of cycles, whereby less gas for separation is available. In the modelling results, the integral purification increases by 7.2 % from 3 to 5 cycles, having a strong deviation from the measurement results. The integral improvement from 3 to 10 cycles is 18.7 %. The modelling with regard to the number of cycles can therefore not be verified on the basis of the experiments.

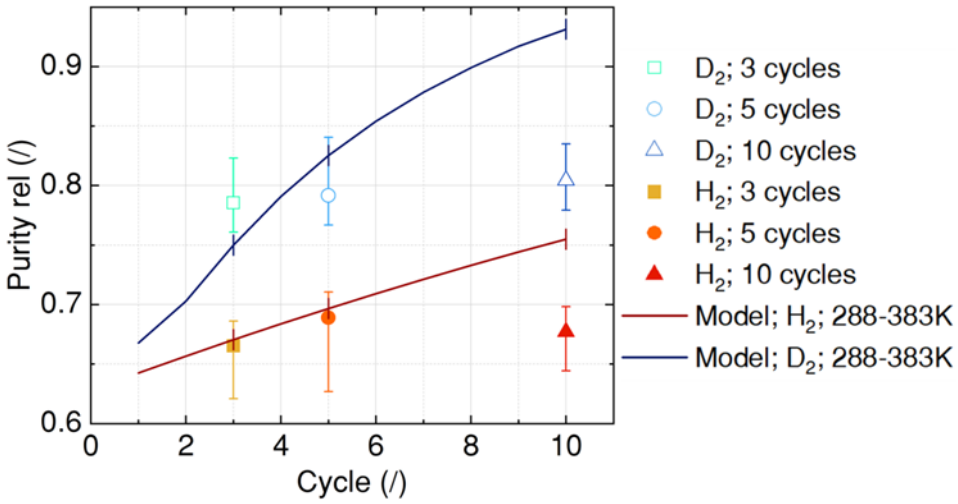

Figure 6.6: Experimental enrichment results for TR1 (288-383 K) of H_2 (filled, orange symbols) and D_2 (open, blue symbols) as a function of the number of cycles and its modelling results shown as a curve with cycle 3, 5 and 10 marked with a line.

Table 6.5 wraps up the enrichment results of protium and deuterium for 3, 5 and 10 cycles.

Table 6.5: Overview of the separation results for 3, 5 and 10 cycles.

Properties	3 cycles	5 cycles	10 cycles
H_2 enrichment (%)	66.54	68.9	67.71
D_2 enrichment (%)	78.54	79.16	80.43

As the results for 3 cycles possess by far the best results in terms of separation efficiency and duration, I conclude that **TR1 – auxiliary vessel – 3 cycles** process leads to the total best overall performance.

6.4 MC – Impact of Temperature and Flow

The results of the membrane experiments are addressed in this section. A membrane with dimensions of L = 0.1 m, d_o = 0.01 m, d_i = 0.007 m and $d_p = 5 \cdot 10^{-9}$ m and material γ-Al_2O_3 has been used, coated on α-Al_2O_3 for a better stability[5]. A picture from the membrane is shown in Figure 6.7.

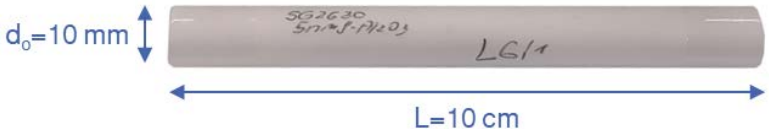

Figure 6.7: Picture of membrane with its dimensions.

The porosity ε is 0.424, the tortuosity τ is 2.75, which have been stated by the manufacturer. For a separation through gaseous diffusion, it is required to be in the free molecular regime. This regime occurs when the Knudsen number is greater than 0.5, which is dependent on the pore diameter and the mean free path (see equations (2.2) and (2.3)). For a worst case calculation, the lowest applied temperature (293 K, minimum ambient temperature as the membrane stage does not have an internal cooling) and the highest pressure (10^5 Pa, as the membrane runs under vacuum) are used. With the diameter of the hydrogen molecule being $d_{H2} = 2.92 \cdot 10^{-10}$ m, the smallest Knudsen number is 21.36. Therefore, a free molecular flow is guaranteed for all parameter settings.

In total, three experiments with different conditions have been conducted. Table 6.6 gives an overview of the measurement results, temperature, pressure and flow. For test 1), at ambient temperature, a flow set with an MFC has been set to 20 sccm. As the mass flow controller has been zeroed before the experiments at the same ambient conditions as the experiments, the temperature has no influence on the flow. To determine the flow rate through the membrane, the differential pressure inlet-retentate has been divided by the pressure on the retentate side. This is represented by the ratio of the flows F_P/F_R in the last row of the table. Under these conditions, 0.044 ± 0.003 % of the total flow permeates through the membrane. For test 2), the temperature has been increased to 373 K. The flow rate ratio increases to 0.095 ± 0.002 %, and for temperature of 473 K (test 3), the ratio is 0.17 ± 0.002 %.

[5] Declaration from the manufacturer Fraunhofer IKTS

Table 6.6: Experimental values of five different experiments with the membrane.

Conditions	1. 296 K	2. 373 K	3. 473 K
T (K)	297.85	351.49	425.09
F (sccm)	19.99	99.22	99.21
p_R (Pa)	1846.44	3992.52	4029.73
P_I (Pa)	1847.24	3996.31	4036.5
$\frac{F_P}{R_R}$ (%)	0.044	0.095	0.17

The separation results are shown in Figure 6.8 for both streams (permeate and retentate) for three different experiments. Several things can be observed here. The permeate stream caused an enrichment of protium, accordingly the retentate stream contains more deuterium particles than before. Slight fluctuations (maximum 2.2 % for D_2 and 7.9 % for H_2 of the mean value) exist between the individual test points, but all points are within the range of uncertainties. In the diagram, the horizontal lines reflect the initial composition. The lower, orange line represents the 42.2 % H_2 and the upper, blue line the 57.8 % D_2. For both isotopes, the real data point must be above the respective line, otherwise an enrichment "in the wrong direction" would have taken place. This means that the uncertainty bar below these lines may be ignored. The experimental results translate in an average enrichment factor of 43.4 % for H_2, which corresponds to an increase of 2.8 %. For deuterium, the average is 58.3 % (increase of 0.9 %). This is significantly below the ideal (molecular flow) separation factor of 1.41 (see chapter 2.2.1), which asserts a higher separation effect than these results exhibit. The real separation factor, however, is smaller than 1.41. A reason might be that the diameter (of the pore) to length (of the pore) ratio is very small leading to a low probability of occurrence.

It is valid for both isotopes that there is no influence of temperature or flow. This confirms the theoretical basis, which states that the separation depends only on the molar masses.

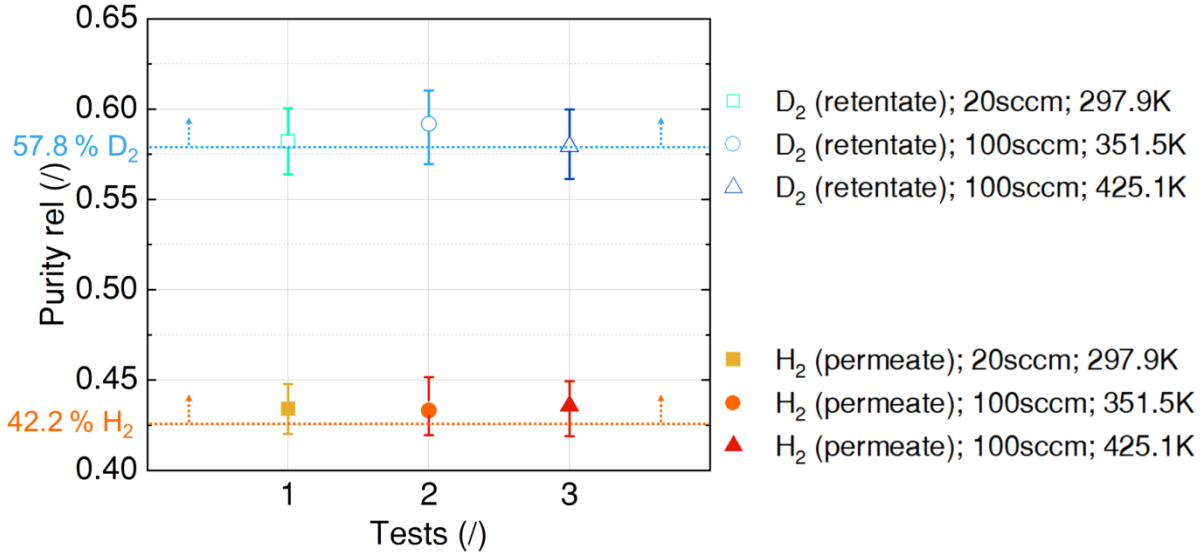

Figure 6.8: Experimental purity as function of three different tests of membrane for a protium enrichment in the permeate stream in the bottom (filled, orange, symbols) and deuterium enrichment in the retentate stream on the top (open, blue symbols).

Two conclusions can be drawn from the results: i) Regarding the throughput, there are **quantitative inconsistencies**, however, the **qualitative behaviour is in line** with the literature and ii) The values in the permeate and retentate **enrichments related to the flow are according the statements from literature**.

Although the found enrichment values seem to be small, it will be shown in the following chapter that the use of MC is inevitable in certain operational cases.

7 Application to a Fusion Reactor assuming EU-DEMO

This chapter consists of three main sections. In the first section, the approach how to extrapolate from protium and deuterium to tritium values is shown. In the second section the results from the modelling and experiments are utilized to describe DEMO relevant conditions. In the last section, next steps are stated.

The experiments demonstrate a separation by means of the developed two stage process MC-TSA. Here it is analysed, if the two technologies have potential to be suitable candidates for DEMO application. Two differences arise here: i) The throughput in DEMO is orders of magnitudes larger than investigated in HESTIA, and ii) Tritium is part of the process to be separated. To do this, calculations are performed with two reference cases, which are described in detail in [6].

7.1 Extrapolation to Tritium and Isotopologues

As experiments with tritium and at the relevant conditions have not been performed, extrapolations and assumptions have to be applied for both separation principles:

TSA: To do this, the model is consulted. The best result regarding separation efficiency and duration has been found for the configuration at TR1 (288-373 K) with auxiliary vessel for 3 cycles. As the auxiliary vessel is not implemented in the model, it is applied only at TR1 for 3 cycles and extended by tritium. It has to be kept in mind, that the results for the auxiliary vessel (D_2: 78.54 %, H_2: 66.54 %) are integrally 7.26 % better than the modelling results (D_2: 75.33 %, H_2: 59.93 %). For that reason, the results are adapted afterwards. Since it has been shown in the experiments that the initial inventory has an influence on the separation result, and therefore the integral result is essential, here all three isotopes results are subsequently improved by 7.26% for simplicity in the adjustment. Also for the TSA experiments at HESTIA, the enrichment values at 40 % of the column length has been used and analysed. For DEMO, however, the complete mixture is extracted and sent further. As the purity is higher at the end of the column, the averaged purity from the end to 40 % of the column is used.

The tritium values have been extrapolated based on the principle of vibrational energies, which has been explained in subchapter 2.3.2. Thereby the following energies have been used: $\hbar\omega_H = 69.0\,meV$, $\hbar\omega_D = 46.5\,meV$ and $\hbar\omega_T = 37\,meV$ [58]. Literature states separation factors for protium-deuterium and protium-tritium in a palladium system. Applying α_{HD} and the ratio $\hbar\omega_D$ to $\hbar\omega_T$, the separation factor for a protium-tritium system has been calculated and compared with α_{HT} from literature [108]. For

the temperature range of TR1, the calculated value deviates from the literature by maximum only 1.2 %. This represents a reasonable assumption, even though only the vibrational contributions have been taken into account for the vibrational energies [58]. For the alloy composition $TiCr_{1.5}$ no information is available regarding the behaviour with tritium. Therefore, this assumption of Pd has also been adopted for the alloy.

Additionally to the tritium extrapolation, the three isotopologues HD, HT and DT are implemented, as they have an impact on the DEMO results. During the TSA experiments, following ratio of $H_2 : HD : D_2$ has been measured:

Pd column: 18.07 % : 4.55 % : 77.38 %

$TiCr_{1.5}$ column: 58.02 % : 7.85 % : 34.13 %

The formation of the isotopologues is a coincidence and depends on the proportions of the individual isotopes. This is also evident in the results. In the titanium-chromium column, more HD has been formed because the ratio of H_2 to D_2 is closer to the equimolar ratio than in the palladium column. The measured values are used and an equation is developed, by extending the boundary conditions for H_2 being equal to 0 and 100 %. All isotopologues are calculated after the model has been run and are added subsequently.

With the extended modelling regarding tritium, I determine the system IRPR in the fuel cycle using DEMO-relevant data. The Aspen model is used with the inlet composition of IRPR, with all numbers listed and explained in Table 7.1. With application of temperature range 288-373 K for three cycles, 40 % of the gas phase is extracted, which results into 15.21 % extraction of the gas in the columns, with 69.75 % extracting from column 1 (numbers from Table 5.4). As only 15.21 % of the gas in the columns is extracted, seven parallel stages have to be used to process a 100 % flow.

MC: The averaged separation values are used and extended for tritium. I extrapolate to the D-T separation by using the theoretical, ideal separation factor and correcting it by the experimental value from H-D. As the ideal separation factor is only dependent on the molar masses (see equation (2.7)), it results in α_{HD}=1.41 and α_{DT}=1.22. These values need to be corrected by the experimental values. The permeate stream is enriched by a mean value of 2.8 %, the retentate stream by 0.9 %. For a deuterium-tritium mixture, this results in an enrichment in the permeate stream by 2.42 %, and 0.78 % for the retentate. As an average, a permeation rate of 0.17 % is set, with a temperature of 350 K applied. Since the mixture is ternary, two binary systems are considered for simplification. Protium is separated from the rest with α_{HD}, deuterium and tritium with α_{DT}. This corresponds to a worst-case assumption. Thus, in reality, rather more protium is separated.

7.2 Upscaling to the EU-DEMO

For the upscaling, two reference cases are considered:

i) Without an application of an NBI
ii) With an application of an NBI

For both cases, an increase of protium due to outgassing is considered. Additionally to this, case ii) includes a deuterium excess due to the operation of the heating system NBI. The protium stream (with H-1 going to IRPR and H-2 going to DIRL) is shown in Figure 7.1 a). The deuterium stream (with D-1a and D-1b going to IRPR and D-2 going to DIRL) is visually shown in Figure 7.1 b). Only hydrogen is considered here, other gases coming from the torus, as noble gases and impurities, do not have to be considered as they are separated in another system block upstream IRPR. The hydrogen gas mixture emerging from the torus is divided into two streams – around 80 % flow in the direct internal recycling loop. The remaining 20 % are led into the IRPR system. The gas mixture, which is sent back to the torus, is assumed to have a 50:50 ratio of deuterium and tritium, as well as a protium content of less than 1 %.

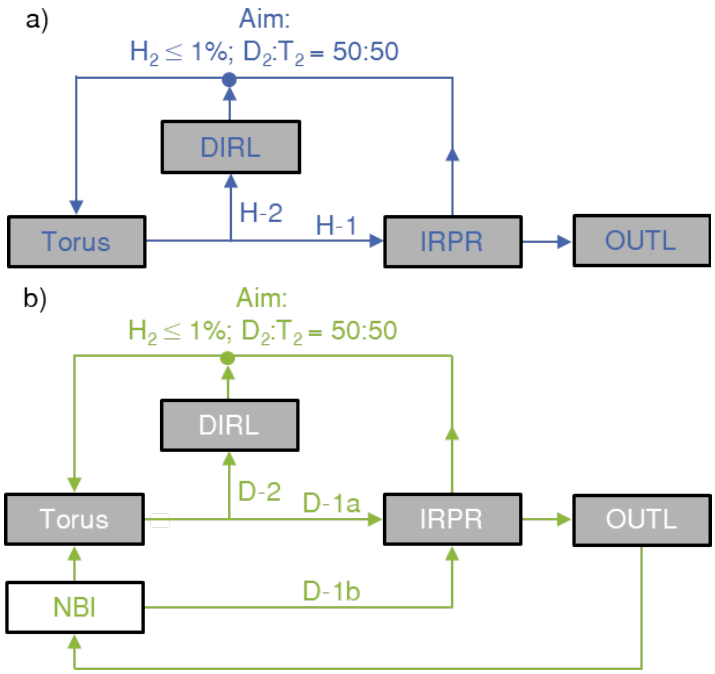

Figure 7.1: Highly simplified flow diagram of the fuel cycle with only the subsystems relevant for IRPR, including its relevant streams for the two cases a) without an NBI and b) with an NBI.

It is not clarified yet, if an NBI will be utilized on DEMO, as an attempt is made, to avoid it and provide heating only with microwave coupling (gyrotrons). However, if it is apparent that an application is inevitable, the throughput rates can be considered as an example of advanced NBI. Anyway, it represents a challenging case, as it considers a strong deuterium imbalance from NBI operation resulting in a constant pure deuterium gas feed of 10 $Pa \cdot m^3 \cdot s^{-1}$ directly into the IRPR system (here, I neglect the trace tritium content that will be contained in this return stream). As part of the

beam, the NBI further sends constantly a small flow, which is treated as part of the exhaust gas, so 80 % of it will arrive at the DIRL, with a flow of 0.6 $Pa \cdot m^3 \cdot s^{-1}$ (D-2).

A protium increase of 0.36 $Pa \cdot m^3 \cdot s^{-1}$ occurs in the DIRL, whereas it is 0.65 $Pa \cdot m^3 \cdot s^{-1}$ in the INTL. Both inputs result from permeation, however the protium increase is bigger in the INTL due to upstream subsystems of the fuel cycle.

Table 7.1 provides the ratios of the individual isotopes as well as the respective throughput for both cases. Most of the deuterium excess is only seen by the IRPR system, resulting in a bigger imbalance compared to DIRL, which results into a small imbalance (≙ 50.07:49.93 for D_2:T_2, when disregarding H_2). In the IRPR system 10 ($Pa \cdot m^3/s$) of pure deuterium enter (when neglecting the ingress of tritium from the plasma side into the NBI vessel) (≙ 55.97:44.03 for D_2:T_2, when disregarding H_2).

Table 7.1: Inlet throughputs and composition of the individual isotopes for both cases [6].

Isotope	Flow – Case 1		Flow – Case 2	
	H-1 ($Pa \cdot m^3 \cdot s^{-1}$)	H-2 ($Pa \cdot m^3 \cdot s^{-1}$)	D-1 ($Pa \cdot m^3 \cdot s^{-1}$)	D-2 ($Pa \cdot m^3 \cdot s^{-1}$)
H_2	1.05 (≙ 1.4 %)	3.81 (≙ 1.1 %)	1.05 (≙ 1.2 %)	3.81 (≙ 1.1 %)
D_2	37.48 (≙ 49.36 %)	170.88 (≙ 49.45 %)	47.48 (≙ 55.3 %)	171.48 (≙ 49.52 %)
T_2	37.41 (≙ 49.24 %)	170.99 (≙ 49.45 %)	37.41 (≙ 43.5 %)	170.99 (≙ 49.38 %)
Total	75.94	345.58	85.94	346.28

Since in both cases too much protium is present and must be removed accordingly, the TSA stage is necessary in any case. For the case without NBI, no membrane stage is necessary. For the case with NBI, two scenarios have been considered: Only the TSA stage and the TSA stage with an upstream membrane cascade. This is crucial to illustrate the importance of the membrane as an upgrade. For all scenarios, the tritium inventory is calculated based on the ideal gas law. For each stage, the corresponding flow rate and tritium fraction are taken. For the membrane stage, the inventory in each system is low, as this process is continuous. For the column stage, the situation is quite different, as three cycles last, according to experimental results, 2406 s (see duration of experiment "auxiliary vessel" in Figure 6.3).

Case 1: Enrichment values for the removal of protium are shown in Table 7.2, where all six isotopologues are listed. For the calculation of the protium concentration, the HD and HT portions are divided in half to simplify the calculation. For the composition to the torus, only H_2, D_2 and T_2 values are stated. Thus, a total amount of 0.46 % is obtained, which is sent back to the torus. The resulting proportion arriving at the torus is therefore 1.02 %, which meets the DEMO requirements. The result is obtained by adding the streams from DIRL in Table 7.1 and the tritium enriched streams from TSA1 in Table 7.2. As deuterium and tritium have been balanced before

the separation, tritium exceeds with a ratio of 50.86 % to 49.14 % (neglecting the protium content and considering isotopologues). This does not pose any complications, as a deuterium buffer tank is available to compensate for the tritium excess if required. The protium and deuterium enriched stream is sent to OUTL for further separation in cryo-distillation. The tritium inventory is high, with 1.2 kg of tritium.

Table 7.2: Overview of a separation example of output streams for a TSA stage for case 1 (no NBI).

Stage	Streams T_2 enrichment ($Pa \cdot m^3 \cdot s^{-1}$)	Streams H_2/D_2 enrichment ($Pa \cdot m^3 \cdot s^{-1}$)	T_2-Inventory (g)
TSA1	H_2: 0.13 (≙ 0.24 %) HD: 0.14 (≙ 0.26 %) D_2: 21.02 (≙ 39.41 %) HT: 0.097 (≙ 0.18%) DT: 4.26 (≙ 7.99 %) T_2: 27.69 (≙ 51.93 %)	H_2: 0.68 (≙ 2.92%) HD: 0.15 (≙ 0.64 %) D_2: 13.83 (≙ 59.29 %) HT: 0.24 (≙ 1.03%) DT: 1.92 (≙ 8.22 %) T_2: 6.5 (≙ 27.92 %)	1195.1
Total	Send to torus (IRPR+DIRL): H_2: 4.06 (≙ 1.02 %) D_2: 194.09 (≙ 48.64 %) T_2: 200.86 (≙ 50.86 %)	Send to OUTL: H_2: 0.87 (≙ 3.75 %) D_2: 14.86 (≙ 63.72 %) T_2: 7.59 (≙ 32.54 %)	1195.1

Case 2a: Isotope rebalancing with the application of an NBI without the pre-staged membrane. The values are shown in Table 7.3. To achieve an equimolar ratio of deuterium and tritium, the complete stream has to be separated. It results into 50.01 % : 49.99 % neglecting protium. The protium content in the stream to the torus is 1.02 %.

Table 7.3: Overview of a separation example for all output streams.

Stage	Streams T_2 enrichment ($Pa \cdot m^3 \cdot s^{-1}$)	Streams H_2/D_2 enrichment ($Pa \cdot m^3 \cdot s^{-1}$)	T_2-Inventory (g)
TSA1	H_2: 0.13 (≙ 0.25 %) HD: 0.14 (≙ 0.26 %) D_2: 24.13 (≙ 45.24 %) HT: 0.1 (≙ 0.18 %) DT: 4.26 (≙ 0.7.99 %) T_2: 24.58 (≙ 46.09 %)	H_2: 3.24 (≙ 0.76 %) HD: 0.64 (≙ 0.15 %) D_2: 15.01 (≙ 64.35 %) HT: 0.24 (≙ 1.03 %) DT: 1.92 (≙ 8.22 %) T_2: 5.26 (≙ 22.54 %)	1195.6
Total	Send to torus (IRPR+DIRL): H_2: 4.06 (≙ 1.02 %) D_2: 197.8 (≙ 49.5 %) T_2: 197.75 (≙ 49.49 %)	Send to OUTL: H_2: 0.95 (≙ 4.07 %) D_2: 16.04 (≙ 68.78 %) T_2: 6.33 (≙ 27.16 %)	1195.6

To compare these result directly with MC-TSA stage (case 2b), either the protium content or the ratio of deuterium to tritium has to be the same. I decided for an identical ratio (50.01 % to 49.99 % neglecting protium).

Case 2b: It is advisable to first carry out a pre-enrichment with the membrane stage for the major part of the flow, and then to carry out a stronger enrichment with the column stage. As a result, the majority is already pre-enriched, as only a small portion permeates through the membrane. Another advantage is that this process runs completely under vacuum conditions. The permeate flow is passed directly to the Outer Tritium Loop, the retentate flow is passed to the next separation stage, where protium is removed. In this case, six membranes are connected in series' first, followed by one column stage. The connection, including the designation of the streams, is shown in Figure 7.2.

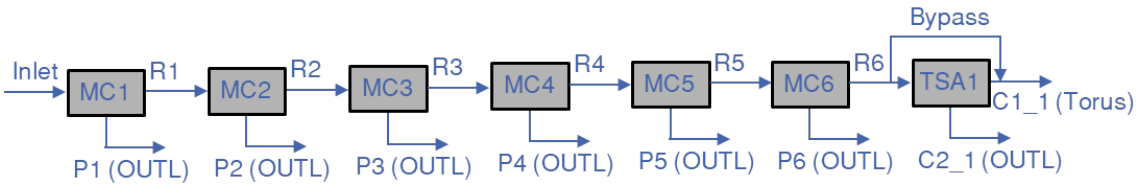

Figure 7.2: Overview of the connection between the separation stages: Membrane with six stages (MC1-MC6), with the retentate (R1-R6) and permeate (P1-P6) streams, and two column stages (TSA1+2) with streams from column 1 (C1_1+2) and column 2 (C2_1+2).

Figure 7.3 shows the composition for the three isotopes (in a)) as well as the formed isotopologues (in b)) after every separation step. For the membrane stage, a small, continuous increase or decrease from MC1 to MC6 is visible. Whereas for the column stage a jump is seen, as this stage is more efficient.

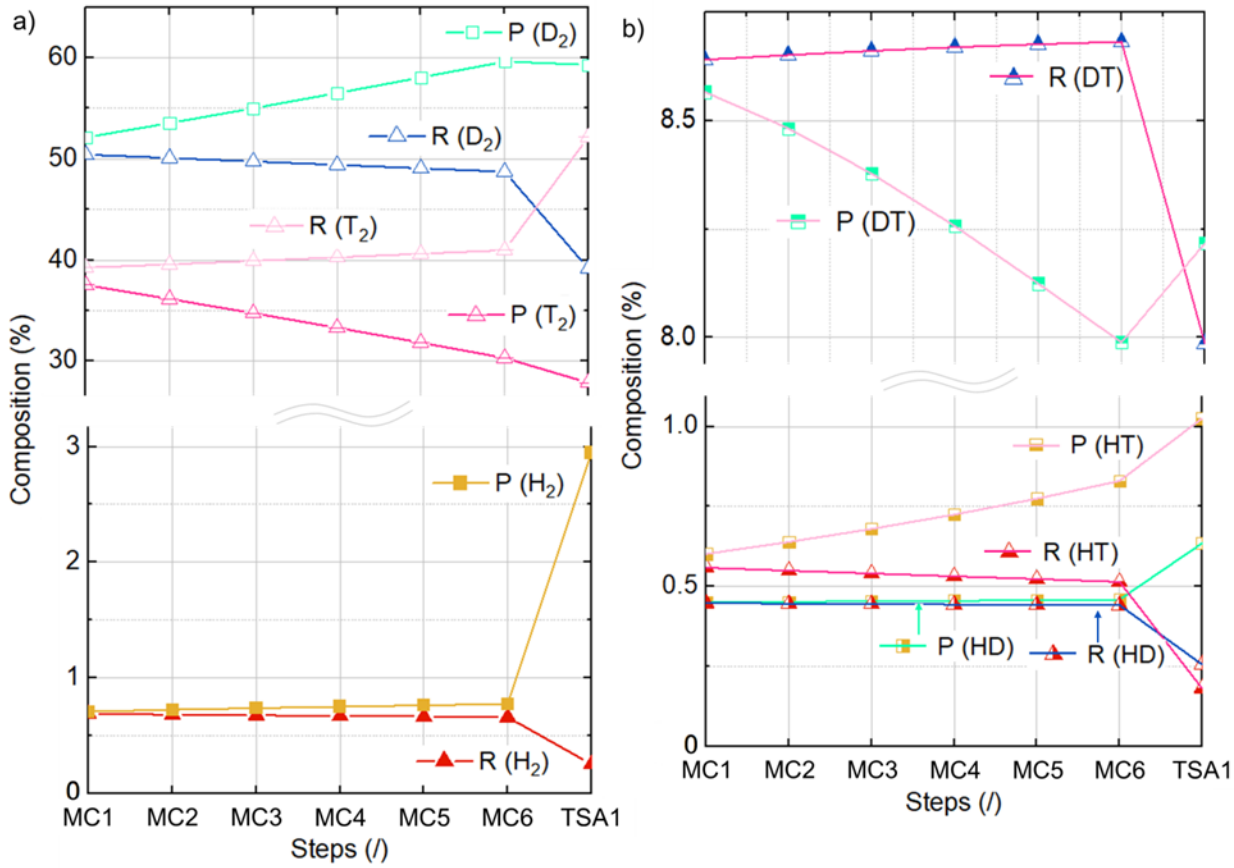

Figure 7.3: Overview of the composition of protium, deuterium and tritium in a) and its isotopologes in b) after each separation step with "P" as the flow going to the ISS system and "R" as the stream leading into the next separation step.

If 38.5 % are bypassed around the TSA stage, an equimolar ratio of deuterium and tritium is reached ((result: 1.06 % H_2, 50.01 % D_2, 49.99 % T_2). This results into a tritium inventory of 763.5 g. All flows coming from the permeate and column 2 are sent directly to the isotope separation system. The total amount is 24.19 Pam³/s. Table 7.4 shows the composition as well as the throughput which is sent back to the torus as well as to the isotope separation system. This corresponds to the sum of all stages (MC1-6 and TSA).

Table 7.4: Overview of the output streams and tritium inventory sent to the tours and ISS if the ratio of D_2 to T_2 is kept the same.

Stage	Send to torus (IRPR+DIRL): ($Pa \cdot m^3 \cdot s^{-1}$)	Send to ISS: ($Pa \cdot m^3 \cdot s^{-1}$)	T_2-Inventory (g)
Total	H_2: 4.37 (≙ 1.06 %) D_2: 203.95 (≙ 49.48 %) T_2: 203.84 (≙ 49.46 %)	H_2: 0.55 (≙ 3.63 %) D_2: 9.67 (≙ 63.52 %) T_2: 5 (≙ 32.84 %)	763.5

If the protium content is to be kept the same between Case2a and b, only 7% can be sent through the bypass. The rest of the gas has to be sent through the TSA stage, which increases the tritium inventory. The composition would thus result in

$H_2 : D_2 : T_2$ at 1.02 % : 48.83 % : 50.14 %, the tritium inventory increases to 1154.58g (see Table 7.5). Depending on the desired requirements, the bypass can thus be adjusted.

Table 7.5: Overview of the output streams and tritium inventory sent to the tours and ISS if the H_2 content is kept the same.

Stage	Send to torus (IRPR+DIRL): ($Pa \cdot m^3 \cdot s^{-1}$)	Send to ISS: ($Pa \cdot m^3 \cdot s^{-1}$)	T_2-Inventory (g)
Total	H_2: 4.12 (≙ 1.02 %) D_2: 196.26 (≙ 48.83 %) T_2: 201.51 (≙ 50.14 %)	H_2: 0.83 (≙ 3.69 %) D_2: 14.35 (≙ 63.6 %) T_2: 7.381 (≙ 32.73 %)	1154.58

Table 7.6 shows the separation results of the three scenarios, holding deuterium and tritium constant. With regard to protium, all scenarios yield similar reduction results, at slightly above 1 %. The protium content in case 2 of the MC-TSA is slightly higher than without the membrane as a pre-stage. The reason for this is that the entire amount passes through the TSA stage, whereas with MC-TSA a significant part is bypassed. If the amount bypassed is reduced, the protium content can be lowered even further. However, the membrane as a pre-stage is reasonable under all circumstances. The amount of deuterium and tritium that has previously been fused and is therefore no longer available is subsequently added to the mixture. In percentage terms, the protium content thus decreases slightly, ensuring a maximum proportion of 1%. Therefore this **DEMO requirement is fulfilled**.

In all three scenarios, the deuterium excess has been reduced. In Case 1 (without NBI), a slight excess of tritium can be seen. For the two considerations from Case 2, a 50:50 balance has been established. In case 2, it is also evident that the tritium inventory can be reduced by 38.5 % by adding a membrane. **The membrane is therefore essential in combination with the TSA stage**.

Table 7.6: Summary of the separation results of the three scenarios, one for protium removal (Case 1 without NBI) and two for isotope rebalancing (Case 2 with NBI).

	Case 1 (no NBI) – TSA	Case 2a (NBI) – MC-TSA	Case 2b (NBI) – TSA
H_2 (%)	1.02 %	1.06 %	1.02 %
D_2 (%)	48.64 %	49.48 %	49.5 %
T_2 (%)	50.34 %	49.46 %	49.49 %
T_2-Inventory (g)	1195.1	763.5	1195.6

The three main requirements, identified by Table A.13 are safety and environment, high separation factor and low tritium inventory. Safety and environment is fulfilled for both stages. The membrane runs under vacuum, and for the columns, hydrogen is stored in the material in case of an accident. The separation factor of the TSA stage is high. The tritium inventory is high in the TSA stage and can be reduced by adding the MC stage. The values are only an approximate indicator and should not be assumed to be fixed. **The two-stage separation has proven to be feasible, despite the high tritium inventory**.

Now that I have proven that separation is possible for DEMO, it is still important to know how many parallel plants are needed. Both stages are scaled up linearly. For the membrane, the length is increased by a factor of 10 up to 1m. For a throughput of 100 sccm, which has been set in HESTIA experiments, 52 membranes are needed in parallel for MC-1 (slowly decreasing for the next membrane stages as the throughput decreases). This results into a relatively small surface area of 1.64 m^2. However, the throughput can also be set much higher and still run under vacuum conditions. Thus, the number of membranes is significantly reduced. If 1000 sccm is set, the number of membranes is reduced to 6, whereby also the surface area of the membrane decreases.

For the TSA stage, 6 stages are set in parallel. To ensure the throughput of 52.3 Pam^3/s (for the NBI case (MC-TSA) with a bypass of 38.5 %) with a functional heat transfer, several stages are required. This can still be fulfilled with a diameter 4.87 times more than for HESTIA. This corresponds to a diameter of 29.2 mm, allowing still a good heat transfer. This results into $m_{Pd} = 7.4\,kg$ and $m_{TiCr1.5} = 5.4\,kg$. The throughput and tritium are, respectively one-sixth for each column. If the protium content is reduced further, 9 parallel columns are required instead of 6. The amount of bulk material increases accordingly.

7.3 Deficits and Improvements for the MC-TSA Technology

This thesis included test application to verify the feasibility of isotope separation. In order to bring this process to a real application for the EU-DEMO, several aspects have to be improved in the future:

The main focus must lie on the reduction of the tritium inventory. There are several factors that can be optimised. The time of heating and cooling has a direct influence. Both, the heat transport in the heating and cooling medium and the heat transfer of the bulk material have an impact. Materials with high thermal conductivity but no sorption capability can be added to optimise the process.

The materials must be manufactured in such a way that a reversible capacity is exhibited. This is currently not the case with titanium chromium. Using other materials

with a higher separation factor will also reduce the tritium inventory. Potential candidates are magnesium to replace palladium and an alloy of lanthanum, nickel and aluminium to replace the titanium chromium alloy.

Some uncertainties are e.g. kinetic effects of hydrogen metal interactions, which need to be considered in more detail, as well as possible inhomogeneities of the temperature. Long-term effects of the materials, such as disproportionation, have not been considered in this work. These are relevant for a long-term application in DEMO.

To reduce the demand on the TSA stage, it is also important to increase the real separation factor for protium in the membrane. The scale up has already shown a large impact of the membrane, which can be further improved by optimisation, such as modification of the pore diameter.

Overall, it can be said that the two-step process still has some uncertainties, however, it has great potential and can be further improved through ongoing development.

8 Summary

This thesis deals with a part of the fusion reactor fuel cycle, the "Isotope Rebalancing and Protium Removal" system block. This is needed to reduce the amount of protium (to less than 1 %) and balance the deuterium-tritium ratio (50:50) for an efficient reactor fuelling. So far, a technology with a high tritium inventory has been used, which separates the isotopes in a time consuming way.

The concept developed and demonstrated is based on two-stage: "Membrane Coupled - Temperature Swing Absorption" process (MC-TSA) for hydrogen isotope separation, being successfully implemented and characterized qualitatively and quantitatively.

The membrane as a preliminary stage has proven to be an important part. The process can be further improved by optimising the membrane geometries.

For the temperature swing absorption stage, the use of suitable materials is crucial. Therefore the test rig MAIA has been designed, built and set into operation showing precise results with low uncertainties. Other materials as well as other operations (e.g. kinetics tests) can be performed with this system. In this work, two materials have been characterized that provide a reasonable baseline for fusion application: Palladium and titanium-chromium ($TiCr_{1.5}$). The experimentally determined separation factor, which is an indicator for the separation efficiency, is of 0.46 (for Pd) and 2.02 (for $TiCr_{1.5}$) at 273 K.

Using these two materials, the main objective, demonstration of hydrogen isotope separation, has been performed successfully in the second test rig HESTIA. The results of this system, which has been developed and constructed, are validated on the basis of an adapted modelling. Parameters that, according to theory, have an influence on separation (such as temperature) have been shown. The system can be versatilely used and has shown good first separation results. The best results in terms of separation effect and time is: 42.2 % to 66.54 % for H_2, 57.8 % to 78.54 % for D_2. It is therefore an outstanding basis for further investigations.

The upscale to DEMO application, including all relevant boundary conditions, has also been demonstrated. The requirements that the protium content shall be less than 1% and the ratio of deuterium to tritium is balanced can be fulfilled with this two-step process. The combination of both separation principles is therefore suitable for DEMO. The tritium inventory, which is still considerably high, can be reduced with further investigations.

References

[1] Tanabe, T. (2017). Tritium: Fuel of Fusion Reactors. Springer, ISBN 978-4-431-56458-4 (Tokyo).

[2] Eurofusion webpage: “Fusion basics”. https://www.euro-fusion.org/fusion/fusion-on-the-sun/. accessed 05.05.2022.

[3] Deutsche Physikalische Gesellschaft e.V. (DPG): “Fusion basics”. https://www.dpg-physik.de/vereinigungen/fachlich/smuk/fvp/weiterfuehrende-informationen/grundlagen-der-kernfusion. accessed 05.05.2022.

[4] Day, C. et al. (2022). The pre-concept design of the DEMO Tritium, Matter Injection and Vacuum Systems.

Internal draft from C. Day, official publication before defense. All missing information will be added

[5] Biel, W., Baar, M. d., Dinklage, A., Felici, F., König, R., Meister, H., Treutterer, W., Wenninger, R. (2015). DEMO diagnostics and burn control. Fusion Engineering and Design, Vol. 96-97, pp. 8-15. https://doi.org/10.1016/j.fusengdes.2015.01.046.

[6] Hörstensmeyer, Y. N. (2022). Holistic fuel cycle modelling of a future fusion reactor.

Internal draft from C. Day, official publication before defense. All missing information will be added

[7] Bainbridge, N., Bell, A.C., Brennan, P. D., Knipe, S., Lässer, R., Stagg, R. (1999). Operational experience with the JET AGHS cryodistillation system during and after DTE1. Fusion Engineering and Design, Vol. 47, pp. 321-332. https://doi.org/10.1016/S0920-3796(99)00089-7.

[8] Mazur, T. R., Klappauf, B., Raizen, M. G. (2014). Demonstration of magnetically activated and guided isotope separation. Nature Physics, Vol. 10, pp. 601-605. https://doi.org/10.1038/NPHYS3013.

[9] Raizen, M. G., Klappauf, B. Magnetically activated and guided isotope separation (2012). New Journal of Physics, Vol. 14, pp. 1-12. https://doi.org/10.1088/1367-2630/14/2/023059.

[10] Becker, E. W., Bier, K., Bier, W., Schütte, R., Seidel, D. (1967). Separation of the Isotopes of Uranium by the Separation Nozzle Process. Angewandte Chemie International, Vol. 6, pp. 507-518. https://doi.org/10.1002/anie.196705071.

[11] Meis, D. D. (2017). Overview on porous inorganic membranes for gas separation. Technical report, RT/2017/5/ENEA, ENEA (Rome). https://doi.org/10.13140/RG.2.2.35571.53287.

[12] Bigeleisen, J. (1969). Isotope Separation Practice. Advances in Chemistry Vol. 89, pp. 1-24. https://doi.org/10.1021/ba-1969-0089.ch001.

[13] Oh, H. (2014). Nanoporous Materials for Hydrogen Storage and H2/D2 Isotope Separation. Doctoral Dissertation at the University Stuttgart, Faculty of Chemistry. https://doi.org/10.18419/OPUS-1422.

[14] Cai, J., Xing, Y., Zhao, X. (2012). Quantum sieving: feasibility and challenged for the separation of hydrogen isotopes in nanoporous materials. The Royal Society of Chemistry Advances, Vol. 2, pp. 8579-8586. https://doi.org/10.1039/c2ra01284g.

[15] Ragheb, M. (2012). Chapter 10 – Isotopic separation and enrichment. Notes, University of Illinois, NPRE 402. http://magdiragheb.com/NPRE%20402%20ME%20405%20Nuclear%20Power%20Engineering/Isotopic%20Separation%20and%20Enrichment.pdf. No doi found (accessed 05.05.2023).

[16] Rutherford, W. M., Lindsay, C. N. (1985). Separation of hydrogen isotopes by thermal diffusion. Fusion Technology, Vol. 8, pp. 2278-2284. https://doi.org/10.13182/FST85-A24620.

[17] Berezkin, V. G., Alishoyev, V. R., Nemirovskaya, I. B. (1977). Gas chromatography of polymers. Journal of Chromatography Library, Vol. 10, pp. 1-31. https://doi.org/10.1016/S0301-4770(08)60223-7.

[18] Lässer, R., Botter, F., Hemmerich, J. L, Laveyry, M., Lupo, J., Milverton, P., Stagg, R., Tistchenko, S., Walker, K. D., Yorkshades, J. (1993). Protium-Deuterium Separation with the Preparative Gas Chromatographic System at JET. 15th IEEE/NPSS Symposium on Fusion Engineering - Supplement (Hyannis, MA, United States of America). https://doi.org/10.1109/SFE.1993.472788.

[19] Heung, L. K, Sessions, H. T., Xiao, S. (2011). TCAP hydrogen isotope separation using palladium and inverse columns. Fusion Science and Technology, Vol. 60, pp. 1331-1334. https://doi.org/10.13182/FST11-T39.

[20] Wong, Y. W., Hill, F. B. (1982). Separation of hydrogen isotopes via single column pressure swing adsorption. Chemical Engineering Communications, Vol. 15, pp. 343-356. https://doi.org/10.1080/00986448208911080.

[21] Sircar, S., Golden, T. C. (2000). Purification of Hydrogen by Pressure Swing Adsorption. Separation Science and Technology, Vol. 35, pp. 667-687 http://dx.doi.org/10.1081/SS-100100183.

[22] Kotoh, K., Tanaka, M., Nakamura, Y., Sakamoto, T., Asakura, Y., Uda, T., Sugiyama, T. (2008). Experimental verification of hydrogen isotope separation by pressure swing adsorption. Fusion Science and Technology, Vol. 54, pp. 411-414. http://dx.doi.org/10.13182/FST08-A1842.

[23] Lee, M. W. Thermal Cycling Absorption Process – A new way to separate hydrogen isotopes (2000). Celebrating 50 years of excellence in science and engineering at the Savannah River Site (Aiken, SC, United States of America). https://sti.srs.gov/fulltext/WSRC-MS-2000-00061.pdf. accessed 05.05.2022.

[24] Neugebauer, C., Hörstensmeyer, Y., Day, C. (2020). Technology Development for Isotope Rebalancing and Protium Removal in the EU-DEMO Fuel Cycle. Fusion Science and Technology, Vol. 76, pp. 215-220. https://doi.org/10.1080/15361055.2019.1704139.

[25] De Falco, M., Marrelli, L., Laquaniollo, G. (2011). Membrane Reactors for Hydrogen Production Processes. 1. Edition, Springer, ISBN: 978-0-85729-150-9 (London).

[26] Jouston, K., (2012). Wutz Handbuch Vakuumtechnik. 11th edition, SpringerVieweg, ISBN: 978-3-8348-1745-7 (Berlin).

[27] Brus, D., Skrabalova, L., Herrmann, E., Olenius, T., Travnickova, T., Makkonen, U., Merikanto, J. (2017). Temperature-Dependent Diffusion of H_2SO_4 in air at atmospherically relevant condition: Laboratory measurements using laminar flow technique. Atmosphere, Vol. 8, pp. 1-15. https://doi.org/10.3390/atmos8070132.

[28] Schulz, G., Michele, H., Werner, U. (1982). Membrane rectification columns for gas separation and determination of the operating lines using the Mccabe Thiele diagram. Journal of Membrane Science, Vol. 12, pp. 183-194. https://doi.org/10.1016/S0376-7388(00)80181-7.

[29] D. Meis, D. (2017). Gas transport through porous membranes. Technical report, ENEA (Rome), ISSN: 0393-3016. https://iris.enea.it/handle/20.500.12079/6775?mode=simple.47.

[30] Li; K. (2007). Ceramic Membranes for Separation and Reaction. Wiley, ISBN: 978-0-470-01440-0 (New York).

[31] Basile, A., Gallucci, F. (2011). Membranes for Membrane Reactors: Preparation, Optimization and Selection. Wiley, ISBN: 978-0-470-74652-3 (New York).

[32] Oyama, S. T., Yamada, M., Sugawara, T., Takagaki, A., Kikuchi, R. (2011). Review on Mechanisms of Gas Permeation through Inorganic Membranes. Journal of the Japan Petroleum Institute, Vol. 54, pp. 298-309.

https://doi.org/10.1627/jpi.54.298.

[33] Manickam, S. S., Gelb, J., McCutcheon, J. R. (2014). Pore structure characterization of asymmetric membranes: Non-destructive characterization of porosity and tortuosity. Journal of Membrane Science, Vol. 454, pp. 549-554. http://dx.doi.org/10.1016/j.memsci.2013.11.044.

[34] Keurentjes, J. T. F., Linders, L. J., Beverloo, W. A., Van't Riet, K. (1992). Membrane cascades for the separation of binary mixtures. Journal of Chemical Engineering Science, Vol. 47, pp. 1561-1568. https://doi.org/10.1016/0009-2509(92)85004-U.

[35] Dekura, S., Kobayashi, H., Kusada, K., Kitagawa, H. (2019). Hydrogen in Palladium and storage properties of related nanomaterials: Size, Shape, Alloying, and Metal-Organic Framework Coating Effects. ChemPhysChem, Vol. 20, pp. 1158-1176. https://doi.org/10.1002/cphc.201900109.

[36] Fukai, Y. (1992). The metal-hydrogen system. Springer, ISBN: 3-540-55637-0 (Berlin, New York, Heidelberg).

[37] Jung, M. (2002). Dynamik und Löslichkeit von Wasserstoff in nanokristallinen Metallen. Doctoral Dissertation at the university Darmstadt, Faculty of Physics. https://tuprints.ulb.tu-darmstadt.de/268/.

[38] Moreno-Pirajan, J. M (ed.). (2011). Thermodynamics - Interaction Studies - Solids, Liquids and Gases. IntechOpen, ISBN: 978-953-307-563-1.

[39] Pisarev, A. A. (2012). Hydrogen adsorption on the surface of metals. Woodhead Publishing Series in Metals and Surface Engineering, Vol. 1, pp. 3-26. https://doi.org/10.1533/9780857095374.1.3.

[40] Peters, B. (2020). Development of a Hydrogen-selective Vacuum Pump on the basis of Superpermeability. Doctoral Dissertation at the Karlsruhe Institute of Technology, Faculty of Mechanical Engineering. https://doi.org/10.5445/IR/1000122305.

[41] Shinbine, A. (2013). In-situ evaluation of the hcp to bcc phase transformation kinetics in commercially pure titanium and Ti-5AlMo-5V-3Cr alloy using laser ultrasonics. Master Thesis, university of British Columbia, Faculty of Materials Engineering. https://dx.doi.org/10.14288/1.0228055.

[42] Shohoji, N. (2013). Statistical Thermodynamic Approach to Interstitial non-stoichiometric Compounds (Hydride, Carbide, Nitride, Phosphide and Sulphide). Laboratorio Nacional de Energia e Geologia. ISBN: 978-3-659-45506-3 (Lisbon).

[43] Pundt, A. (2005). Nanoskalige Metall-Wasserstoff-Systeme. Universitätsverlag Göttingen, ISBN: 3-938616-11-3 (Göttingen).

[44] Andreev, B. M., Magomedbekov, E. P., Sicking, G. H. (1996). Interaction of Hydrogen Isotopes with Transition Metals and Intermetallic Compounds. Vol. 132, Springer Tracts in Modern Physics, ISBN: 978-3-540-48675-6 (Berlin Heidelberg).

[45] Züttel, A., Borgschulte, A., Schlapbach, L. (2008). Hydrogen as a Future Energy Carrier. Wiley-VCH Verlag, ISBN: 978-3-527-30817-0 (Weinheim).

[46] Adams, B. D., Chen, A. (2011). The role of palladium in a hydrogen economy. Materials Today, Vol. 14, pp. 282-289. https://doi.org/10.1016/S1369-7021(11)70143-2.

[47] Züttel, A. (2003). Materials for hydrogen storage. Materials Today, Vol. 6, pp. 24-33. https://doi.org/10.1016/S1369-7021(03)00922-2.

[48] Chandra, D., Reilly, J. J., Chellappa, R. (2014). Metal hydrides for Vehicular Applications: The State of the Art. Journal of the Minerals, Metals & Materials Society, Vol. 58, pp. 26-32. https://doi.org/10.1007/s11837-006-0005-0.

[49] Sandrock, G. (1997). State of the art review of hydrogen storage in reversible metal hydrides for military fuel cell applications. Report, Defense Technical Report Center (Fort Belvoir). https://apps.dtic.mil/sti/citations/ADA328073.

[50] Leon, A. (ed.) (2008). Hydrogen Technology. Springer, ISBN: 978-3-540-69925-5 (Berlin Heidelberg).

[51] Luo, W. (2009). Equilibrium Isotope Effect for Hydrogen Absorption in Palladium. The Journal of Physical Chemistry, Vol. 112, pp. 8099-8105. https://doi.org/10.1021/jp905614x.

[52] Pozio, A., Tosti, S. (2019). Pd-Ag Electrical Resistivity in Hydrogen and Deuterium: Temperature Effect. Materials, Vol. 12, pp. 1-13. https://doi.org/10.3390/ma12213551.

[53] Teufel, S. (2012). Experimental investigation of H2/D2 isotope separation by cryo-adsorption in metal-organics frameworks. Doctoral Dissertation Max-Planck-Institut für Intelligente Systeme (Stuttgart), Faculty of Chemistry. http://dx.doi.org/10.18419/opus-6808.

[54] Andreev, B. M, Magomedbekov, E. P. (2001). Separation of hydrogen isotopes by chemical isotope exchange in systems involving metal and intermetallic compound hydrides. Separation Science and Technology, Vol. 36, pp. 2027-2086. http://dx.doi.org/10.1081/SS-100104766.

[55] Basmadjian, D. (1960). Adsorption in equilibria of hydrogen, deuterium, and their mixtures. Part 2. Canadian Journal of Chemistry, Vol. 38, pp. 149-156. https://doi.org/10.1139/v60-017.

[56] Basmadjian, D. (1960). Adsorption in equilibria of hydrogen, deuterium, and their mixtures. Part 1. Canadian Journal of Chemistry, Vol. 38, pp. 141-148. https://doi.org/10.1139/v60-016.

[57] Tanabe, T., Miura, S., Imoto, S. (1979). Isotope Effect in Dissociation of Uranium Hydride. Journal of Nuclear Science and Technology, Vol. 16, pp. 690-696. https://doi.org/10.1080/18811248.1979.9730965.

[58] Lässer, R. (1989). Tritium and Helium-3 in Metals, Springer, ISBN: 978-3-642-73512-7 (Berlin Heidelberg).

[59] Staykov, A., Yamabe, J., Somerday, B. P. (2014). Effect of Hydrogen Gas Impurities on the Hydrogen Dissociation of Iron Surface. International Journal of Quantum Chemistry, Vol. 114, pp. 626-635. https://doi.org/10.1002/qua.24633.

[60] Chabane, D., Harel, F., Djerdir, A., Ibrahim, M., Candusso, D., Elkedim, O., Fenineche, N. (2017). Influence of the key parameters on the dynamic behaviour of the hydrogen absorption by $LaNi_5$. International Journal of Hydrogen Energy, Vol. 42, pp. 1412-1419. http://dx.doi.org/10.1016/j.ijhydene.2016.06.110.

[61] Heung, L. K., Staack, G. C., Klein, J. E., Jacobs, W. D. (2008). Tests of isotopic separation efficiency of palladium packed columns. Fusion Science and Technology, Vol. 54, pp. 391-394. https://doi.org/10.13182/FST08-A1837.

[62] Sakintuna, B., Lamari-Darkrim, F., Hirscher, M. (2007). Metal hydride materials for solid hydrogen storage:A review. International Journal of Hydrogen Energy, Vol. 32, pp. 1121-1140. doi:10.1016/j.ijhydene.2006.11.022.

[63] Sandrock, G. (1999). A panoramic overview of hydrogen storage alloys from a gas reaction point of view. Journal of Alloys and Compounds, Vol. 293-295, pp. 877-888. https://doi.org/10.1016/S0925-8388(99)00384-9.

[64] Kolachev, B. A., (1991). Properties of Hydrogen Storage Alloys. Soviet materials science, Vol. 26, pp. 642-645. https://doi.org/10.1007/BF00723650.

[65] Godula-Jopek, A., Jehle, W., Wellnitz, J. (2012). Hydrogen Storage Technologies. Wiley VCH, ISBN: 978-3-527-32683-9 (Weinheim).

[66] Züttel, A. (2004). Hydrogen storage methods. The Science of Nature, Vol. 91, pp. 157-172. https://doi.org/10.1007/s00114-004-0516-x.

[67] Besserer, U. A., (2002). Tritiumspeicherung in ZrCo. Doctoral Dissertation, Philipps-university Marburg, Faculty of Chemistry. https://doi.org/10.17192/z2003.0108.

[68] Luo, W., Kuji, T., Clewley, J. D., et al. (1991). The thermodynamic properties of the niobium-hydrogen system measured by reaction calorimetry. Journal of Chemical Physics, Vol. 94, pp. 6179-6189. https://doi.org/10.1063/1.460404.

[69] Schober, T. (1990). Tritium in metals. Progress report, Forschungszentrum Jülich GmbH. https://inis.iaea.org/search/search.aspx?orig_q=RN:23003967. No doi found (accessed 05.05.2023).

[70] Garrett, S., Bisker, J. (2020). Primer on spontaneous heating and pyrophoricity. Standard, U.S. department of energy, DOE-HDBK-1081-2014 (Washington D.C.). https://www.standards.doe.gov/standards-documents/1000/1081-bhdbk-2014-cn1. No doi found (accessed 05.05.2023).

[71] Wille, G. W., Davis, J. W. (1981). Hydrogen in titanium alloys. Technical report, The U.S. Department of Energy, DOE/ET/52039-2. https://doi.org/10.2172/6420120.

[72] Sujan, G. K., Pan, Z., Li, H., Liang, D., Alam, N. (2020). An overview on TiFe intermetallic for solid-state hydrogen storage: microstructure, hydrogenation and fabrication processes. Critical Reviews in Solid State and Materials Sciences, Vol. 45, pp. 410-427. https://doi.org/10.1080/10408436.2019.1652143.

[73] Burch, R., Mason, N. B. (1979). Absorption of hydrogen by titanium-cobalt and titanium-nickel intermetallic alloys. Journal of the Chemical Society, Faraday Transactions 1, Vol. 75, pp. 561-577. https://doi.org/10.1039/F19797500561.

[74] Nobuki, T., Crivello, J. C., Cuevas, F., Joubert, J.M. (2019). Fast synthesis of TiNi by mechanical alloying and its hydrogenation properties. International Journal of Hydrogen Energy, Vol. 44, pp. 10770-10776. https://doi.org/10.1016/j.ijhydene.2019.02.203.

[75] Baranowski, B., Filipek, S. M. (2005). 45 years of nickel hydride – history and perspectives. Journal of Alloys and Compounds, Vol. 404-406, pp. 2-6. https://doi.org/10.1016/j.jallcom.2005.02.102.

[76] Vajeeston, P., Ravindran, P., Hauback, B. C., Fjellvag, H., Kjekshus, A:, Furuseth, S., Hanfland, M. (2006). Structural stability and pressure-induced phase transitions in MgH_2. Journal of Physical Review B, Vol. 73, pp. 224101-8 https://doi.org/ 10.1103/PhysRevB.73.224102.

[77] Yartys, V. A. et al (2019). Magnesium based materials for hydrogen based energy storage: Past, present and future. International Journal of Hydrogen Energy, Vol. 44, pp. 7809-7859.

https://doi.org/10.1016/j.ijhydene.2018.12.212.

[78] Aldridge, F. T. (1985). Gas chromatographic separation of hydrogen isotopes using metal hydrides. Journal of the Less-Common Metals, Vol. 108, pp. 131-150. https://doi.org/10.2172/6753644.

[79] Ponthieu, M., Cuevas, F., Fernandez, J. F., Laversenne, L., Porcher, F., Latroche, M. (2013). Structural Properties and Reversible Deuterium Loading of MgD_2-TiD_2 Nanocomposites. The Journal of Physical Chemistry C, Vol. 117, pp. 18851-18862. https://doi.org/10.1021/jp405803x.

[80] Leardini, F., Ares, J.R., Fernandez, J. F., Bodega, J., Sanchez, C. (2011). An investigation on the thermodynamics and kinetics of magnesium hydride decomposition based on isotope effects. International Journal of hydrogen energy, Vol. 36, pp. 8351-8357. https://doi.org/10.1016/j.ijhydene.2011.04.069.

[81] Jones, P. M. S., Southall, J., Goodhead, K. (1964). The Thermal Stability of Metal Hydrides. Part 1: Rate Earth and Yttrium Hydrides and Deuterides. Technical report, United Kingdom Atomic Energy Authority, O-22/64 (Aldermaston). https://www.osti.gov/servlets/purl/4063536
No doi found (accessed 05.05.2023)

[82] Begun, G. M., Land, J. F., Beil, J. T. (1980). High temperature equilibrium measurements of the yttrium-hydrogen isotope (H_2, D_2, T_2) systems. The Journal of Chemical Physics, Vol. 72, pp. 2959-2966. https://doi.org/10.1063/1.439496.

[83] Lässer, R., Meuffels, P., Feenstra, R. (1988). Datenbank der Löslichkeiten der Wasserstoffisotope Protium (H), Deuterium (D) und Tritium (T) in den Metallen V, Nb, Ta, Pd und den Legierungen $V_{1-x}Nb_x$, $V_{1-x}Ta_x$, $Nb_{1-x}Mo_x$, $Pd_{1-x}Ag_x$, JUEL-2183, ISSN: 0366-0885 (Jülich).
No doi found (accessed 05.05.2022).

[84] Steel, S. (2018). Study of the Properties of Hydrogen and Deuterium in Beta Phase Palladium Hydride and Deuteride. Doctoral Dissertation, university of Salford Manchester, Engineering and Physical Sciences Research Council (EPSRC). http://usir.salford.ac.uk/id/eprint/46767/.

[85] Lässer, R. (1985). Isotope dependence of phase boundaries in the PdH, PdD and PdT systems. Journal of Physics and Chemistry of Solids, Vol. 46, No. 1, pp- 33-37. https://doi.org/10.1016/0022-3697(85)90192-1.

[86] Alefeld, G. et al (2014). Hydrogen in Metals 2. Springer, ISBN: 9783662311981 (Berlin).

[87] Laesser, R. (1982). Palladium-tritium system. Physical Review B: Condensed Matter and Materials Physics, Vol. 25, pp. 3517-3519. https://doi.org/10.1103/PhysRevB.26.3517.

[88] Wiswall, R. H., Reilly, J. J. (1972). Inverse Hydrogen Isotope Effects in some Metal Hydride Systems. Inorganic Chemistry, Vol. 11, pp. 1691-1696. https://doi.org/10.1021/ic50113a050.

[89] Hatano, Y. Livshits, A., Nakamura, Y., Busynuk, A., Alimov, V., Hirom, C. Ohyabu, N., Watanabe, K. (2006). Influence of oxygen and carbon on performance of superpermeable membranes. Fusion Engineering and Design, Vol. 81, pp. 771-776. https://.doi.org/10.1016/j.fusengdes.2005.06.368.

[90] Huo, Y. et al (2019). The effect of surface oxides and grain sizes on the deuterium permeation behaviour of niobium membranes. Fusion Engineering and Design, Vol. 149, pp. 1-11. https://doi.org/10.1016/j.fusengdes.2019.111340.

[91] Devillers, M., Sirch, M., Bredendiek-Kämper, S., Penzhorn, R.-D. (1990), Characterization of the ZrCo-Hydrogen Systems in view of its use for Tritium Storage. Chemistry of Materials, Vol. 2, pp. 255-262. https://doi.org/10.1021/cm00009a014.

[92] Shirasaki, K., Kuriiwa, T., Tamura, T., Kamegawa, A., Takamura, H., Okada, M. (2002). Effects of Al Addition on Structures and Protium Absorption-Desorption Properties of TiCr- Alloys. Materials Transactions, Vol. 43, pp. 1173-1177. https://doi.org/10.2320/matertrans.43.1173.

[93] Betekhtin, V. I., Kadomtsev, A. G., Narykova, M. V. (2017). Effect of the Allotropic Transition in Titanium on its Interatomic Interaction Energy. Technical Physics Letters, Vol. 43, No. 8, pp. 708-711. https://doi.org/10.1134/S1063785017080028.

[94] Motyka, M., Kubiak, K., Sieniawski, J., Ziaja, W. (2014). Phase Transformation and Characterization of α+β Titanium Alloys. Materials Science and Materials Engineering, Vol. 2, pp. 7-36. https://doi.org/10.1016/B978-0-08-096532-1.00202-8.

[95] Baumann, W. (2010). Phase-Transformation Kinetics of $TiCr_2$ Laves Phases. Doctoral Dissertation, University of Stuttgart, Faculty of Chemistry. https://dx.doi.org/10.18419/opus-6746.

[96] Ghosh, G. (2011). Thermodynamic and Kinetic Modeling of the Cr-Ti-V System. Journal of Phase Equilibria, Vol. 23, pp. 310-328. https://doi.org/10.1361/105497102770331569.

[97] Broom, D. P. (2007). The accuracy of hydrogen sorption measurements on potential storage materials. International Journal of Hydrogen Energy, Vol. 32, pp. 4871-4888. https://doi.org/10.1016/j.ijhydene.2007.07.056.

[98] Blach, T. P., Gray, E. A. (2007). Sieverts apparatus and methodology for accurate determination of hydrogen uptake by light-atom hosts. Journal of

Alloys and Compounds, Vol. 446-447, pp. 692-697.
https://doi.org/10.1016/j.jallcom.2006.12.061.

[99] Grote, K.-H., Feldhusen, J. (2011). Dubbel-Taschenbuch für den Maschinenbau. 23rd edition, Springer, ISBN: 978-642-17305-9 (Berlin Heidelberg).

[100] Linde: "Data sheet protium gas bottle", https://produkte.linde-gase.de/reingase_in_druckbehaltern/wasserstoff_5.0.html. accessed: 05.05.2022.

[101] Linde: "Data sheet deuterium gas bottle", https://produkte.linde-gase.de/laserbetriebsgase/deuterium_stabiles-wasserstoff-isotop.html. accessed: 05.05.2022.

[102] Celebi, M., Karakas, K., Ertas, I. E., Kaya, M., Zahmakiran, M. (2017). Palladium nanoparticles decorated graphene oxide: active and reusable nanocatalyst for the catalytic reduction of hexavalent chromium (VI). Journal of Materials Science inc. Nanomaterials & Polymers, Vol. 2, pp. 8312-8319 . https://doi.org/10.1002/slct.201700967.

[103] Dunikov, D. O., Borzenko, V. I., Malyshenko, S. P. (2010). Optimization of Heat Transfer in Metal Hydride Reactor. 18th World Hydrogen Energy Conference (WHEC 2010) Proceedings, Vol. 78-4, ISBN: 978-3-89336-654-5 (Essen).

[104] Dmitriyeva, O., Cantwell, R., McConnell, M. (2012). Mechanisms for Heat Generation during Deuterium and Hydrogen Loading of Palladium Nanostructures. Journal of Condensed Matter Nuclei, Vol. 8, pp. 29-36 ISSN: 2227-3123.

[105] Robinson, I. K. (2015). Computational Studies of Hydrogen in Palladium. Doctoral. Dissertation at the university of Salford, College of Science and Technology. https://doi.org/10.13140/RG.2.2.33376.71682.

[106] Rosa, S. Shmayda, W. T., Sharpe, M. (2020). Investigations of the Hydrogen-Palladium and Deuterium-Palladium Systems. Thesis, Laboratory for Laser Energetics (Rochester). https://www.lle.rochester.edu/index.php/publications-2/high-school-reports/.

[107] Kruijtzer, G. L. (1978). Hydrogen in Magnesium Palladium This Layer Structures. Doctoral Dissertation of the university in Utrecht. ISBN: 978-90-9022403-9.

[108] Nishikawa, M., Shiraishi, T., Murakami, K. (2012). Solubility and Separation factor of protium-deuterium binary component system in Palladium. Journal of Nuclear Science and Technology, Vol. 33:6, pp. 504-510. https://doi.org/10.1080/18811248.1996.9731943.

[109] Luo, W., Cowgill, D. F., Flanagan T. B. (2013). Separation factors for Hydrogen Isotopes in Palladium Hydride. The Journal pf Physical Chemistry, Vol. 117, pp. 13861-13871. https://doi.org/10.1021/jp4032332.

[110] Liu, M., Yang, J.-R., Qin, C., Zhu, X.-L., Wang, H., Zhu, H.-Z-, Yang, J.S., Su, Y.-J. (2017). Tritium aging effects on separation factors in palladium-hydrogen system. Journal of Alloys and Compounds, Vol. 704, pp. 742-747. http://dx.doi.org/10.1016/j.jallcom.2017.01.218.

[111] Homma, H., Saitoh, H., Kamegawa, A., Okada, M. (2002). Hydrogenation Behaviour in Ti-Cr alloys with compositions around $TiCr_2$ Laves Phase. Materials Transactions, Vol. 43, pp. 2741-2747. https://doi.org/10.2320/matertrans.43.2741.

[112] Mihara, S., Sagara, H. (1977). The compressibility factors of hydrogen-methane, hydrogen-ethane and hydrogen-propane gaseous mixtures. Journal of Chemical Engineering of Japan, Vol. 10, pp. 395-399. https://doi.org/10.1252/jcej.10.395.

[113] Delphin Technology: "ProfiMessage", https://www.delphin.de/produkte/mess-und-pruefgeraete/profimessage.html. accessed: 05.05.2022.

[114] Data Loggers "Data acquisition and control system", https://www.dataloggerinc.com/product/profimessage-data-acquisition-system/l. accessed: 05.05.2022.

[115] Xiukui, S., Jian, X., Yiyi, L. (1989). Hydrogen permeation behaviour in austenitic stainless steel. Materials Science and Engineering, Vol. 114, pp. 179-187. https://doi.org/10.1016/0921-5093(89)90857-5.

[116] Lee, S. K., Yun, S.-H., Joo, H. G., Noh, S. J. (2014). Deuterium transport and isotope effects in type 316L stainless steel at high temperatures for nuclear fusion and nuclear hydrogen technology applications. Current Applied Physics, Vol. 14, pp. 1385-1388. http://dx.doi.org/10.1016/j.cap.2014.08.006.

[117] Day, C. (1998). The use of a high-resolution quadrupole gas mass spectrometer system for selective detection of helium and deuterium. Vacuum, Vol. 51, pp. 21-30. https://doi.org/10.1016/s0042-207x(98)00129-8.

[118] Joint Committee for Guides in Metrology (2008). Evaluation of measurement data – guide to the expression of uncertainty in measurement , JCGM 100:2008 https://www.bipm.org/en/committees/jc/jcgm/publications.

Appendix

A1 Selection and comparison of technologies for the IRPR system – pairwise comparison

The most important criterion needed for the IRPR system are evaluated with the pairwise comparison method, see Table A.1. In total, 11 requirements have been identified, which need to be taken into account. With the pairwise comparison method, the requirements are individually and directly compared with each other. For a criterion that is more relevant than another one, it is ranked with a "2", if both are similar important, it is ranked with a "1", and for less important, it is ranked with a "0". All values are summed up and the requirements with the highest total result are the most important ones. Here, safety and environment has been ranked first, directly followed by a high separation factor and low tritium inventory.

Table A.1: Pairwise comparison for the different requirements for the subsystems "Isotope Rebalancing" and "Protium Removal" with the three most important criteria.

	1)	2)	3)	4)	5)	6)	7)	8)	9)	10)	11)
1) Low T_2-Inventory		1	1	0	1	1	0	0	0	0	0
2) High separation factor	1		0	0	1	1	0	0	1	0	0
3) Continuous process	1	2		1	2	2	0	0	0	1	0
4) Non-cryogenic technology	2	2	1		2	2	0	1	1	0	0
5) Safety and environment	1	1	0	0		0	0	0	0	0	0
6) Technical readiness level	1	1	0	0	2		0	1	1	1	0
7) Operational costs	2	2	2	2	2	2		2	2	2	1
8) Operation temperature	2	2	2	1	2	1	0		1	0	0
9) Operating pressure	2	1	2	1	2	1	0	1		0	1
10) Capacity	2	2	1	2	2	1	0	2	2		1
11) Disproportion	2	2	2	2	2	2	1	2	1	1	
Total result	**16**	**16**	11	9	**18**	13	1	9	9	5	3

In total nine technologies are compared with each other for each requirement (see Table A.2 to Table A.12).

Cryo-distillation (CD): The technology ranking showed has low result for this technology if used for DEMO and is therefore not selected.

Magnetically Activated and Guided Isotope Separation (MAGIS): This process is limited to gases with a low vapour pressure at a given chamber temperature.

Since tritium is still gaseous at 25 K, this technology proves difficult for the separation of hydrogen isotopes [9]. This technology has also been ranked low and is therefore not pursued further.

Gaseous Diffusion (GD) and Gas Centrifugation (GCE): Both technologies are used for uranium purification. Gaseous diffusion has an advantage of being a continuous process, which reduces the tritium inventory. Since the technology is based on pure diffusion without any reactions, it is a safe system and can operate under vacuum. The enrichment near the equimolar equilibrium is high, which is good for isotope rebalancing. However, this process is not suitable for protium removal, as high purification involves the need for many stages in sequence, making the process very inefficient. For this reason, this technology on its own cannot be used. Gas centrifugation has proven to be more energy efficient than GD for the purification of uranium [12]. For GCE, the process of "protium removal" is even less suitable, since the separation factor for the hydrogen atoms is even lower than for GD. This technology is therefore eliminated.

Quantum Sieving (QS): So far, a lot of theoretical research has been put into quantum sieving. Some materials have also been tested experimentally, but it is difficult to find a suitable material [13; 14]. The usage of cryogenic temperature is inevitable, as it has been shown that the separating ability of the isotopes decreases with increasing temperature [14].

Thermal Diffusion (TD): Even this technology works for uranium isotopes, hydrogen has the property of very rapid isotope exchange, unlike uranium, making effective separation difficult [15; 16].

Gas chromatography (GC): As it is a batch process, the column has to be heated up after every separation [17; 18]. This technology fulfils important criteria. Materials can be selected that do not require cryogenic temperature. In addition, a high purity can be achieved. However, the process is performed in batch operation, resulting in a long process and thus a high tritium inventory.

Thermal Cycling Absorption Process (TCAP) and Pressure Swing Adsorption (PSA):

The last two technologies have similar properties. Materials can be used in the cryogenic range as well as at higher temperatures. However, from a safety point of view, TCAP has a clear advantage as in the event of an accident, the gas remains stored in the material due to chemisorption, whereas with PSA the gas is only adsorbed to the material due to pressure. In addition, the pressure for PSA is significantly higher than for TCAP, which can result in a higher tritium inventory [19; 22]. In practical terms, the largest challenge comes from the necessity to involve a tritium-compatible compressor (I 6speak about some 10^7 Pa), which is not available. With regard to the

separation efficiency, it is difficult to give a statement, as this depends strongly on the materials used.

All technologies are individually compared with each other based on each criterion and are ranked again with “2”, “1” or “0”. In the end, the results are weighted with the total results from Table A.1, that the most important criterion has more influence.

Table A.2: Pairwise comparison for 1) low tritium inventory for the nine different technologies.

	1)	2)	3)	4)	5)	6)	7)	8)	9)
1) CD		2	2	2	2	2	1	2	1
2) MAGIS	0		1	1	1	1	1	1	1
3) GD	0	1		0	1	1	0	0	0
4) GCE	0	1	2		1	1	0	1	1
5) QS	0	1	1	1		1	0	0	0
6) TD	0	1	1	1	1		1	1	1
7) GC	1	1	2	2	2	1		2	2
8) TCAP	0	1	2	1	2	1	0		0
9) PSA	1	1	2	1	2	1	0	2	
Total result	2	9	13	9	12	9	3	9	6
Total result weighted	32	144	208	144	192	144	48	144	96

Table A.3: Pairwise comparison for 2) high separation factor for the nine different technologies.

	1)	2)	3)	4)	5)	6)	7)	8)	9)
1) CD		0	0	0	0	0	1	1	1
2) MAGIS	2		2	2	2	2	2	2	2
3) GD	2	0		1	2	1	2	2	2
4) GCE	2	0	1		1	1	2	2	2
5) QS	2	0	0	1		1	2	2	2
6) TD	2	0	1	1	1		2	2	2
7) GC	1	0	0	0	0	0		1	1
8) TCAP	1	0	0	0	0	0	1		1
9) PSA	1	0	0	0	0	0	1	1	
Total result	13	0	4	5	6	5	13	13	13
Total result weighted	208	0	64	80	96	80	208	208	208

Table A.4: Pairwise comparison for 3) continuous process for the nine different technologies.

	1)	2)	3)	4)	5)	6)	7)	8)	9)
1) CD		1	2	1	2	2	1	2	2
2) MAGIS	1		1	1	2	1	1	1	1
3) GD	0	0		0	1	1	0	0	0
4) GCE	1	1	2		2	2	0	1	1
5) QS	0	0	1	0		1	0	0	0
6) TD	0	1	1	1	0		0	0	0
7) GC	1	1	2	2	2	1		2	2
8) TCAP	0	1	2	1	2	2	0		1
9) PSA	0	1	2	1	2	2	0	1	
Total result	3	6	13	6	14	12	2	7	7
Total result weighted	33	66	143	66	154	132	22	77	77

Table A.5: Pairwise comparison for 4) non-cryogenic technology for the nine different technologies.

	1)	2)	3)	4)	5)	6)	7)	8)	9)
1) CD		2	2	2	1	2	2	2	2
2) MAGIS	0		1	1	0	1	1	1	1
3) GD	0	1		1	0	1	1	1	1
4) GCE	0	1	1		0	1	1	1	1
5) QS	1	2	2	2		2	2	2	2
6) TD	0	1	1	1	0		1	1	1
7) GC	0	1	1	1	0	1		1	1
8) TCAP	0	1	1	1	0	1	0		1
9) PSA	0	1	1	1	0	1	1	1	
Total result	1	10	10	10	1	10	10	10	10
Total result weighted	90	90	90	90	9	90	90	90	90

Table A.6: Pairwise comparison for 5) safety and environment for the nine different technologies.

	1)	2)	3)	4)	5)	6)	7)	8)	9)
1) CD		2	2	2	1	2	2	2	1
2) MAGIS	0		1	1	0	1	1	1	1
3) GD	0	1		1	1	1	0	1	0
4) GCE	0	1	1		0	1	1	2	1
5) QS	1	2	1	2		2	2	2	1
6) TD	0	1	1	1	0		1	2	1
7) GC	0	1	2	1	0	1		1	0
8) TCAP	0	1	1	0	0	0	1		0
9) PSA	1	1	2	1	1	1	2	2	
Total result	2	10	11	9	3	9	10	13	5
Total result weighted	36	180	198	162	54	162	180	234	90

Table A.7: Pairwise comparison for 6) technical readiness level for the nine different technologies.

	1)	2)	3)	4)	5)	6)	7)	8)	9)
1) CD		0	0	0	0	0	1	0	0
2) MAGIS	2		2	2	2	2	2	2	2
3) GD	2	0		1	1	1	2	1	1
4) GCE	2	0	1		0	1	2	1	1
5) QS	2	0	1	1		1	2	1	1
6) TD	2	0	1	1	1		2	1	1
7) GC	1	0	0	0	0	0		0	0
8) TCAP	2	0	1	1	1	1	2		1
9) PSA	2	0	1	1	1	1	2	1	
Total result	15	0	7	7	6	7	15	7	7
Total result weighted	195	0	91	91	78	91	195	91	91

Table A.8: Pairwise comparison for 7) operational costs for the nine different technologies.

	1)	2)	3)	4)	5)	6)	7)	8)	9)
1) CD		2	2	2	1	2	2	1	2
2) MAGIS	0		1	1	1	1	1	1	1
3) GD	0	1		0	0	1	0	0	0
4) GCE	0	1	2		0	1	0	0	0
5) QS	1	1	2	1		2	1	1	1
6) TD	0	1	1	1	0		0	0	0
7) GC	0	1	2	2	1	2		1	1
8) TCAP	1	1	2	2	1	2	1		1
9) PSA	0	1	2	2	1	2	1	1	
Total result	2	9	14	11	5	13	6	5	6
Total result weighted	2	9	14	11	5	13	6	5	6

Table A.9: Pairwise comparison for 8) operation temperature for the nine different technologies.

	1)	2)	3)	4)	5)	6)	7)	8)	9)
1) CD		2	2	2	1	1	2	2	2
2) MAGIS	0		1	1	0	0	1	1	1
3) GD	0	1		1	0	0	1	1	1
4) GCE	0	1	1		0	0	1	1	1
5) QS	1	2	2	2		1	2	2	2
6) TD	1	2	2	2	1		2	2	2
7) GC	0	1	1	1	0	0		1	2
8) TCAP	0	1	1	1	0	0	1		2
9) PSA	0	1	1	1	0	0	0	0	
Total result	2	11	11	11	2	2	10	10	13
Total result weighted	18	99	99	99	18	18	90	90	117

Table A.10: Pairwise comparison for 9) operation pressure for the nine different technologies.

	1)	2)	3)	4)	5)	6)	7)	8)	9)
1) CD		2	2	1	1	1	1	1	0
2) MAGIS	0		1	1	1	1	0	0	0
3) GD	0	1		0	1	1	0	0	0
4) GCE	1	1	2		1	1	1	1	0
5) QS	1	1	1	1		1	1	1	0
6) TD	1	1	1	1	1		1	1	0
7) GC	1	2	2	1	1	1		1	0
8) TCAP	1	2	2	1	1	1	1		0
9) PSA	2	2	2	2	2	2	2	2	
Total result	7	12	13	8	9	9	7	7	0
Total result weighted	63	107	117	72	81	81	63	63	0

Table A.11: Pairwise comparison for 10) capacity for the nine different technologies.

	1)	2)	3)	4)	5)	6)	7)	8)	9)
1) CD		0	0	0	0	0	0	1	1
2) MAGIS	2		2	2	2	2	2	2	2
3) GD	2	0		1	1	1	2	2	2
4) GCE	2	0	1		1	1	2	2	2
5) QS	2	0	1	1		1	2	2	2
6) TD	2	0	1	1	1		2	2	2
7) GC	2	0	0	0	0	0		1	1
8) TCAP	1	0	0	0	0	0	1		0
9) PSA	1	0	0	0	0	0	1	2	
Total result	14	0	5	5	5	5	12	14	12
Total result weighted	70	0	25	25	25	25	60	70	60

Table A.12: Pairwise comparison for 11) disproportion for the nine different technologies.

	1)	2)	3)	4)	5)	6)	7)	8)	9)
1) CD		0	1	1	1	1	1	1	1
2) MAGIS	2		1	1	1	1	1	1	1
3) GD	1	1		1	1	1	1	1	1
4) GCE	1	1	1		1	1	1	1	1
5) QS	1	1	1	1		1	1	1	1
6) TD	1	1	1	1	1		1	1	1
7) GC	1	1	1	1	1	1		1	1
8) TCAP	1	1	1	1	1	1	1		1
9) PSA	1	1	1	1	1	1	1	1	
Total result	9	7	8	8	8	8	8	8	8
Total result weighted	27	21	24	24	24	24	24	24	24

Table A.13 gives an overview of all results. The technology TCAP has been ranked first, followed by a gaseous diffusion (GD).

Table A.13: Pairwise comparison for the different technologies, ranked with the weighted requirements.

	CD	MAGIS	GD	GCE	QS	TD	GC	**TCAP**	PSA
1) Low T_2-Inventory	32	144	208	144	192	144	48	144	96
2) High separation factor	208	0	64	80	96	80	208	208	208
3) Continuous process	33	66	143	66	154	132	22	77	77
4) Non-cryogenic technology	9	90	90	90	9	90	90	90	90
5) Safety and environment	36	180	198	162	54	162	180	234	90
6) Technical readiness level	195	0	91	91	78	91	195	91	91
7) Operational costs	2	9	14	11	5	13	6	5	6
8) Operation temperature	18	99	99	99	18	18	90	90	117
9) Operating pressure	63	108	117	72	81	81	63	63	0
10) Capacity	70	0	25	25	25	25	60	70	60
11) Disproportion	27	21	24	24	24	24	24	24	24
Total result	693 ≙ 35 %	717 ≙ 36 %	1073 ≙ 54 %	864 ≙ 44 %	736 ≙ 37 %	860 ≙ 43 %	986 ≙ 50 %	**1096** ≙ 55 %	859 ≙ 43 %

A2 Derivations and Results of Uncertainty Calculation

Uncertainty calculations are important to assess the reliability of empirical results. This section discusses the uncertainty analysis for the experiments conducted in this work. All equations and assumptions are based on the "Guide to the expression of uncertainty in measurement" (GUM) [118].

Every experimental measurement is subject to uncertainty. Two types of uncertainty exist: statistic (also called random) and systematic uncertainty of measurements. The statistic uncertainty of measurements is a result of an observer-dependent measuring process. In general errors in measurement are inevitable, and can be estimated through revision of tests and proper evaluations. The systematic uncertainty of measurement is caused by the imprecision of the gauges as well as changes in the experimental conditions.

Furthermore, one can distinguish between two types of evaluations to assess errors: type A and type B. Type A is "a method of evaluation of uncertainty by the statistical analysis of series of observation". Type B is "a method of evaluation of uncertainty by means other than the statistical analysis of series of observations". Both of these errors are relevant to our analysis. The focus here is on type A, as this constitutes the main part of the uncertainty calculation. Type B will be considered afterwards.

Type A evaluations for sensor readings commence: There are two influences on sensor readings: i) Sensor-specific behaviour, which can be determined from the manufacturer's specifications, and ii) Variation of the measured values. An example for i) Using a 10^6 Pa capacitance manometer, with the coherences stated from the manufacturer, is given as:

$$\Delta p = \sqrt{\Delta p_{R,FS}{}^2 + \Delta p_{A,Rdg}{}^2 + \left((p_{TZ,FS} + p_{TS,Rdg}) \cdot (T_{1.2} - 296\,K)\right)^2}, \qquad \text{(A1)}$$

with dependencies on the resolution of full scale (10^6 Pa): ($\Delta p_{R,FS}$ = f($0.00001 \cdot p_{FS}$), accuracy of reading (the actual value during an experiment) ($\Delta p_{A,Rdg}$ = f $0.0012 \cdot p_{Rdg}$), temperature coefficient zero of full scale ($\Delta p_{TZ,FS}$ = f($\frac{0.00002 \cdot p_{FS}}{T_{Cal}}$) and temperature coefficient span of reading $\Delta p_{TS,Rdg}$ = f ($\frac{0.0002 \cdot p_{Rdg.}}{T_{Cal}}$), with a calibration at 296 K. A K-element is attached to every pressure sensor in order to measure the influence of the temperature during the test and thus to be able to evaluate it.

To quantify the variance (ii), descriptive statistics can be used. The first one is the arithmetic average $\hat{\mu}$ or $\bar{q}$ to estimate the mean of the measurement distribution:

$$\hat{\mu} = \bar{q} = \frac{1}{n}\sum_{k=1}^{n} q_k, \qquad \text{(A2)}$$

with n for the number of independent observations and q_k for the respective values. Based on this, the standard deviation can be estimated by

$$\bar{\sigma} = s(q_k) = \sqrt{\frac{1}{n-1} \cdot \sum_{j=1}^{n} (q_j - \bar{q})^2}. \quad \text{(A3)}$$

The total uncertainty of a sensor is the square root of the sum of sensor specifics and the estimated standard deviation.

If the uncertainty of a parameter (as for the concentration), depends on several factors (as pressure and temperature), which are independent from each other, a partial derivation can be used, to single out the contribution of the individual factors (X_k) to the overall error. Again, the individual results can be summed in the square root to obtain the total uncertainty. :

$$\Delta Y = \sqrt{\sum_{k=1}^{N} (\frac{dY}{dX_k})^2 \cdot \Delta {X_k}^2 + \sum_{i=1}^{N} s(q_k)}. \quad \text{(A4)}$$

The ultimate measure of interest is a coverage factor that yields confidence values on the measured values. Since measurement errors often follow a normal distribution, this factor indicates the probability with which the calculated uncertainty is within the interval. The coverage factor depends on the number of observations and the selected fraction of distribution and can be selected from a table in GUM.

Type B evaluations require a different approach. This is because statistics are not useful with a single observation. In this thesis, it is used for the uncertainty calculation of the mass spectrometer, which is used for the analysis of the separation.

The following equation is defined for the degree of freedom, and is applied onto the manufacturer's declaration of the mass spectrometer:

$$\nu_i = 0.5 \cdot \frac{u^2(x_i)}{\sigma^2[u(x_i)]} \approx 0.5 \cdot [\frac{\Delta u_B(x_i)}{u(x_i)}]^{-2}. \quad \text{(A5)}$$

In contrast to type A errors, the evaluation of uncertainty does not depend on a statistical analysis. Rather, the standard uncertainty $u_B(x_i)$ needs to be assessed based on auxiliary information such as preceding experimental data, experience of the behaviour of the sensor or machine and specifications from the manufacturer.

Calculation of components

Some components (as pressure sensors and mass flow controllers) use full scale (F.S.) and reading (Rdg.), whereby with F.S. the maximum value and with Rdg. the actual value is meant.

For all sensors from type A, two influences arise: i) Sensor-specific behaviour and ii) variation of the measured values. Both have an impact on the uncertainty and are taken into account by the sum of both influences under the square root.

The derivations and its explanations are separated into the individual components. The resulting values are displayed in the next subchapters, according to the different test rigs.

As the accuracy is also a function of the temperature, at every sensor additional temperature sensors have been implemented in order to measure the actual temperature reaching the component.

Pressure sensors – Capacitance manometer:

This uncertainty calculation can be applied to both test rigs, MAIA and HESTIA. For MAIA, sensors with a full scale of 10^6 Pa are used, for HESTIA 10^6 Pa as well as 10^3 Pa. For the sensor-specific behaviour four factors influence the accuracy: i) Resolution with 0.001 % of F.S., ii) Accuracy with 0.12 % of Rdg., iii) Temperature coefficient zero with 0.002 % of F.S./K and iv) Temperature coefficient span with 0.02 % of Rdg./K. The sensors have been calibrated at 296 K. For the variation, 50 values have been taken. The uncertainty is calculated as follows:

$$\Delta p = \sqrt{\begin{matrix}(0.00001 \cdot FS)^2 + (0.0012 \cdot Rdg)^2 + \left(0.00002 \cdot FS \cdot (T - 296K)\right)^2 \\ +(0.0002 \cdot Rdg \cdot (T - 296K))^2 + \overline{\sigma}^2\end{matrix}}. \quad \text{(A6)}$$

Temperature sensor:

The uncertainty calculation for the sheath resistance thermometer in K, which is used in MAIA and HESTIA, is calculated with:

$$\Delta T = 0.001 \cdot T + 0.1. \quad \text{(A7)}$$

Volumes:

To have an exact value for the volume is of high importance in order to achieve results with a low uncertainty, as it has a direct influence on the concentration. In this section, all calibrated volumes are explained individually. All results are listed in the end of this section in Table A.3 for MAIA and Table A.4 for HESTIA volumes.

For both test rigs, the method of pressure balancing has been applied, as it is the most accurate method for the dimensions and geometry of the facilities (e.g. compared to calibration with distilled water). Thereby a previous calibrated volume is attached to the vessel and filled with argon. By opening a valve between the vessels, a pressure balancing leads to a value for the unknown volume by applying the Boyle-Mariotte law. For MAIA, a calibration volume "TOM" has been used for applying the pressure balancing method for the pre vessel and the vessel. It is located between the dosage and the pre-vessel and has been disassembled after the calibration. TOM consists of a 300 ml cylinder, a capacitance manometer and two valves. This volume has previously been calibrated using the distilled water method (measure volume filled (m_{H2O}) and empty (m_0)) and calculated as follows:

$$V_{TOM} = \frac{m_{H_2O} - m_0}{\rho_{H_2O}}. \quad \text{(A8)}$$

The two influences on the uncertainty are i) Imprecision of the scale, which has been calibrated (Error of calibration weight for scale with 0.0001·m) and ii) Error of temperature sensor for determination of density with 0.00059·ϱ. The calculation is including the mentioned sensors dependent influences as well as the standard deviation, as the weighting has been repeated several times (three times empty, five times with distilled water):

$$\Delta\bar{V}_{TOM} = \sqrt{\left(\frac{1}{\rho_{H_2O}} \cdot \Delta\bar{m}_{H_2O}\right)^2 + \left(-\frac{1}{\rho_{H_2O}} \cdot \Delta\bar{m}_0\right)^2 + \left(-\frac{\bar{m}_{H_2O} - \bar{m}_0}{{\rho_{H_2O}}^2} \cdot \Delta\rho_{H_2O}\right)^2 + {s_{V_{TOM}}}^2}. \quad \text{(A9)}$$

The volume of the pre vessel is calculated by the pressure and the TOM-volume:

$$V_{PV} = \frac{p_{V2.1,closed}}{p_{V2.1,open}} \cdot V_{TOM} - V_{TOM}. \quad \text{(A10)}$$

The two influences of the pre vessel are i) Uncertainty of the TOM-volume with 0.0063·V_{TOM} and ii) Uncertainty of the capacitance manometer. Also here, the sensor dependent and user dependent errors have to be taken into account. Since the pressure is not linear, the uncertainties have to be calculated for each measurement with the partially deviation and afterwards the mean value can be determined, including the standard deviation:

$$\Delta\bar{V}_{PV} = \sqrt{\frac{1}{n}\sum_{i=1}^{n} \sqrt{\left(\left(\frac{p_{V,\,closed}}{p_{V,\,open}} - 1\right) \cdot \Delta V_{TOM}\right)^2 + \left(\frac{V_{TOM}}{p_{V,\,open}} \cdot \Delta p_{V,\,closed}\right)^2 + \left(-\frac{p_{V,\,closed}}{{p_{V,\,open}}^2} \cdot V_{TOM} \cdot \Delta p_{V,\,open}\right)^2}} + s_{V_{PV}}. \quad \text{(A11)}$$

The same approach applies for the calibration of the vessel, the pre vessel is simply added:

$$V_V = \frac{p_{V2.1,closed}}{p_{V2.1,open}} \cdot V_{TOM} - V_{TOM} - V_{PV} \quad \text{(A12)}$$

For the uncertainty calculation the influence of the pre vessel needs to be added, with i) 0.0138·V_{PV}. This results into the equation for the uncertainty of the vessel:

$$\Delta\bar{V}_V = \sqrt{\frac{1}{n}\sum_{i=1}^{n} \sqrt{\left(\left(\frac{p_{V,\,closed}}{p_{V,\,open}} - 1\right) \cdot \Delta V_{TOM}\right)^2 + \left(\frac{V_{TOM}}{p_{V,\,open}} \cdot \Delta p_{V,\,closed}\right)^2 + \left(-\frac{p_{V,\,closed}}{{p_{V,\,open}}^2} \cdot V_{TOM} \cdot \Delta p_{V,\,open}\right)^2 + {\Delta V_{PV}}^2}} + s_{V_{PV}}. \quad \text{(A13)}$$

After the volumes have been calibrated, bulk material has been filled in the vessel and the volume of the vessel excluding the volume of the bulk material has been determined with the same approach as described above. This value is needed for the calculation of the concentration in the end.

Table A.14: Calibrated volumes for MAIA including their uncertainties.

Vessel	Calibrated volume (ml)	Applied calibration method
TOM	312.71 ± 1.96 (0.63 %)	1. Distilled water
Pre vessel	32.00 ± 0.44 (1.38 %)	3. Pressure balancing
Vessel	73.7 ± 0.93 (1.26 %)	3. Pressure balancing
Vessel – filled with Pd	72.77 ± 0.63 (0.87 %)	3. Pressure balancing
Vessel – filled with $TiCr_{1.5}$	72.57 ± 0.64 (0.88 %)	3. Pressure balancing

Table A.15: Calibrated volumes for HESTIA including their uncertainties.

Vessel	Calibrated volume (ml)	Applied calibration method
Calibration volume	2241.75 ± 0.002	1. Distilled water
Column 1	271.2 ± 3.01 (1.11 %)	3. Pressure balancing
Column 2	390.32 ± 3.39 (0.87 %)	3. Pressure balancing

Mass flow controller (MFC):

This uncertainty calculation can be applied to both test rigs, MAIA and HESTIA. Different ranges of MFC, up to 100 sccm and 1000 sccm are applied. For both controllers, same conditions apply. The control range is 2 % to 100 % of full range. Three factors influence the accuracy: i) Repeatability with 0.3 % of reading, ii) Resolution with 0.1 % of full scale and iii) Accuracy with 1 % of setpoint 20-100 % of FS and 0.2 % for 2-20 % of FS:

$$\Delta\bar{F}_{>20} = \sqrt{(0.003 \cdot Rdg)^2 + (0.001 \cdot FS)^2 + (0.01 \cdot Rdg)^2}. \quad \text{(A14)}$$

$$\Delta\bar{F}_{<20} = \sqrt{(0.003 \cdot Rdg)^2 + (0.001 \cdot FS)^2 + (0.002 \cdot Rdg)^2}. \quad \text{(A15)}$$

Concentration:

This calculation is necessary to calculate the uncertainty for the PCT diagrams in MAIA, parts of it can also be used for HESTIA.

$$\Delta\bar{c}_{i+1} = \sqrt{\begin{aligned}&\frac{1}{n}\cdot\sum_{i=1}^{n}\left(2\cdot\frac{V_{PV}}{R\cdot T_{amb}}\cdot\frac{M_{Pd}}{m_{Pd}}\cdot\Delta p_{V_{23,closed,i+1}}\right)^2+\left(2\cdot(-\frac{(V_{PV}+V_{V-BM})}{R\cdot T_{amb}}+\frac{V_{V-BM}}{R\cdot T_{elev}})\cdot\frac{M_{Pd}}{m_{Pd}}\cdot\Delta p_{V_{23,open,i+1}}\right)^2\\&+\left(2\cdot\frac{V_{V-BM}}{R\cdot T_{amb}}\cdot\frac{M_{Pd}}{m_{Pd}}\Delta p_{V_{23,open,i}}\right)^2+\left(-2\cdot\frac{V_{V-BM}}{R\cdot T_{elev}}\cdot\frac{M_{Pd}}{m_{Pd}}\cdot\Delta p_{V_{23,\mathrm{closed},i+1,\mathrm{T}}}\right)^2\\&+\left(2\cdot\frac{p_{V23,closed,i+1}-p_{V23,open,i+1}}{R\cdot T_{amb}}\cdot\frac{M_{Pd}}{m_{Pd}}\cdot\Delta V_{PV}\right)^2\\&+\left(\left(2\cdot\frac{-p_{V23,open,i+1}+p_{V23,open,i}}{R\cdot T_{amb}}-2\cdot\frac{\left(p_{V23,closed,i+1,T}-p_{V23,open,i+1}\right)}{R\cdot T_{elev}}\right)\cdot\frac{M_{Pd}}{m_{Pd}}\cdot\Delta V_{V-BM}\right)^2\\&+\left(\begin{aligned}&(2\cdot\frac{p_{V23,closed,i+1}\cdot V_{PV}-\left[p_{V23,open,i+1}\cdot(V_{PV}+V_{V-BM})-p_{V23,open,i}\cdot V_{V-BM}\right]}{R\cdot T_{amb}\cdot M_{Pd}}\\&-2\cdot\frac{\left(p_{V23,closed,i+1,T}-p_{V23,open,i+1}\right)\cdot V_{V-BM}}{R\cdot T_{elev}})\cdot\frac{M_{Pd}}{\mathrm{m}_{Pd}^2}\cdot\Delta m_{Pd}\end{aligned}\right)^2+\\&\left(2\cdot\frac{p_{V23,closed,i+1}\cdot V_{PV}-\left[p_{V23,open,i+1}\cdot(V_{PV}+V_{V-BM})-p_{V23,open,i}\cdot V_{V-BM}\right]}{R\cdot T_{amb}^2}\cdot\frac{M_{Pd}}{m_{Pd}}\cdot\Delta T\right)^2+\\&(2\cdot\frac{\left(p_{V23,closed,i+1,T}-p_{V23,open,i+1}\right)\cdot V_{V-BM}}{R\cdot T_{elev}^2}\cdot\frac{M_{Pd}}{m_{Pd}}\cdot\Delta T_{elev})^2+\Delta\bar{c}_i{}^2\end{aligned}} \tag{A16}$$

Gas inventory

The total gas inventory in HESTIA is calculated based on the flow from the MFC, with its calculation:

$$I=\frac{F\cdot C_f\cdot t-p\cdot V_0}{R\cdot T}, \tag{A17}$$

with a corrections factor C_f in (mbar·l·s^{-1}·sccm^{-1}), which corrects the unit of the MFC. It is calculated with:

$$C_f=1.013\cdot\frac{\frac{T}{K}}{273K\cdot 60}. \tag{A18}$$

This factor can be calculated based on the applied temperature. When the valve towards the column is closed, some gas remains in the supply pipe (V_0) which has to be subtracted. The uncertainty calculation for the inventory is the following:

$$\Delta\bar{I}=\sqrt{\begin{aligned}&\left(\frac{C_f\cdot t}{R\cdot T}\cdot\Delta F\right)^2+\left(\frac{F\cdot t\cdot 1.013\cdot\frac{60}{273K}}{R\cdot T}\cdot\Delta T\right)^2+\left(-\frac{V_0}{R\cdot T}\cdot\Delta p\right)^2+\left(-\frac{p}{R\cdot T}\cdot\Delta V_0\right)^2\\&+\left(\frac{F\cdot C_f\cdot t-p\cdot V_0}{R\cdot T^2}\cdot\Delta T\right)^2\end{aligned}}. \tag{A19}$$

A3 MAIA – List of Components used

Table A.16: List of components and their properties in MAIA.

Abbr.	Type	Model	Properties
BM1	Buk material	Palladium	• 30 wt-% palladium coated on γ-Al2O3
		Titanium-chromium	• 40 at.-% Ti, 60 at.-% Cr
	Hydrogen sensor	Polytron 7000 - Dräger	
F1.1	Mass flow controller	GE50A - mks	• 8mm connection • 100sccm range • Calibrated
M2.1	Pre vessel	Swagelok T-piece 8mm	• 32.00 ± 0.44 ml
M3.1 M3.2 M3.3	Filters	Swagelok T-filter	•
M4.1	vessel	Swagelok T-piece 8mm	• 73.07 ± 0.92 ml
P1.1 P1.2	Capacitance Manometer	Baratron 627F - mks	• Measurement range: 1 mbar ± 0.1 mbar – 10000 mbar ± 12 mbar • Heated to 45 °C
P2.1	Pressure transducer		• Measurement range: 0 – 40 mbar
PR2.1	Pressure regulator	KPR - Swagelok	• 8mm connection • Pressure range outlet: 0 – 3.4 bar • Maximum pressure inlet: 34.4 bar • Discharge coefficient: 0.06Cv
T1.1	Sheath resistance thermometer	Type 17 – TC direct	• calibrated range: 263 – 473 K • 293 K ± 0.12 K – 473 K ± 0.3 K
V2.1 V2.2 V2.3 V2.4	Bellows valve	SS-12BG-MM-5CM - Swagelok	• Leakage rate: 10^{-9} mbar·l/s • Pneumatic

V2.5			
V2.6			
V3.1	Bellows valve	SS-12BG-MM - Swagelok	• Leakage rate: 10^{-9} mbar·l/s
V3.2			• Hand operation
V3.3			
V4.1	Ball valve	SS-43GS8MM - Swagelok	• Hand operation
V4.2			• 8mm connection
VP1.1	Pumping station	T-Station 85H Dry - Edwards	• Membrane pump • Turbo molecular pump

A4 MAIA – List of terms for concentration calculation

Table A.17: Overview of the different terms including a schematic description for calculation of the amount of hydrogen absorbed in the bulk material.

Schematic description	Term for amount of hydrogen
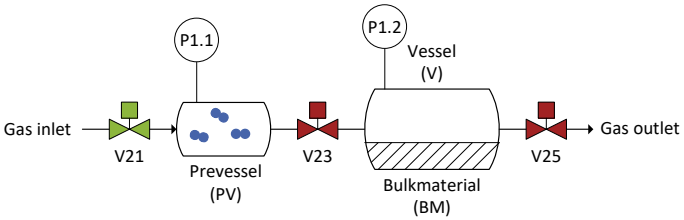	a) $2 \cdot \frac{p_{V23,closed,i+1} \cdot V_{PV}}{R \cdot T_{amb}}$
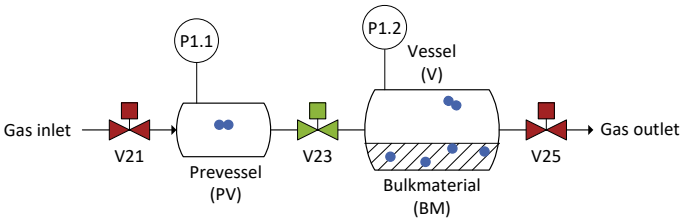	b) $2 \cdot \frac{[p_{V23,open,i+1} \cdot (V_{PV} + V_{V-BM})]}{R \cdot T_{amb}}$
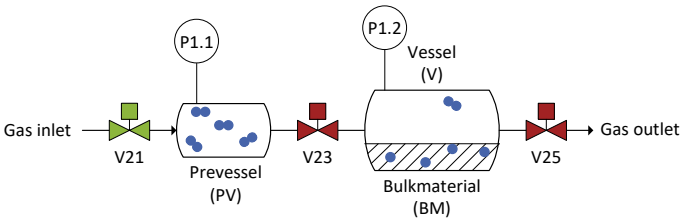	c) $2 \cdot \frac{[-p_{V23,open,i} \cdot V_{V-BM}]}{R \cdot T_{amb}}$
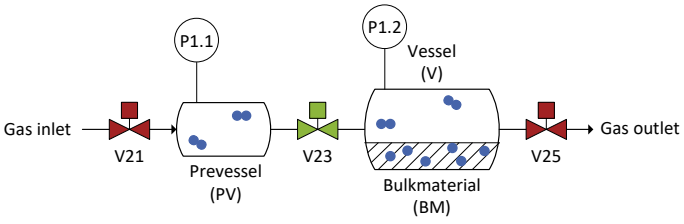	
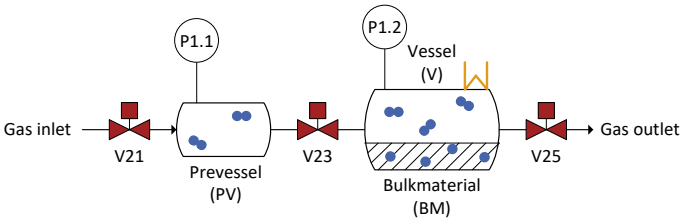	d) $2 \cdot \frac{(p_{V23,closed,i+1,T} - p_{V23,open,i+1}) \cdot V_{V-BM}}{R \cdot T_{elev}}$

A5 MAIA – experimental values

In the following, the PCT uncertainties for protium and deuterium in palladium and titanium-chromium are presented. In each case, a graph is shown to illustrate the magnitude of the error based on three temperatures and then the values are listed in a table. The higher the pressure, the more accurate the pressure sensors. The worst case is therefore at low pressures. For the concentrations, the values become less accurate in theory as the concentration increases, since the values, and thus also the errors, add up. However, since the errors are relatively small, the values are relatively stable. Since the best and worst case assumption is presented for both values, the specification of these data is completely sufficient. The uncertainties of all other curves fall in between.

i) Protium in Palladium:

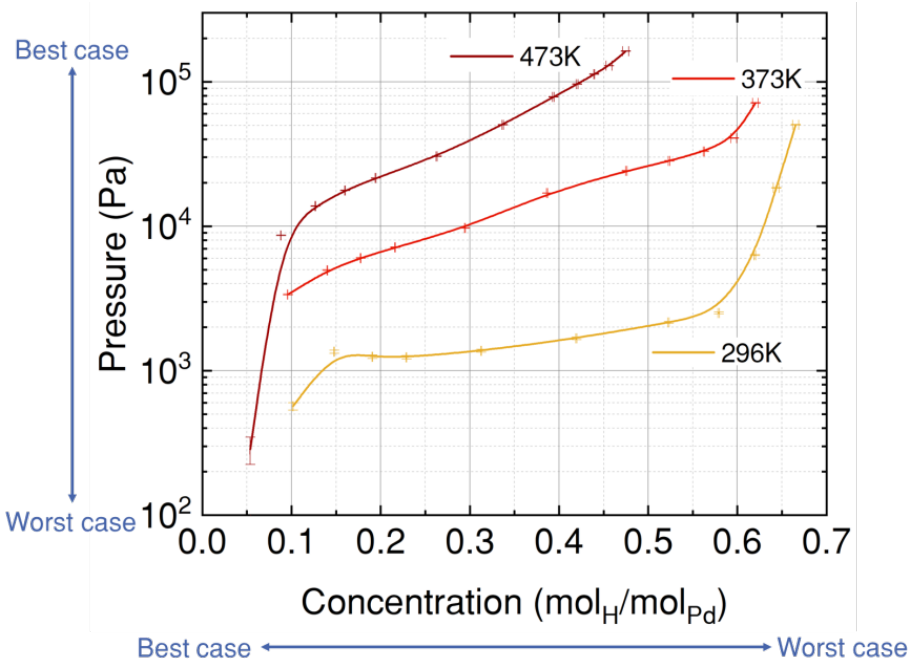

Figure A.1: Experimental data and its uncertainties of H_2-Pd at 296 K, 373 K and 473 K.

Table A.18: Overview of experimental values of the Pd-H_2 system at 296 K including its uncertainties.

p (Pa)	c (mol_H/mol_{Pd})	T (K)
0 ± 0 (≙ 0 %)	$0.01 \pm 4.22 \cdot 10^{-5}$ (≙ 0.41 %)	298.99 ± 0.13 (≙ 0.49 %)
0 ± 0 (≙ 0 %)	$0.054 \pm 1.84 \cdot 10^{-4}$ (≙ 0.34 %)	297.56 ± 0.12 (≙ 0.51 %)
$5.67 \cdot 10^2 \pm 33.1$ (≙ 5.84 %)	$0.102 \pm 2.81 \cdot 10^{-4}$ (≙ 0.28 %)	296.16 ± 0.12 (≙ 0.53 %)
$1.35 \cdot 10^3 \pm 33.49$ (≙ 2.47 %)	$0.148 \pm 3.51 \cdot 10^{-4}$ (≙ 0.24 %)	299.65 ± 0.13 (≙ 0.5 %)
$1.25 \cdot 10^3 \pm 33.69$ (≙ 2.69 %)	$0.191 \pm 3.98 \cdot 10^{-4}$ (≙ 0.21 %)	296.7 ± 0.2 (≙ 0.84 %)

$1.24{\cdot}10^{3} \pm 33.37$ (≙ 2.69 %)	$0.229 \pm 4.32{\cdot}10^{-4}$ (≙ 0.19 %)	296.01 ± 0.12 (≙ 0.54 %)
$1.37{\cdot}10^{3} \pm 33.47$ (≙ 2.44 %)	$0.313 \pm 5.64{\cdot}10^{-4}$ (≙ 0.18 %)	295.1 ± 0.12 (≙ 0.56 %)
$1.67{\cdot}10^{3} \pm 33.75$ (≙ 2.02 %)	$0.42 \pm 7.28{\cdot}10^{-4}$ (≙ 0.17 %)	295.58 ± 0.12 (≙ 0.55 %)
$2.16{\cdot}10^{3} \pm 34.11$ (≙ 1.58 %)	$0.523 \pm 8.55{\cdot}10^{-4}$ (≙ 0.16 %)	296.44 ± 0.12 (≙ 0.53 %)
$2.51{\cdot}10^{3} \pm 34.47$ (≙ 1.37 %)	$0.579 \pm 8.91{\cdot}10^{-4}$ (≙ 0.15 %)	295.37 ± 0.12 (≙ 0.55 %)
6302.44 ± 41.55 (≙ 0.66 %)	$0.62 \pm 9.19{\cdot}10^{-4}$ (≙ 0.15 %)	299.14 ± 0.13 (≙ 0.49 %)
$1.84{\cdot}10^{4} \pm 79.97$ (≙ 0.43 %)	$0.644 \pm 3.19{\cdot}10^{-3}$ (≙ 0.5 %)	297.0 ± 0.12 (≙ 0.52 %)
$5.04{\cdot}10^{4} \pm 201.98$ (≙ 0.4 %)	$0.665 \pm 3.25{\cdot}10^{-3}$ (≙ 0.5 %)	295.02 ± 0.12 (≙ 0.56 %)

Table A.19: Overview of experimental values of the Pd-H_2 system at 373 K including its uncertainties.

p (Pa)	c (mol_H/mol_{Pd})	T (K)
0 ± 0 (≙ 0 %)	$0.01 \pm 4.22{\cdot}10^{-5}$ (≙ 0.41 %)	372.96 ± 0.2 (≙ 0.2 %)
0 ± 0 (≙ 0 %)	$0.054 \pm 1.84{\cdot}10^{-4}$ (≙ 0.36 %)	373.0 ± 0.2 (≙ 0.2 %)
$3.37{\cdot}10^{3} \pm 33.95$ (≙ 1.01 %)	$0.088 \pm 2.84{\cdot}10^{-4}$ (≙ 0.33 %)	372.99 ± 0.2 (≙ 0.2 %)
$4.96{\cdot}10^{3} \pm 36.72$ (≙ 0.74 %)	$0.127 \pm 3.54{\cdot}10^{-4}$ (≙ 0.29 %)	373.04 ± 0.2 (≙ 0.2 %)
$6.02{\cdot}10^{3} \pm 38.78$ (≙ 0.64 %)	$0.16 \pm 4.01{\cdot}10^{-4}$ (≙ 0.26 %)	373.03 ± 0.2 (≙ 0.2 %)
$7.15{\cdot}10^{3} \pm 40.8$ (≙ 0.57 %)	$0.194 \pm 4.36{\cdot}10^{-4}$ (≙ 0.23 %)	372.96 ± 0.2 (≙ 0.2 %)
$1.06{\cdot}10^{4} \pm 43.02$ (≙ 0.41 %)	$0.263 \pm 5.69{\cdot}10^{-4}$ (≙ 0.22 %)	372.99 ± 0.2 (≙ 0.2 %)
$1.7{\cdot}10^{4} \pm 52.17$ (≙ 0.31 %)	$0.337 \pm 7.36{\cdot}10^{-4}$ (≙ 0.23 %)	373.01 ± 0.2 (≙ 0.2 %)
$2.42{\cdot}10^{4} \pm 76.76$ (≙ 0.32 %)	$0.394 \pm 8.68{\cdot}10^{-4}$ (≙ 0.25 %)	373.02 ± 0.2 (≙ 0.2 %)
$2.83{\cdot}10^{4} \pm 126.84$ (≙ 0.45 %)	$0.42 \pm 9.13{\cdot}10^{-4}$ (≙ 0.25 %)	373.12 ± 0.2 (≙ 0.2 %)
$3.3{\cdot}10^{4} \pm 167.32$ (≙ 0.51 %)	$0.439 \pm 1.1{\cdot}10^{-3}$ (≙ 0.24 %)	372.94 ± 0.2 (≙ 0.2 %)
$4.07{\cdot}10^{4} \pm 149.5$ (≙ 0.37 %)	$0.456 \pm 3.2{\cdot}10^{-3}$ (≙ 0.71 %)	373.0 ± 0.2 (≙ 0.2 %)
$7.14{\cdot}10^{4} \pm 235.14$ (≙ 0.33 %)	$0.475 \pm 3.26{\cdot}10^{-3}$ (≙ 0.7 %)	373.0 ± 0.2 (≙ 0.2 %)

Table A.20: Overview of experimental values of the Pd-H_2 system at 473 K including its uncertainties.

p (Pa)	c (mol_H/mol_{Pd})	T (K)
0 ± 0 (≙ 0 %)	$0.01 \pm 4.22{\cdot}10^{-5}$ (≙ 0.41 %)	472.03 ± 0.2 (≙ 0.15 %)
$2.85{\cdot}10^{2} \pm 60.99$ (≙ 21.4 %)	$0.054 \pm 1.92{\cdot}10^{-4}$ (≙ 0.36 %)	473.0 ± 0.2 (≙ 0.15 %)
$8.64{\cdot}10^{3} \pm 41.48$ (≙ 0.48 %)	$0.088 \pm 2.86{\cdot}10^{-4}$ (≙ 0.33 %)	472.99 ± 0.2 (≙ 0.15 %)
$1.38{\cdot}10^{4} \pm 77.1$ (≙ 0.56 %)	$0.127 \pm 3.62{\cdot}10^{-4}$ (≙ 0.29 %)	472.95 ± 0.2 (≙0.15 %)

$1.77{\cdot}10^{4} \pm 89.58$ (≙ 0.51 %)	$0.16 \pm 4.12{\cdot}10^{-4}$ (≙ 0.26 %)	473.02 ± 0.2 (≙0.15 %)
$2.16{\cdot}10^{4} \pm 77.03$ (≙ 0.36 %)	$0.194 \pm 4.47{\cdot}10^{-4}$ (≙ 0.23 %)	472.98 ± 0.2 (≙ 0.15 %)
$3.05{\cdot}10^{4} \pm 114.61$ (≙ 0.38 %)	$0.263 \pm 5.88{\cdot}10^{-4}$ (≙ 0.22 %)	472.99 ± 0.2 (≙ 0.15 %)
$5.04{\cdot}10^{4} \pm 201.13$ (≙ 0.4 %)	$0.337 \pm 7.8{\cdot}10^{-4}$ (≙ 0.23 %)	472.99 ± 0.2 (≙ 0.15 %)
$7.84{\cdot}10^{4} \pm 344.94$ (≙ 0.44 %)	$0.394 \pm 9.69{\cdot}10^{-4}$ (≙ 0.25 %)	472.99 ± 0.2 (≙ 0.15 %)
$9.62{\cdot}10^{4} \pm 389.49$ (≙ 0.4 %)	$0.42 \pm 1.04{\cdot}10^{-3}$ (≙ 0.25 %)	473.14 ± 0.2 (≙ 0.15 %)
$1.13{\cdot}10^{5} \pm 519.02$ (≙ 0.46 %)	$0.439 \pm 1.1{\cdot}10^{-3}$ (≙ 0.24 %)	472.96 ± 0.2 (≙ 0.15 %)
$1.29{\cdot}10^{5} \pm 436.47$ (≙ 0.34 %)	$0.456 \pm 3.25{\cdot}10^{-3}$ (≙ 0.71 %)	473.01 ± 0.2 (≙ 0.15 %)
$1.63{\cdot}10^{5} \pm 541.64$ (≙ 0.33 %)	$0.475 \pm 3.32{\cdot}10^{-3}$ (≙ 0.7 %)	473.02 ± 0.2 (≙ 0.15 %)

ii) Deuterium in Palladium:

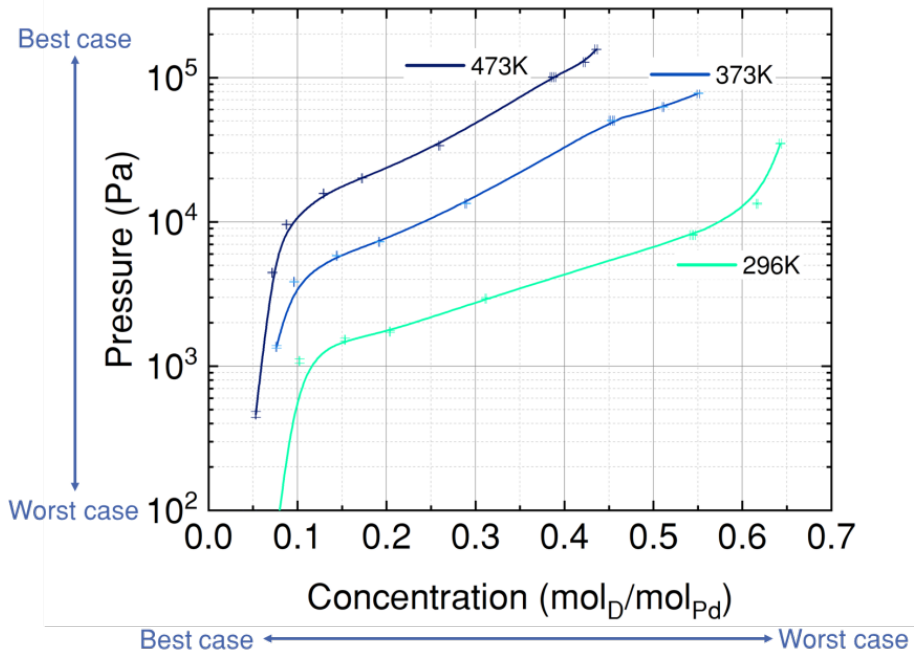

Figure A.2: Experimental data and its uncertainties of D_2-Pd at 296 K, 373 K and 473 K.

Table A.21: Overview of experimental values of the Pd-D_2 system at 296 K including its uncertainties.

p (Pa)	c (mol_D/mol_{Pd})	T (K)
0 ± 0 (≙ 0 %)	$0.0096 \pm 3.92{\cdot}10^{-5}$ (≙ 0.41 %)	293 ± 0.12 (≙ 0.54 %)
0 ± 0 (≙ 0 %)	$0.023 \pm 6.8{\cdot}10^{-5}$ (≙ 0.29 %)	293 ± 0.13 (≙ 0.54 %)
0 ± 0 (≙ 0 %)	$0.039 \pm 2.97{\cdot}10^{-4}$ (≙ 0.76 %)	293 ± 0.12 (≙ 0.54 %)
0 ± 0 (≙ 0 %)	$0.054 \pm 3.07{\cdot}10^{-4}$ (≙ 0.57 %)	299.67 ± 0.13 (≙ 0.48 %)
$9.05{\cdot}10^{1} \pm 26.64$ (≙ 29.45 %)	$0.079 \pm 3.27{\cdot}10^{-4}$ (≙ 0.41 %)	298.46 ± 0.12 (≙ 0.48 %)

$1.08{\cdot}10^{3} \pm 38.18$ (≙ 3.52 %)	$0.10 \pm 3.49{\cdot}10^{-4}$ (≙ 0.34 %)	299.65 ± 0.13 (≙ 0.47 %)
$1.52{\cdot}10^{3} \pm 33.67$ (≙ 2.21 %)	$0.15 \pm 4.18{\cdot}10^{-4}$ (≙ 0.27 %)	299.15 ± 0.12 (≙ 0.47 %)
$1.74{\cdot}10^{3} \pm 22.69$ (≙ 1.3 %)	$0.20 \pm 4.71{\cdot}10^{-4}$ (≙ 0.23 %)	297.87 ± 0.12 (≙ 0.49 %)
$2.94{\cdot}10^{3} \pm 35.18$ (≙ 1.19 %)	$0.31 \pm 6.71{\cdot}10^{-4}$ (≙ 0.22 %)	299.16 ± 0.12 (≙ 0.47 %)
$8.12{\cdot}10^{3} \pm 40.05$ (≙ 0.49 %)	$0.54 \pm 9.04{\cdot}10^{-4}$ (≙ 0.17 %)	298.68 ± 0.12 (≙ 0.48 %)
$1.34{\cdot}10^{4} \pm 56.82$ (≙ 0.42 %)	$0.62 \pm 3.13{\cdot}10^{-3}$ (≙ 0.51 %)	298.83 ± 0.13 (≙ 0.47 %)
$3.49{\cdot}10^{4} \pm 115.53$ (≙ 0.33 %)	$0.64 \pm 3.15{\cdot}10^{-3}$ (≙ 0.49 %)	298.46 ± 0.12 (≙ 0.48 %)
$9.35{\cdot}10^{4} \pm 276.57$ (≙ 0.3 %)	$0.66 \pm 3.33{\cdot}10^{-3}$ (≙ 0.5 %)	298.24 ± 0.13 (≙ 0.53 %)

Table A.22: Overview of experimental values of the Pd-D_2 system at 373 K including its uncertainties.

p (Pa)	c (mol_D/mol_{Pd})	T (K)
0 ± 0 (≙ 0 %)	$0.0096 \pm 3.92{\cdot}10^{-5}$ (≙ 0.41 %)	373 ± 0.2 (≙ 0.2 %)
0 ± 0 (≙ 0 %)	$0.023 \pm 6.8{\cdot}10^{-5}$ (≙ 0.29 %)	373 ± 0.2 (≙ 0.2 %)
0 ± 0 (≙ 0 %)	$0.039 \pm 3.97{\cdot}10^{-4}$ (≙ 1.02 %)	372.99 ± 0.2 (≙ 0.2 %)
0 ± 0 (≙ 0 %)	$0.054 \pm 3.09{\cdot}10^{-4}$ (≙ 0.57 %)	373.02 ± 0.2 (≙ 0.2 %)
$1.36{\cdot}10^{3} \pm 29.22$ (≙ 2.15 %)	$0.076 \pm 3.28{\cdot}10^{-4}$ (≙ 0.43 %)	372.95 ± 0.2 (≙ 0.2 %)
$3.84{\cdot}10^{3} \pm 32.46$ (≙ 0.85 %)	$0.096 \pm 3.51{\cdot}10^{-4}$ (≙ 0.37 %)	372.98 ± 0.2 (≙ 0.2 %)
$5.83{\cdot}10^{3} \pm 34.2$ (≙ 0.59 %)	$0.14 \pm 4.2{\cdot}10^{-4}$ (≙ 0.29 %)	373.28 ± 0.2 (≙ 0.2 %)
$7.28{\cdot}10^{3} \pm 22.69$ (≙ 0.3 %)	$0.19 \pm 4.73{\cdot}10^{-4}$ (≙ 0.25 %)	373 ± 0.2 (≙ 0.2 %)
$1.34{\cdot}10^{4} \pm 60.79$ (≙ 0.45 %)	$0.29 \pm 6.77{\cdot}10^{-4}$ (≙ 0.23 %)	372.96 ± 0.2 (≙ 0.2 %)
$5.04{\cdot}10^{4} \pm 194.13$ (≙ 0.38 %)	$0.45 \pm 9.6{\cdot}10^{-4}$ (≙ 0.21 %)	373.05 ± 0.2 (≙ 0.2 %)
$6.25{\cdot}10^{4} \pm 220.25$ (≙ 0.35 %)	$0.51 \pm 3.15{\cdot}10^{-3}$ (≙ 0.62 %)	373.99 ± 0.2 (≙ 0.2 %)
$7.78{\cdot}10^{4} \pm 273.46$ (≙ 0.35 %)	$0.55 \pm 3.18{\cdot}10^{-3}$ (≙ 0.58 %)	372.99 ± 0.2 (≙ 0.2 %)
$1.22{\cdot}10^{5} \pm 396.08$ (≙ 0.32 %)	$0.6 \pm 3.36{\cdot}10^{-3}$ (≙ 0.56 %)	372.99 ± 0.2 (≙ 0.2 %)

Table A.23: Overview of experimental values of the Pd-D_2 system at 473 K including its uncertainties.

p (Pa)	c (mol_D/mol_{Pd})	T (K)
0 ± 0 (≙ 0 %)	$0.0096 \pm 3.92{\cdot}10^{-5}$ (≙ 0.41 %)	473 ± 0.3 (≙ 0.15 %)
0 ± 0 (≙ 0 %)	$0.023 \pm 6.8{\cdot}10^{-5}$ (≙ 0.29 %)	473 ± 0.3 (≙ 0.15 %)
0 ± 0 (≙ 0 %)	$0.039 \pm 3.62{\cdot}10^{-4}$ (≙ 0.93 %)	472 ± 0.3 (≙ 0.15 %)
$4.62{\cdot}10^{2} \pm 22.4$ (≙ 4.85 %)	$0.054 \pm 3.08{\cdot}10^{-4}$ (≙ 0.58 %)	472.98 ± 0.3 (≙ 0.15 %)

$4.44{\cdot}10^{3} \pm 29.22$ (≙ 0.89 %)	$0.072 \pm 3.29{\cdot}10^{-4}$ (≙ 0.46 %)	473.01 ± 0.3 (≙ 0.15 %)
$9.6{\cdot}10^{3} \pm 39.74$ (≙ 0.42 %)	$0.088 \pm 3.52{\cdot}10^{-4}$ (≙ 0.4 %)	472.92 ± 0.3 (≙ 0.15 %)
$1.57{\cdot}10^{4} \pm 76.96$ (≙ 0.49 %)	$0.13 \pm 4.28{\cdot}10^{-4}$ (≙ 0.33 %)	472.95 ± 0.3 (≙ 0.15 %)
$2.01{\cdot}10^{4} \pm 58.3$ (≙ 0.29 %)	$0.17 \pm 4.81{\cdot}10^{-4}$ (≙ 0.28 %)	473.26 ± 0.3 (≙ 0.15 %)
$3.38{\cdot}10^{4} \pm 79.91$ (≙ 0.24 %)	$0.26 \pm 6.88{\cdot}10^{-4}$ (≙ 0.27 %)	473.07 ± 0.3 (≙ 0.15 %)
$1.01{\cdot}10^{5} \pm 259.65$ (≙ 0.26 %)	$0.39 \pm 1.02{\cdot}10^{-3}$ (≙ 0.26 %)	472.97 ± 0.3 (≙ 0.15 %)
$1.28{\cdot}10^{5} \pm 276.84$ (≙ 0.22 %)	$0.42 \pm 3.18{\cdot}10^{-3}$ (≙ 0.75 %)	473.05 ± 0.3 (≙ 0.15 %)
$1.57{\cdot}10^{4} \pm 345.18$ (≙ 0.22 %)	$0.44 \pm 3.21{\cdot}10^{-3}$ (≙ 0.74 %)	472.95 ± 0.3 (≙ 0.15 %)
$2.24{\cdot}10^{5} \pm 566.36$ (≙ 0.25 %)	$0.44 \pm 3.41{\cdot}10^{-3}$ (≙ 0.77 %)	472.95 ± 0.3 (≙ 0.15 %)

iii) Protium in Titanium-Chromium:

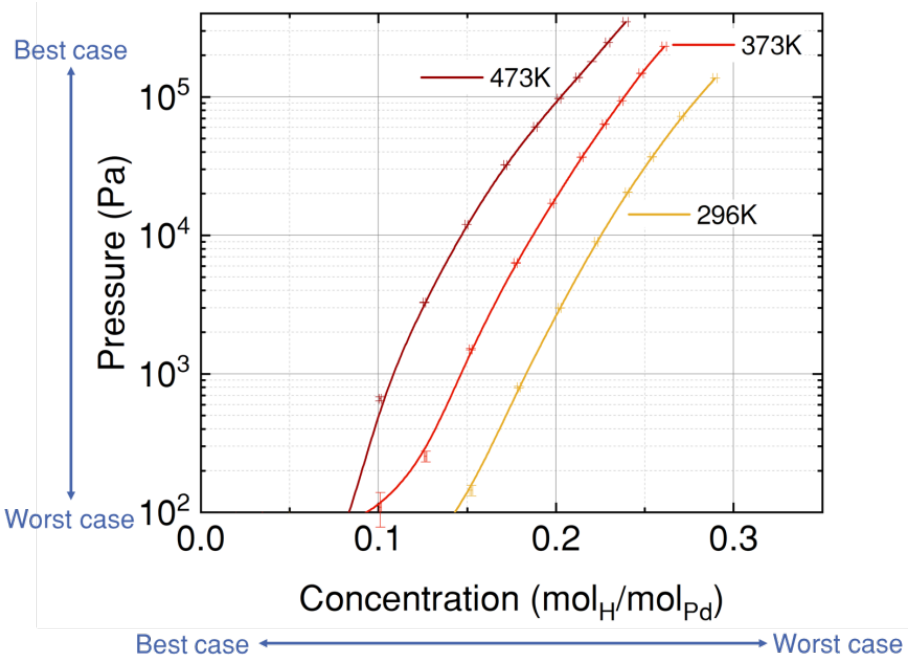

Figure A.3: Experimental data and its uncertainties of H_2-$TiCr_{1.5}$ at 296 K, 373 K and 473 K.

Table A.24: Overview of experimental values of the $TiCr_{1.5}$-H_2 system at 296 K including its uncertainties.

p (Pa)	c ($mol_H/mol_{TiCr1.5}$)	T (K)
0 ± 0 (≙ 0 %)	$0.01 \pm 1.38{\cdot}10^{-4}$ (≙ 1.37 %)	296 ± 0.12 (≙ 0.54 %)
0 ± 0 (≙ 0 %)	$0.02 \pm 2.01{\cdot}10^{-4}$ (≙ 1.01 %)	296 ± 0.13 (≙ 0.55 %)
0 ± 0 (≙ 0 %)	$0.035 \pm 2.95{\cdot}10^{-4}$ (≙ 0.85 %)	296 ± 0.12 (≙ 0.54 %)
0 ± 0 (≙ 0 %)	$0.054 \pm 3.62{\cdot}10^{-4}$ (≙ 0.73 %)	294.49 ± 0.12 (≙ 0.58 %)
$5.84{\cdot}10^{1} \pm 35.72$ (≙ 61.21 %)	$0.076 \pm 5.23{\cdot}10^{-4}$ (≙ 0.67 %)	292.58 ± 0.12 (≙ 0.63 %)

$4.07{\cdot}10^{1} \pm 11.2$ (≙ 27.52 %)	$0.10 \pm 6.27{\cdot}10^{-4}$ (≙ 0.62 %)	296.46 ± 0.12 (≙ 0.53 %)
$4.82{\cdot}10^{3} \pm 23.49$ (≙ 48.7 %)	$0.13 \pm 7.21{\cdot}10^{-4}$ (≙ 0.57 %)	293.88 ± 0.12 (≙ 0.59 %)
$1.44{\cdot}10^{2} \pm 12.37$ (≙ 8.58 %)	$0.15 \pm 8.05{\cdot}10^{-4}$ (≙ 0.53 %)	295.29 ± 0.12 (≙ 0.56 %)
$8.01{\cdot}10^{2} \pm 10.9$ (≙ 1.36 %)	$0.18 \pm 8.87{\cdot}10^{-4}$ (≙ 0.5 %)	295.6 ± 0.12 (≙ 0.55 %)
$2.99{\cdot}10^{3} \pm 11$ (≙ 0.37 %)	$0.2 \pm 9.46{\cdot}10^{-4}$ (≙ 0.47 %)	295.84 ± 0.12 (≙ 0.54 %)
$8.98{\cdot}10^{3} \pm 15.5$ (≙ 0.17 %)	$0.22 \pm 9.99{\cdot}10^{-3}$ (≙ 0.45 %)	296.04 ± 0.12 (≙ 0.54 %)
$2.05{\cdot}10^{4} \pm 27.63$ (≙ 0.14 %)	$0.24 \pm 1.04{\cdot}10^{-3}$ (≙ 0.44 %)	295.82 ± 0.12 (≙ 0.54 %)
$3.68{\cdot}10^{4} \pm 48.48$ (≙ 0.13 %)	$0.25 \pm 1.08{\cdot}10^{-3}$ (≙ 0.43 %)	295.82 ± 0.12 (≙ 0.54 %)
$7.22{\cdot}10^{4} \pm 97.96$ (≙ 0.14 %)	$0.27 \pm 1.17{\cdot}10^{-3}$ (≙ 0.43 %)	295.88 ± 0.12 (≙ 0.53 %)
$1.37{\cdot}10^{5} \pm 195.87$ (≙ 0.14 %)	$0.29 \pm 3.35{\cdot}10^{-3}$ (≙ 0.47 %)	296.65 ± 0.12 (≙ 0.52 %)

Table A.25: Overview of experimental values of the $TiCr_{1.5}$-H_2 system at 373 K including its uncertainties.

p (Pa)	c ($mol_H/mol_{TiCr1.5}$)	T (K)
0 ± 0 (≙ 0 %)	$0.01 \pm 1.38{\cdot}10^{-4}$ (≙ 1.37 %)	373.07 ± 0.2 (≙ 0.2 %)
0 ± 0 (≙ 0 %)	$0.02 \pm 2.01{\cdot}10^{-4}$ (≙ 1.01 %)	373.06 ± 0.2 (≙ 0.2 %)
0 ± 0 (≙ 0 %)	$0.035 \pm 2.95{\cdot}10^{-4}$ (≙ 0.85 %)	372.84 ± 0.2 (≙ 0.2 %)
$9.75{\cdot}10^{1} \pm 22.55$ (≙ 27.52 %)	$0.05 \pm 3.63{\cdot}10^{-4}$ (≙ 0.73 %)	373.18 ± 0.2 (≙ 0.2 %)
$7.66{\cdot}10^{1} \pm 21.19$ (≙ 48.7 %)	$0.076 \pm 5.23{\cdot}10^{-4}$ (≙ 0.69 %)	373.07 ± 0.2 (≙ 0.2 %)
$1.09{\cdot}10^{2} \pm 30.55$ (≙ 8.58 %)	$0.10 \pm 6.27{\cdot}10^{-4}$ (≙ 0.62 %)	373.1 ± 0.2 (≙ 0.2 %)
$2.54{\cdot}10^{2} \pm 22.41$ (≙ 1.36 %)	$0.13 \pm 7.21{\cdot}10^{-4}$ (≙ 0.57 %)	373.03 ± 0.2 (≙ 0.2 %)
$1.5{\cdot}10^{3} \pm 19.28$ (≙ 0.37 %)	$0.15 \pm 8.05{\cdot}10^{-4}$ (≙ 0.53 %)	373.19 ± 0.2 (≙ 0.2 %)
$6.31{\cdot}10^{3} \pm 21.17$ (≙ 0.17 %)	$0.18 \pm 8.87{\cdot}10^{-4}$ (≙ 0.5 %)	373.07 ± 0.2 (≙ 0.2 %)
$1.7{\cdot}10^{4} \pm 22.95$ (≙ 0.14 %)	$0.2 \pm 9.47{\cdot}10^{-4}$ (≙ 0.48 %)	373.03 ± 0.2 (≙ 0.2 %)
$3.67{\cdot}10^{4} \pm 60.01$ (≙ 0.13 %)	$0.21 \pm 1.0{\cdot}10^{-3}$ (≙ 0.47 %)	373.0 ± 0.2 (≙ 0.2 %)
$6.34{\cdot}10^{4} \pm 119.39$ (≙ 0.14 %)	$0.23 \pm 1.06{\cdot}10^{-3}$ (≙ 0.47 %)	373.08 ± 0.2 (≙ 0.2 %)
$9.36{\cdot}10^{4} \pm 148.64$ (≙ 0.14 %)	$0.24 \pm 1.1{\cdot}10^{-3}$ (≙ 0.46 %)	373.07 ± 0.2 (≙ 0.2 %)
$1.48{\cdot}10^{5} \pm 321.02$ (≙ 0.14 %)	$0.25 \pm 1.2{\cdot}10^{-3}$ (≙ 0.49 %)	373.07 ± 0.2 (≙ 0.2 %)
$2.31{\cdot}10^{5} \pm 526.98$ (≙ 0.14 %)	$0.26 \pm 3.4{\cdot}10^{-3}$ (≙ 0.54 %)	373.07 ± 0.2 (≙ 0.2 %)

Table A.26: Overview of experimental values of the $TiCr_{1.5}$-H_2 system at 473 K including its uncertainties.

p (Pa)	c ($mol_H/mol_{TiCr1.5}$)	T (K)
0 ± 0 (≙ 0 %)	$0.01 \pm 1.38 \cdot 10^{-4}$ (≙ 1.37 %)	472.89 ± 0.3 (≙ 0.15 %)
0 ± 0 (≙ 0 %)	$0.02 \pm 2.01 \cdot 10^{-4}$ (≙ 1.01 %)	473.09 ± 0.3 (≙ 0.15 %)
0 ± 0 (≙ 0 %)	$0.035 \pm 2.95 \cdot 10^{-4}$ (≙ 0.85 %)	472.78 ± 0.3 (≙ 0.15 %)
0 ± 0 (≙ 0 %)	$0.05 \pm 3.62 \cdot 10^{-4}$ (≙ 0.73 %)	473.15 ± 0.3 (≙ 0.15 %)
$3.89 \cdot 10^{1} \pm 17.95$ (≙ 46.11 %)	$0.076 \pm 5.23 \cdot 10^{-4}$ (≙ 0.69 %)	473.08 ± 0.3 (≙ 0.15 %)
$6.59 \cdot 10^{2} \pm 23.06$ (≙ 3.5 %)	$0.10 \pm 6.27 \cdot 10^{-4}$ (≙ 0.62 %)	473.12 ± 0.3 (≙ 0.15 %)
$3.28 \cdot 10^{3} \pm 14.81$ (≙ 0.45 %)	$0.13 \pm 7.21 \cdot 10^{-4}$ (≙ 0.57 %)	473.06 ± 0.3 (≙ 0.15 %)
$1.2 \cdot 10^{4} \pm 25.67$ (≙ 0.21 %)	$0.15 \pm 8.06 \cdot 10^{-4}$ (≙ 0.54 %)	473.19 ± 0.3 (≙ 0.15 %)
$3.22 \cdot 10^{4} \pm 45.26$ (≙ 0.14 %)	$0.17 \pm 8.89 \cdot 10^{-4}$ (≙ 0.52 %)	473.08 ± 0.3 (≙ 0.15 %)
$6.07 \cdot 10^{4} \pm 73.94$ (≙ 0.12 %)	$0.19 \pm 9.55 \cdot 10^{-4}$ (≙ 0.51 %)	473.07 ± 0.3 (≙ 0.15 %)
$9.73 \cdot 10^{4} \pm 117.18$ (≙ 0.12 %)	$0.2 \pm 1.02 \cdot 10^{-3}$ (≙ 0.5 %)	473.0 ± 0.3 (≙ 0.15 %)
$1.38 \cdot 10^{5} \pm 220.49$ (≙ 0.16 %)	$0.22 \pm 1.08 \cdot 10^{-3}$ (≙ 0.51 %)	473.09 ± 0.3 (≙ 0.15 %)
$1.79 \cdot 10^{5} \pm 336.58$ (≙ 0.19 %)	$0.22 \pm 1.13 \cdot 10^{-3}$ (≙ 0.52 %)	473.06 ± 0.3 (≙ 0.15 %)
$2.47 \cdot 10^{5} \pm 397.12$ (≙ 0.16 %)	$0.23 \pm 1.24 \cdot 10^{-3}$ (≙ 0.54 %)	473.08 ± 0.3 (≙ 0.15 %)
$3.48 \cdot 10^{5} \pm 524.93$ (≙ 0.15 %)	$0.24 \pm 3.43 \cdot 10^{-3}$ (≙ 0.6 %)	473.1 ± 0.3 (≙ 0.15 %)

iv) Deuterium in Titanium-Chromium:

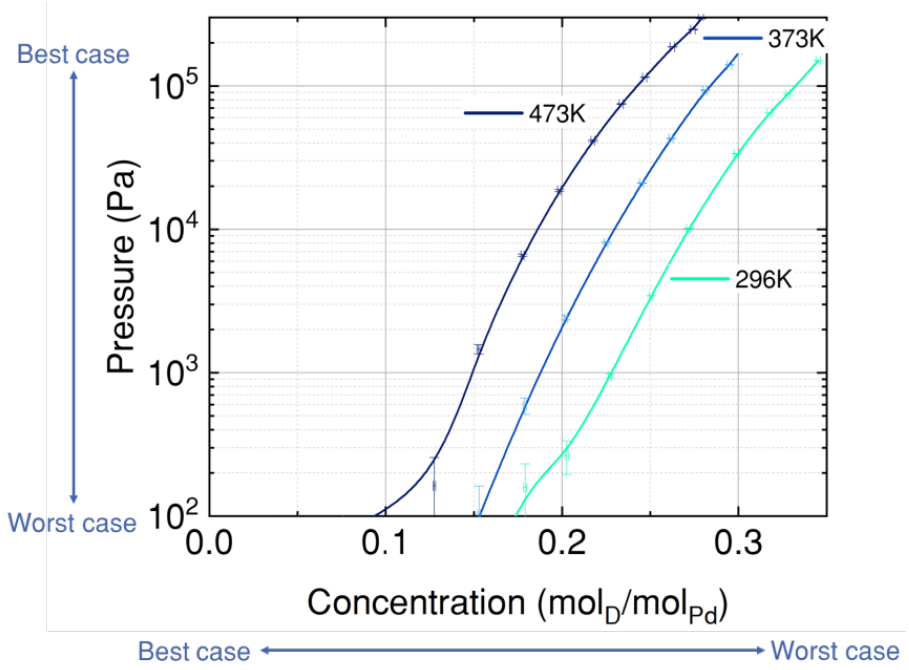

Figure A.4: Experimental data and its uncertainties of D_2-$TiCr_{1.5}$ at 296 K, 373 K and 473 K.

Table A.27: Overview of experimental values of the $TiCr_{1.5}$-D_2 system at 296 K including its uncertainties.

p (Pa)	c ($mol_D/mol_{TiCr1.5}$)	T (K)
0 ± 0 (≙ 0 %)	$0.13 \pm 7.08 \cdot 10^{-4}$ (≙ 0.55 %)	297.04 ± 0.27 (≙ 1.09 %)
$2.69 \cdot 10^{1} \pm 20.43$ (≙ 76 %)	$0.15 \pm 7.94 \cdot 10^{-4}$ (≙ 0.52 %)	297.78 ± 0.14 (≙ 0.54 %)
$1.58 \cdot 10^{2} \pm 73.09$ (≙ 46.17 %)	$0.18 \pm 8.78 \cdot 10^{-4}$ (≙ 0.49 %)	299.23 ± 0.13 (≙ 0.5 %)
$2.64 \cdot 10^{2} \pm 69.29$ (≙ 26.22 %)	$0.2 \pm 9.43 \cdot 10^{-4}$ (≙ 0.47 %)	299.27 ± 0.13 (≙ 0.48 %)
$9.5 \cdot 10^{2} \pm 34.29$ (≙ 3.61 %)	$0.23 \pm 1.01 \cdot 10^{-3}$ (≙ 0.44 %)	299.25 ± 0.13 (≙ 0.54 %)
$3.44 \cdot 10^{3} \pm 12.31$ (≙ 0.36 %)	$0.25 \pm 1.07 \cdot 10^{-3}$ (≙ 0.43 %)	296.34 ± 0.12 (≙ 0.5 %)
$1.01 \cdot 10^{4} \pm 36.77$ (≙ 0.36 %)	$0.27 \pm 1.12 \cdot 10^{-3}$ (≙ 0.41 %)	298.1 ± 0.13 (≙ 0.5 %)
$3.37 \cdot 10^{4} \pm 111.42$ (≙ 0.33 %)	$0.3 \pm 1.24 \cdot 10^{-3}$ (≙ 0.42 %)	298.47 ± 0.13 (≙ 0.5 %)
$6.49 \cdot 10^{4} \pm 174.02$ (≙ 0.27 %)	$0.32 \pm 1.33 \cdot 10^{-3}$ (≙ 0.42 %)	298 ± 0.13 (≙ 0.53 %)
$8.71 \cdot 10^{4} \pm 141.94$ (≙ 0.16 %)	$0.33 \pm 1.4 \cdot 10^{-3}$ (≙ 0.43 %)	296.71 ± 0.13 (≙ 0.5 %)
$1.5 \cdot 10^{5} \pm 379.96$ (≙ 0.25 %)	$0.35 \pm 1.61 \cdot 10^{-3}$ (≙ 0.47 %)	297.76 ± 0.12 (≙ 0.54 %)

Table A.28: Overview of experimental values of the $TiCr_{1.5}$-D_2 system at 373 K including its uncertainties.

p (Pa)	c ($mol_D/mol_{TiCr1.5}$)	T (K)
0 ± 0 (≙ 0 %)	$0.13 \pm 7.08 \cdot 10^{-4}$ (≙ 0.56 %)	372.96 ± 0.2 (≙ 0.2 %)
$1.03 \cdot 10^{2} \pm 58.65$ (≙ 57.03 %)	$0.15 \pm 7.94 \cdot 10^{-4}$ (≙ 0.52 %)	373.08 ± 0.2 (≙ 0.2 %)
$5.87 \cdot 10^{2} \pm 76.81$ (≙ 13.07 %)	$0.18 \pm 8.81 \cdot 10^{-4}$ (≙ 0.49 %)	372.52 ± 0.2 (≙ 0.2 %)
$2.41 \cdot 10^{3} \pm 84.23$ (≙ 3.49 %)	$0.2 \pm 9.44 \cdot 10^{-4}$ (≙ 0.47 %)	373.16 ± 0.2 (≙ 0.2 %)
$8.07 \cdot 10^{3} \pm 103.55$ (≙ 1.28 %)	$0.22 \pm 1.01 \cdot 10^{-3}$ (≙ 0.45 %)	372.96 ± 0.2 (≙ 0.2 %)
$2.1 \cdot 10^{4} \pm 94.47$ (≙ 0.45 %)	$0.25 \pm 1.07 \cdot 10^{-3}$ (≙ 0.44 %)	372.89 ± 0.2 (≙ 0.2 %)
$4.31 \cdot 10^{4} \pm 184.03$ (≙ 0.43 %)	$0.26 \pm 1.13 \cdot 10^{-3}$ (≙ 0.43 %)	373.04 ± 0.2 (≙ 0.2 %)
$9.32 \cdot 10^{4} \pm 430.4$ (≙ 0.46 %)	$0.28 \pm 1.27 \cdot 10^{-3}$ (≙ 0.45 %)	373.04 ± 0.2 (≙ 0.2 %)
$1.4 \cdot 10^{5} \pm 188.54$ (≙ 0.13 %)	$0.3 \pm 1.35 \cdot 10^{-3}$ (≙ 0.46 %)	373.1 ± 0.2 (≙ 0.2 %)
$1.77 \cdot 10^{5} \pm 680.33$ (≙ 0.38 %)	$0.3 \pm 1.46 \cdot 10^{-3}$ (≙ 0.48 %)	373.09 ± 0.2 (≙ 0.2 %)
$2.61 \cdot 10^{5} \pm 982.92$ (≙ 0.38 %)	$0.31 \pm 1.71 \cdot 10^{-3}$ (≙ 0.55 %)	373.24 ± 0.2 (≙ 0.2 %)

Table A.29: Overview of experimental values of the $TiCr_{1.5}$-D_2 system at 473 K including its uncertainties.

p (Pa)	c ($mol_D/mol_{TiCr1.5}$)	T (K)
0 ± 0 (≙ 0 %)	$0.13 \pm 7.09 \cdot 10^{-4}$ (≙ 0.56 %)	472.8 ± 0.3 (≙ 0.15 %)
$1.46 \cdot 10^3 \pm 110$ (≙ 7.55 %)	$0.15 \pm 7.95 \cdot 10^{-4}$ (≙ 0.52 %)	473.01 ± 0.3 (≙ 0.15 %)
$6.58 \cdot 10^3 \pm 124.43$ (≙ 1.89 %)	$0.18 \pm 8.83 \cdot 10^{-4}$ (≙ 0.5 %)	473.05 ± 0.3 (≙ 0.15 %)
$1.87 \cdot 10^4 \pm 295.14$ (≙ 1.58 %)	$0.2 \pm 9.52 \cdot 10^{-4}$ (≙ 0.48 %)	473.14 ± 0.3 (≙ 0.15 %)
$4.15 \cdot 10^4 \pm 590.69$ (≙ 1.42 %)	$0.22 \pm 1.07 \cdot 10^{-3}$ (≙ 0.49 %)	472.98 ± 0.3 (≙ 0.15 %)
$7.48 \cdot 10^4 \pm 223.34$ (≙ 0.3 %)	$0.23 \pm 1.08 \cdot 10^{-3}$ (≙ 0.46 %)	473.08 ± 0.3 (≙ 0.15 %)
$1.14 \cdot 10^5 \pm 250.49$ (≙ 0.22 %)	$0.25 \pm 1.15 \cdot 10^{-3}$ (≙ 0.47 %)	473.04 ± 0.3 (≙ 0.15 %)
$1.87 \cdot 10^5 \pm 675.76$ (≙ 0.36 %)	$0.26 \pm 1.31 \cdot 10^{-3}$ (≙ 0.5 %)	473.08 ± 0.3 (≙ 0.15 %)
$2.47 \cdot 10^5 \pm 918.07$ (≙ 0.37 %)	$0.27 \pm 1.44 \cdot 10^{-3}$ (≙ 0.53 %)	473.07 ± 0.3 (≙ 0.15 %)
$2.94 \cdot 10^5 \pm 951.8$ (≙ 0.32 %)	$0.28 \pm 1.52 \cdot 10^{-3}$ (≙ 0.54 %)	473.05 ± 0.3 (≙ 0.15 %)
$3.93 \cdot 10^5 \pm 1182.75$ (≙ 0.3 %)	$0.29 \pm 1.76 \cdot 10^{-3}$ (≙ 0.6 %)	473.15 ± 0.3 (≙ 0.15 %)

A6 HESTIA – experimental values

Table A.30 shows the range of concentration, its respective pressure and temperature in thermodynamic equilibrium (experiment from <n_{cycle}< process steps). For the gas feed, 0.105 mol of gas is led into column1, resulting into a total concentration of 0.671 mol_Q/mol_{Pd} and a pressure of $1.08 \cdot 10^5$ Pa. For the heating of column1, the concentration decreases to 0.592 mol_Q/mol_{Pd}, while the pressure increases to $2.52 \cdot 10^5$ Pa. The desorbed gas in column1 is absorbed in column2 (Des(C1) – Abs(C2)) after the valve is opened. For column2 only a concentration difference can be given, as the material doesn't behave reversible, whereby the exact position of the concentration is not known. Pressure in column1 is in the lower range of 10^3 (for absorption) and 10^5 Pa (for desorption), for column2 a bit lower.

Table A.30: Overview of concentration, pressure and temperature for both columns in the different phases.

Process step	$\bar{c}_{Pd}$ ($\frac{mol_Q}{mol_{Pd}}$)	$\Delta\bar{c}_{TiCr1.5}$ ($\frac{mol_Q}{mol_{TiCr1.5}}$)	$\bar{p}_{Pd}$ (Pa)	$\bar{p}_{TiCr1.5}$ (Pa)	$\bar{T}_{Pd}$ (K)	$\bar{T}_{TiCr1.5}$ (K)
Gas feed	0.669	0	$1.08 \cdot 10^5$	0	286.64	303.52
Heat(C1) – Cool(C2)	0.623	0	$2.52 \cdot 10^5$	0	381.08	296.15
Des(C1) – Abs(C2)	0.623	0.0149	$2.17 \cdot 10^4$	$2.14 \cdot 10^4$	382.98	288.62
Cool(C1) – Heat(C2)	0.63	0.00975	$1.95 \cdot 10^3$	$6.3 \cdot 10^4$	287.41	387.60
Abs(C1) – Des (C2)	0.675	0.00975	$4.58 \cdot 10^3$	$5.18 \cdot 10^3$	287.29	389.50
Heat(C1) – Cool(C2)	0.629	0.0105	$1.12 \cdot 10^5$	$7.87 \cdot 10^1$	375.68	290.95
Des(C1) – Abs(C2)	0.629	0.0187	$1.19 \cdot 10^4$	$1.11 \cdot 10^4$	376.77	288.87
Cool(C1) – Heat(C2)	0.634	0.0102	$1.64 \cdot 10^3$	$7.05 \cdot 10^4$	285.51	373.96
Abs(C1) – Des(C2)	0.686	0.0102	$4.35 \cdot 10^3$	$4.41 \cdot 10^3$	287.39	382.87
Heat(C1) – Cool(C2)	0.647	0.0109	$1.05 \cdot 10^5$	$8.01 \cdot 10^1$	380.1	289.41
Des(C1) – Abs(C2)	0.647	0.0185	$5.46 \cdot 10^3$	$5.29 \cdot 10^3$	385.92	287.98

A7 HESTIA – PID and list of components

Table A.31 gives an overview of all components which are implemented in the HESTIA test rig.

Table A.31: Overview of the different components of the HESTIA test rig.

Nr.	Component	Model	Properties
B101.1 B101.2	Gas bottle	Linde	• Protium, Deuterium or a mixture • Gas from gas storage, 10 l, 200 bar • Amount: 2x
B102.1	Gas bottle		• Argon • Gas from gas storage , 50 l, 200 bar • Amount: 1x • Cleanliness: 6.0
B103.1	Gas bottle		• Nitrogen • Gas from gas storage , 50 l, 200 bar • Amount: 1x • Cleanliness: 6.0
B301.1 B401.1	Connecting tank	Manufactured in workshop	• Dimensions: 1200x150x80 mm, 1. 5 mm shim • Sleeve welded and screwed with hand valve (HV301, HV401) • Connection tank each for the column
B600.1	Connecting tank	Manufactured in workshop	• Dimensions: 1760x870x65 mm, 1,.5 mm shim • Sleeve welded and screwed with hand valve HV601 • Connection tank for the chiller and the heaters
B701.1	Sample taking	Swagelok HDF4	• Amount: 1x • 2.25 l
BK301.1 BK401.1	Columns inclusive bulk material		• Different geometries: o d=6 mm, L=6 m o d=6 mm, L=3 m o d=10 mm, L=6 m o d=10 mm, L=3 m • Bulk material BK301: o Palladium, ...

			• Bulk material BK401: o $TiCr_{1.5}$, ...
BK312.1, BK412.1,	Sample taking filled with bulk material	Swagelok HDF4 Merck Kieselguhr	• Amount: 2x • 2.25 l • Amount: 2 kg • Hazards: H372 Safety hazards: P260, P264, P270
BK501.1	Membrane	IKTS γ-Al_2O_3	• Amount: 1x Dimensions: L=0.1 m; d_o = 0.01 m; d_i = 0.007 m; d_p = $5 \cdot 10^{-9}$ m; ε=0.424, τ=2.75.
BS301.1 BS312.1 BS401.1 BS412.1	Bursting disc		• Amount: 4x Burst pressure: 30 bar(a)
F303.1 F305.1 F307.1 F309.1 F311.1 F312.1 F403.1 F405.1 F409.1 F411.1 F412.1	Filter	Swagelok T-Filter	• Amount: 11x • <u>Mechanic:</u> o Filter element can be replaced without having to remove the filter o Install VCR adapter between column and filter so that column can be opened more easily.
FCV203.1	MFC	MKS GE50A	• 0-100 sccm • Normal operating pressure Differential pressure : Δp: 0,69-2,76 bar • Maximum inlet pressure : 150 psig (=10,34 bar) • Test pressure : 1000 psig (=68,95 bar) • MFCs need to be zeroed • Minimum operating flow: 2 sccm • Implement correction factor via Delphin

			• Ar=1.39, H_2=1
FCV204.1	MFC	MKS GE50A	• 0-1000 sccm • Minimum operating flow: 20 sccm • For remaining properties see FCV203.1
FV302.1	Flow meter	Brooks MT3809/G	• Amount: 1x • 150 °C, -7,2bar • Calibration : 1-15 bar und 0-200 °C • HV302.1 integrated in the flow meter
FV313.1	Flow meter	Brooks MT3809/G	• Amount: 1x • 150 °C, -9,8bar • Calibration: 1-15 bar und 0-200 ° • HV313.1 integrated in the flow meter
FV413.1	Flow meter	Brooks MT3809/G	• Amount: 1x • 150 °C, -5,1bar • Calibration: 1-15 bar und 0-200 °C (siehe Messbereiche-Tabelle) • HV413.1 integrated in the flow meter
HV201.1 HV201.2 HV201.3 HV201.4	Ball valve hand	Swagelok SS-43GS8MM	• 8mm connection • Amount: 3x
HV205.1	Dosage valve	Festo	
HV200.1 HV200.2 HV203.1 HV206.1 HV206.2 HV206.3 HV302.2 HV302.3 HV302.4 HV313.2 HV407.2 HV413.2 HV701.1	Bellows valve hand	Type 12BG	• Amount: 12x • range: -28 °C (68,9 bar) – 315 °C (27,5 bar) 34.4 bar at 204 °C
HV301.1	Ball valve		½“ Kugelhahn PN16

HV401.1 HV600.1	hand		
HV401.1 HV404.1 HV405.1 HV407.1 HV407.3 HV408.1 HV409.1	Ball valve hand	Swagelok SS-43GS8MM	• Amount: 7x Filling of bulk material
HV601.1 HV602.1 HV603.1	Needle valve hand	Parker VEZN33HR	Amount: 3x
IB301.1 IB401.1	Plate	Presstherm WD 25-1	• Plate milled out, in which hot oil flows through • Dimensions: o 1050x500x25 mm o 1050x350x25 mm • λ=0.23 W/mK
LSHI600.1 LSHI602.1 LSHI603.1	Float switch	WIKA Typ FLS-SE	
MS701.1	Mass spectrometer		GAIA
N200.1 N200.2 N200.3 N200.4 N307.1	T-Piece		• <u>Mechanics:</u> o 8x8x8mm o N200.1: Connection of a gas bottle or similar possible o N200.2-N200.4: Bypass between membrane and columns possible o N307.1: Possible connection of vacuum pumps or similar.
P205.1	Scroll pump	Edwards XDS10i	
P206.1	Combined pumps MP+TMP	Edwards 85H Trocken	
PIR305.1	Capacitance	MKS 627F	• Amount: 2x • Range: 0-10 mbar

PIR405.1	manometer	Baratron	• Calibrated • Power supplies ±15V, 24 V power supply
PIR309.1 PIR409.1	Capacitance manometer	MKS 627F Baratron	• Amount: 2x • Range: 0-10 kmbar • Calibrated • Power supplies ±15V, 24 V power supply
PIR304.1 PIR308.1 PIR312.1 PIR404.1 PIR408.1 PIR412.1	Pressure transducer	Wika Typ S-11	• Amount: 6x
PIR501.1, PIR501.3	Capacitance manometer	MKS 627F Baratron	• Amount: 2x • Range: 0-1000 mbar • Power supplies ±15V, 24 V power supply • Calibrated • Power supplies ±15V, 24 V power supply
PIR501.2	Convection Pirani vacuum meter	InstruTech CDM900 Micro Bee	• 10 Torr • Gas independent Analogue output: linear 0-10V
PIR701.1			• Pfeiffer Vacuum: Compact Capacitance Gauge • Type: CMR 263 – 10 mbar
PIR701.2			• Wallace & Tiernan o Part-No: UXB – 95942 o Range: 0 – 2 bar(a)
PISHR205.1 PISHR206.1		WIKA A-10000	• Circuit with the bellows valves - safety-related function • Output signal: 4 ... 20 mA, • 2-wire • Auxiliary power: 8...30 V DC
PR101.1	Pressure	Rotarex CMI304-	• Protium + Deuterium-coil (2x)

PR101.2 PR102.1 PR103.1	reducing stations	SM/SP/KR10	• Protium/Deuterium mixture coil (1x) • Argon-coil (1x) • Nitrogen-coil (1x) Additionally with contact manometer
PR202.1	Pressure reducer	Swagelok Typ KPR	• Maximum inlet pressure: 34.4 bar • Pressure regulation range : 0 - 3,4 bar
PR205.1	Pressure controller		Festo
SV202.1	Safety valve	Pressluft Stoelzl Baureihe 861	• Gunmetal safety valve • TÜV CE component tested • Including material test certificate and TÜV/DEKRA individual approval • Pressure: 3.4 bar set fix
TI304.1 TI305.1 TI308.1 TI309.1 TI404.1 TI405.1 TI408.1 TI409.1 TI501.3 TI501.4 TI501.5	Temperature sensors	Typ K	• Self-adhesive thermocouple • For monitoring the temperature at the pressure sensors and for inaccuracy calculation
TIR306.1 TIR310.1 TIR406.1 TIR410.1	Sheath resistance thermometer	TC Direct Typ 17	• Amount: 4x • Calibrated: 11 TP von 0-200 °C • For optimal temperature measurement, the sheath tube has to be 50 mm in the medium • Length: 100mm, diameter:6mm/3mm (depending on column) • Recording of temperature over time

			in Profibus • On PLC, display/change on HMI • ADVT module and transmitter, terminal box
TICR312.1 TICR412.1	Sheath resistance thermometer	TC Direct Typ 17	• Amount: 2x • Not calibrated • For optimal temperature measurement, the sheath tube has to be 50 mm in the medium • Length: 100mm, diameter:6mm/3mm (depending on column) • Recording of temperature over time in Profibus • On PLC, display/change on HMI • ADVT module and transmitter, terminal box
TICR501.1	Sheath resistance thermometer	TC Direct Typ 17	• Amount: 1x • Not calibrated • For optimal temperature measurement, the sheath tube has to be 50 mm in the medium • Length: 100mm, diameter:6mm • Recording of temperature over time in Profibus • On PLC, display/change on HMI • ADVT module and transmitter, terminal box
TIR501.2	Sheath resistance thermometer	TC Direct Typ 17	• Amount: 1x • Not calibrated • For optimal temperature measurement, the sheath tube has to be 50 mm in the medium • Length: 100mm, diameter:6mm • Recording of temperature over time in Profibus • On PLC, display/change on HMI • ADVT module and transmitter, terminal box
TIC601.1	Sheath	TC Direct Typ 17	• Amount: 2x

TIC601.2	resistance thermometer		• Not calibrated • For optimal temperature measurement, the sheath tube has to be 50 mm in the medium • Length: 100mm, diameter:6mm • Recording of temperature over time in Profibus • On PLC, display/change on HMI • ADVT module and transmitter, terminal box
V101.1 V101.2 V101.3 V102.1	Pneumatic bellows ATEX valves	Swagelok	• Amount: 4x • Valves for the gas storage • ATEX certification for zone 2
V200.1 V204.1 V204.2 V205.1 V205.2 V206.1 V206.2 V302.1 V303.1 V305.1 V307.1 V309.1 V311.1 V312.1 V313.1 V403.1 V405.1 V409.1 V411.1 V412.1 V413.1	Pneumatic bellows valves	Swagelok Serie 8BG	• Amount: 21x • Range: -28 °C (68,9 bar) – 315 °C (27,5 bar) 34,4 bar bei 204 °C
V601.1 V602.1 V603.1	Overflow valve	Pressluft Stoelzl Baureihe 617	• Amount: 3x • Red brass overflow/control valve • Pressure range: 0,5-2bar
V601.2 V601.3	Pneumatic ball valve	Festo	Amount: 12x

V601.4 V601.5 V602.2 V602.3 V602.4 V602.5 V603.2 V603.3 V603.4 V603.5			
W312.1 W412.1	Heating cord	Hillesheim Typ HST	• Amount : 2x • Operating temperature: 250 °C 6 m, 125 W
W501.1	Heating cord	Hillesheim Typ HS	• Amount: 1x • Temperature range : 20-200 °C 0,75 m, 94 W
W601.1	Chiller	Huber Typ 025	• Amount: 1x • Temperature range : -10 – 40°C • 2,5 kW cooling power (at15°C)
W602.1 W603.1	Heating bath thermostat	Huber Typ CC-208B	• Amount: 1x • • Temperature range: 25 –200°C • Heating power: 2 kW
	Hydrogen safety sensor	Dräger	margin: 200ppm und 400ppm

Below the PID of HESTIA is shown. The PID is split in individual parts. An overview of the parts is shown in Figure A.5 a), the correlation of the six steps in the PID is given in Figure A.5 b). This overview simply shows how the individual parts are connected, it is not meant to be read. The individual parts are, including of a visual location in the PID, shown in Figure A.6 to Figure A.11 and are readable.

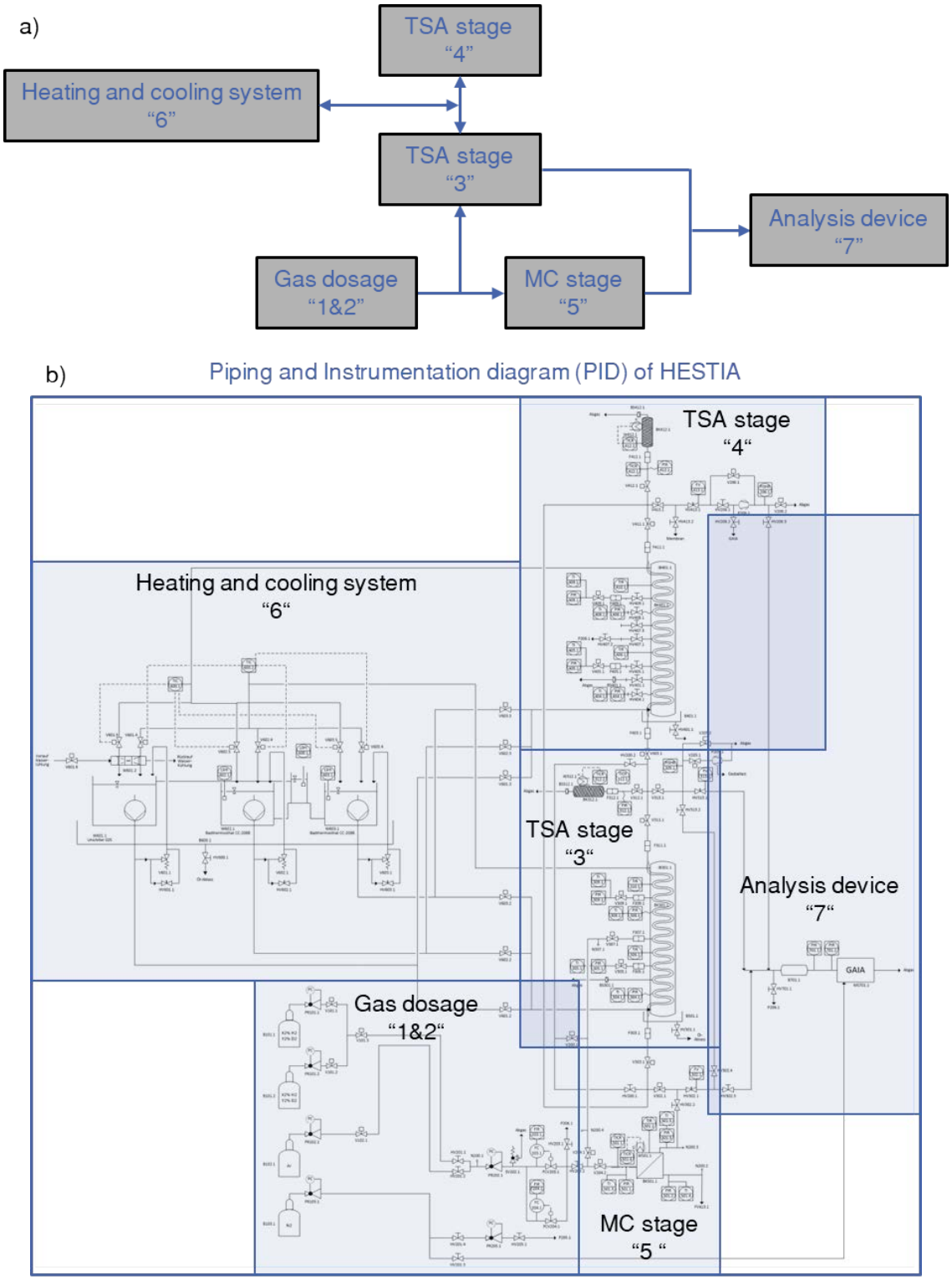

Figure A.5: a) Overview of the individual parts of the PID and b) correlation of the parts in the PID: 1&2) Gas dosage, 3) TSA stage (column 1), 4 TSA stage (column 2), 5) MC stage, 6) Heating and cooling system and 7) Analysis device.

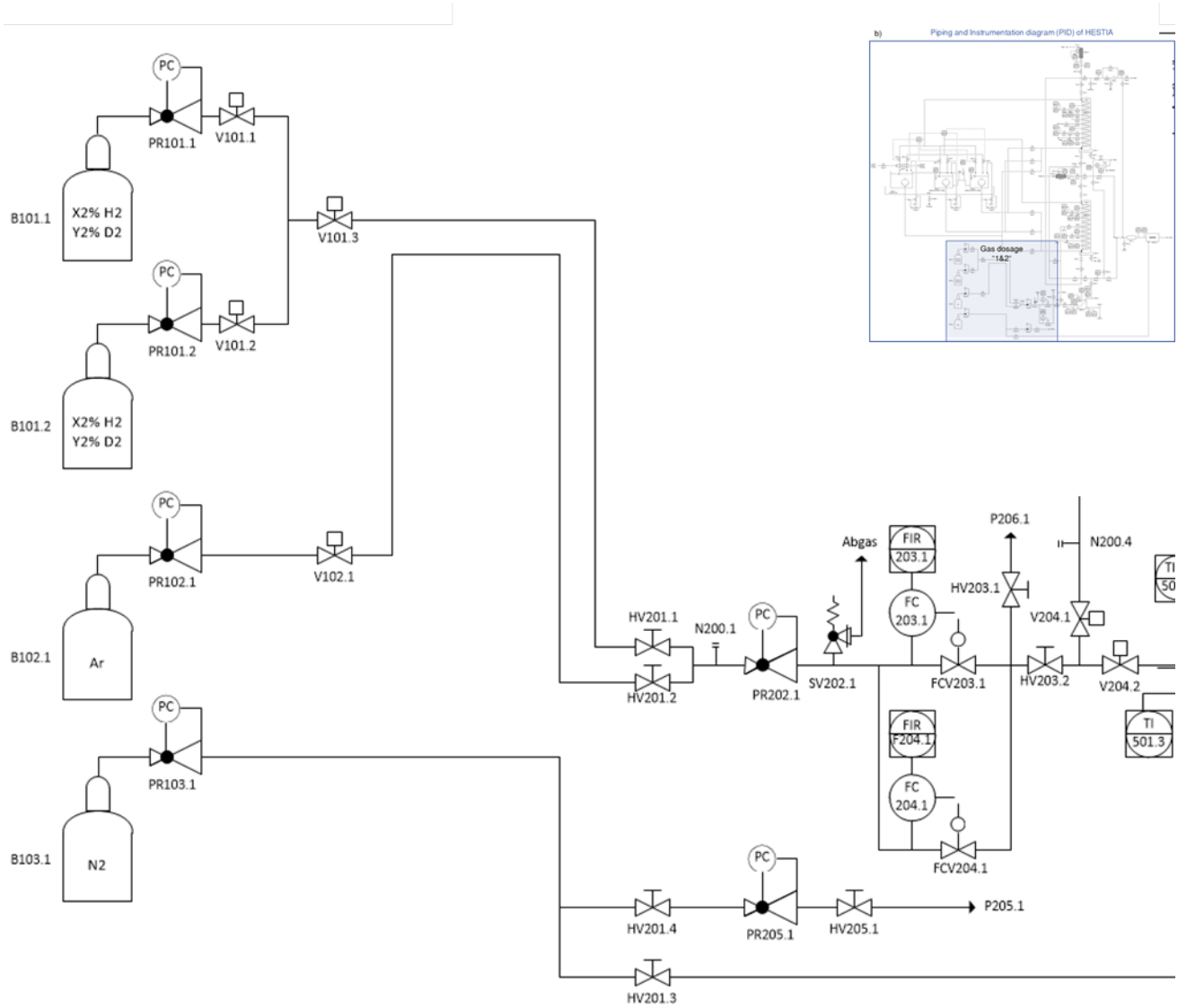

Figure A.6: Gas dosage (part 1&2).

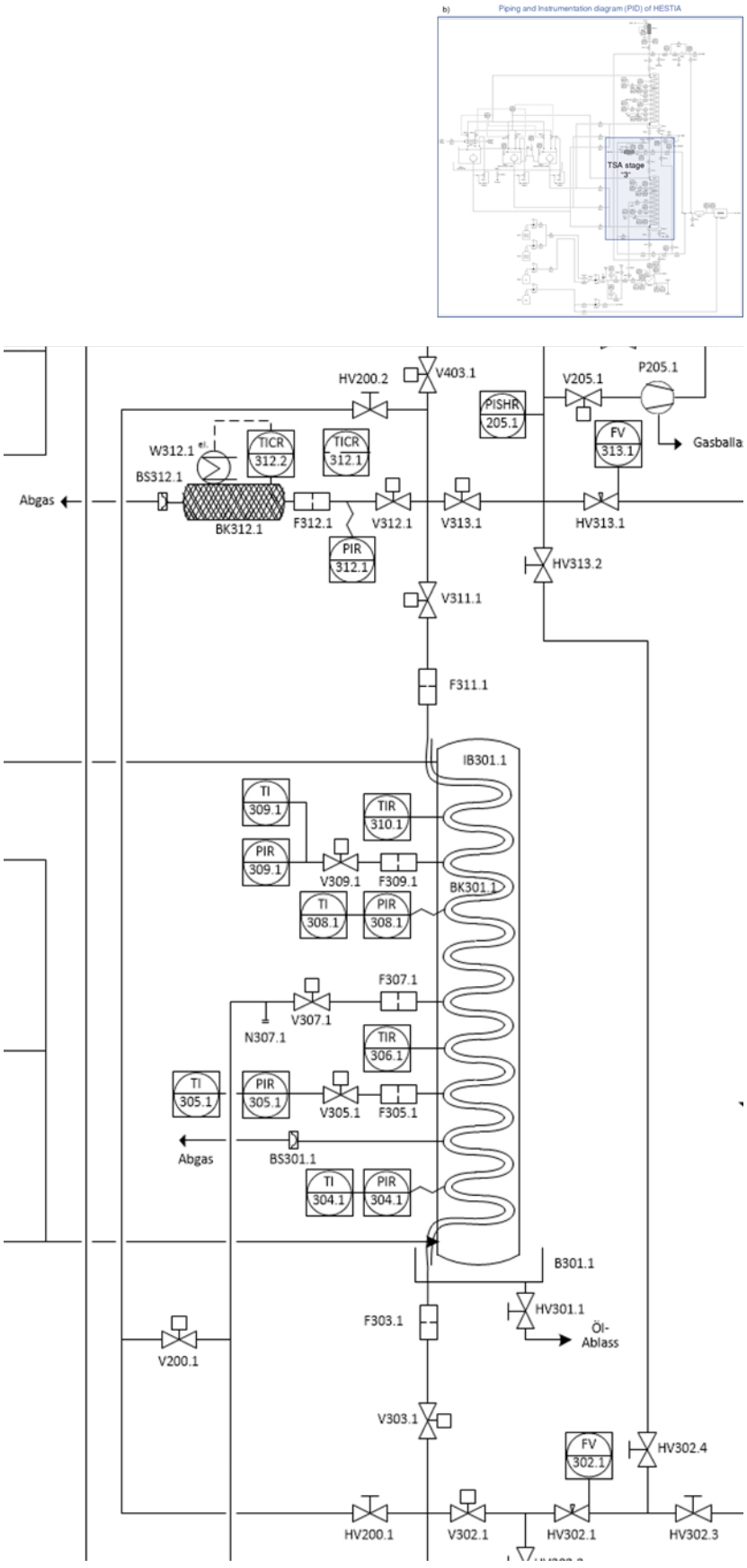

Figure A.7: TSA stage (column 1 filled with Pd; part 3).

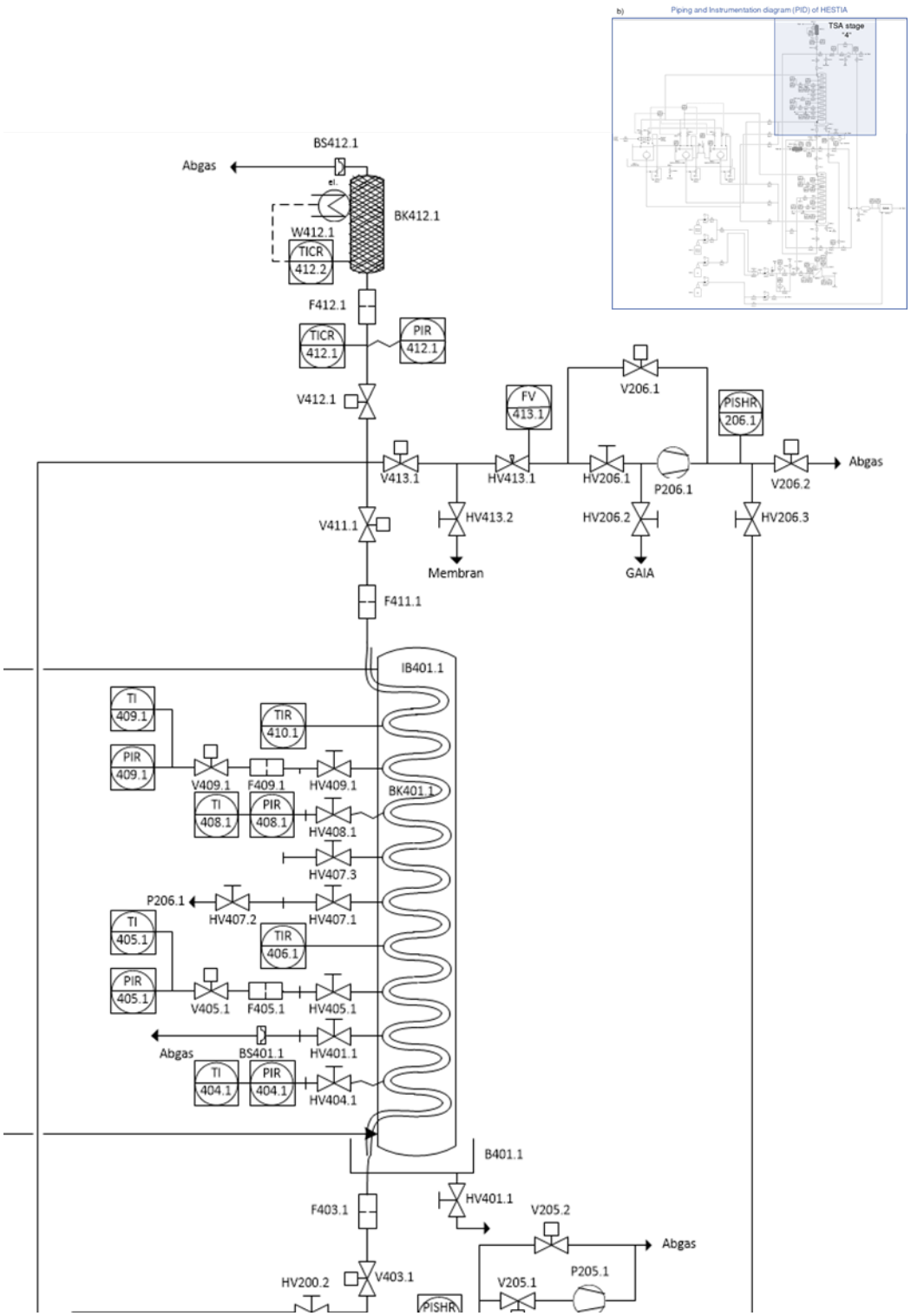

Figure A.8: TSA stage (column 1 filled with $TiCr_{1.5}$, part 4).

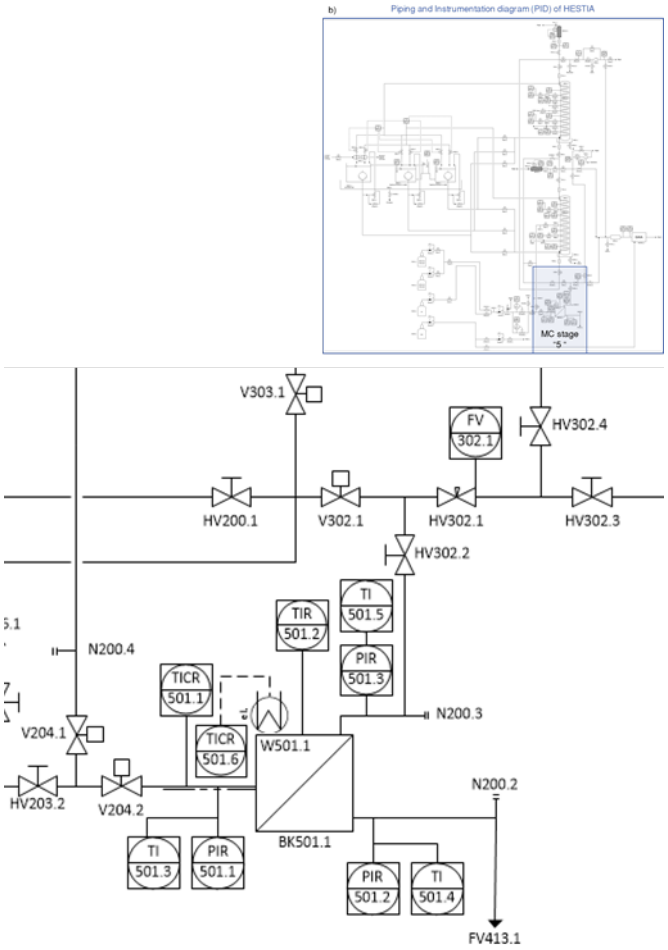

Figure A.9: MC stage (part 5).

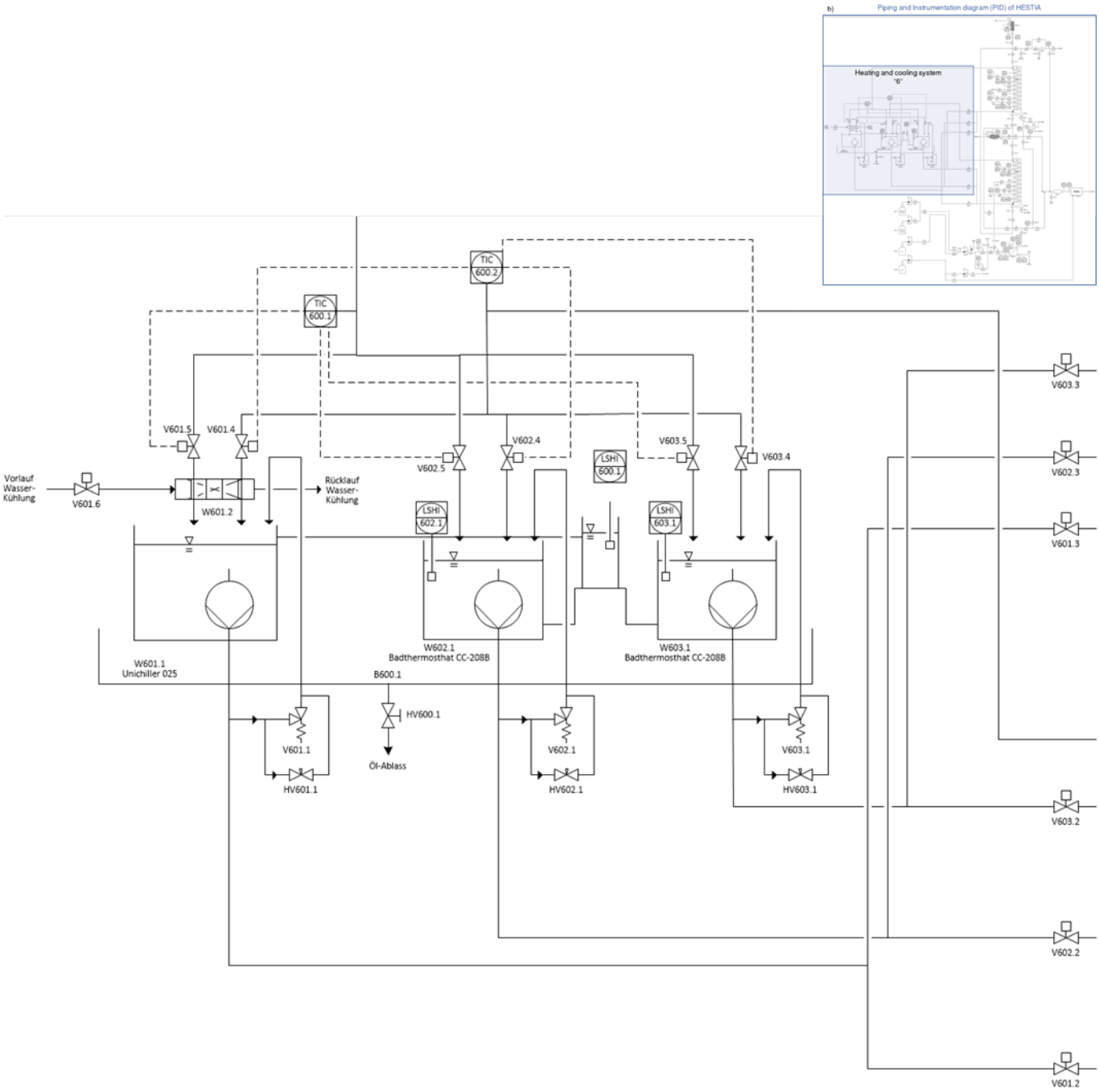

Figure A.10: Heating and cooling system (part 6).

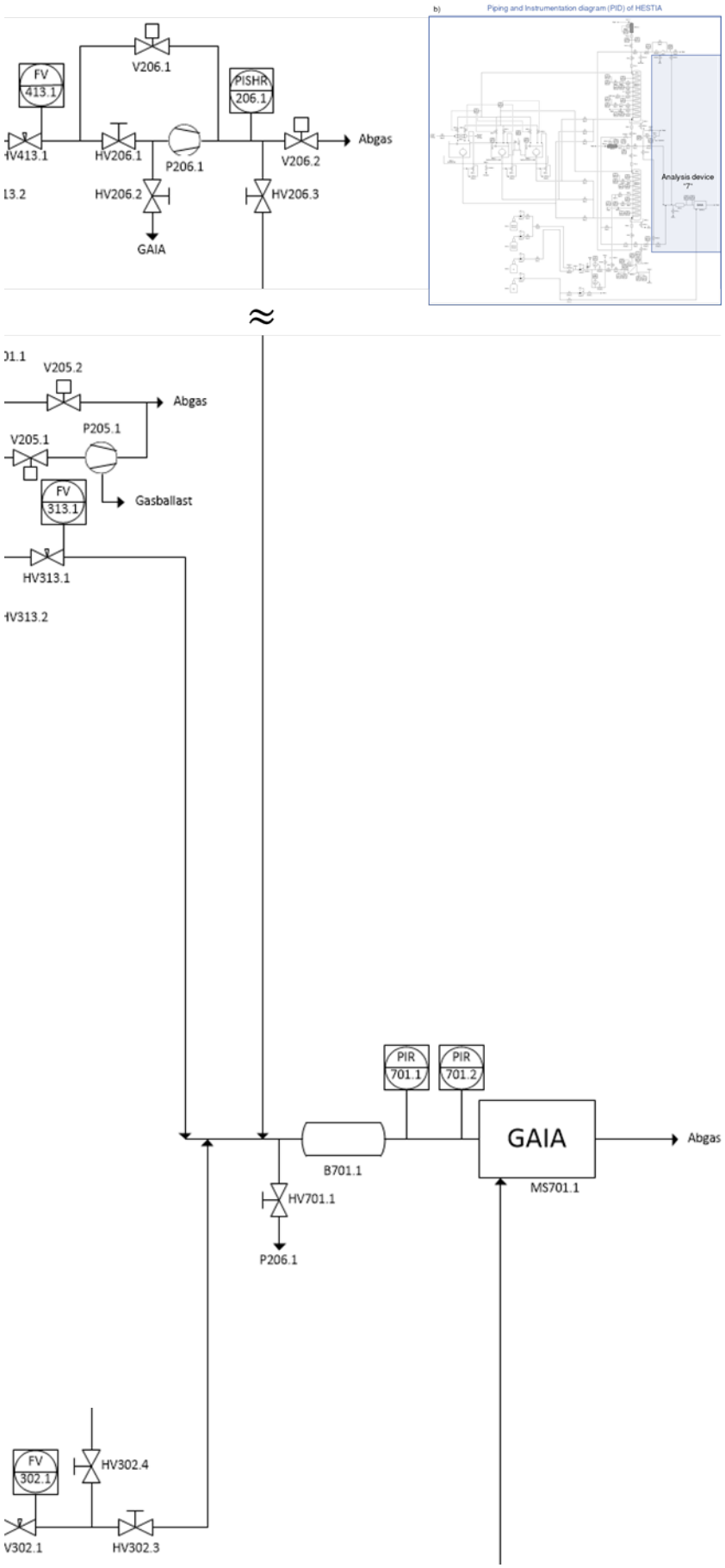

Figure A.11: Analysis device (part 7).

A8 HESTIA – Technical drawing of the columns and the milled heating and cooling plate